Synthetic Aperture Vector Flow Imaging

Villagómez Hoyos, Carlos Armando; Jensen, Jørgen Arendt; Stuart, Matthias Bo

Publication date:
2016

Document Version
Publisher's PDF, also known as Version of record

Citation (APA):
Villagómez Hoyos, C. A., Jensen, J. A., & Stuart, M. B. (2016). Synthetic Aperture Vector Flow Imaging. Technical University of Denmark, Department of Electrical Engineering.

PhD Thesis

Synthetic Aperture Vector Flow Imaging

Carlos Armando Villagómez Hoyos

Supervised by: Prof. Jørgen Arendt Jensen, PhD, Dr. Techn.

Co-supervised by: Matthias Bo Stuart, PhD

Carotid bifurcation during systole

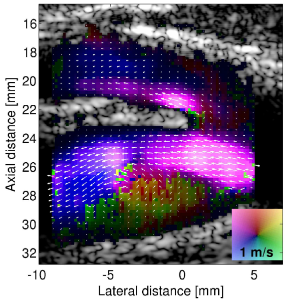

Up-stream Jugular valve before opening

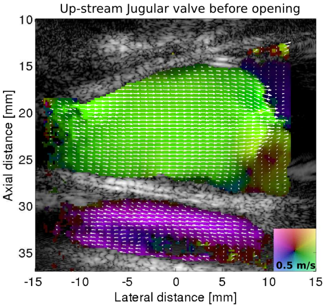

Aortic valve during systole

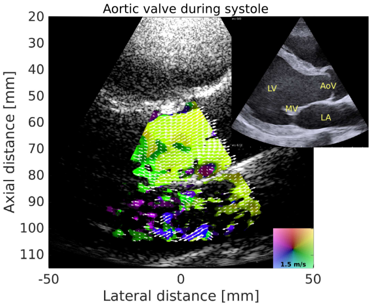

Carotid bifurcation during systole

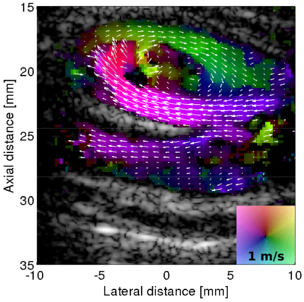

Down-stream Jugular valve before closing

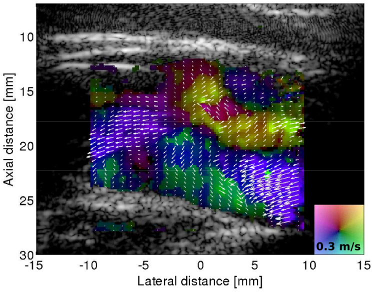

Left ventricle during diastole

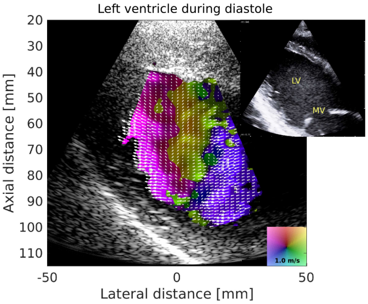

Technical University of Denmark
Kgs. Lyngby, Denmark 2016

Cover image: Synthetic aperture vector flow imaging frames from six different acquisitions. The left column show two distinct carotid bifurcation during systole, both acquisition presents a vortex in the carotid bulb. The center column present two distinct acquisitions of the same jugular vein presenting valves; (top) an up-stream frame just before the flow opens the valve, (bottom) a down-stream frame showing retrograde flow before the valve closes. The right column show two different views of the heart; (top) a standard parasternal long-axis view during systole, (bottom) a modified parasternal long-axis view during the filling stage of the heart.

Technical University of Denmark
Department of Electrical Engineering
Center for Fast Ultrasound Imaging (CFU)
Ørsteds Plads 349
2800 Kgs. Lyngby
DENMARK
Tel: (+45) 4525 3902
Web: www.bme.elektro.dtu.dk
Author e-mail: cavh@elektro.dtu.dk

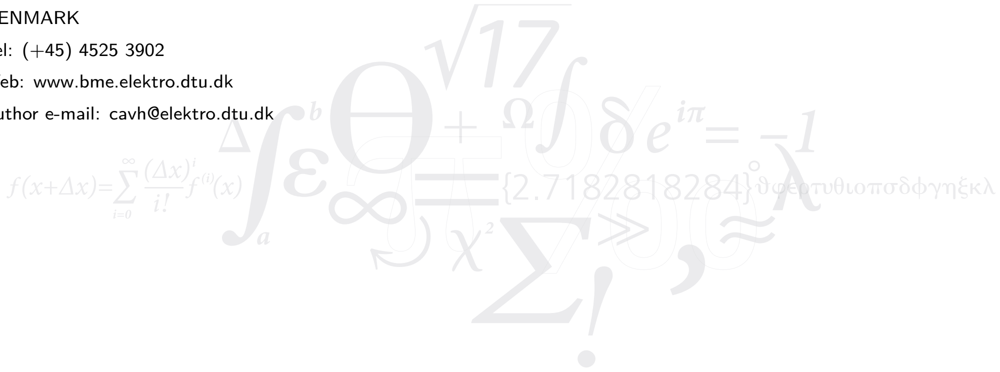

Contents

Preface

This PhD thesis has been submitted to the Department of Electrical Engineering at the Technical University of Denmark in partial fulfillment of the requirements for acquiring the PhD degree. The research providing the foundation for the thesis has been conducted over a period of three years from June 15, 2013, to June 14, 2016 at the Center for Fast Ultrasound Imaging (CFU), Department of Electrical Engineering. The project has been supervised by Prof. Jørgen Arendt Jensen, PhD, Dr. Techn, and co-supervised by Matthias Bo Stuart, PhD. The project was financially supported by grant 024-2008-3 from the Danish Advanced Technology Foundation, BK Medical Aps, Denmark and by Radiometer A/S, Denmark.

Carlos Armando Villagómez Hoyos
Kgs. Lyngby, Denmark
June 2016

Summary

The main objective of this project was to continue the development of a synthetic aperture vector flow estimator. This type of estimator is capable of overcoming two of the major limitations in conventional ultrasound systems: 1) the inability to scan large region of interest with high temporal resolutions; 2) the lack of capability in detecting flow other than the one along the direction of the beam. Addressing these technical limitations would translate in the clinic as a gain in valuable clinical information and a removal of operator-dependant sources of error, which would improve the diagnosis.

The main contribution of this work was the development of an angle estimator which features high accuracy and low standard deviation over the full 360° range. The estimator demonstrated its capability of operating at high frame rates (> 1000 Hz), and simultaneously detecting a large range of flow velocities ($0.05 – 3\,\mathrm{m\,s^{-1}}$). The estimator was also extended to a variety of geometries without major modifications, including a 2-D matrix array for full 3-D velocity estimation. Furthermore, a developed novel energy based tissue echo-canceler provided a new effective perspective for removing the tissue signal, specially when the tissue and flow spectra overlaps. The approach was investigated with a series of flow simulations that included vessel wall movement, and demonstrated its capability of diminish the effects of a moving vessel wall in both simulations and in vivo measurements.

Finally, this thesis showed that novel information can be obtained with vector velocity methods providing quantitative estimates of blood flow and insight into the complexity of the hemodynamics dynamics. This could give the clinician a new tool in assessment and treatment of a broad range of diseases.

Resumé

Hovedformålet med dette projekt var at fortsætte udviklingen af en syntetisk aperatur vektor flow estimator. Denne type af estimator har potentiale til at overkomme to af de største udfordringer, som begrænser konventionelle ultralydssystemer, da de mangler to essentielle egenskaber: 1) evnen til at scanne store områder med høj temporal opløsning; 2) evnen til at estimere blodstrømninger, der løber på tværs af ultralydsbølgens udbredelsesretning. En løsning på disse tekniske begrænsninger ville være en stor gevinst for klinikkerne i form af et værdifuldt klinisk værktøj der fjener operatørafhængige fejlkilder, hvilket ville forbedre diagnosen.

Den primære anledning til, at dette arbejde kunne lade sig gøre, var udviklingen af en vinkelestimator, som besidder lav bias og lav standard afvigelse over alle 360°. Estimatoren demonstrerede sin evne til at operere ved høje frame rates (> 1000 Hz), og samtidig opfange en bred vifte af blodhastigheder($0.05 - 3\,\mathrm{m\,s^{-1}}$). Estimatoren blev også udvidet til en række forskellige transducere uden større modifikationer, inklusiv et 2-D matrix array, der kunne estimere hastighedder i alle tre rumlige dimensioner. Derudover kunne en nyudviklet, energibaseret tissue echo-canceler give et nyt effektivt perspektiv på, hvordan vævsignaler kan fjernes, i særdeleshed når væv- og blodspektre overlapper hinanden. Denne fremgangsmåde blev undersøgt med en række simulationer, som inkluderede bevægelse at karvæggen, og demonstrerede dets evne til at reducere effekterne af bevægelse i karvæggen for både simulationer såvel som *in vivo* målinger.

Denne afhandling viser, at ny information kan opnås ved hjælp af vinkeluafhængige vektorteknikker, som kan tilvejebringe kvantitative målinger, der kan give en øget forståelse af blodets komplekse flowmønstre. Det kan blive et nyttigt redskab for klinikeren i diagnosticeringen og behandlingen af en lang række sygdomme.

Acknowledgements

First of all, I would like to thank my supervisor, Prof. Jørgen Arendt Jensen, who gave me the honor and the privilege to work with him and his exceptional research group, and by offering his support and guidance throughout these three years. I would also like to thank my co-supervisor, Postdoc. Matthias Bo Stuart, who vast knowledge, attention to detail, and guidance has been extremely vital for the completion of this project.

My warmest thanks goes to all of my colleagues at the Center for Fast Ultrasound Imaging, the guys at DTU Nanotech and all the MDs at Rigshospitalet. Thank you for making these three years in the cold Denmark a really warm experience. Special thanks to David Pierson Bradway, Michael Johannes Pihl, Morten Fisher Rasmussen, Thomas Lehrmann Christiansen; who in the first year of my stay embrace me as a friend and make that year the warmest of all. To Mette Funding la Cour that despite the distance kept encouraging me through the three years. To Jacob Bjerring Olesen with whom I have spent many great hours together, and to who I owe the biggest thanks for all the support in not only the elaboration of this thesis but in any aspect of life, thank you for making me feel so welcomed. Further, I would like to thank Caroline Ewertsen, Kristoffer Lindskov Hansen, Simon Holbek, and Tommaso di Ianni that offer some of their precious time to help proof-reading parts of this thesis, and special thank to Elna Sørensen to proof-read the entire thesis.

Finally, a huge thanks goes to my parents for all their affection and love. To my brother and sisters who I miss so much, and to all my family and friends that I left to pursue this dream. Last, but definitely not least, I would like to thank Nanna Staugaard for all your love and unconditional support throughout the final stages of this project.

List of Figures

List of Tables

Abbreviations

2-D	Two-Dimensional
3-D	Three-Dimensional
CFM	Color flow map
DTU	Danmarks Tekniske Universitet (Technical University of Denmark)
$F_{\#}$	f-number, equal to the focal length divided by the aperture diameter
FDA	Food and Drug Administration
PIV	Particle Imaging Velocimetry
PRF	Pulse Repetition Frequency
RF	Radio frequency
Rx	Receive
RT	Residence time
ROI	Region of interest
SAFI	Synthetic aperture flow imaging
SAI	Synthetic aperture imaging
SARUS	Synthetic aperture real-time ultrasound system
SNR	Signal to Noise Ratio
SD	Standard deviation
TO	Transverse oscillation
Tx	Transmit
US	Ultrasound
VFI	Vector flow image

CHAPTER 1

Introduction

1.1 Motivation

The circulatory system is essential for the correct functioning of our body. It is through its extensive network of arteries, capillaries, and veins that the body maintains the cell homeostasis and our well being. This is achieved by the gigantic task of transporting essential messengers (hormones), vital nutrients (such as vitamins and minerals), and removal of cellular and metabolic waste products through the entire body by means of blood flow. In order for such a balance to occur, it is a necessary that blood flow is present along the whole circulatory network. The partial or complete restriction of blood flow would generate a lost of homeostasis, which could derive to cell death, organ failure, and lastly death.

The understanding of the mechanisms that can lead to a failure of the circulatory system is indispensable for the prevention of such events. As research scientists, we know that the understanding of these mechanisms can only be achieved by observation, formulation and testing of hypothesis. However, observation and experimentation on living individuals are difficult to achieve, either for ethical or practical purposes, and it has previously relied on clinical events; sometimes limited to postmortem observations.

The advent of new imaging techniques has enabled the study of the circulatory system, and has facilitated the observations in living individuals. These advancements have dramatically changed the understanding and approach to the study of vascular and cardiovascular diseases. One example is the use of imaging techniques to identify the development of preclinical atherosclerosis lesions in patients. Early detection of such lesions provides a clinical predictor of cardiovascular events (Novo et al. 2013).

A large number of imaging techniques have been proposed for the study of the function of blood vessels, each one of them with their own advantages and limitations. Ultrasound has evolved as one of the important clinical tools for the non-invasive imaging of the circulatory system, as it presents several advantages compared to the other imaging technologies: (1) Safe, as it is based on non-ionizing radiation it does not have the same risks as X-rays or other types of imaging systems that use ionizing radiation; (2) Inexpensive, ultrasound is the least expensive of the imaging modalities; (3) Portable, the only modality that keeps following the Moore's law by becoming smaller, faster, more powerful every year.

In recent years, ultrasound has become the frontline imaging modality for the diagnosis, treatment planning and therapy evaluation of patients. Nevertheless, the lower sensitivities and specificities of ultrasound compared to other imaging modalities have kept it as a pre-diagnosis tool, which results need confirmation from another imaging technique. The reasons are several and are mainly linked to technical limitations of current ultrasound systems, which requires a manual intervention of the operator for counteracting them. This sets a burden on the operators, who even with appropriate training and expertise are not assured of the validity or reproducibility of their results and their diagnosis.

For the last 30 years, research effort has been spent on proposing solutions to overcome these technical limitations. The limitations are several, but some of the most studied ones are: (1) flow dimensionality, which in conventional Doppler ultrasound is limited to one out of three dimensions; (2) temporal and spatial dependencies, which has marked a trade-off between frame-rate and available image size or image quality in conventional systems ; (3) flow sensitivity, where the detection and measurement of slow or high velocities are limited by the traditional measuring principles.

In this PhD project, the aforementioned limitations will be addressed. However, this work is not a single effort but a continuation of years of effort to propose novel solutions to these problems. For example, the appearance of vector flow systems that overcame the dimensionality limitation was first proposed in the 1970s (Hansen, Cross, and Light 1974), then refined into a single transducer simple implementation (Jensen and Munk 1998), and finally implemented into a commercial scanner (VFI Assist, BK ultrasound, 2013). The temporal/spatial independence has previously been achieved by the development of synthetic aperture and plane-wave techniques used in combination with parallel systems (Jensen, Holm, et al. 1999; Sandrin et al. 1999). Lastly, great efforts have been also imposed to the development of new tissue echo-canceling techniques that have improved the flow sensitivity (Demene et al. 2015; Yu and Løvstakken 2010). These previous techniques have paved the way for the work presented in this thesis, where a vector flow technique with temporal/spatial independence and improved flow sensitivity is presented.

1.2 Scientific contributions

The thesis compiles the research presented in a manuscript that has been submitted for publication in an ISI journal, and a patent application that was taken up by Analogic. Additionally, four conference proceedings and an abstract are included in the project. Besides the included papers, the author has contributed to publications on pressure gradients estimation and carotid strain imaging. A full publication list is given below.

1.2.1 Journal papers

I **C. A. Villagómez-Hoyos**, M. B. Stuart, K. L. Hansen, M. B. Nielsen, and J. A. Jensen. Accurate angle estimator for high-frame-rate 2-D vector flow imaging. In *IEEE Trans. Ultrasons., Ferroelec., Freq. Contr.*, Vol. 63, No. 6, 2016, p. 842-853.

1.2.2 Conference papers

II **C. A. Villagómez-Hoyos**, M. B. Stuart, and J. A. Jensen. Increasing the dynamic range of synthetic aperture vector flow imaging. In *Proc. SPIE Ultrasound Imaging. Symp.*, Vol. 9040, 2014.

III **C. A. Villagómez-Hoyos**, M. B. Stuart, and J. A. Jensen. Adaptive multi-lag for synthetic aperture vector flow imaging. In *Proc. IEEE Ultrasons. Symp.*, p. 1722-1725, 2014.

IV **C. A. Villagómez-Hoyos**, M. B. Stuart, and J. A. Jensen. In-vivo high dynamic range vector flow imaging. In *Proc. IEEE Ultrasons. Symp.*, p. 1-4, 2015.

V **C. A. Villagómez-Hoyos**, M. B. Stuart, T. Bechsgaard, M. B. Nielsen, and J. A. Jensen. High frame rate synthetic aperture vector flow imaging for transthoracic echocardiography. In *Proc. SPIE Ultrasound Imaging. Symp.*, Vol. 9790, 2016.

1.2.3 Abstracts

I **C. A. Villagómez-Hoyos**, S. Holbek, M. B. Stuart, and J. A. Jensen. High frame rate synthetic aperture 3D vector flow imaging. In *IEEE Ultrasons. Symp. 2016*, Accepted for oral presentation.

1.2.4 Patent application

I **C. A. Villagomez-Hoyos**, M. B. Stuart, J. B. Olesen, and J. A. Jensen. Novel Tissue Filtering Approach For Perfusion and Slow-Flow Imaging, International Patent Application, December 30, 2015, number: ANA1293-WO.

1.2.5 Second-author journal paper

SA-I J. A. Jensen, M. F. Rasmussen, M. J. Pihl, S. Holbek, **C. A. Villagomez-Hoyos**, D. P. Bradway, M. B. Stuart, and B. T. Tomov. Safety assessment of advanced imaging sequences I: measurements . In *IEEE Trans. Ultrasons., Ferroelec., Freq. Contr.*, Vol. 63, No. 1, 2016, p. 110-119.

1.2.6 Additional papers and patents

Additional publications are listed here in chronological order.

2014

- H. H. G. Hansen, M. B. Stuart, **C. A. Villagomez-Hoyos**, J. A. Jensen and C. L. de Korte. Jensen. Accuracy and Sources of Error for an Angle Independent Volume Flow Estimator. *Proc. IEEE Ultrasons. Symp.*, p. 1814-1817, 2014.

- J. B. Olesen, **C. A. Villagomez-Hoyos**, M. S. Traberg, and J. A. Jensen. Non-invasive estimation of pressure gradients in pulsatile flow using ultrasound. In *Proc. IEEE Ultrasons. Symp.*, p. 2257-2260, 2014.

2015

- E. Moghimirad,**C. A. Villagomez-Hoyos**, A. Mahloojifar, A. B. Mohammadzadeh, and J. A. Jensen. Fourier beamformation of multistatic synthetic aperture ultrasound imaging . In *Proc. IEEE Ultrasons. Symp.*, p. 1-4, 2015.

- J. B. Olesen, **C. A. Villagomez-Hoyos**, M. S. Traberg, and J. A. Jensen. Non-invasive Estimation of Intravascular Pressure Changs using Ultrasound. In *Proc. IEEE Ultrasons. Symp.*, p. 1-4, 2015.

- J. B. Olesen, **C. A. Villagomez-Hoyos**, and J. A. Jensen. Non-invasive Estimation of Intravascular Pressure Changes using Vector Velocity Ultrasound (US), International Patent Application, filed on March 3, 2015, number: ANA1268-WO (BKM-10-7778-PCT).

- J. B. Olesen, **C. A. Villagomez-Hoyos**, and J. A. Jensen. Flow Acceleration Estimation Directly From Beamformed Ultrasound Data, International Patent Application, filed on September 23, 2015, number: ANA1282-WO-US (BKM-10-7837-US-PCT).

2016

- J. B. Olesen, **C. A. Villagomez-Hoyos**, M. S. Traberg, A. J. Y. Chee, B. Y. S. Yiu, C. K. Ho, A. C. H. Yu, and J. A. Jensen. Preliminary investigation of an ultrasound method for estimating pressure changes in deep-positioned vessels. In *Proc. SPIE Ultrasound Imaging. Symp.*, Vol. 9790, 2016.

- R. Moshavegh, J. Jensen, **C. A. Villagomez-Hoyos**, M. B. Stuart, M. C. Hemmsen, and J. A. Jensen. Optimization of synthetic aperture image quality. In *Proc. SPIE Ultrasound Imaging. Symp.*, Vol. 9790, 2016.

1.3 Structure of the thesis

The thesis falls in three parts. After a brief description of the state-of-the-art techniques, the first three chapters are devoted to the angle estimator, which development is the corner stone of this thesis. The subsequent chapter concerns the development of energy based tissue echo-canceler, which proposes a new approach to tackle the flow sensitivity problem. Finally, a chapter is devoted to push forward ideas for clinical applications for the proposed techniques. The thesis is presented as a whole, and the chapters are intended to be read in succession. To improve the flow of the text, not all details from the described studies have been included, and the reader is therefore occasionally referred to the appended papers.

Chapter 2 introduces the state-of-the-art vector flow techniques in parallel systems, giving a brief overview of the previous published literature on vector velocity estimation in ultrasound. The chapter, also, describes the directional beamforming method, which provides the basis for the proposed angle estimator approach.

Chapter 3 presents an overview of the results obtained in the first peer-reviewed paper appended in the project. The work concerns to the experimental validation of the vector velocity estimation using the proposed angle estimator. After briefly giving a theoretical description, the approach is first tested against simulations and measurements of simple straight vessels. Secondly, a spinning disk phantom is simulated to evaluate the overall performance of the angle estimator around the full 360° range. Further, a CFD model of a carotid bifurcation is used in combination with simulations to assess the method at more clinical similar setting. Finally, an *in vivo* example on the carotid bifurcation of a healthy volunteer is presented.

Chapter 4 presents an investigation on the range of the detectable blood velocities using the proposed method. The maximum velocity is explored first, where simulations and a measurement on a 70% constriction phantom are used for the study. The study investigates the low velocity limit and with the use of continuous data proposes an adaptive lag to expand its low velocity range.

Chapter 5 follows the findings from Chapter 3 and makes an expansion of the proposed technique to a larger set of transducer geometries and ultrasound waves. It performs a spinning disk study in each of the geometries and assesses its performance along the 360° range. The chapter is closed with a proof-of-concept example of the extension of the proposed method to a full 3-D vector velocity estimates by the use of a matrix array probe.

Chapter 6 deviates from the previous chapters as it presents a new perspective on tissue echo-canceling. The energy based approach is first introduced and then investigated against straight vessel simulations with a moving vessel wall. The study is followed by the proposal of an adaptive method for automatically estimating the energy threshold required in the energy based approach. Finally, *in vivo* investigations of the method are presented. The proposed technique was taken up by Analogic, who in collaboration with the author wrote the patent proposal included in the project.

Chapter 7 puts forward ideas on clinical applications for the developed vector velocity estimator and tissue echo-canceler. The chapter is devoted primarily to applications related to atherosclerosis, which is closely related to cardio-vascular diseases. The chapter closes on a proof-of-concept example of flow quantification in small vasculature.

Chapter 8 concludes the thesis by summarizing some of the major learnings that were achieved in the process of overcoming the current ultrasound limitations. The chapter further provides suggestions for future research, before putting the project into perspective.

CHAPTER 2

Vector flow imaging in parallel systems

2.1 A historic perspective

In 1979 Delannoy proposed one of the first ultrasound analog parallel processing system, primarily designed for fast cardiac imaging (Delannoy et al. 1979). The system was capable of generating 20 beamformed lines simultaneously and was a big breakthrough in parallel technology. However, the appearance of large grating lobes artefacts due to the unavailability of transducers with enough spatial sampling limited its cardiac application.

In 1984, Shattuck proposed another analog parallel system (Shattuck et al. 1984), where additional tapped delay lines were added after the conventional ones, achieving four-to-one lines parallelism. The approach was implemented on a Siemens scanner and dramatically improved the image quality in cardiac applications. However, the approach required the use of low-noise analog delay lines, which were expensive and complicated to manufacture, making systems with large channel count prohibitive.

In the late 1980s, Trahey and co-workers proposed one of the first attempts to measure 2-D blood vector flow using a parallel processing approach (G. E. Trahey, Allison, and Ramm 1987). Even though the acquisition was not truly parallel, since the ultrasound scanner operated in a conventional sequential fashion, it was possible to estimate 2-D velocities in an entire scan region without sacrificing any frame rate. However, due to the sequential nature of the scanner, the frame rate was limited to 12 Hz, and the detectable velocities to 12 mm/s. Furthermore, Trahey and co-workers had to modify the approach to work within a sequential context in a line-by-line acquisition to increase the velocity range and to avoid decorrelation issues (L. N. Bohs, Friemal, et al. 1993). Although the velocity range was increased, the performance was degraded by speckle motion occurring in between line acquisitions (L. Bohs, Friemel, and G. Trahey 1995). They hypothesized that a parallel processing would solve these problems (L. N. Bohs, Geiman, et al. 2000). It was not until 20 years later that Trahey's hypothesis was confirmed through means of plane-waves and parallel processing (Udesen et al. 2008).

In the 1990s, the widespread availability of digital beamformers changed the design of ultrasound systems. Digital beamformers permitted high precision imaging with a very simple system architecture. As higher channel count systems became available the development of parallel processing methods also came along. One of them known as

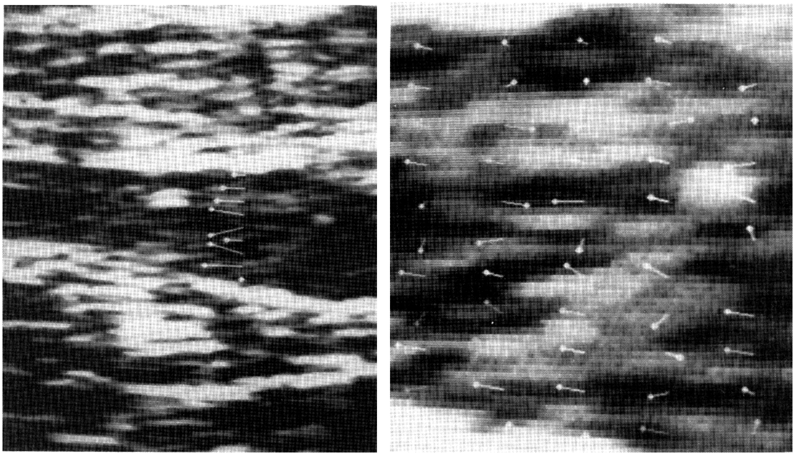

(a) (b)

Figure 2.1: (a) First 2-D vector flow image from popliteal vein estimated using speckle tracking. The velocity field could be estimated in the whole scan region without sacrificing frame rate. (b) Magnified image of the popliteal vein. Obtained from (G. E. Trahey, Allison, and Ramm 1987)

synthetic aperture (SA) became popular due to its flexibility on system architectures (Karaman, Li, and O'Donnell 1995; O'Donnell and Thomas 1992; Ozaki et al. 1988). The approach, which reconstructed the entire image by applying the appropriate delays to each digitized channel and then summed the contributions of each element, did not require the complete simultaneous acquisition of the element signals, however, it required that the target was kept motionless or was motion compensated. The appearance of full digital parallel systems with high sampling rates (>15MHz), large ADC bit counts (> 8 bits), and large memories was until the end of the 1990s. One of the first research parallel system was built by Jensen and colleagues, which consisted of 64 simultaneous sampled channels at 40 MHz and 12 bits precision (J. A. Jensen, Holm, et al. 1999). Additionally, around the same time another system was introduced by Sandrin, which also had 64 channels sampling at 30 MHz but only with a 8 bit precision (Sandrin et al. 1999). Both systems were capable of acquiring data for parallel beamformation and performing successive velocity estimation, however, Sandrin's 8 bit system, with a smaller dynamic range (48dB), was limited to tissue only applications when measuring *in-vivo*.

Following the two pioneers, more parallel acquisition research systems emerged in the 2000s (Lu, Cheng, and Wang 2006; Tortoli, Bassi, et al. 2009), and some became commercially available for research during the early 2010s (Sonix DAQ, Verasonics Vantage). The new research platforms provided new research capabilities and permitted the development of a variety of different methods for estimating blood velocities. Today, the availability of large computational capability from new GPUs architectures, capable of massive parallel processing, has taken these techniques a step closer to practical implementations in the clinic.

2.2 Technical background

2.2.1 Imaging principle

The imaging principle in parallel ultrasound systems is, as in sequential systems, based on time-of-flight calculations. The time-of-flight is the time it takes for an emitted ultrasound wave to travel through a media and reach a receiver. The time-of-flight can be estimated for the whole scan region if the characteristics of the media, such as the speed of sound, are known. If these characteristics are unknown, assumptions must be made to calculate the time-of-flight. The assumptions can be many and can each affect the resulting image to a different degree; in this work the subsequent assumptions are made: (1) the media has a constant speed of sound; (2) the Green function is a spherical Dirac delta; (3) no secondary scattering (Born approximation). Thus, with this assumptions the time-of-flight is directly calculated as the distance divided by the media's speed of sound.

For a pulse-echo system such as the one illustrated in Fig. 2.2(a), the time-of-flight is decomposed as the sum of the transmit time and receive time. In these systems the time-of-flight is not unique for a single point, given the transmit/receive pair, but it lays in an elliptical time-of-flight curve as illustrated in Fig. 2.2(b). Therefore, to clearly distinguish the desired point, a set of distinct receive elements can be used to focus (add up coherently) the energy coming for the selected position (main lobe), and lower energy coming from other regions (side lobes), as illustrated in Fig. 2.2(c). The principle of reciprocity is still valid, so that the receive elements can be interchanged by transmit elements generating the same focus, as illustrated in Fig. 2.2(d). This principle is fundamental in synthetic aperture, where combinations of transmit and receive elements are used to form fully focused images.

The use of distinct transmit/receive combinations has been thoroughly investigated in parallel systems, such as synthetic aperture (Montaldo et al. 2009; Nikolov 2001). The consequence of these combinations can be summarized within the point spread function (PSF), which is the response of the ultrasound imaging system to a point source. From a signal processing perspective, the PSF fully represents the response of an ultrasound system. As the PSF reflects the performance of ultrasound systems is important to characterize it. The PSF shape is normally characterized by a different set of metrics; a conventionally accepted metric for the PSF is the full width at half-maximum which defines the axial and lateral resolution. Another metric is the cystic resolution, which is measured as the ratio of energy inside the resolution ellipse (mainlobe) and the energy

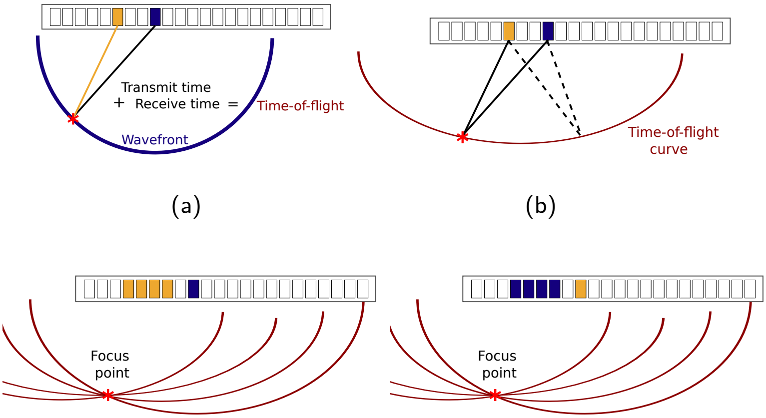

(a) (b)

(c) (d)

Figure 2.2: (a) Time-of-flight calculation for a single transmit/receive pair. (b) Scatterers echoes laying on the time-of-flight curve that will contribute to the received signal. (c) Distinct receive elements can be used to focus, add up coherently, the signal from the desired focusing point. (d) The principle of reciprocity can be applied, which freely interchanges the transmitters and receivers.

outside (sidelobes) at a given radius (Ranganathan and Walker 2007). Additionally, the steering angle or the angle in which the higher frequency content is present is also important. It is worth noticing that PSFs in an ultrasound systems are spatially variant, thus, their characteristics will vary in space and this will affect the performance of the velocity estimation methods.

2.2.2 Velocity estimation principle

The first 1-D velocity estimation systems in ultrasound were based in a continuous wave operation; which made use of the Doppler frequency shift principle, however, it did not have any spatial resolving capabilities along its scan line. To obtain spatial resolving capabilities, ultrasound systems operating within a pulse-echo scheme were proposed (Baker and Watkins 1967). The systems operated by emitting an ultrasound pulse, where a snapshot of the scatterers along the ultrasound beam was created, subsequently a second pulse was used for obtaining a second snapshot. The snapshots were compared to obtain a spatial shift, and thus, a velocity. In literature different techniques have been proposed for obtaining the spatial shift, the two more widespread one are the phase shift estimator and the spatial/time shift estimator.

2.2.2.1 Phase shift estimator

The phase shift estimator is the most used velocity estimator in pulse-echo ultrasound systems, primarily due to its computational efficiency. The estimator calculates the velocity by determining the phase shift between two subsequent acquired signals. The signals are assumed to be pure sinusoidal tones (narrowband) within a certain frequency, which in general matches the transmitted frequency. However, the received signals are not necessarily pure sinusoidal tones due to the pulse-echo nature of the system, random distribution of scatterers, attenuation, etc. An example of two subsequent blood ultrasound signals is shown in Fig. 2.3, the received signals are shown on top, and the instantaneous phase shift at the bottom.

The instantaneous phase shift is obtained by subtracting the instantaneous phases,

$$\begin{aligned}\frac{\Delta\phi(t_n)}{\Delta t_n} &= \phi(t_n) - \phi(t_{n-1}) \\ &= \arctan\left(\frac{y(t_n)}{x(t_n)}\right) - \arctan\left(\frac{y(t_{n-1})}{x(t_{n-1})}\right), \end{aligned} \tag{2.1}$$

from the received sampled quadrature ultrasound signal $r_s(t_n) = x(t_n) + jy(t_n)$.

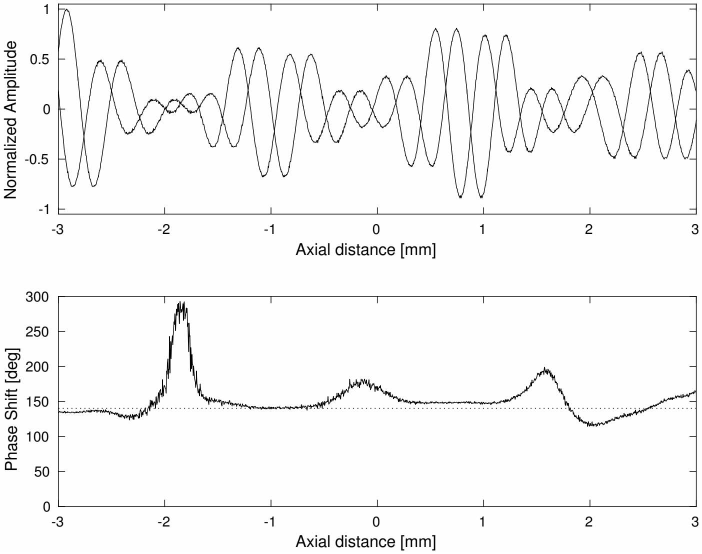

Figure 2.3: (Top) Example of subsequent received ultrasound signals. (Bottom) Estimated instantaneous phase shift and correct phase shift at f_0 denoted by the dotted line.

The velocity is subsequently estimated from the phase shift

$$v_z = -\frac{c}{2\pi f_0 \cdot 2T_{prf}} \cdot \arctan\left(\frac{y(t_n)x(t_{n-1}) - y(t_{n-1})x(t_n)}{x(t_n)x(t_{n-1}) + y(t_n)y(t_{n-1})}\right), \tag{2.2}$$

where f_0 denotes the assumed center frequency, c the speed of sound, and T_{prf} the pulse repetition frequency.

One major concern of the method is its narrowband assumption, since whenever the condition is not met, errors will arise from the estimated instantaneous phase measurement. The reason is that the instantaneous phase is a ponderate sum of the instantaneous phases from all the frequencies in the signal and not only from the assumed frequency. This effect can be observed in Fig. 2.3, where inside the segments the center frequency f_0 becomes smaller, the instantaneous phase drifts, and noise increases. Thus, a similar effect from tissue attenuation will be found, which varying effect of the frequency content will drift the instantaneous phase. Additionally, the phase shift estimator is aliasing limited, where the phase shift cannot be unambiguously determined when phase shifts are larger than 180°.

Improvements on the estimator have been proposed to counteract some of these effects; e.g. averaging over the pulse length (J. A. Jensen 1996), 2D broadband phase-domain techniques (Loupas, Powers, and Gill 1995), etc. Despite the disadvantages, the estimator has remained widely used in the clinic due to its easy and efficient implementation.

2.2.2.2 SPATIAL/TIME SHIFT ESTIMATOR

Unlike the phase shift estimator, the spatial/time shift estimator does not make any assumption on the frequency content of a signal and therefore has access to the full information carried by it. The time shift estimator is based on cross-correlation, which represents one of the fundamental and most thoroughly investigated tools in digital signal processing.

Cross-correlation in the time domain is defined as the sliding dot product of two signals,

$$R_{12}(\tau) = \frac{1}{2T}\int_T r_{s1}(t) r_{s2}(t+\tau)dt, \tag{2.3}$$

where $r_{s1}(t)$ and $r_{s2(t)}$ are the signal to correlate.

However, a more intuitive explanation can be obtained if the cross-correlation is expressed in the Fourier domain by using the convolution theorem,

$$\begin{aligned} \mathcal{F}\{R_{12}(\tau)\} &= \mathcal{F}\{r_{s1}(t)\}\left(\mathcal{F}\{r_{s2}(t)\}\right)^* && (2.4)\\ &= |R_{s1}||R_{s2}| \exp^{j(\phi_{s2}-\phi_{s1})}, && (2.5) \end{aligned}$$

where the operation is described as the multiplication of the spectra amplitude and subtraction of the spectra phases.

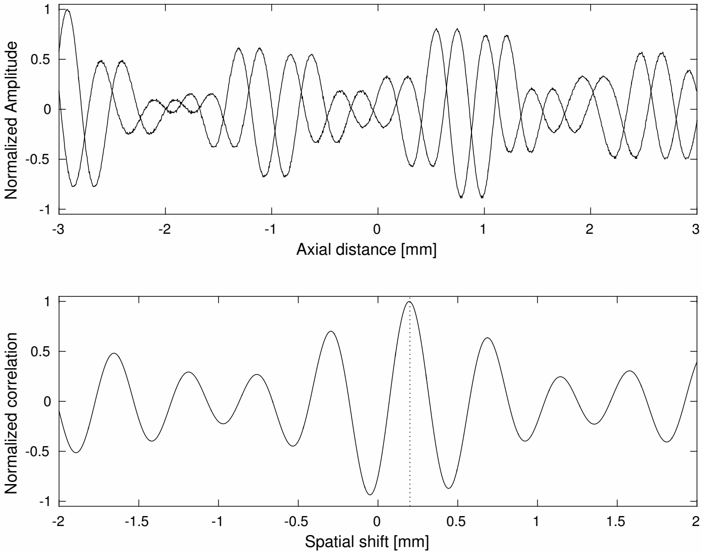

Figure 2.4: (Top) Example of subsequent received ultrasound signals. (Bottom) Estimated spatial shift and correct spatial shift denoted by the dotted line.

Therefore, for a narrowband signal the cross-correlation would be equivalent to a phase shift estimation, and the resulting $R_{12}(\tau)$ would be a sinusoid with the phase equivalent to the phase shift. When operating in a broadband term, the resulting signal will be the in-phase sum of the distinct weighted frequencies, thus, the frequencies containing the same spatial shift will add up and generate a peak in that position, as shown in Fig. 2.4.

In ultrasound velocity estimation, the relevance of the cross-correlation was first demonstrated by Bonnefous and Pesqué (Bonnefous, Pesqué, and Bernard 1986). Their work had a great impact, because it caused researchers to reconsider the established Doppler frequency-shift paradigm and think of the velocity estimation in terms of backscattered signal time shifts between successive snapshots. Despite the superior performance of the cross-correlation estimator compared to the phase shift estimator (Hoeks et al. 1993), the estimator was rarely implemented in commercial systems. The reason for this has been normally attributed to computational expense of the algorithm, even though computational efficient implementations were also available (J. A. Jensen 1993). However, another reason could be the high sensitivity of the method to signal decorrelation and velocity gradients, as investigated by Foster (Foster, Embree, and O'Brien 1990). The performance of the estimator highly degrades when higher beam-to-flow angles are investigated.

2.3 Previous Literature

The availability of complete scan regions with the use of parallel systems has shifted the research towards techniques used in image processing disciplines, where estimation of 2-D or 3-D velocity components by the use of e.g. particle image velocimetry is widely accepted (Raffel et al. 2007). From an image processing perspective, a velocity estimation is performed by the measurement of spatial shifts from subsequent snapshots and dividing it by the time between them. However, in ultrasound, due to the coherent nature of ultrasound signals and the interference patterns generated by a random distribution of scatterers, measuring the spatial shift is not straightforward.

In this section a brief overview of previously proposed techniques for measuring the additional velocity components using ultrasound is presented. The section starts with speckle tracking, being this the first approach to measures the 2/3-D blood scatterers displacements in a parallel system context (G. E. Trahey, Allison, and Ramm 1987). Its followed by cross-beam method, which is a trigonometric extension of conventional 1-D methods for measuring 2/3-D blood velocities and has been recently extended to parallel systems with the use of plane waves (Ekroll et al. 2013). Finally, the transverse oscillation method is reviewed, which parallel system implementation has been also investigated (Lenge et al. 2015).

Its important to acknowledge the existence of other velocity estimation methods that are not covered in this section. Most notably, the ones based on the intrisic spectral broadening principle (Newhouse et al. 1987), from which accurate angle estimators have been also developed (Tortoli, Bambi, and Ricci 2006), and most recently have been proof to measure out-of-plane components as well (Osmanski, Montaldo, and Tanter 2015). Fourier based methods are not covered(Oddershede et al. 2008; Wilson 1991).

2.3.1 Speckle Tracking method

The first technique that measured 2-D blood velocities designed for parallel ultrasound systems was speckle tracking (G. E. Trahey, Allison, and Ramm 1987). It was adapted from particle image velocimetry (PIV), an optical method for flow estimation in experimental fluid dynamics developed in the early 1980s (Adrian 1991). Thus, speckle tracking operates under the same principles as optical PIV, where closely timed images are compared for estimating the distance tracer particles have travelled during this time.

In blood flow ultrasound tracking, the tracer particles are the blood cells themselves, unless contrast agents are used (Kim, Hertzberg, and Shandas 2004). Speckle refer then to the interference patterns created by many sub-resolution blood cells scatterers. Therefore, the local brightness of the speckle pattern reflects the local echogenicity of the underlying blood scatterers, which can be used to estimate the motion. The speckle displacements are commonly determined by means of optical flow (Mailloux et al. 1989), or block matching techniques (Yeung, Levinson, and Parker 1998). Block-matching is usually better adapted to extract the relatively large displacements occurring in blood flows. Although several block-matching algorithms have been inspired from computer vision, the normalized cross-correlation is the most applied approach in ultrasound imaging.

Speckle tracking is basically a three-step process: (1) splitting the image in small template kernels; (2) normalized cross-correlation of the template kernel within a larger search kernel for finding the peak; (3) peak fitting and estimation of the displacements. The cross-correlation can be performed either on the beamformed RF (radio-frequency) signals or on the log-compressed real envelopes (B-mode images).

A disadvantage of the speckle tracking algorithm is that the performance of it is closely related to the selection of the kernels' sizes. Where a larger template kernel size results in an improvement in the performance due to the increased uniqueness of the kernel (Ramamurthy and G. E. Trahey 1991). However, as this template kernel size increases the spatial velocity resolution degrades. Another parameter to adjust is the size search region kernel, which defines the maximum axial and lateral displacements that can be detected. Making a search region large for the purpose of detecting larger velocities will also provoke an increase in the false peak detection probability. A work around for detecting higher velocities is to use high frame rate techniques to reduce the inter-frame displacements, and thereby using smaller search kernels. Despite the disadvantages, speckle tracking is a promising technique for flow estimation and has been proved to work well in-vivo (Fadnes et al. 2014; Hansen, Udesen, Gran, et al. 2009).

2.3.2 Cross-Beam methods

The use of beams from different angles to derive the 2-D/3-D velocity components can be considered as one of the earliest approaches developed in the field (Dunmire et al. 2000). In this early developments two or three fixed transducers would be aimed to measure 1-D velocity components, and subsequently triangulating the velocity vector at a small scan region. The velocity components can be measured by any of the 1-D methods reviewed in section 2.2.2, however, due to its simplicity and spatial resolving capabilities the phase shift estimator was generally preferred. However, given this choice the velocity range in such systems will be essentially limited by aliasing; determined by the T_{prf} and angle of flow relative to either transducer.

In current cross-beam implementations on parallel systems, the velocity estimation is performed using the same principles as the ones proposed by the early developers. The availability of parallel beamformers has enabled the extension of scan regions to whole image planes (Ekroll et al. 2013). The computational simplicity of 1-D estimators applied to such cross-beam methods is one of its advantages, since enables real-time implementations on current scanner technologies (Ricci, Bassi, and Tortoli 2014). However, this simplicity comes with a sacrifice, as the lateral resolution has to be kept low to achieve the 1-D simplification that the method requires. This trade-off was well known in the early Doppler systems, where higher F-numbers were used to diminish the effects of the transit times of the blood scatterers at larger angles (Griffith, Brody, and Goodman 1976). Surprisingly, the effects of transit times and F-numbers are not mentioned in recent parallel cross-beam implementations, which are generally used for large beam-to-flow angles. Nevertheless, these effects are still present on such parallel implementations since they rely on the 1-D simplification of earlier systems. Therefore, in the same way beam-width was traded for better accuracy at larger angles in earlier systems, lateral resolution must be traded for better accuracy in the more recent cross-beam parallel implementations.

2.3.3 Transverse Oscillation method

The basic idea in transverse oscillation (TO) was introduced by Jensen, Munk and Anderson (Anderson 1998; J. A. Jensen and Munk 1998), and consisted in creating an overlaying transverse field on top of the PSF of the ultrasound system. The transverse oscillation was originally generated by the use of two receive apodization peaks, but new k-space based approaches have also emerged (Liebgott 2010).

The TO method was originally conceived for a line-by-line acquisitions setups, however, recent research on parallel systems using plane wave in combination with TO has yielded promising results (J. Jensen, Stuart, and J. A. Jensen 2015; Lenge et al. 2015). Despite these encouraging results, it has to be kept in mind that the TO algorithm is still based in a phase shift method, which is limited by aliasing, and even though the oscillation period at the transverse direction can be selected dynamically, it cannot exceed the PSF lateral size, which is determined by the aperture size (F-number).

2.4 The directional beamforming method

In 2003, Jensen (J. A. Jensen 2003), as an extension of Bonnefous' idea of lateral beamforming (Bonnefous 1988), introduced the idea of directional lines. The technique took advantage of the availability of element RF-data obtained from an in-house parallel research system (J. A. Jensen, Holm, et al. 1999), to beamform receive beams in any desirable direction.

The capability of focusing in arbitrary directions other than the ultrasound beam, allowed for the beamforming along the blood flow direction. The advantage of this beamforming strategy is that the signal correlation is kept higher along the flow direction. Therefore, enabling the capability of estimating larger displacements if the flow direction is known. The directional beamforming method has been validated in the clinic and showed promising results, especially when used in combination with synthetic aperture techniques (Hansen, Udesen, Oddershede, et al. 2009).

2.4.1 Basic principle

The basic idea of the velocity estimation process is illustrated in Fig. 2.5(a), where ellipses are used to represent a PSF response of an upward-right moving scatterer during four subsequent emissions. The two distinct transmit beams ($M = 2$), illustrated in this sequence, are represented in either gray or blue. For each transmit beam, a directional line is focused along the movement direction (θ). The beamformed directional line $g(r, \theta_{line})$, centred on the desired velocity estimation point $\vec{p}$ with a beamformed angle of θ_{line}, is taken at two subsequent snapshots.

The signals snapshots $g(r, \theta_{line})$ from the same transmitted beam, illustrated in Fig.2.5(b), are then cross-correlated. The cross-correlation, described in Sec. 2.2.2.2, results in an estimated displacement (d), which divided by the effective time between emissions yields the velocity magnitude. The directional velocity estimation is thoroughly described by Jensen (J. A. Jensen 2003), the reader is referred to his paper for further details.

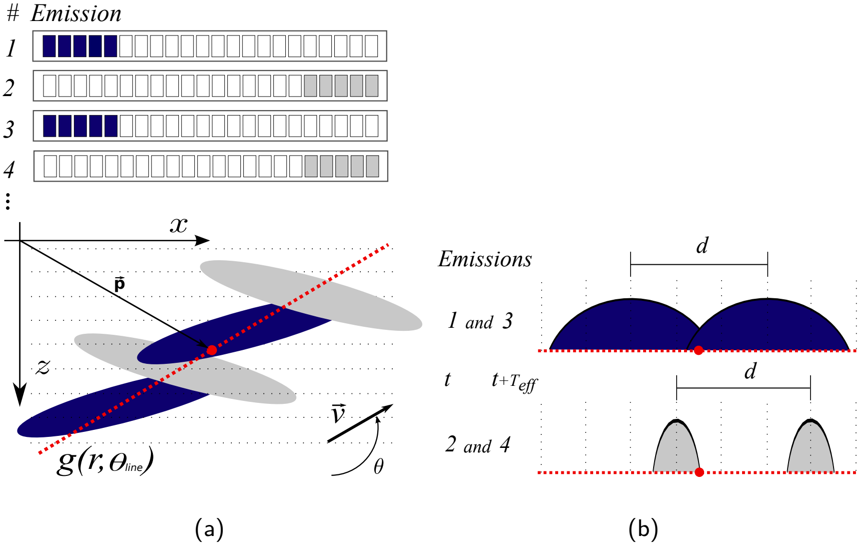

(a) (b)

Figure 2.5: Point spread functions of a moving scatterer from 4 firings of a sequence using $M = 2$ distinct transmit beams. (a) The directional line $g(r, \theta_{line})$ centred at estimation point $\vec{p}$, represented by the red dotted line, is beamformed at each emission in the angle θ_{line} coinciding with the movement direction θ. (b) Cross-sectional area of the point spread functions crossed as seen by the directional line. Emissions from the same transmit beam are correlated to obtain the spatial shift d. Obtained from (Villagomez-Hoyos et al. 2016)

CHAPTER 3

An accurate angle estimator: Experimental validation

Summary *This chapter presents an overview of the findings made in the peer-reviewed paper that is included in the project. The paper concerns of a novel approach for accurately estimating 2-D flow angles using a high-frame-rate ultrasound method. This chapter provides a brief description of the basic principle behind the estimator, and the experimental set-up used for its validation. For a further in-depth explanation of the technical details, the reader is referred to Paper I in Appendix.*

3.1 Basic principle

The proposed angle estimation is based on a numerical triangulation algorithm. The triangulation is performed over directional velocity estimates obtained from distinct transmit beams. The proposed method follows the same principles as other triangulation methods such as the cross-beam method, introduced in Sec. 2.3.2. However, unlike previously described techniques this method operates in a 2-D regime, thus, the 1-D directional velocity estimates are direct projections of a 2-D dataset.

The numerical triangulation is performed by first projecting 2-D data onto a 1-D polar grid of directional velocities centered at the estimation point. The directional velocities are then estimated along a set of beamformed angles (θ_{line}), as described in section 2.4. The beamformed angles are distributed to cover the full 360° range, as illustrated in Fig. 3.1 (top). The numerical triangulation then consists on finding the intersection point between the estimated directional velocities curves for each PSF, as shown in Fig. 3.1 (bottom). The distinct PSFs are generated by using different transmit/receive beams as investigated by Nikolov (Nikolov 2001).

The intersection point between the estimated velocity curves is found using a minimum distance criterion (MDC) approach, though a variety of methods could be proposed for finding the intersection. Here, the angle estimation relies on estimating the difference between normalized velocities from distinct directional velocity curves, i.e. angle velocity functions ($V(\theta_{line})$). The use of a normalization factor is required to avoid that low velocity estimates are regarded as presenting smaller absolute differences. The selected angle (θ_{MDC}) is the one presenting the minimum difference and is estimated using:

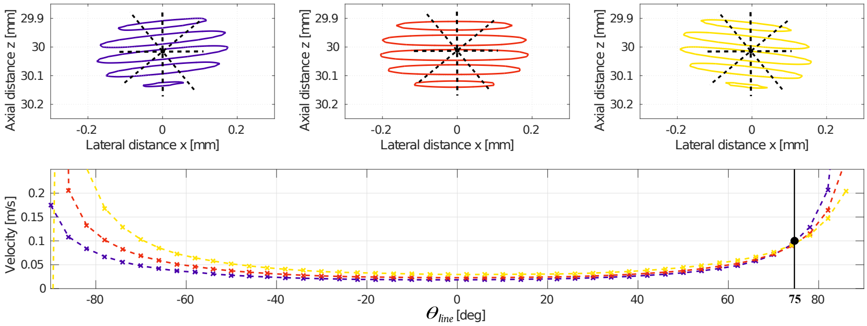

Figure 3.1: The top graph shows point spread functions generated from the first, third, and fifth emission in the sequence described in Section 3.2, with a set of beamformed lines in a polar grid. The bottom plot shows the angle velocity functions from the center of a Field II simulated straight vessel with flow moving at 0.1 m/s and 75°. The true angle and velocity are marked with a black dot, which coincides with the intersection of the curves. Obtained from (Villagomez-Hoyos et al. 2016)

$$\theta_{MDC} = \underset{\theta_{line}}{\text{Arg min}} \sum_{k=1}^{M-1} \sum_{l=k+1}^{M} \left| \frac{V_k(\theta_{line}) - V_l(\theta_{line})}{\min(V_k(\theta_{line}), V_l(\theta_{line}))} \right| . \tag{3.1}$$

The robustness of the estimator is enhanced by using more than two distinct PSFs (M). Additionally, due to the discrete nature of the beamformed θ_{line} angles, non-equidistant sampling of θ_{line} and inverse cosine interpolation of the $V_M(\theta_{line})$ curves are used to reduce the computational burden of estimating a large dataset of directional velocities. Further details on the method are found in Paper I in Appendix.

3.2 Experimental setup

Experiments are designed to test the effectiveness of the proposed method. The method is evaluated by studying its precision and accuracy during various flow conditions. Simulations and measurements are used for evaluating the performance of the method, first in straight vessels in Sec. 3.3, then in a spinning disk in Sec. 3.4, furthermore, in a realistic model of the carotid bifurcation in Sec.3.5, and finally in *in vivo* investigation in Sec. 3.6.

The method's imaging, beamformation, velocity and angle estimation parameters are kept the same during all validation tests. The only exceptions are the pulse repetition frequency, the echo-canceling filter, and the post-processing filtering of the estimates, which are changed from the standard value to investigate their effects. The changes are clearly stated on the text. A brief description of these parameters is given in the next sections, however, the reader is referred to Paper I in Appendix for more in-depth details.

3.2.1 Imaging setup

A 128-element linear array probe is used for the investigation. A duplex synthetic aperture sequence is used to acquire both B-mode and flow data sets. The emissions are interleaved, so that for every five flow emissions a B-mode emission is transmitted. The B-mode image is composed of a synthetic aperture sequence with 128 individual emissions having virtual sources located behind the transducer. The transducer and simulation/measurements parameters are listed in Table 3.1.

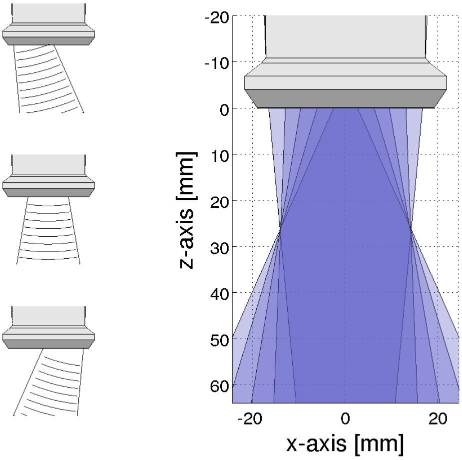

Figure 3.2: Example of spherical waves emanated from the first, third, and fifth emission used in the flow sequence (left). Overlay of the insonified area from each emission, and the actual region of interest shown in a darker shade (right). (Villagomez-Hoyos et al. 2016)

The flow sequence is implemented using a 64-element sub-aperture for each emission to emulate a spherical wave emanating from a virtual point source located behind the sub-aperture (negative F-number). The transmitted wavefront is directed towards a region of interest (ROI), so the ROI is completely insonified in every emission (Fig. 3.2). A 3-cycle sinusoidal pulse weighted by a 50% Tukey window is used as the excitation waveform. The same transmit voltage is used for both B-mode and flow imaging.

3.2.2 Simulation setup

The simulations are performed using Field II (Jensen 1996; Jensen and Svendsen 1992), in which tissue and blood are modeled as a collection of random point scatterers. The

Table 3.1: Transducer and Acquisition/Simulation parameters

Transducer		Transmit Parameters		
Parameter	Value	Parameter	B-mode	Flow
Type	Linear array	Emitting elements	16	64
Number of elements	128	Tx Apodization window	Hanning	
Element pitch	0.3 mm	F-number	-1	-3.5
Element kerf	0.035 mm	Number of distinct beams	128	5
Element height	4 mm	Excitation signal	3 sinusoids with 50% Tukey	
Elevation focus	20 mm			
Center frequency	8 MHz	Pulse repetition frequency	15 kHz	

scattering strength is modeled using a normal distribution of scattering amplitudes with mean and standard deviation varying according to approximated tissue and blood properties. The spatial impulse response of each scatterer is calculated and then added for obtaining the simulated RF signal. Approximately 10 point scatterers per resolution cell are sufficient to ensure a Gaussian distributed RF signal. The size of the resolution cell was calculated based on the F-number in receive, transmit frequency, and pulse length. In between every emission the scatterer position is updated given a pre-estimated velocity field. The simulation temporal sampling frequency was set to 100 MHz in all simulations. No frequency dependent attenuation is included in the simulations.

3.2.3 Measurement setup

The experimental ultrasound scanner, SARUS (Jensen, Holten-Lund, et al. 2013), is used for acquiring data. The system acquires RF data from the individual transducer channels, and these data are transferred to a computing cluster, where they are saved and processed off-line. The received RF data contains 128 channels sampled at 35 MHz and have 12 bits resolution for each individual channel.

Measurements are made on a flow-rig system. A Cole-Parmer centrifugal pump (Vernon Hills, IL, USA) circulates a blood-mimicking fluid (Ramnarine et al. 1998) (Danish Phantom Design, Frederikssund, Denmark) in a closed loop circuit. The entrance length of the flow tube is long enough to ensure fully developed laminar flow with a parabolic profile. The volume flow rate is measured by a calibrated MAG1100 flowmeter (Danfoss, Nordborg, Denmark) and used for calculating the true peak velocity based on the expected parabolic profile.

3.3 Straight vessels

Parabolic flow through a rigid vessel is used to verify the simulation findings with measurements. A vessel with a radius of 6 mm, centered at 30 mm is simulated and measured at flow angles of $75°$ and $90°$. One hundred consecutive velocity estimations are calculated. Velocity direction and magnitude are estimated along the profile through the tube, and the estimated velocities are compared to the expected profile. No spatial or time averaging is performed to the obtained estimates.

The peak velocities in the measurement are reduced from $0.5\,\mathrm{m\,s^{-1}}$ to $0.1\,\mathrm{m\,s^{-1}}$ for maintaining a Reynolds number below 2300 for a laminar flow. However, the peak velocity-to-PRF ratio was maintained by lowering the PRF in the measurements to 3 kHz for matching the same ratio in the simulation. The processing between simulations and measurements is kept the same.

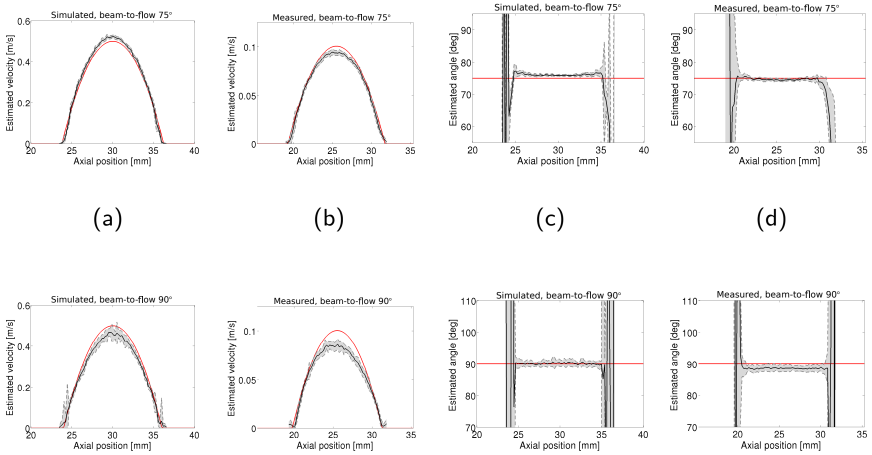

(a) (b) (c) (d)

(e) (f) (g) (h)

Figure 3.3: Comparison between the estimated velocities profiles from the simulated (left) and measured (right) straight vessels. The peak velocity in the measurement is 5 times lower to match the same velocity-to-PRF ratio as in the simulations. The plots show the profiles for the true (red), the mean magnitude with standard deviation (a, b, e and f), and the mean angle with standard deviation (c, d, g and h) for beam-to-flow angles of $75°$ and $90°$. Obtained from (Villagomez-Hoyos et al. 2016)

3.3.1 Results

Results obtained from the simulated and measured straight vessels are seen in Fig. 3.3. Here, the estimated mean velocity and angle profiles and their corresponding standard deviations are plotted. The true velocity and the angle profiles are plotted in red. A summary of the results are listed in Table 3.2. Statistics are calculated over 100 estimated profiles.

Correspondence is observed between the measurements and the simulations. All the estimated profiles approximate the true values denoted in red. However, different angle biases are present between measurements and simulations. In the 75° vessel simulation, the angle was overestimated generating an overestimation of the velocity magnitude. In the measurement, the angle was slightly underestimated, but a larger underestimation is present in the velocity magnitude. The same underestimation is present in both simulations and measurements of the 90° vessel regardless of the negative or positive angle bias. The underestimation appears to be quantitatively reproducible and may be correctable in post-processing. The large deviations on the angle plots on the edges of the vessel are simply due to the echo-canceler, which removes all blood/tissue energy, leaving only noise for the velocity estimator.

Table 3.2: Mean bias and standard deviation of the vessel estimates.

	rel. vel.[%]		angle [deg]	
Type	bias	std. dev.	bias	std. dev.
Angle	75°			
Simulated	2.42	1.87	1.20	0.45
Measured	-3.88	2.81	-0.31	0.67
Angle	90°			
Simulated	-6.44	4.06	0.13	1.05
Measured	-9.73	4.65	-1.38	1.09

3.4 Spinning disk

The simulated disk consists of a circular collection of scatterers, and a speed-of-sound of $1540\,\mathrm{m\,s^{-1}}$. The scatterers are rotated around the disk center at a constant angular velocity. Therefore, the velocity magnitude linearly increases as a function of distance from the disk center. The phantom rotates clock-wise, having a diameter of 1.5 cm, and a peak velocity v_{max} at the outer edge. The center of the spinning disk is placed at a depth of 2.5 cm below the center line of the array. The elevation extent of the spinning disk is 5 mm. White noise is added by estimating the average signal power to generate noise powers at the specified signal to noise ratios (SNR) in dB. The estimates are constructed

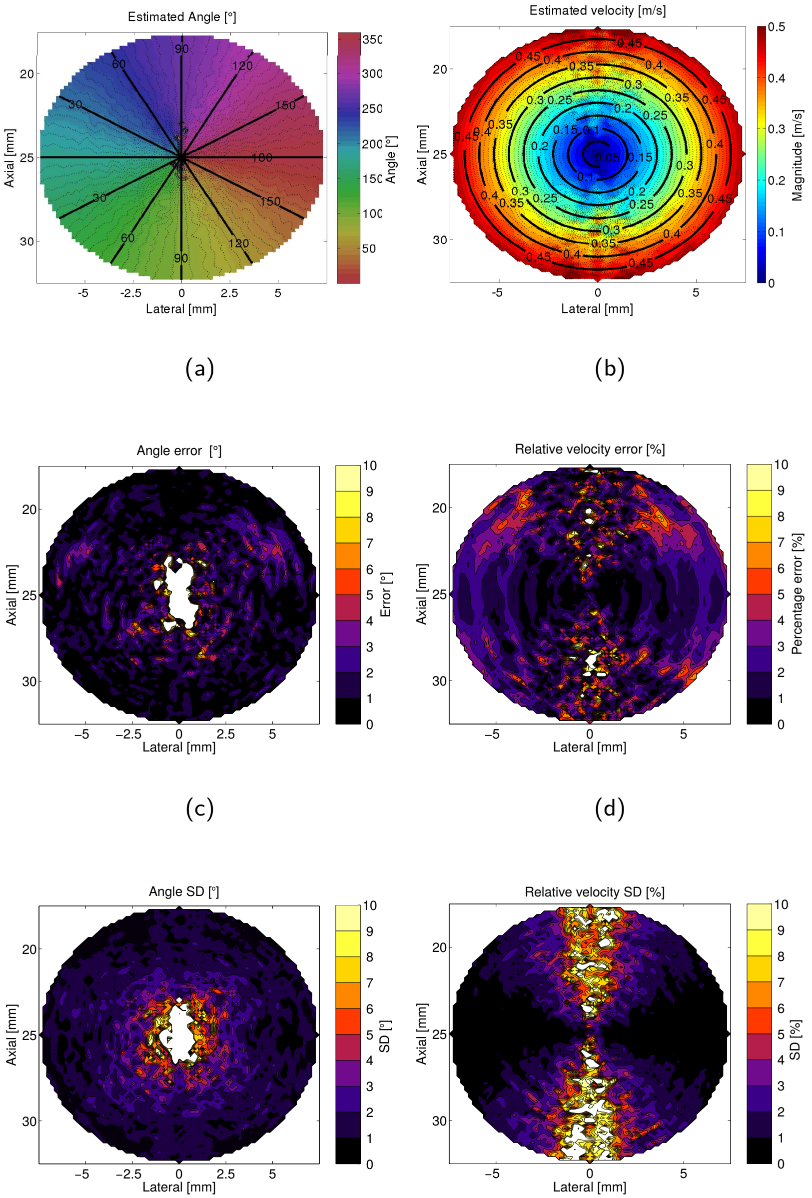

(a)

(b)

(c)

(d)

(e)

(f)

Figure 3.4: Vector velocities obtained from a spinning disc phantom with 10 dB SNR. The estimated velocity angle (a). The estimated velocity magnitude (b). The angle error (c). The relative velocity error (d). The angle standard deviation (e). The relative velocity standard deviation (f). Obtained from (Villagomez-Hoyos et al. 2016)

over a grid with a spatial sampling of 0.2 mm in both the lateral and axial dimensions. A binary mask is applied on the velocity estimates to remove estimates outside the borders of the phantom.

Two simulation studies are performed with the spinning disk; the first assesses the method's performance over one hundred consecutive estimates at SNR ratios of 20, 10, and 0 dB with a peak velocity of $0.5\,\mathrm{m\,s^{-1}}$. No spatial or temporal averaging is performed on the estimates. A second study evaluates the impact of stationary echo-canceling on the method. Estimates with and without echo-canceling are compared. Note that the spinning disk does not contain static scatterers. The second spinning disk is simulated to have a peak velocity of $0.2\,\mathrm{m\,s^{-1}}$ and a SNR of 30 dB. The estimates were spatially filtered in a region of $1.0\,\mathrm{mm} \times 1.0\,\mathrm{mm}$ with a median filter, and ten consecutive estimates are used to match this study to the one performed by Fadnes (Fadnes et al. 2015).

3.4.1 Results

The spinning disk with $v_{max} = 0.5\,\mathrm{m\,s^{-1}}$ is used to assess the 360° performance of the method. Mean and standard deviation are calculated based on 100 different measurement realizations. The accuracy of the vector velocity estimates are assessed by calculating an error percentage between the mean estimates and the ground truth. The precision is assessed using the standard deviation (SD) of the one hundred realizations divided by $v_{max} = 0.5$ to obtain a relative velocity SD. Fig. 3.4 shows these performance results with 10 dB SNR.

The left column on Fig. 3.4 contains the angle estimation performance. It is seen from Fig. 3.4 (c) and (e) that both the accuracy and precision of the angle estimator are maintained constant along the complete 360° angle range. However, at small curvature radii the angle estimator fails to estimate the correct values. This can be attributed to the beamformed line length, since in smaller radii, a line of the same size will transverse larger velocity gradients. A simple solution is to beamform smaller lines, but this also limits the amount of information available for the correlation.

The right column in Fig. 3.4 provides the performance of the estimated velocity magnitude. The performance in this case is not homogeneous along the angles. A noticeably larger standard deviation exists, when the flow movement approaches the lateral direction, due to the lower frequency content in that dimension. The issue could be addressed by using longer lines in that dimension, but due to the geometry of the phantom, longer lines will also increase the bias given that they will transverse larger velocity gradients.

The estimator performance is also investigated for different levels of SNR. The observed performance showed a similar pattern as for the results in Fig. 3.4 where a SNR of 10 dB was selected. The degradation of the estimates due to the loss in SNR are manifested as a general increase of errors. As the spatial error distribution is not normal, the overall performance measurement for the SNR comparison is taken as the median and interquartile ranges in the errors and standard deviations of the entire disk. However, to

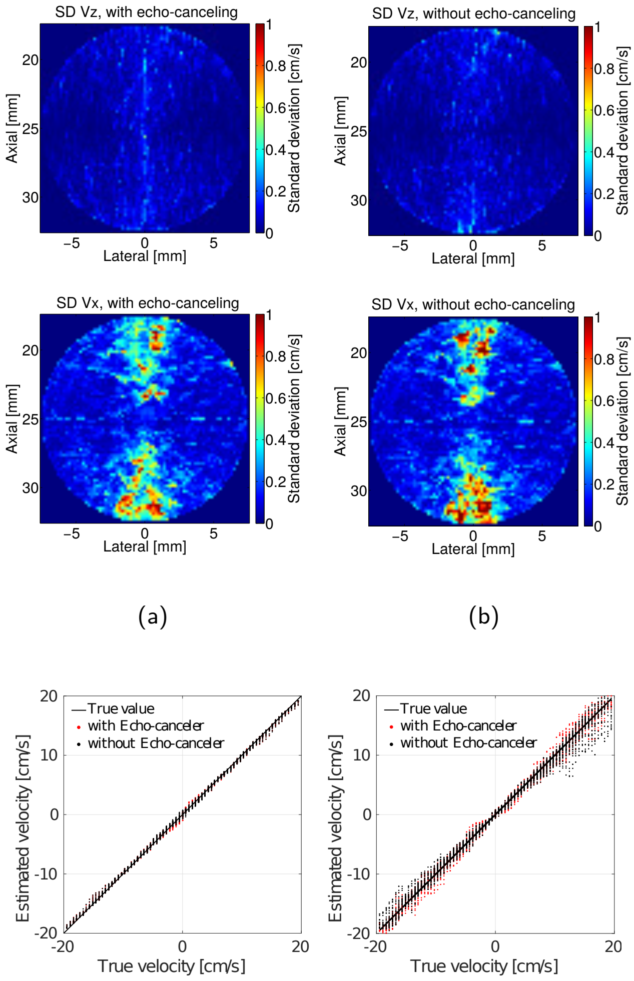

(a)

(b)

(c)

Figure 3.5: Standard deviation (SD) of the velocity estimator over 10 realizations of the simulated spinning disk. The SDs are in centimetres per second and for the V_x and V_z components (top/bottom). SD with and without echo-canceling are shown in (a) and (b), respectively. A scatterer plot from a single realization of the estimated versus the reference velocity is shown in (c). The red dots correspond to the setup with echo-canceling, while the black dots to the setup without echo-canceler. Obtained from (Villagomez-Hoyos et al. 2016)

avoid the highly wrong estimates at smaller radii, the mean values are calculated using the estimated values inside the radius range of 0.2 cm $\leq r \leq$ 0.75 cm, which corresponds to 26% $\leq r \leq$ 100%. The overall performance at different SNRs is summarized in Table 3.3. The performance decreases significantly when the SNR approaches 0 dB. This effect has previously been investigated for time shift estimators by Jensen (Jensen 1993), establishing a limit around 6 dB as the minimum SNR for a reliable estimation of the velocity. It should be noted that the stationary echo-canceler removes a greater amount of energy from the lower frequency content. Lateral movement estimates in lower SNR scenarios will therefore degrade first, and this will be observed as an expansion of the white areas in Fig. 3.4 (f).

Table 3.3: Median bias and interquartile ranges from the spinning disk phantom at different SNR.

	Angle		Velocity	
SNR [dB]	bias [deg] med | *iqr*	std. dev. [deg] med | *iqr*	bias [%] med | *iqr*	std. dev. [%] med | *iqr*
20	0.92 | *1.22*	1.35 | *1.04*	2.36 | *4.43*	0.76 | *3.08*
10	1.01 | *1.40*	1.80 | *1.29*	2.57 | *4.99*	1.02 | *3.88*
0	7.96 | *13.2*	17.5 | *20.8*	5.84 | *20.4*	6.78 | *19.4*

The impact of the stationary echo-canceler is also measured on a spinning disk phantom with $v_{max} = 0.2$ m/s as shown in Fig. 3.5. In this figure the V_x and V_z components are shown instead. These are obtained by simply multiplying the velocity magnitude by the cosine or sine of the corresponding angle. The standard deviations on each of the components for 10 realizations are shown in Fig. 3.5 (a) and (b) for the echo-canceled and non echo-canceled case, respectively. Fig 3.5 (c) shows a scatter plot of the estimated versus the reference velocities for the proposed method. Velocity estimates plotted in red are estimates obtained when the echo-canceler is enabled. The results show no significant difference between them. Therefore, the echo-canceling has only an effect on the estimates when the SNR is lower than the 6 dB SNR threshold needed for the estimation. The results are formatted in a similar manner as published in (Fadnes et al. 2015) for comparison with speckle tracking and cross-beam Doppler.

3.5 CFD carotid bifurcation model

Computational fluid dynamics (CFD) models of realistic vasculatures represent more complete, and therefore more complex flow conditions. Distinct in-house CFD vasculature models are present in the literature (Marshall et al. 2004; Taylor, Hughes, and Zarins 1998; Tsai and Sheu 2007), however, the only models with openly available geometries and velocity data sets are the ones published by Swillens and colleagues (Swillens et al.

2009). In this work, the carotid bifurcation CFD dataset from Swillens' work is used, in which the bifurcation geometry is generated from of a healthy volunteer and an artificially eccentric plaque is inserted in the interna. The geometry is reconstructed from CT-scans and meshed using appropriate software (Mimics; Materialise, Leuven, Belgium). The flow is estimated using the CFD-package Fluent with an imposed inlet velocity profile obtained from a Doppler measurement of the same volunteer. Rigid walls are assumed in the CFD model, and no vessel wall or tissue movement is present. The cardiac cycle (length 1 s) is divided into 200 equally spaced time steps on the CFD simulation.

Additionally to the CFD dataset, a CFD-US simulation framework is also openly available from Swillens' website (@BioMMeda). The framework couples the CFD 3-D velocities with the propagation of scatterers used in Field II for ultrasound simulations. The framework matches the large disparity in time scales between the CFD modeling (5 ms) and ultrasound simulations (0.067 ms) using an inter-frame linear interpolation. Additionally, to couple the CFD velocity field information to the positions of the point scatterer distribution used by Field II, a linear 3-D spatial interpolation from the CFD grid is done for each scatterer.

The US simulation is then performed on the CFD propagated scatterers data. However, as commented by Swillens, and artificial dilution and aggregation of point scatterers may occur due to relatively long scanning times. The original author solution was to reset the scatterers between each scan line (ensemble length). However, the uninterrupted nature of the data using synthetic aperture forbids this solution, therefore to circumvent the effect, a higher density of scatterers was imposed (>20 per resolution cell) and the density of the scattered was verified to be above 10 per resolution cell for a completely developed speckle pattern.

3.5.1 Results

The resulting vector flow imaging (VFI) frames are shown on Fig. 3.6 during three phases of the cardiac cycle: peak systole, late systole, and diastole. The reference VFI frame from the reference CFD model is shown in the left column, and the estimated velocity fields from ultrasound in the right column. The CFD velocities were interpolated to the exact same locations as in the ultrasound image at the same time instances the involved frames were processed. In general, the estimated VFI frames show good agreement with the reference CFD results for all three frames.

There are some minor observable differences between the reference CFD model and the estimated velocities in Fig. 3.6. In the peak systole frame (a), an artefact is visible in the bifurcation entrance, where a set of angles are falsely and consistently pointing upwards. The artefact arises from the MDC algorithm, on which the velocity normalization factor in 3.1 could influence in benefiting higher velocities, specially when they are closer to transverse angles where large non-linearities exist. A solution could be to first detect the Cartesian quadrant the velocity vector is pointing, and discard the angles pointing otherwise. On the late systole frame (b), the borders of the measured vortices

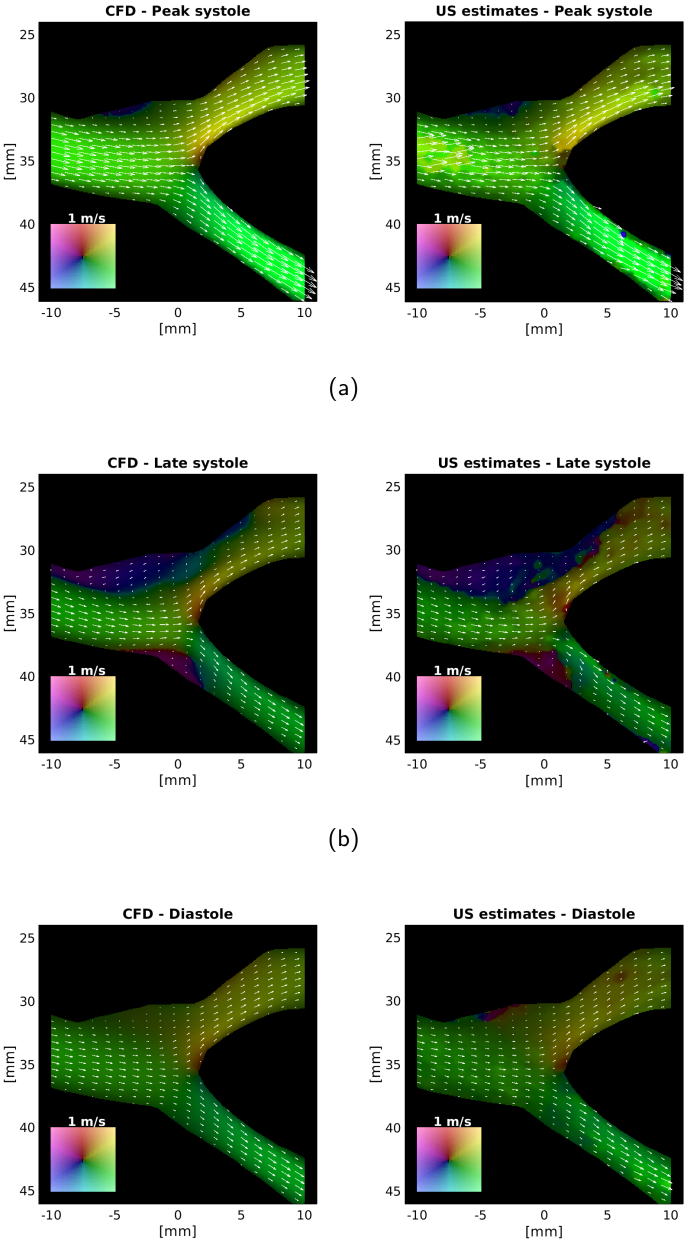

(a)

(b)

(c)

Figure 3.6: Vector flow imaging (VFI) frames from the reference CFD model (left), and the estimated velocity fields from ultrasound (right). Three distinct stages of the cardiac cycle are shown; (a) Peak systole, (b) late systole, (c) Diastole.

are not as well defined as in the CFD reference model but they expand from their actual extent. The effect is probably due to the fixed radial length of the beamformed polar grid. This problem could be solved if smaller lines are adaptively selected when slow velocities are estimated and longer lines when larger velocities are present.

To quantify the performance of the CFD bifurcation model, scatterer plots are generated. The scatter plots, shown in Fig. 3.7, include all spatial positions of the estimated velocities and angles at the selected frame. The scatter color is encoded to represent either the angle or the velocity magnitude. In the left column, the velocity magnitudes show a systematic under-estimation of the velocity; observable as a higher concentration of estimates below the red line. For quantifying the under-estimation, linear regression analysis is performed to the velocities. The resulting regression values are 0.94 for the peak systole, 0.82 for the late systole, and 0.92 for the diastole, where a value of 1 is the ideal match. The absolute dispersion of the estimates along the regression line is also measured in inter quartile ranges (IQR); being $5.64\,\mathrm{cm\,s^{-1}}$, $3.37\,\mathrm{cm\,s^{-1}}$, and $2.75\,\mathrm{cm\,s^{-1}}$, respectively. In the right column, the estimated angles show less dispersion around the true value; no systematic under or over estimation is noticed in the plots. However, both the angle artefact and the vortex miss-delimitation are observable; corresponding to the parallel line around 100°, and the dispersive cloud of estimates around 200°, respectively. The calculated linear regression values are 0.98, 1.02, and 1.00 for the peak systole, late systole, and diastole respectively. The absolute angle dispersion of the estimates along the regression line is 3.02° , 23°, and 4.99°, respectively.

3.6 *In vivo* carotid bifurcation

An *in-vivo* acquisition is performed after approval by The Danish National Committee on Biomedical Research Ethics with approval number H-1-2014-FSP-072. A healthy volunteer with no history of cardiovascular disease (52 year old woman) is scanned after informed consent. The ultrasound scan sequence are acquired on the left carotid bifurcation on a longitudinal view. The scans were recorded with the volunteer in supine position and carried out by an experienced radiologist.

Intensity measurements were carried out prior to the scan, the measured intensities must satisfy limits regulated by the U.S. Food and Drug Administration (FDA)(FDA 2008). These limits concern the mechanical index, $MI \leq 1.9$, the derated spatial-peak-temporal-average intensity, $I_{spta} \leq 720\,\mathrm{mW/cm^2}$. The measured values using the scheme described in (Jensen, Rasmussen, et al. 2016), are $MI = 0.91$ and $I_{spta} = 144.3\,\mathrm{mW/cm^2}$, which are both below the FDA limits. The transducer surface temperature was also tested, where the transducer surface should not exceed an increase of 30° or 6° Celsius in air and in a simulated usage test, respectively. The pulse repetition frequency (PRF) complying with these regulations was 15 kHz.

A 3 second acquisition is recorded, yielding 7,500 velocity estimates at 2,500 frames per second. For displaying only the blood flow estimates, a binary mask is generated by us-

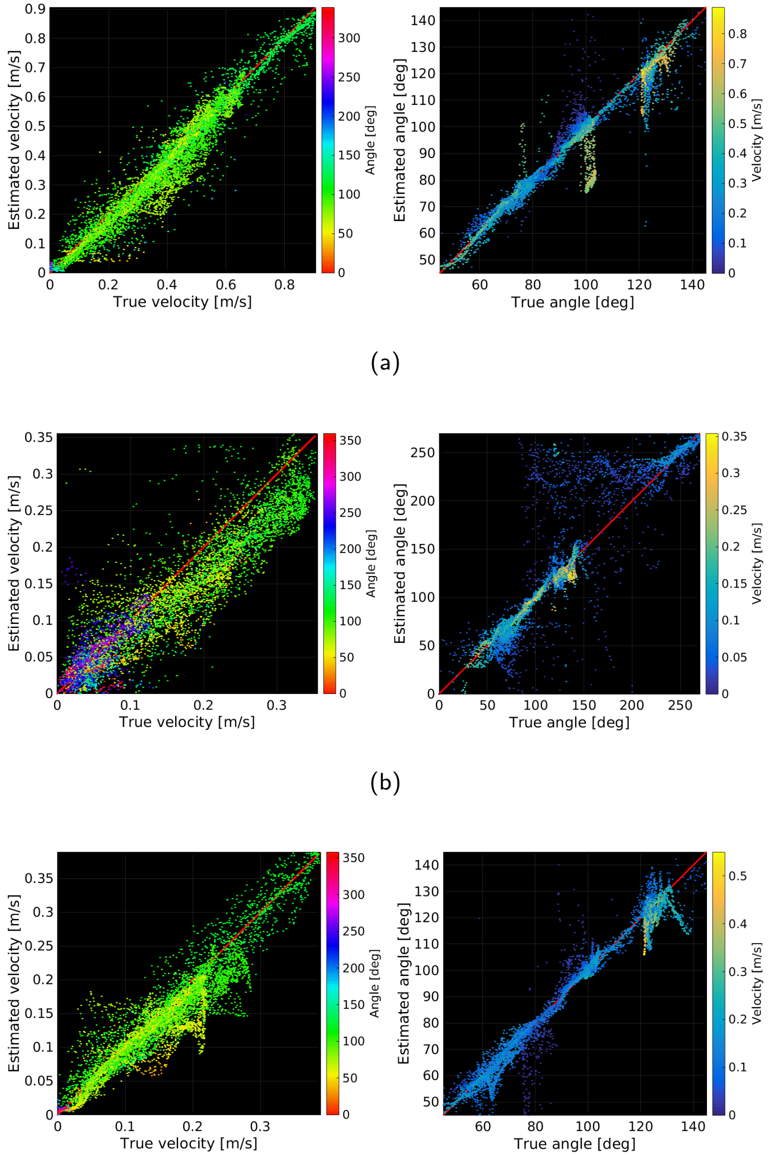

(a)

(b)

(c)

Figure 3.7: Scatter plots comparing the reference CFD values to the ultrasound estimates. (Left) The scatter plot of the estimated velocities color coded with the estimated angle. (Right) The scatter plot of the estimated angles color coded with the estimated velocity. The reference values is shown as the red line in both graphs. Three distinct stages of the cardiac cycle are shown; (a) Peak systole, (b) late systole, (c) Diastole.

ing the intensity values from the B-mode image. The binary mask is constructed from each B-mode frame after median filtering the log-compressed image using a $0.6\,\mathrm{mm} \times 0.6\,\mathrm{mm}$ kernel. All intensities below a certain threshold value in the B-mode image are then considered to be blood, where the velocity estimates are displayed. Additionally, a median filter is applied to the velocity magnitude estimates in the time domain, using a $35\,\mathrm{ms}$ sliding window, as well as in the spatial domain where a kernel of $1.0\,\mathrm{mm} \times 1.0\,\mathrm{mm}$ is applied. Hereby false peak detection errors in the velocity magnitudes are removed. However, neither spatial filtering nor regularization process is applied to the estimated angles, to actually show the raw performance of the algorithm.

3.6.1 Results

One image frame from the *in-vivo* acquisition in the left carotid bifurcation during systole is shown in Fig. 3.8.A B-mode image is overlayed with the 2-D velocity estimates. The velocity color map depends on both the flow magnitude and direction according to the color wheel map provided in the lower right corner of Fig. 3.8. The provided longitudinal view shows both the internal and external carotid, which are seen as the deep and shallower vessel, respectively.

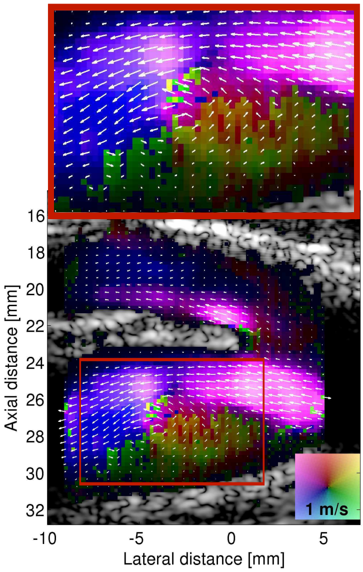

Figure 3.8: A vortex was present in the carotid bulb of the internal carotid artery during the entire cardiac cycle. The internal carotid artery is seen as the deep vessel.

A vortex with low velocities in the carotid bulb of the internal carotid artery is shown as the zoom in area in Fig. 3.8. Apart from this vortical recirculation in the bulb, no retrograde flow was present during the entire heart cycle. A non axis-symmetric flow can also be observed in the upper part of the vortex as the presence of two distinct peaks in the flow trajectory. This is probably due to the presence of out of plane motion in the internal carotid artery.

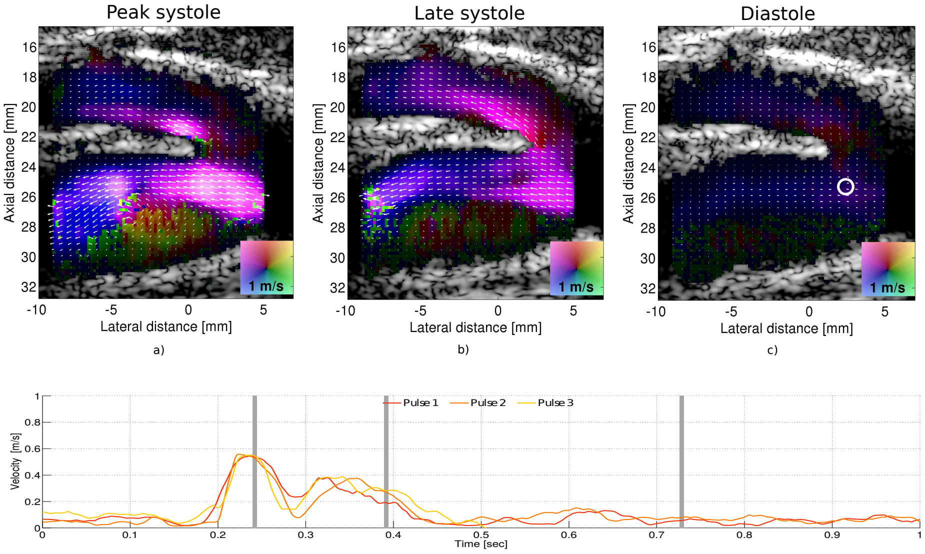

a) b) c)

d)

Figure 3.9: Carotid bifurcation of a 52 year old healthy individual. Time aligned velocity magnitude profiles at the entrance of the internal carotid at the position denoted by the white circle in (c) is shown in the bottom graph. Vector flow frames during three different stages of the cardiac cycle are shown above. The first frame (b) corresponds to time point ≈0.25 s, the second frame (b) to time point at ≈0.39 s, and the third frame (c) to time point at ≈0.73 s.

Fig. 3.9 (a,b,c) shows the 2-D velocity estimates at different stages of the cardiac cycle, where a low velocity vortex is present in the carotid sinus at the three stages.

Three distinct heart cycles are captured during the 3 seconds acquisition. Fig. 3.9 (d) shows the quantitative velocity estimates after aligning the peak systole in the cardiac cycles for the same anatomical position at the entrance of the internal carotid denoted by the white circle in Fig. 3.9 (c). The peak velocity at the denoted location is $0.55\,\mathrm{cm\,s^{-1}}$ and is consistent for the three heart cycles. The alignment was performed during the peak period, however, during the rest of the cardiac cycle the same spatial position is used.

CHAPTER 4

An accurate angle estimator: Velocity range

Summary *This chapter presents an investigation on the velocity range for the proposed method, as traditional Doppler limits are not longer applicable. The maximum velocity is explored first, where straight vessel simulations and a measurement on a 70% constriction phantom are used for the study. The study then investigates the low velocity limit, and with the use of continuous data proposes an adaptive lag to expand its low velocity range.*

In medical ultrasound, the velocity detection has been typically related to the Doppler effect, where the frequency shift of signals is used for estimating the blood velocity. Therefore, the capability of ultrasound systems for measuring this frequency shift has been traditionally associated to the range of velocities that the system can detect.

In continuous mode (CW) systems, an uninterrupted ultrasound signal is emitted from which the Doppler shift is measured. The CW mode systems are able to measure very high blood flow velocities, in excess of 6-7 $\mathrm{m\,s^{-1}}$. However a disadvantage of CW is a complete lack of depth specificity. A high velocity might be detected, but if no other source of information is available, it is impossible to determine at what depth this velocity is located.

Pulsed wave (PW) systems overcome this depth ambiguity. The PW mode uses a series ultrasound pulses to detect the movement of blood, in terms of a phase shift (Sec. 2.2.2.1), from which an artificial Doppler frequency is obtained at the selected depth. However, the discrete operation of this emitted pulses introduces a new ambiguity, which is that the artificially generated Doppler frequency can become aliased. Therefore, restricting the velocity range to frequencies below the Nyquist limit, thus, creating a limit on the maximum unambiguously detected velocity; which is

$$v_{max} = \frac{c}{2} \frac{PRF}{2f_0}. \tag{4.1}$$

Here c is the speed of sound, f_0 the ultrasound transmit frequency, and the pulse repetition frequency (PRF).

An additional requisite for the PW artificial Doppler frequency is its need for narrow-band pulses. These come at the expense of poorer axial resolution and greater acoustic exposure, since narrowband pulses tend to be long in duration (5-25 cycles).

Another approach in PW systems is to detect the movement of blood in terms of a spatial shift (Sec. 2.2.2.2), from which the velocity is directly estimated. The advantage is that the generation of an artificial Doppler frequency is avoided, thus, the aliasing ambiguity is removed.

The theoretical velocity range of such spatial shift estimator is not constrained by aliasing, however, previous investigations have shown that the standard deviation of this type of estimator is inversely proportional to the maximum correlation coefficient between the received signals (Foster, Embree, and O'Brien 1990). Although this advantageous lack of limit, the spatial estimator is not widely used in conventional ultrasound. This is probably because correlation coefficients are heavily degraded in the presence of large beam-to-flow angles when the velocity is measured along the the ultrasound beam. This is avoided if instead of estimating along the ultrasound beam, the velocity is estimated along the flow. This was investigated by Jensen and showed that higher correlations are attained in both simulations (Jensen 2003) and measurements (Jensen and Bjerngaard 2003).

In this section, we extend Jensen's work of investigating the velocity range to the proposed angle estimator. The limits are tested using both simulations and measurements. However, the effect of tissue movement on the lower bound is not considered during this investigation. The reason for this is that the effects of tissue movement on the velocity estimates will be investigated together with a proposed new echo-canceler in Chapter 6.

4.1 The maximum velocity limit

The limit of a maximum detectable velocity when using a spatial shift estimator against a continuous, broadband, and infinite-extent signals and just one velocity component is non existent. However, in ultrasound all these requirements are not met; the signals have restricted bandwidth (both axially and laterally), they might contain distinct velocities, and furthermore, decorrelate due to the individual movement of blood scatterers. Therefore, a limit on the maximum detectable velocity will depend on the flow conditions.

To test the limit of the proposed estimator, two set of experiments were performed. The first one consist of a straight vessel simulation study, where scatterers are displaced along a straight line, thus, avoiding decorrelation. The purpose is to obtain a theoretical maximum velocity for the proposed method in perfect non-decorrelation conditions. The second experiment is a measurement on a 70% constricted vessel phantom, where the effects of distinct velocities and decorrelation due to the individual movement of scatterers are present. The purpose is to obtain a greater insight on the maximum velocity achievable in more realistic circumstances. In both experiments the parameters were kept equivalent to the ones describe in Sec. 3.2, unless the changes are specifically described on the text.

4.1.1 Straight vessel case

A straight vessel with a radius of 6 mm, centered at 30 mm is simulated at flow angles of 0°, 30°, 60°, and 90°. A parabolic flow profile is set with peak velocity magnitudes ranging from $0.5\,\mathrm{m\,s^{-1}}$ til $5.5\,\mathrm{m\,s^{-1}}$ in steps of $0.5\,\mathrm{m\,s^{-1}}$. One hundred consecutive pulse emissions are performed. Velocity direction and magnitude are estimated in the center of the vessel, and the estimated velocity is compared to the expected peak velocity.

The line lengths of directional lines are varied on multiples of the wavelength from 7.5λ til 24λ, which for a 8 MHz transducer ranges from 1.4 mm to 4.7 mm. The pulse repetition frequency (PRF) in this experiment was set to 10 kHz, and effective time between correlated lines is $T_{eff} = T_{prf}/(5+1)$, see Sec. 3.2.1 for the sequence details. The scatterers displacements, thus, varied from 0.3 mm to 3.3 mm.

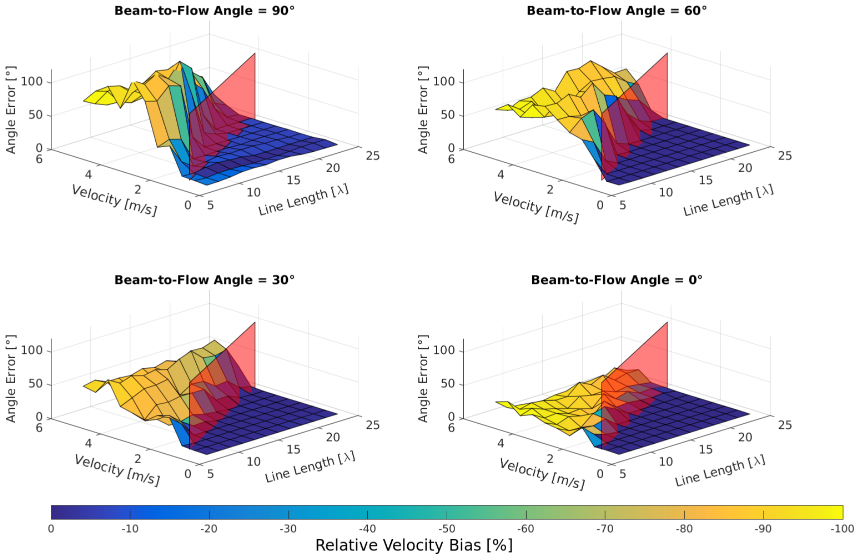

Figure 4.1: Angle error surface plot with color encoded relative velocity biases for the flow angles of 0°, 30°, 60°, and 90°. The semi-transparent red plane indicates when the scatterer displacement at the selected velocity is above the 50% of the selected line length.

The estimated angle errors are shown in Fig. 4.1 as a surface plots for each flow angle. The velocity magnitude relative bias is color encoded on the angle error surface plot, only a negative bias scale is shown due to the systematic under-estimation of velocities, as also reported in Sec. 3.3.1 . The plots show that both angles and magnitudes are consistently estimated with a high precision until the scatterer displacement exceeds the 50% of the selected line length. The 50% limit is indicated by the transparent red plane. The limit is around 50% because new scatterers have replaced the previous ones on the new sampled line, and thus, less than 50% of the sampled line correlate with the previously sampled line.

In conclusion, if decorrelation effects are not present, higher velocities detection are achievable by solely increasing the line length. Caution must be taken when increasing the line length as non-straight velocity paths can decrease the accuracy of the angle estimator, as reported in Sec. 3.4.1.

4.1.2 A 70% constriction vessel case

A 70% constricted straight-tube phantom is used to assess the maximum attainable velocity at more clinical realistic conditions. A constriction is used because it decreases the outflow area, which results in a significant increase of the flow velocity. The constriction phantom geometry is designed using a SolidWorks (Education edition, Dassault Systèmes SolidWorks Corp., Vélizy, France) and is as shown in Fig. 4.2. The phantom core is then 3-D printed and fixed to an individual container before casted in an in-house made polyvinyl alcohol (PVA) cryogel mixture to make a surrounding medium mimicking the properties of human tissue(Lai et al. 2013). The phantom is afterwards connected to a flow system (CompuFlow 1000, Shelley Medical Imaging Technologies, Toronto, Canada), where customizable flow rates are set.

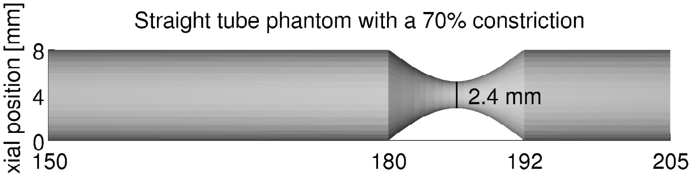

Figure 4.2: Straight tube phantom with an inner diameter of 8 mm and a concentric constriction of 70 % of the inlet diameter.

The experimental flow rates (Q) are increased in predetermined steps, as listed in Table 4.1, before performing a steady flow acquisition. Four hundred realizations are acquired and used for the statistics, covering a total of 180 ms for the selected PRF of 13.5 kHz. The line length is fixed to 15λ allowing for a maximum velocity of approximately $3.25\,\mathrm{m\,s^{-1}}$, which is around the calculated average velocity for the constriction at the flow rate of $15\,\mathrm{ml\,s^{-1}}$. The average velocities are calculated from the continuity equation for steady flow,

$$v = \frac{Q}{A} = \frac{Q}{4\pi D}. \tag{4.2}$$

where D is the diameter of the vessel either at the entrance or at the constriction.

The mean average velocities are calculated for profiles at both entrance and constriction together with the standard deviation (SD). Results for these investigations are listed in Table 4.1. The results show a systematic over-estimation for the entrance flow, and under-estimation for the constriction. This is because these values are heavily influenced by the selected integration interval along the depth axis, thus, they are operator dependent. Furthermore, the impact is greater when flow rates are estimated based on these calculations as well, as seen in the last column of Table 4.1. It is important to note that for a parabolic profile, the average velocity is half of its peak velocity.

Table 4.1: Flow rates and Avg. Velocities for the 70% constriction phantom.

Flow Rate $\mathrm{ml\,s^{-1}}$	Avg Vel. [m/s]		Estimated Avg Vel. [m/s]		Estimated Flow Rate	
	Entrance	Constriction	Entrance	Constriction	Entrance	Constriction
3	0.06	0.66	0.08 ± 0.003	0.60 ± 0.06	3.95	2.70
5	0.10	1.10	0.13 ± 0.015	1.04 ± 0.12	6.58	4.71
7	0.14	1.55	0.18 ± 0.023	1.37 ± 0.18	9.26	6.19
10	0.20	2.21	0.27 ± 0.011	2.01 ± 0.17	13.5	9.11
13	0.26	2.87	0.34 ± 0.060	2.43 ± 0.64	17.1	10.98
14	0.28	3.10	0.38 ± 0.060	2.69 ± 0.48	19.0	12.17
15	0.30	3.32	0.41 ± 0.042	2.93 ± 0.35	20.4	13.23

A VFI frame at the maximum flow rate of $15\,\mathrm{ml\,s^{-1}}$ is shown in Fig. 4.3, along with three velocity profiles. A jet-like flow is observable at the exit of the constriction, where high velocities are present in the center while a slow retrograde flow is recognizable in the lower part of the vessel. This behaviour matches well with the observations seen during the conventional B-mode scan.

The flow profiles present an increase in the estimated SD as the flow pass through the constriction into the exit port. This was expected as the flow becomes more distorted, the signal looses correlation, which affects the estimation. The spatial effect of the decorrelation, shown on Fig. 4.4, is seen as an increase in the SD of the estimated angle and magnitude. Additionally, an increase in SD of the estimates could also be used as an indirect measurement of unstable blood flow (Reynolds number) at constriction or valves, thereby, yielding new diagnostic measure.

Even though a maximum limit on the detectable velocity was not devise on the proposed experiments, the experiments have shown capability of the method for measuring high velocities (above 3 m/s) at a relatively low effective PRFs ($\approx$ 2 kHz).

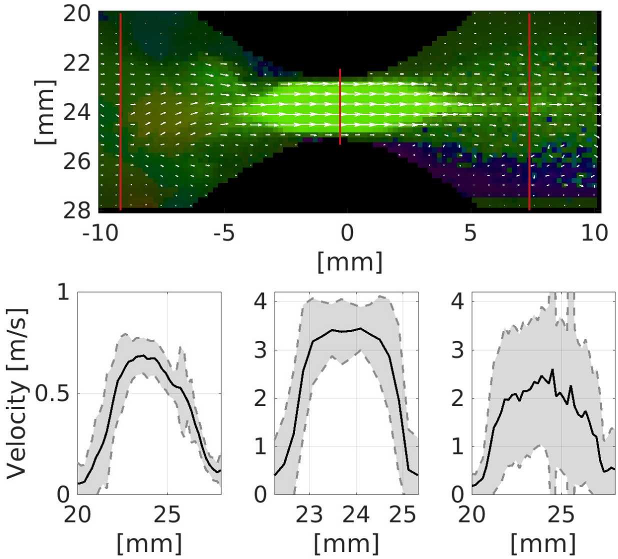

Figure 4.3: (Top) A VFI frame at the maximum flow rate of $15\,\mathrm{ml\,s^{-1}}$ generated from the median of the 400 hundred estimates. (Bottom) Three velocity profiles with mean and SD at the entrance, constriction, and output.

4.2 The minimum velocity limit

The minimum detectable velocity in spatial shift estimators is related to the level of jitter on the system. Jitter occurs when signal decorrelation, noise, and finite window lengths cause a slight displacement of the true peak of the cross correlation function. The level of jitter can be determined by the Cramer Rao Lower Bound as investigated by Walker (Walker and Trahey 1995). In that work it was estimated that for a 5 MHz transducer with 50% fractional bandwidth a jitter of 31.1 ns is expected for a blood flow signal (0 dB SNR). This corresponds to a spatial jitter of around 24 µm, which for an effective PRF of 2 kHz is approximately a velocity jitter of 0.048 m/s.

In conventional systems, this would have set the limit due to the fixed PRF and line-by-line acquisitions these systems operate on. However, in parallel systems such as synthetic aperture, where continuous data are available, an artificially lower PRF can be generated by simply skipping emissions. This approach was first investigated in (Villagomez-Hoyos, Stuart, and Jensen 2014b), and later an adaptive selection of the lag was proposed in (Villagomez-Hoyos, Stuart, and Jensen 2014a). Finally, the approach

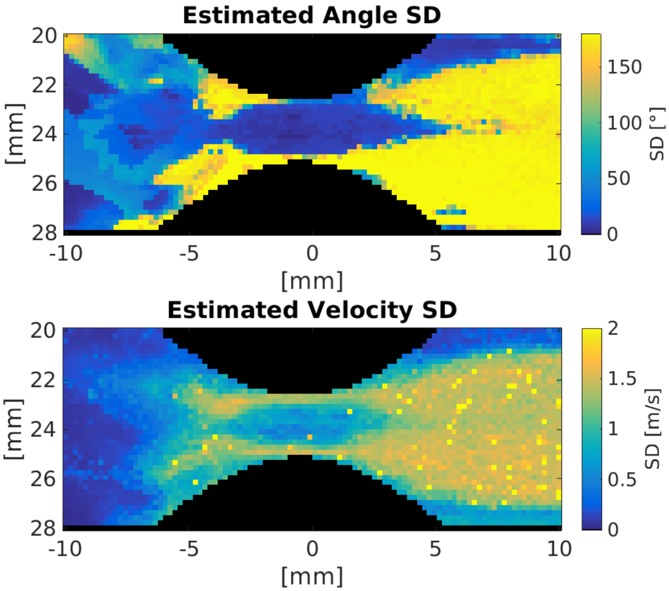

Figure 4.4: Estimated angle and velocity standard deviations for the constriction phantom at the maximum flow rate of $15\,\mathrm{ml\,s^{-1}}$ wit a peak velocity of $3.25\,\mathrm{m\,s^{-1}}$.

was validated in-vivo in (Villagomez-Hoyos, Stuart, and Jensen 2015). The three cited papers are included as Paper II, III, and IV in the Appendix. The next section provides a brief description of the adaptive lag method as proposed in (Villagomez-Hoyos, Stuart, and Jensen 2014a), together with a summary of the obtained results.

4.2.1 Adaptive Lag

To attain more accurate estimates an optimal synthetic PRF or lag needs to be selected. As the magnitude of the velocity is not known a priori, the exactitude of the estimates cannot be used as a criteria. However, the precision of the estimates can be improved by selecting the measurement with the lowest standard deviation, and this is the criteria proposed for selecting the optimal lag.

As the nature of the blood flow is pulsatile, the standard deviation cannot be estimated over the whole measurement period. Therefore, it is necessary to generate a piecewise linear approximation of the flow waveform by fitting a line to the velocity estimates. The size of the segments is selected, so that the approximation resembles the flow waveform as close as possible. The value used here is 2 ms or 25 velocity estimates.

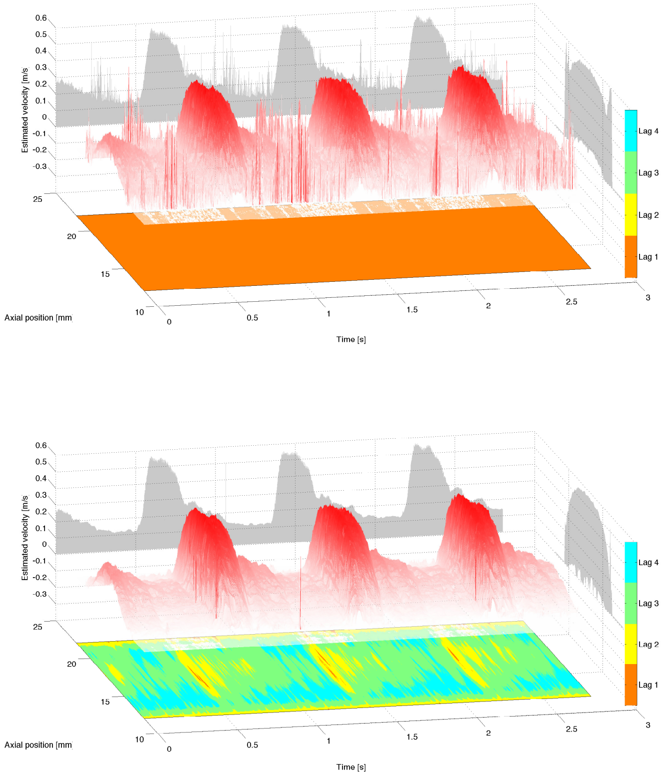

Figure 4.5: Velocity profiles of the center line of the vessel through time. Projections of the two axis are shown as shadows. (Top) The velocity estimates using a fixed lag. (Bottom) The velocity estimates using the adaptive algorithm. Figure from (Villagomez-Hoyos, Stuart, and Jensen 2014a)

The optimal lag is selected by minimizing the standard deviation of subtracting a piecewise linear approximation from the velocity estimate at each point as denoted by

$$Lag(\mathbf{r_x}, tn) = \arg\min_{Lag} \left[std\{\hat{v}'(\mathbf{r_x}, t_n, Lag) - \hat{v}_{pl}(\mathbf{r_x}, t_n, Lag)\}\right], \qquad (4.3)$$

where $\hat{v}'(\mathbf{r_x}, t_n, Lag)$ is the segment from the estimated velocity and $\hat{v}_{pl}(\mathbf{r_x}, t_n, Lag)$ is the piecewise linear approximation at that segment.

Finally the $Lag(\mathbf{r_x}, tn)$ is smoothed using a Gaussian filter to reduce Lag jumps due to noise. For that the size of the window used was 49 by 49 (4.9[mm] by 3.9[ms]).

To validate the approach a pulsatile carotid flow profile was programmed in the flow system (CompuFlow 1000, Shelley Medical Imaging Technologies, Toronto, Canada). The peak flow rate is set to $25\,\mathrm{ml\,s^{-1}}$ and the period between pulses is set to $0.820\,\mathrm{s}$. A multi-lag velocity estimation is performed, and a lag is adaptively selected at every estimation point. The results of this shown as the XY plane in Fig. 4.5. The velocity estimates are shown as a surface, where the X axis is the spatial dimension and the center line, and the Y axis is the temporal dimension showing the progression of the pulse through time.

In the lower part of Fig. 4.5 a fixed lag is used as represented by the uniform color in the XY plane, and the velocity estimates are also shown as a surface. The estimates in this figure are more noisy compared to the multi-lag approach. The lower velocities are specially affected when using a lower lag, since the backscattered noise degrades the signal. For contrast, the XY plane in the upper part of Fig. 4.5, follows the shape of the pulse; selecting a lower lag around the peak velocities and increasing it towards the outer part of the vessel.

CHAPTER 5

An accurate angle estimator: Other geometries

Summary *The previous chapters reported experimental results produced using a linear array transducer. However, the proposed method does not requires a specific wave type or geometry. Therefore, in this chapter the proposed method is explored when used in conjunction with a larger set of transducer geometries and wave types. The performance metrics are investigated following the spinning disk simulation layout realized during the validation study in Chapter 3. The effects and artefacts are discussed for each transducer geometry. The chapter is closed with a proof-of-concept example of an extension of the method to a full 3-D vector velocity implementation using a matrix array probe.*

Many types of medical ultrasound transducers are used in clinical practice. They operate at different center frequencies, have different physical dimensions, footprints, and shapes, and provide different image formats. However, high-frame-rate vector flow estimators have been limited to only linear array implementations. This has restricted the clinical applications to shallower scan depths ($< 60\ mm$).

The reasons for the lack of implementations is that additional challenges emerge when extending velocity estimation methods to new geometries and deeper scan depths, being some of them: (1) limited aperture size, mostly in regards to a faster drop of lateral resolution at increasing depth but also intrinsic limitations for some methods, e.g. non-overlapping region when using plane waves; (2) aliasing limit, which is traditionally shortened when using lower PRF needed for deeper depths. (3) lower blood SNR at deeper depths, as the increase in penetration depth translates to a decrease in signal energy increased.

The possibility of expanding from the initial linear array implementation to other array geometries is an important characteristic for any flow estimation method. The expansion to phased arrays could lead to visualizing at complex flow phenomena in the heart and deeper vessels such as the aorta, providing important features of the flow that are not currently quantified. The availability of a convex array implementation would allow for abdominal scanning, which may provide new information of abdominal fluid dynamics and yield both velocity and angle estimates for a more realistic flow characterization.

In this section, the proposed method is extended to several implementations; a plane wave linear array, a phased array, a convex array, and an 2-D array for full 3-D vector flow investigations. For each array extension, the emitted ultrasound sequence is first defined, followed by performance results on a spinning disk simulation at a SNR of 10 dB. All the processing is performed in the same manner after beamformation, as described in Sec. 3.4. No echo-canceling is considered. The only exception is for the 2-D array, where the method is expanded to a 3-D implementation, however, the same principles are followed.

5.1 Plane Wave

In recent years, linear array implementations using plane wave have gain popularity (Tanter and Fink 2014). The ease of adaptation of cross-beam techniques to parallel processing schemes using plane waves has been used as an advantage. In this section, we present an implementation of the proposed method using plane waves. The advantage of the proposed method is that it is easily adapted to any emitted waveform type, similarly to other 2-D methods such as speckle tracking.

5.1.1 Imaging setup

A 128-element linear array probe is used for this investigation.Five plane wave emissions ($-10°, -5°, -1°, 5°$, and $10°$) are used to acquire a flow data set. The sequence is implemented using the full 128-element aperture for each emission. The transmitted wavefront and the region of interest (ROI) are shown in Fig. 3.2. A 3-cycle sinusoidal pulse weighted by a 50% Tukey window is used as the excitation waveform. The transducer and simulation parameters are listed in Table 5.1.

Table 5.1: Transducer and Acquisition/Simulation parameters

Transducer		Transmit Parameters	
Parameter	Value	Parameter	Flow
Type	Linear array	Emitting elements	128
Number of elements	128	Tx Apodization window	None
Element pitch	0.3 mm	Angles	$[-10°, -5°, -1°, 5°, 10°]$
Element kerf	0.035 mm	Number of distinct beams	5
Element height	4 mm	Excitation signal	3 sinusoids with 50% Tukey
Elevation focus	25 mm		
Center frequency	5 MHz	Pulse repetition frequency	10 kHz

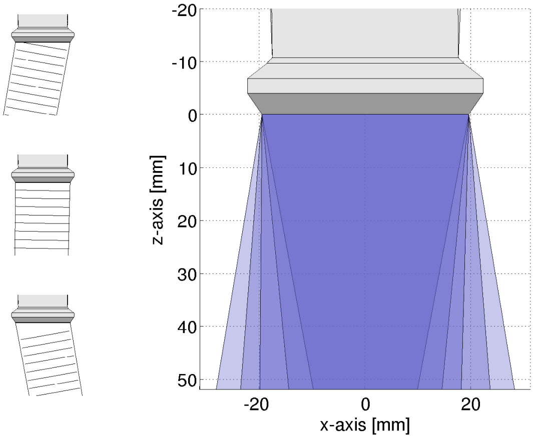

Figure 5.1: Example of plane waves emanated from the first, third, and fifth emission used in the flow sequence (left). Overlay of the insonified area from each emission, and the actual region of interest shown in a darker shade (right).

5.1.2 Spinning disk

The spinning disk simulation layout described in Sec. 3.4 is followed and used to assess the 360° performance of the method using plane waves. Median and inter-quartile ranges are calculated based on 100 different measurement realizations. The accuracy of the vector velocity estimates are assessed in the similar manner as in Sec. 3.4 by calculating an error percentage between the median estimates and the ground truth. The precision is assessed by using the inter quartile ranges (IQR) of the one hundred realizations divided by the peak velocity v_{max} =$0.5\,\mathrm{m\,s^{-1}}$ to obtain a relative velocity IQR. Fig. 5.2 shows this performance results at 10 dB of SNR.

In the left column on Fig. 5.2 the angle estimation performance is presented, the format follows the previously presented on Sec. 3.4. From the results in Fig. 5.2 (a) it is seen that the angles are correctly estimated, however, it is clear in (c) and (e) that the errors and IQR have increased significantly compared to the initial implementation in Sec. 3.4.1. One possible explanation for this is that the effective PRF has been lowered for this investigation from the original 2.5 kHz to 2 kHz. Another important difference is the significant increase in artefacts, as noticed on the upper and lower sections around the transverse flow region. The artefacts seem to present a mirroring effect, which was also observed in the CFM model (Fig. 3.6). These artefacts are produced due to symmetry in the angle velocity function, which is a consequence of the symmetry in the PSF. The considerable increase in artefacts is why median and IQR are used instead of mean and SD reported in Sec. 3.4.1.

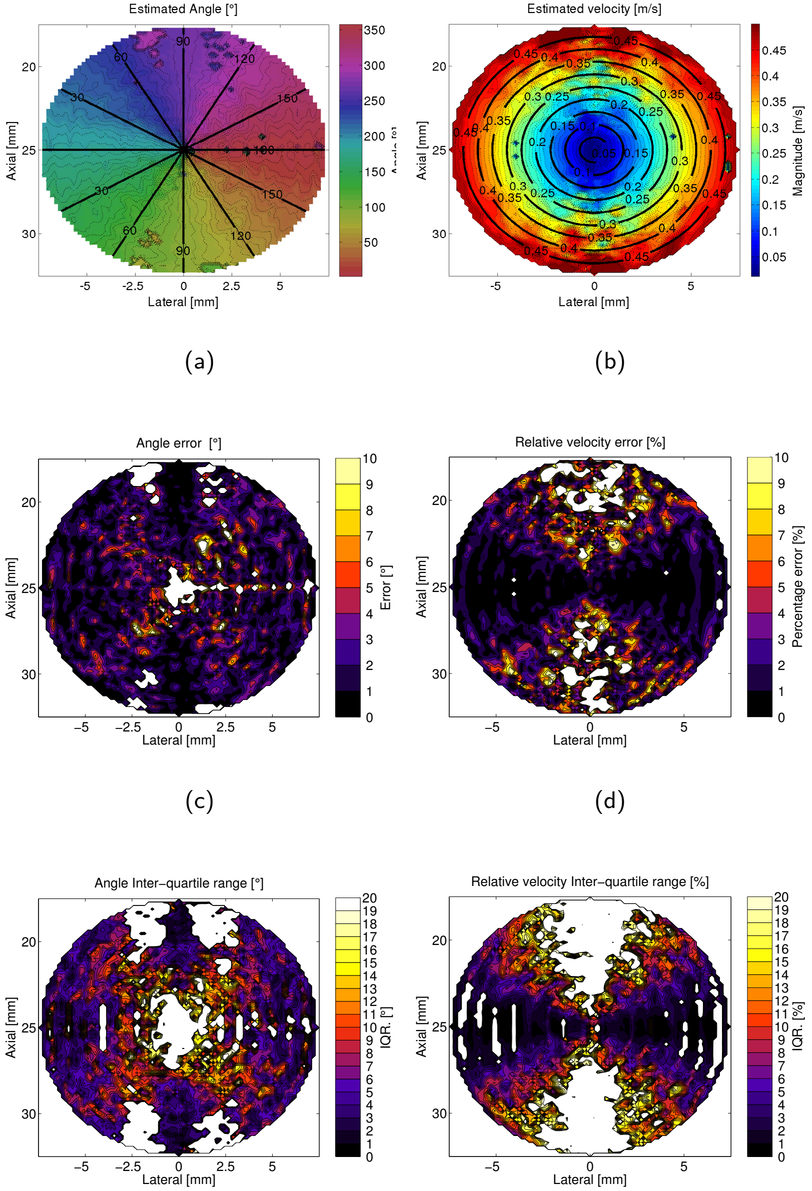

(a) (b)

(c) (d)

(e) (f)

Figure 5.2: Vector velocities obtained from a spinning disc phantom with 10 dB SNR on a linear array using plane wave. The estimated velocity angle (a). The estimated velocity magnitude (b). The angle error (c). The relative velocity error (d). The angle inter-quartile range (e). The relative velocity inter-quartile range (f).

The right column in Fig. 5.2 provides the performance of the estimated velocity magnitude. The performance of the velocity estimation is directly affected by the performance of the angle estimator. The previously observed behaviour of estimates worsens when approaching the lateral direction, due to the lower frequency content is also present. However, there is an additional artefact occurring, which is presented as concentric arcs in Fig. 3.4 (f). The cause for this effect is unknown and should be further investigated.

In the same way, the overall performance measurement is taken as the median and interquartile ranges of the errors and IQRs of the entire disk. However, to avoid the highly wrong estimates at smaller radii, the values are calculated using the radius range of 0.2 cm $\leq r \leq 0.75$ cm, which corresponds to $26\% \leq r \leq 100\%$. The overall calculated performance is listed in Table 5.4, at the end of Sec. 5.3.2.

5.2 Phased array

The use of an array with smaller footprint and beam steering capabilities, such as the phased array, is preferred for cardiac imaging. This is because a limited acoustic window exists when scanning through the rib cage, which requires a cone shaped insonification if the heart is to be scanned. For this reasons in high-frame-rate cardiac flow imaging the use of diverging waves algorithms is preferred.

The work in this section is an extension for the paper V found on the Appendix, where findings from an in-vivo transthoracic acquisition were presented. The phased array diverging wave sequence used in the mentioned paper is evaluated using a spinning disk simulation, where its performance is assessed. As mentioned in the previous sections, the evaluation is performed without considering any echo-canceling.

5.2.1 Imaging setup

A 128-element phased array probe is used for the investigation. A three emissions synthetic aperture sequence is used to acquire the flow data. The flow sequence is implemented using the full 128-element aperture for each emission to emulate a spherical wave emanating from a virtual point source located behind the aperture. The transmitted wavefront is directed towards a region of interest (ROI), so the ROI is completely insonified in every emission (Fig. 5.3). A 3-cycle sinusoidal pulse weighted by a 50% Tukey window is used as the excitation waveform. An effective pulse repetition time is $T_{eff} = \frac{T_{prf}}{3}$, where T_{prf} is the inverse of the system pulse repetition frequency (PRF). The transducer and acquisition parameters are listed in Table 5.2.

5.2.2 Spinning disk

The results from the spinning disk simulations are shown in Fig. 5.4, however, compared to previous spinning disk simulations the size and position of the spinning disk have been changed to match the dimensions and depths of a transthoracic cardiac scan. The spinning

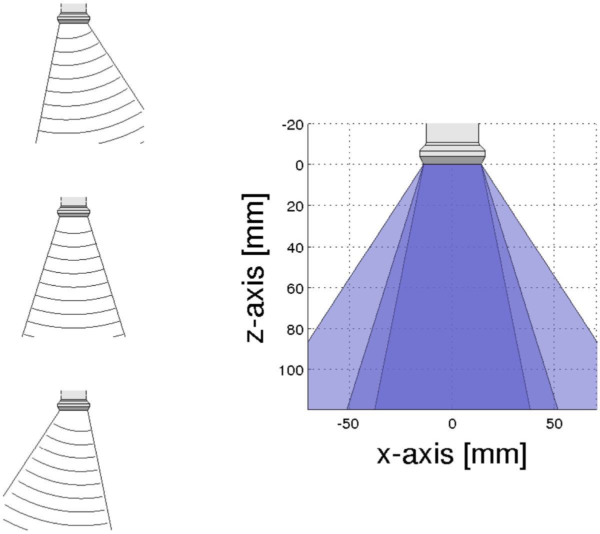

Figure 5.3: Example of spherical waves emanated from the first, second, and third emission used in the flow sequence (left). Overlay of the insonified area from each emission, and the actual region of interest shown in a darker shade (right).

disk now has a radius of 30 mm and is centred at a depth of 80 mm. The maximum velocity is kept at v_{max} =0.5 m s^{-1}, and again 100 different measurement realizations are used for the statistics. A lowered PRF of 6.2 kHz is, thus, used due to the extended depth. The number of distinct emission is then restricted to only three. This have a general impact on the calculated estimates, as observed on Fig. 5.4, where the error and IQR

Table 5.2: Transducer and Acquisition parameters

Transducer		Transmit Parameters	
Parameter	Value	Parameter	Value
Type	Phased array	Excitation signal	3 period sine
Number of elements	128	Number of emitting elements	128
Element pitch	0.22 mm	Apodization window	Hanning
Element kerf	0.022 mm	Number of distinct emissions	3
Element height	15 mm	Pulse repetition frequency (PRF)	6.2 kHz
Elevation focus	85 mm	F-number	-1.6
Center frequency	3.5 MHz		

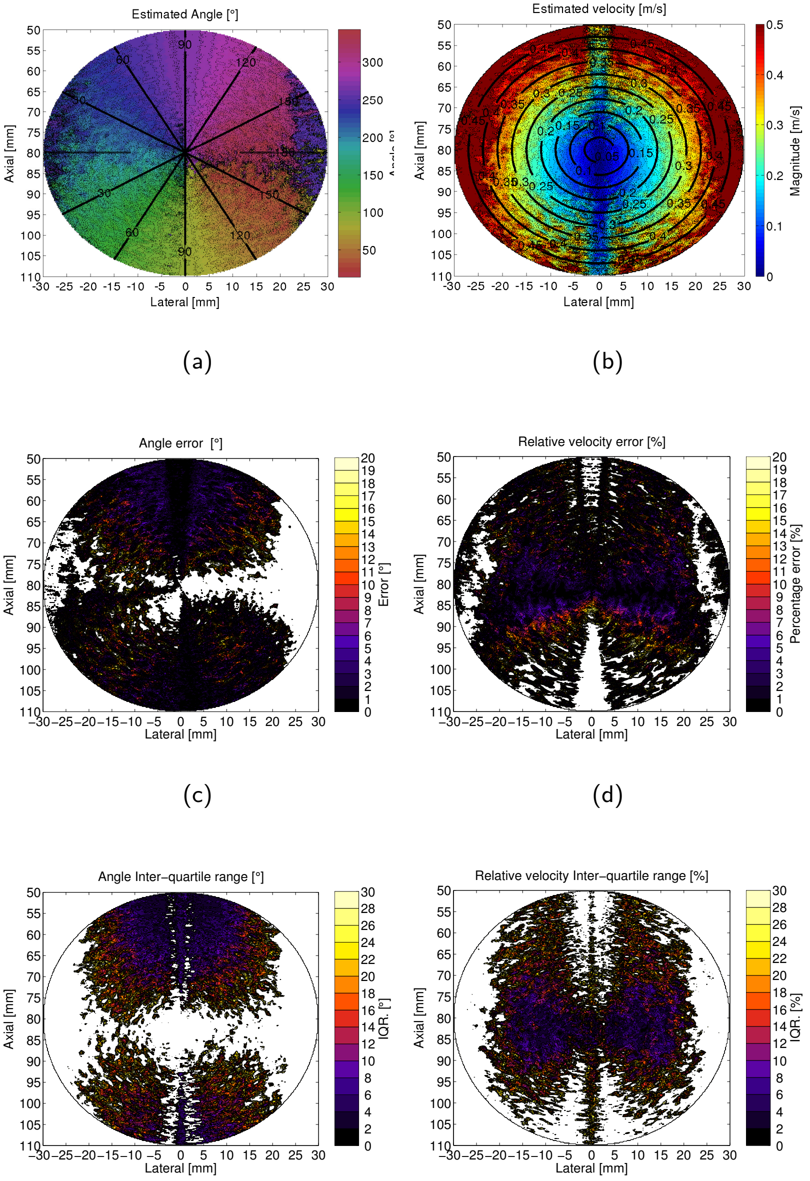

(a) (b)

(c) (d)

(e) (f)

Figure 5.4: Vector velocities obtained from a spinning disc phantom with 10 dB SNR on a phased array. The estimated velocity angle (a). The estimated velocity magnitude (b). The angle error (c). The relative velocity error (d). The angle inter-quartile range (e). The relative velocity inter-quartile range (f).

ranges are extended to account for the increase on errors. It is also observable that the external part of the spinning disk that partially extends outside the ROI delimited on Fig. 5.3, is miss-estimated.

The left column in Fig. 5.4 containing the angle estimation performance shows a more homogeneous performance, when excluding the areas beyond the insonified ROI. The increasing error at the region close to 0° and 360° in (c), is due to an incorrect unwrapping of the angle estimates. The IQR in (e) also presents the expected homogeneous behaviour, however, two straight lines with increased IQRs are visible in the center of the spinning disk. This lines could be attributed to the mirror artefact previously mentioned.

In the right column on Fig. 5.4 the velocity estimates present another interesting phenomenon. The center of the spinning disk is systematically underestimated. The underestimation increases with the increase of depth, confirming the relation to the lower frequency content due to the decrease of lateral resolution.

The overall performance measurement is taken from the radius range of 0.75 cm $\leq r \leq 2.25$ cm, which corresponds to $25\% \leq r \leq 75\%$. This is to avoid both the wrong estimates due to the smaller radii and the estimates outside the ROI. The overall calculated performance is listed in Table 5.4, at the end of Sec. 5.3.2.

5.3 Convex array

Convex arrays are the transducer of choice for most general ultrasound imaging applications involving the abdomen. The large field of view coverage with its relatively small form factor, compared to the large abdominal linear arrays that preceded them, has make the convex array widely used, specially in fields like obstetrics and emergency medicine.

Disciplines in medicine that use convex arrays could have a major benefit from availability of vector flow imaging techniques. This is why the first attempts to translate these techniques to this geometry are an on going process(Jensen, Brandt, and Nielsen 2014, 2015), however, this is the first time a high-frame-rate vector flow imaging techniques is investigated in a convex array. In this section, an implementation of the proposed method on a convex array is demonstrated by means of simulations using a spinning disk.

5.3.1 Imaging setup

A 192-element convex array is used for the investigation. A five emission synthetic aperture sequence is used to acquire the flow data set. The flow sequence is implemented using a 33-element sub-aperture for each emission to emulate a spherical wave emanating from a virtual point source located behind the aperture. The transmitted wavefront is directed towards a region of interest (ROI), so the ROI is completely insonified in every emission (Fig. 5.5). A 3-cycle sinusoidal pulse weighted by a 50% Tukey window is used as the excitation waveform. An effective pulse repetition time is $T_{eff} = \frac{T_{prf}}{5}$, where T_{prf} is the inverse of the system pulse repetition frequency (PRF). The transducer and acquisition parameters are listed in Table 5.3.

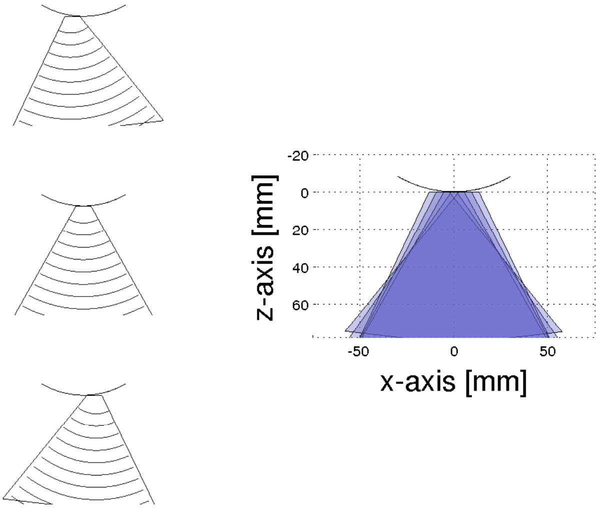

Figure 5.5: Example of spherical waves emanated from the first, third, and fifth emission used in the flow sequence (left). Overlay of the insonified area from each emission, and the actual region of interest shown in a darker shade (right).

5.3.2 Spinning disk

The results from the spinning disk simulations are shown in Fig. 5.6. The spinning disk has a radius of $22.5\,\mathrm{mm}$ and is centred at a depth of $47.5\,\mathrm{mm}$. The maximum velocity is kept at v_{max} =$0.5\,\mathrm{m\,s^{-1}}$, and the 100 different measurement realizations are used for the statistics. The PRF is set to 9.5 kHz, which is slightly higher than the phased array. This is to accommodate five emissions instead of the three used in that experiment, however,

Table 5.3: Transducer and Acquisition parameters

Transducer		Transmit Parameters	
Parameter	Value	Parameter	Value
Type	Convex array	Excitation signal	3 period sine
Number of elements	192	Number of emitting elements	33
Element pitch	0.33 mm	Apodization window	Hanning
Element kerf	0.022 mm	Number of distinct emissions	5
Element height	13 mm	Pulse repetition frequency (PRF)	9.5 kHz
Elevation focus	65 mm	F-number	-1
Center frequency	3.5 MHz		

this is at the cost of a limited scanning depth($\approx 80\,\mathrm{mm}$).

The advantage of the five emissions is the enhance on robustness, which is observable as the decrease of the error ranges needed for representing the results in Fig. 5.6 compared to Fig. 5.4. However, the appearance of strengthen concentric arcs artefacts demands a further investigation of the problem. A hint for the reason of this appearance might be now observed in the left column of Fig. 5.6, where the same artefacts are visible in the angle estimator. These inner concentric arcs show the same mirror angle behaviour as the previously observed around transverse flow regions, but present only at certain flow velocities and angles. The artefact could be corrected by first estimating the axial flow direction, and then discarding the angles that oppose these premise. However, this first estimate should be robust since errors on this pre-detection could discard the real flow angle. Additionally, in the right column of Fig. 5.6 the performance of the velocity estimation is drastically degraded as the depth increases when confronted to transverse flow. The systematic under-estimation of transverse flow as depth increases is due to the lower frequency content present at these depths, and has been previously discussed in Sec. 3.4.1.

Lastly, the overall performance measurement is taken from the radius range of 0.45 cm $\leq r \leq$ 2.25 cm, which corresponds to $20\% \leq r \leq 100\%$.. The overall calculated performance for all the explored geometries is listed in Table 5.4. It is obvious that the diverging wave implementation on the linear array performs better than the plane wave implementation. However, is important to keep in mind that the proposed technique was developed using this sequence and due the difference in PRF a direct comparison cannot be made. Surprisingly, the convex array performs considerably well, however, time effort should be spent correcting the artefacts before *in-vivo* studies. The phase array is the worst performer of the explored geometry, and it could be benefited if more emission could be used. Therefore, a multi-frequency encoding such as the one presented by (Oddershede, Gran, and Jensen 2008) should be explored for this implementation.

Table 5.4: Median Bias and interquartile ranges from the spinning disk phantom for different array implementations.

	Angle		Velocity	
SNR [dB]	bias [deg] med I *iqr*	IQR [deg] med I *iqr*	bias [%] med I *iqr*	IQR [%] med I *iqr*
Linear (Diverging)	1.01 I *1.40*	1.80 I *1.29*	2.57 I *4.99*	1.02 I *3.88*
Linear (Plane-wave)	1.77 I *2.52*	7.77 I *7.01*	1.49 I *8.48*	4.83 I *16.5*
Phased array	8.34 I *11.7*	20.9 I *21.3*	6.96 I *17.7*	8.62 I *15.5*
Convex array	1.24 I *1.71*	4.85 I *3.77*	1.53 I *6.15*	3.61 I *10.78*

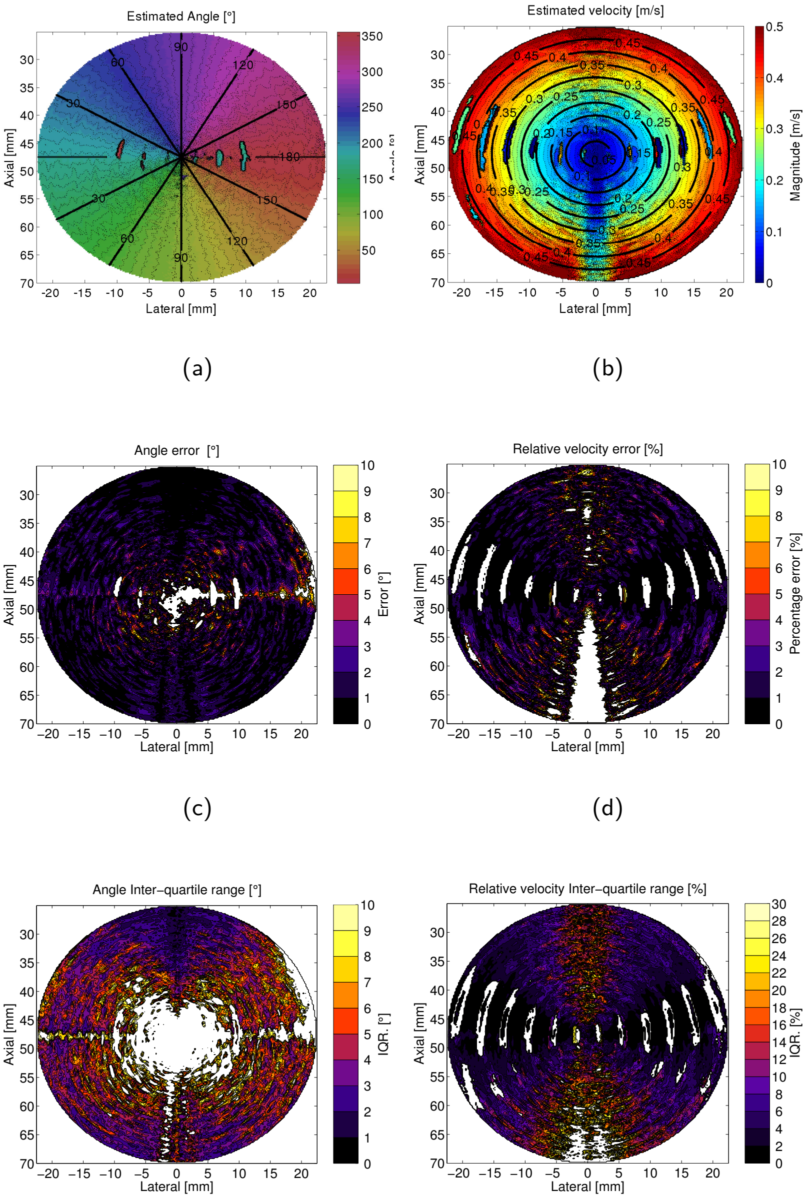

(a) (b)

(c) (d)

(e) (f)

Figure 5.6: Vector velocities obtained from a spinning disc phantom with 10 dB SNR for a convex array. The estimated velocity angle (a). The estimated velocity magnitude (b). The angle error (c). The relative velocity error (d). The angle inter-quartile range (e). The relative velocity inter-quartile range (f).

5.4 2-D array

To this point, all the discussed high frame rate flow velocity implementations have been restricted to 2-D rendering in a single plane. However, blood flow in the cardiovascular system is complex as it generally moves in all three spatial dimensions and furthermore as a function of time. The availability of the full vectors could give additional insight into the complex hemodynamics of the human body, furthermore the high frame rates could uncover transient events, such as vortices, which can arise and vanish within hundredth of miliseconds.

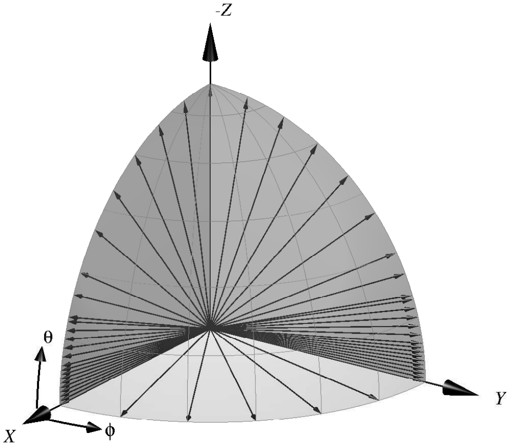

Figure 5.7: Spherical grid for the directional beamformed lines for obtaining the angle velocity function $V(\theta, \phi)$ in the 3-D implementation of the method. The θ angle is non-linearly sample, similarly to the 2-D version, to compensate for the higher non-linearities. There is no need to non-linearly sample the ϕ angle due to the similarity between the lateral and the elevation resolution.

In this work, the proposed method is extended to a full 3-D vector implementation, which is capable of generating more than 1000 volumes per second. The extended implementation make use of a 2-D matrix array to receive RF signals from diverging wave emissions. The received signals are then directionally beamformed in a spherical grid along all directions, as illustrated in Fig. 5.7, where directional velocity estimates are obtain for each of them. The angle is resolved by using the same minimum distance criterion (MDC) by finding first the minimum along the θ angles, and then the minimum across ϕ from the estimated angle velocity function $V(\theta, \phi)$. The velocity magnitude is then obtained along the estimated angle. The work is part of the Abstract I included in the Appendix, and is planned to be presented on the IEEE International Ultrasonics Symposium 2016 in Tours, France.

5.4.1 Imaging setup

A 2-D 32x32 Vermon matrix array is used in combination with the experimental scanner SARUS to transmit and acquire data from 1024 channels. A five diverging wave emissions sequence is transmitted to acquire the flow data set. The flow sequence uses the complete 32x32 aperture for each emission to emulate a spherical wave emanating from a virtual point source located behind the aperture. The virtual sources are angulated by $\pm 12^{\circ}$ with respect the z-axis against the other two axis, with fifth emission coinciding with the z-axis. The transmitted wavefront is directed towards a volume of interest (VOI), so the VOI is completely insonified in every emission (Fig. 5.8). A 3-cycle sinusoidal pulse is used as the excitation waveform. An effective pulse repetition time is $T_{eff} = \frac{T_{prf}}{5}$, where T_{prf} is the inverse of the system pulse repetition frequency (PRF). The transducer and acquisition parameters are listed in Table 5.5.

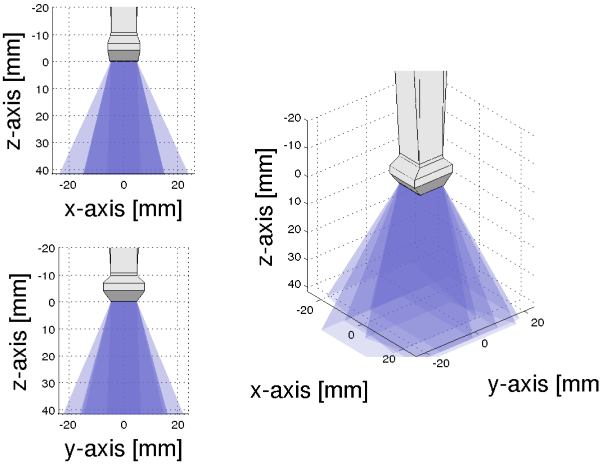

Figure 5.8: Overlay of the insonified area from each emission, along the XZ and YZ plane (left), and the full volume of interest shown in a darker shade (right).

5.4.2 Straight vessel

The preliminary study is performed on a straight vessel flow phantom ($\oslash = 8\text{mm}$). The phantom is connected to a flow system (CompuFlow 1000, Shelley Medical Imaging Technologies, Toronto, Canada), where a constant flow rate of $4\,\text{ml}\,\text{s}^{-1}$ is set. One hundred and sixty consecutive velocity estimations are calculated corresponding to a time period of 100 ms.

Results for the experiment are shown in Fig. 5.8. The mean velocity magnitude is shown in (a) as a surface plot from the XZ plane when $Y = 0$. The plot presents

Table 5.5: Transducer and Acquisition parameters

Transducer		Transmit Parameters	
Parameter	Value	Parameter	Value
Type	2-D Matrix array	Excitation signal	3 period sine
Number of elements	1024	Number of emitting elements	1024
Element pitch (both)	0.3 mm	Apodization window	2-D Hanning
Element kerf (both)	0.022 mm	Number of distinct emissions	5
Center frequency	3 MHz	Pulse repetition frequency (PRF)	10 kHz
		F-number	-2

a parabolic flow profile, as expected for laminar flows, with an estimated flow rate of $3.23\,\mathrm{ml\,s^{-1}}$. The velocity profiles along the Z and X axis are shown in (b) and (c), respectively. The expected true parabolic profiles are shown in red for the distinct velocity components. The relative standard deviation is found to be 20%, 12%, 1.1%; for Vx, Vy, and Vz components, respectively.

The method is able to estimate 3-D velocities in a 1x1x1 cm 3-D-volume with a high temporal resolution (0.6 ms). The work shows that is feasible, with synthetic aperture techniques, to estimate 3-D velocities on 3-D-volumes, potentially providing more insight into the hemodynamics of the cardiovascular system.

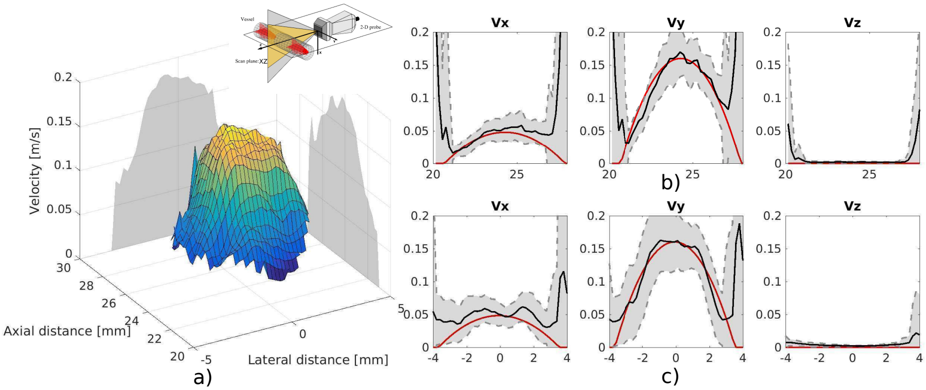

Figure 5.9: (a) Surface plot of the estimated velocity magnitude presenting a parabolic flow profile. (b) The velocity profiles along the Z axis. (c) The velocity profiles along the X axis.

CHAPTER 6

Energy based tissue echo-canceling

Summary *This chapter presents the basic idea for the submitted Patent I which introduces a new perspective for tissue echo-canceling methodologies in medical ultrasound. The first part of the chapter the proposed method which applies an energy based cut-off instead of the conventional Doppler frequency one is explained. It is shown that the approach is advantageous when used for 2-D vector flow estimation, specially when fully transverse flow is present. The second part presents work regarding an adaptive algorithm based on a Gaussian adaptive model which is used for automatically calculating the energy cut-off for the presented tissue echo-canceling model. Finally, the proposed approach is validated in straight vessel simulations with wall movement and in-vivo measurements.*

6.1 Purpose

In the same way astronomers need the sun to be absent for observing the stars; sonographers needs to remove signal originated from the surrounding tissue before exploring blood cells movement. For this purpose a tissue echo-canceling filter is created, which task is to remove tissue signals that are 100 to 10,000 stronger than blood cells echoes. The task is challenging since blood echoes are overpowered by the tissue signal, however, the surrounding tissues and vessel wall are either stationary or moving very slowly compared to the blood. These two basic characteristics of tissue signals, namely high amplitude and low frequency, are key features for identifying clutter and filtering it from the signal.

6.2 The conventional frequency cut-off model

Over the last 30 years, substantial work has been conducted for suppressing tissue signals as they hinder the estimation of blood flow using ultrasound (Bjærum, Torp, and Kristoffersen 2002). This operation have remained a major challenge because tissue echoes and blood scatterers tend to share signal characteristics, specially when blood flow velocities become low or when tissue motion is considerable. An additional challenge is that in conventional line-per-line scanning systems few temporal samples are available (8-16 samples) for the filter when an extended field of view is desired. Therefore, filter designs have been predominantly difficult since low order tissue echo-canceling filters with a sufficient stopband attenuation and a steep transition to passband are required to work with only a few temporal samples.

Several strategies for designing these filters have emerged (Yu and Løvstakken 2010), and with new parallel ultrasound technologies increasing the number of available temporal samples the use of more advanced filters is on the rise (Demene et al. 2015). However, the design principle has remain basically the same, i.e. the signals are separated based on the difference of their spectral frequency. Where the tissue and blood signal are considered of having non-overlapping spectra centred at the zero frequency and the Doppler frequency, respectively.

6.2.1 Principle

The tissue echo-canceling process can be more intuitively followed if the signals are represented in the Fourier domain, where the velocity from moving tissue and blood signals is represented by their Doppler frequency. According to the model developed by Torp et al (Torp, Kristoffersen, and Angelsen 1994) and furtherly investigated by Løvstakken(Løvstakken, Bjærum, and Torp 2007). The signal spectrum will follow a 1-D statistical Gaussian distribution, assuming that contributions come from a large number of independent scatterers, and the pulse and lateral beam profiles are constant over the sample volume.

The Gaussian shaped signal spectrum, thus, is expressed as

$$G(\omega) = R(0)\sqrt{2\pi}\sigma \exp^{-\frac{1}{2}(\omega-\omega_d)^2\sigma^2}, \tag{6.1}$$

where the mean frequency is given by the Doppler frequency ω_d, the bandwidth by σ; which is related to the transit-time of the scatterers (Løvstakken, Bjærum, and Torp 2007), and total energy of the signal expressed as the auto-correlation function at zero lag $R(0)$.

In general, the velocity for a specific tissue structure is low compared to the pulse repetition frequency (PRF), therefore, its Doppler frequency ω_t will be centred near zero. Additionally, transit-time effects are less prominent than for blood flow, thus, the σ_t bandwidth will be narrow. These characteristics of the tissue spectra are used for removing their contribution in the ultrasound signal.

In a frequency cut-off tissue echo-canceling model, a high pass filter with a cut-off frequency ω_c, as illustrated in Fig. 6.1 , is used as a threshold for preserving the flow spectrum but removing the tissue contributions to it. The standard assumption is that the tissue and blood spectra are non-overlapping, however, tissue Doppler frequency (ω_t) and bandwidth (σ_t) can be increased by accelerated movement of the tissue, and by the vibration of muscle both in the operator holding the probe and inside the patient itself. This can generate overlapping spectra since the tissue frequency components are neither narrow or zero-centred.

The presence of tissue movement requires more advanced filtering methods that are able to adapt their cut-off frequency. Several approaches have been proposed, for example down-mixing the ultrasound signal by compensating for the tissue motion so the spectrum is shifted back to the zero frequency (Bjærum, Torp, and Kristoffersen 2002; Thomas and Hall 1994); eigen-based clutter which seek a new basis for applying a regression filtering

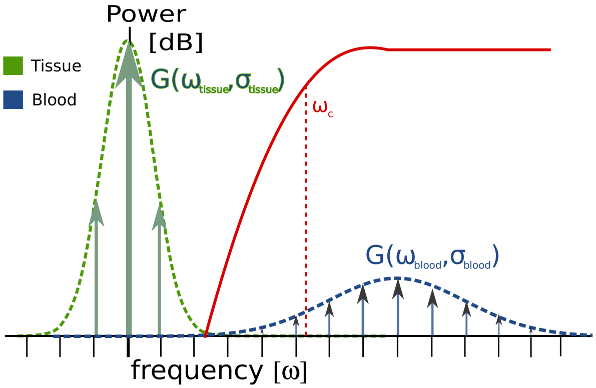

Figure 6.1: Representation of the Fourier spectra using the Gaussian model. The tissue signal, represented in green, as a higher amplitude, narrowband, and zero centred spectrum. The blood signal, represented in blue, as a lower amplitude, broadband, and centred at the Doppler frequency. The spectra are considered non-overlapping, and therefore, separable by a frequency cut-off filter represented in red.

by using the eigenvectors of the estimated signal correlation matrix (Løvstakken, Bjærum, Kristoffersen, et al. 2006).

In all these approaches, it is considered that the difference between the Doppler frequencies ω_t and ω_b is significant to tell them apart. However, this is only the case when low beam-to-flow angles are considered. Whenever the beam-to-flow angles are increased, the Doppler frequency decreases until the point when both frequencies are zero centred, i.e. complete transverse flow.

To illustrate the effects of echo-canceling on distinct beam-to-flow angles surface plots of the Fourier spectra across depth of simulated vessels are shown in Fig. 6.2. The tissue power spectra are visible on the leftmost frequency axis appearing as a higher energy yellowish wall. The tissue signal is seen fully concentrated on the zero Doppler frequency, however, tissue movement will result in an to expand in bandwidth. The blood scatterers power spectra are distributed on the higher frequencies, where the parabolic flow profile in the vessel is observable due to the direct relationship between velocity and frequency. A transparent red plane is used to illustrate an hypothetical ideal filter's cut-off frequency, where all the signal below the selected frequency threshold would be removed. It is evident that in the 60° beam-to-flow angle most of the blood scatterers power is above the frequency threshold, however, for the same threshold at the 90° beam-to-flow angle the blood power spectrum is severely affected. As an important note, high order

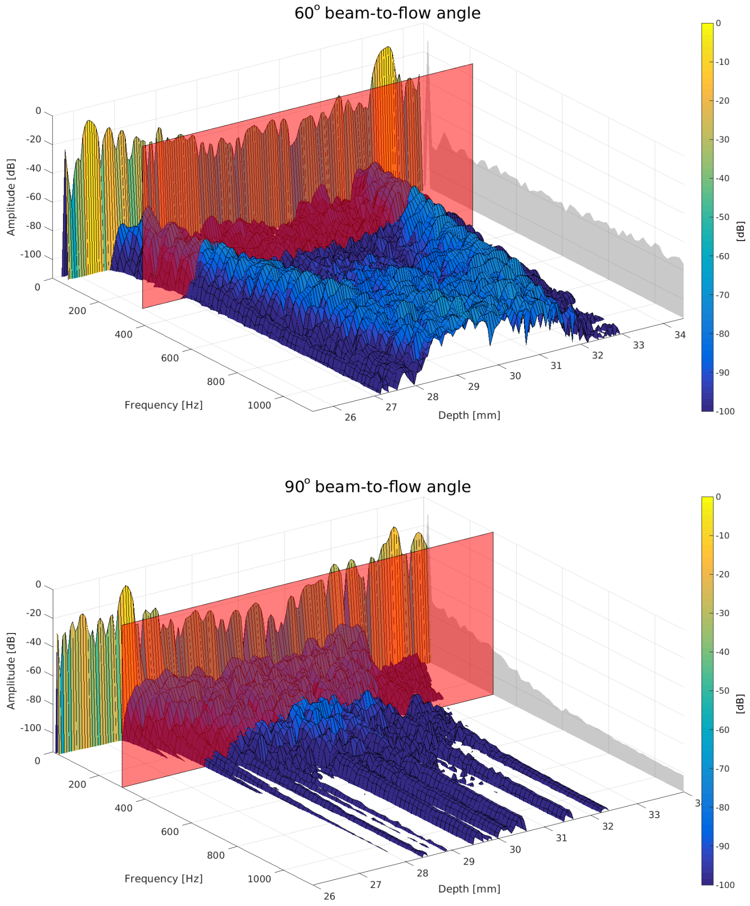

Figure 6.2: Fourier spectra of simulated straight vessels for a beam-to-flow angle of 60° (top), and 90° (bottom). The spectra is evaluated along depth at the center of the vessel. A parabolic flow profile was simulated and is also visible in the shape of the flow spectra. A frequency cut-off threshold is illustrated as a transparent red plane, where the spectra components below this threshold are normally considered tissue are removed.

filters with a sharp transition zone between the stopband and the passband are difficult to design, sometime requiring complex filter initialization schemes (Kadi and Loupas 1995). Therefore, the frequency cut-off should be not considered as a hard threshold but more like a frequency transition band.

6.3 The energy based cut-off model

Another perspective for tissue echo-canceling is to approach the problem from an energy based point of view. Here the Fourier spectrum is grouped such that a high signal amplitude would indicate tissue, and low signal amplitude would indicate either blood or noise. The use of the energy or amplitude characteristic as a discriminator is not new, and has been previously incorporated in other tissue echo-canceling methodologies such as eigen-vectors (Yu and Løvstakken 2010) or singular value decomposition (Demene et al. 2015). The difference relies on these methods using a signal basis transform to account for the energy content. However, the generated transform basis is unique and, thus, a specific decision on how many components from the new basis to remove is challenging. These methods sometimes recur in an additional Fourier transform of the new basis for further decision making (Yu and Cobbold 2006).

6.3.1 Principle

In this section, the energy based approach is directly incorporated in the Fourier representation of the signal, thus, no additional steps are required. The tissue echo-canceling process will also be followed in the Fourier domain, where, as described previously the velocity from moving tissue and blood signals are represented by their Doppler frequency. The same 1-D Gaussian model developed by Torp (Torp, Kristoffersen, and Angelsen 1994), will be considered for representing the frequency spectra of the signals. However, the standard assumption that the tissue and blood spectra are non-overlapping will be no longer considered valid.

The tissue energy removal process relies on Parseval's theorem, which states that the total energy of a signal and the sum of the energy components of the signal's Fourier transform are equal. Therefore, a blood Gaussian shaped spectrum expressed as in 7.1, with a total energy $R_b(0)$ distributed into a bandwidth σ_b could overpower a higher energy tissue signal, if the tissue spectrum was distributed on a narrower bandwidth, and its energy was limited to the blood signal amplitude, as illustrated in Fig. 6.3. The area under the curve, i.e. the total signal energy of the blood signal, is clearly larger than the area of the modified tissue spectra curve. These means that when the inverse Fourier transform is applied the obtained signal will still be a combination of tissue and blood signals but with the blood signal overpowering the tissue's. It is important to notice that the assumption that the tissue signal bandwidth (σ_t) should be smaller that the blood signal bandwidth (σ_b), and that for slow moving flow this could not be the case.

In general, tissue bandwidths are narrow due to their limited transit-time effects. Additionally, the bandwidth will get narrower when tissue movements are aligned with the ultrasound beam, which is the case for a transverse vessel. This is advantageous because in this scenario the signals spectra overlap the most.

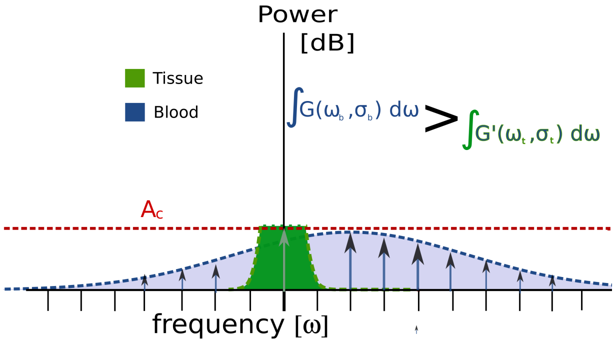

Figure 6.3: Fourier spectra of the tissue (green) and blood (blue) signal. The tissue spectra has been limited by the amplitude cut-off (red), which effectively reduces the energy level of the tissue signal.

6.4 The adaptive Gaussian model

For the energy based tissue echo-canceler to perform properly, it is essential to choose a suitable energy threshold whose value can adequately suppress tissue signal without distorting the desired blood echoes. This threshold selection process essentially involves finding the energy level of the blood signal. In particular, the blood components need to be identified from the other two constituents of the spectrum signal, namely: (1) tissue clutter, which arises from reverberations and beam side lobes covering tissue regions; (2) random white noise, which originates from thermal and electronic fluctuations. Once the blood components energy level are identified, a threshold above this energy level is selected.

Several strategies for identifying the distinct signal constituents could be adopted. In this work a down to top energy approach is suggested, which starts from the lowest energy level and search for energy levels boundaries. The boundaries are defined as energy intensity deviations from previously estimated energy models. The models are based on Gaussian distributions which are know to be adequate for modelling any of the three signal constituents. The algorithm is inspired by the dynamic noise power detection described by Siggia and Passarelli (Siggia and Passarelli 2004).

The signal constituents will vary spatially as different regions might contain distinct amounts of tissue clutter signal. Therefore, the algorithm is applied along small subregions, where the signal spectra are averaged before energy level detection. After an energy threshold is estimated for each subregion, a smoothing filter is used to maintain a similar threshold in neighboring subregions. This conserves the spatial information of the blood signal more coherently, and avoids blocks artefacts in the resulting signal.

6.4.1 Energy levels detection

It is known that the tissue or blood signal can be represented by Gaussian models, Sec. 6.2.1. In this work, such representation is used for identifying the distinct constituents of the received signal. However, instead of operating directly on the Doppler spectrum the cumulative distribution function (CDF) is preferred. This allows for probing the spectrum from the lowest energy to the highest energy level in a more robust manner, due to the integral nature of the CDF.

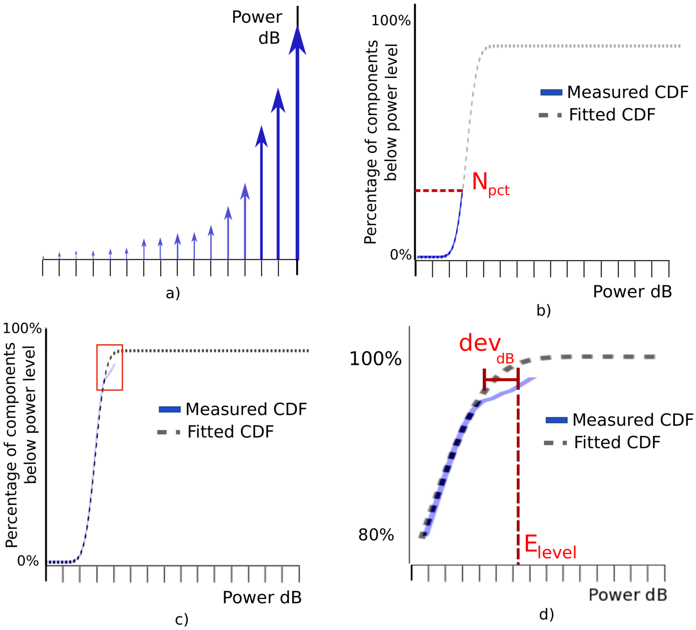

Figure 6.4: Steps for finding the energy levels boundaries. (a) Sorting of the components from lowest energy to the highest. (b) Estimate the cumulative distribution function (CDF) until N_{pct} and fit a theoretical Gaussian CDF. (c) Continue to estimate the CDF. (d) When the estimated CDF deviates more than dev_{dB} from the theoretical Gaussian CDF, the E_{level} boundary is marked.

The Doppler spectrum components are first sorted in order of their power. As shown in Fig. 6.4 (a), the sorting places the weakest component to the left and the strongest to the right. The CDF then starts accumulating from the weakest component, as shown in Fig. 6.4 (b), where the horizontal axis is the energy in dB of the component, and the vertical axis is the percentage of components that have a power less than the x-axis. The CDF is first accumulated until a user defined threshold N_{pct} is reached. This defines the minimum percentage of components that should be considered part of the first constituent level (normally noise). A theoretical Gaussian cumulative distribution is then fitted to the partial CDF curve. The CDF accumulation process is then continued until the curve deviation becomes larger than the threshold dev_{dB} . The curve deviation is measured in terms of the energy difference between the actual CDF curve and the predicted theoretical Gaussian model, as shown in Fig. 6.4 (c) and (d). The energy point, where the deviation occurs, marks the boundary of the current energy level E_{level}. The next energy level boundary search starts from the previously found energy boundary. When a new search is started, a new model is fitted from this point until the next N_{pct} point. The same level boundary procedure is continued until either the three constituents are found or the 95% of the CDF curve is reached.

The three constituents might not be always found in the receive signal. The reasons for the detection of only two energy levels is twofold: (1) the blood signal is not present; (2) the blood signal is aliased. In case of aliasing the velocities in the subregion are higher than the aliasing limit, and the blood signal is spread along the whole spectrum. These two cases are undistinguishable from each other, however, by setting the blood energy threshold at the estimated boundary, the blood signal is kept in the second case, and for the first case the threshold is irrelevant. Whenever three levels are found, it is considered that the three constituents are in order of increasing energy: (1) noise; (2) blood; (3) tissue. The energy threshold E_{level} is, therefore, at the boundary between blood and tissue.

6.5 Performance investigation

This section investigates the influence of the tissue echo-canceling filter on the vector velocity estimation. First, a straight vessel simulation study with vessel wall movement is examined. The vessel wall is moved radially at a constant velocity. The use of both frequency and energy based models are explored and compared to the simulated dataset. The adaptive energy threshold is then added to the energy based model, and the consequences of it are analysed. Finally, both cut-off models are tested against *in vivo* acquisitions on the common carotid. The effects of tissue movement are shown to be more pronounced in the early systolic phase producing a blinding artefact, which hinders the blood flow velocity estimates.

6.5.1 Straight vessels simulations

Vessels with a diameter of 5 mm centred at 30 mm are simulated with the same imaging parameters as described in Sec.3.2. Blood scatterers are moved using a parabolic profile with a peak velocity of $0.25\,\mathrm{m\,s^{-1}}$. Additionally to the blood scatterers, a concentric expanding vessel wall is simulated and moved at velocities of 0, 1.25, 2.5, and 3.75 $\mathrm{mm\,s^{-1}}$. The vessel wall scatterers mean amplitudes are set 10 dB above the tissue signal mean amplitude, while the blood flow is set 40 dB below. The vessels are simulated with beam-to-flow angles of 60° and 90°.

6.5.1.1 THE CONVENTIONAL FREQUENCY CUT-OFF MODEL

Two types of tissue echo-canceling filters are investigated: (1) moving average filter (MA), which is a linear time invariant filter with a response fully characterized by its frequency transfer function; (2) linear regression filter (LR), which is an adaptive time variant filter designed by Hoeks (Hoeks et al. 1991). The regression filter response is more complicated to characterize since it adapts the frequency response to the clutter signal, and thus, its cut-off depend on it; an approximate expression for it is $0.87\frac{PRF}{N_{ec}}$ where N_{ec} is the ensemble length. For both filter investigations the ensemble lengths are kept at 16, and 50 consecutive estimates are used for the statistics which correspond to 20 ms. The axial -3 dB cut-off frequency is 392 Hz for the MA filter, and 120 Hz for the LR filter.

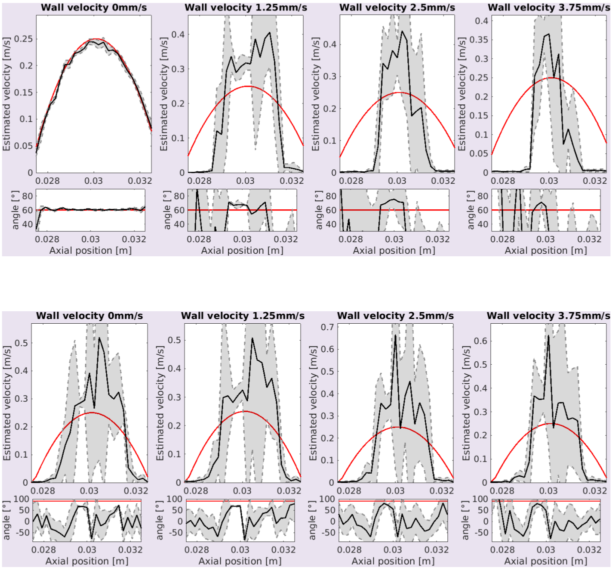

Figure 6.5: Effects of vessel wall movement on the velocity estimation for the 60° beam-to-flow angle vessel. Profiles shows the mean and the standard deviation compared to the true profile (red) for the moving average (top) and the Hoeks regression filter (bottom).

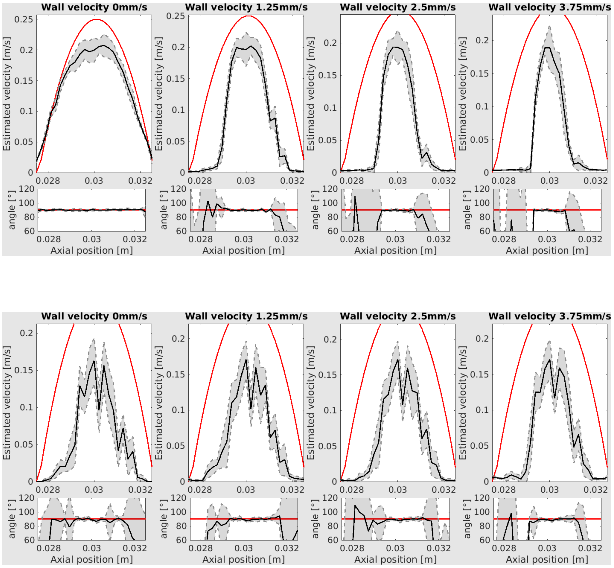

Figure 6.6: Influence of the vessel wall movement on the velocity estimation for the 90° beam-to-flow angle vessel. Profiles show the mean and the standard deviation compared to the true profile (red) for the moving average (top) and the Hoeks regression filter (bottom).

In Fig. 6.5 the estimated velocity profiles for the 60° beam-to-flow angle vessel are shown. The linear time invariant MA filter is shown in the top, while the adaptive time variant LR filter in the bottom. The performance of the estimates using the MA filter when no tissue movement is present is in accordance to the low bias and the low standard deviations reported in Sec. 3.3.1. However, the presence of tissue movement degrades the estimates, the more affected being on the edges. As the vessel wall velocity increases the affected region is increased towards the inner part of the vessel. Surprisingly, the performance of the method in combination with the LR filter is poor in all wall motion scenarios, even when no wall motion is present.

On the other hand on Fig. 6.6, the LR filter presented a high robustness against wall motion when used on the 90° beam-to-flow angle vessel. The velocity estimates with the LR filter seems unaffected by the wall movement. However, the under-estimation of the velocity magnitude is more prominent on the LR filter. For both filters the standard deviations are lower compared to the 60° vessel case. The most likely reason for this is that as the wall movement is aligned with the ultrasound beam (perpendicular to the flow), a narrower spectrum is present, thus, affecting in less degree the flow spectrum.

6.5.1.2 The energy based cut-off model

The energy based model is investigated first with a manually selected threshold and then using the proposed adaptive scheme. In both experiments the echo-canceling ensemble length is increased to 128 to achieve a better energy distribution along the Fourier energy bins. However, the velocity estimation is still performed using an ensemble length of 16 to maintain the same averaging as the previous experiment. An 80% passband Tukey window is applied to the echo-canceling ensemble samples before performing the Fourier transform for minimizing spectral leakage effects. Additionally, to reduce further influence of the vessel wall to the velocity estimates, a low cut-off (70 Hz) frequency cut-off filter is used for attenuating the lower frequency Doppler components.

The manual selected threshold is determined by inspection of the simulated blood signal spectrum, shown in Fig. 6.2. The energy threshold is selected in such a way, that the blood flow spectrum is left unmodified but the tissue spectrum is limited to a energy level just above the blood flow, in this case the selected threshold was -70 dB.

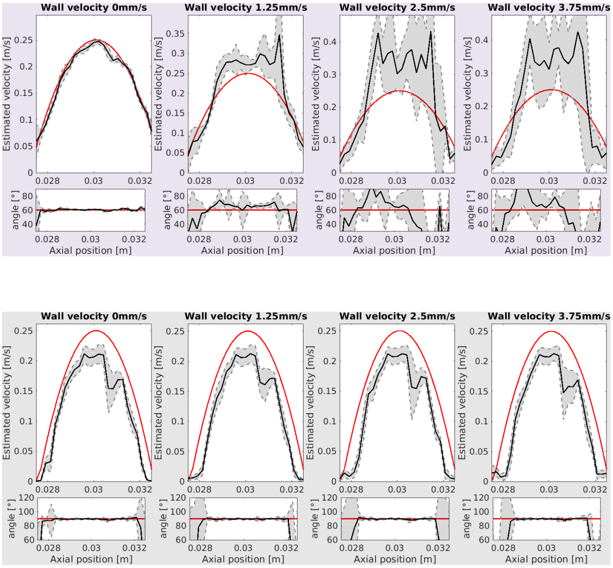

Figure 6.7: Effects of vessel wall movement on the velocity estimation using the energy based tissue echo-canceler. Profiles show the mean and the standard deviation compared to the true profile (red) for the 60° (top) and 90° (bottom) beam-to-flow angle vessels.

In Fig. 6.7 the estimated velocity profiles for the manually selected threshold at different magnitude of wall motion are shown. The profile results for 60° beam-to-flow angle are shown on top and the 90° on the bottom. For both vessels, the performance of the velocity estimator is practically unaffected when no vessel wall motion is present. The 90° beam-to-flow vessel has also presented a constant behaviour regardless of the vessel wall movement. However, the angle estimates in the 60° beam-to-flow setup, degrade as the vessel wall motion increases. The most likely explanation is that there is an increase of the tissue spectra broadness at a lower beam-to-flow angles, generating that the tissue energy components which contaminates the flow spectrum.

The selected threshold of -70 dB is adequate for removing the tissue signal and maintaining the flow signal for the simulated example. Therefore, given the same example, an adaptive threshold algorithm must be able to mimic the manually selected one. Fig. 6.8 shows the spatial estimated thresholds for the proposed Gaussian adaptive algorithm. To the left the 60° beam-to-flow vessel thresholds are estimated on the appropriate range. However, on the 90° vessel the threshold seems to be under estimated by orders of several dBs. The explanation for this is that the algorithm seems to detect only two energy levels, thus, wrongly selecting the noise floor level as the threshold. This low clutter scenario is not currently well handled by the algorithm and should be improved.

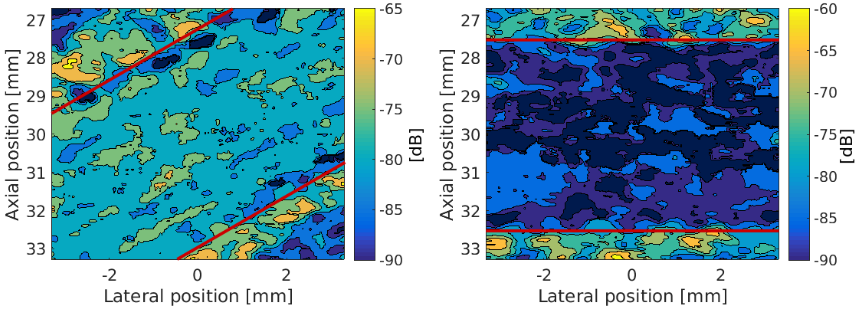

Figure 6.8: Estimated spatial energy thresholds for the 60° (left) and 90° (right) beam-to-flow angle vessels at a single time instance. The actual vessel is outlined by the red lines.

The effects of the adaptive threshold to the velocity estimations are shown in Fig. 6.9. The angle and velocity profiles for the 60° beam-to-flow vessel are similar to the ones presented in Fig. when the manually selected threshold was used. This is because the estimated thresholds shown in Fig 6.8 (left) are in the energy range of the blood signal. However, the estimated profiles for the 90° beam-to-flow present a degraded performance, mostly because the estimated thresholds shown in Fig. 6.8 (right) are under-estimated, therefore, partially removing the energy of the blood signal. Finally, is worth noticing that small variations of the estimation of the energy thresholds do not have a strong impact on the velocity estimation unless the thresholds are off by several orders of dBs.

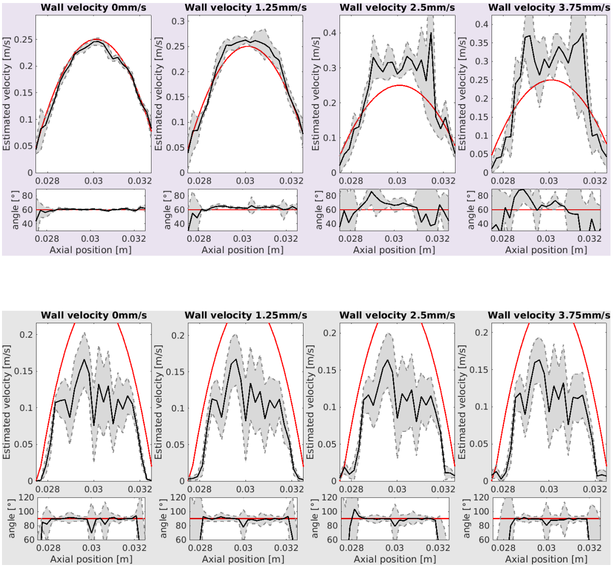

Figure 6.9: Effects of vessel wall movement on the velocity estimation using the energy based tissue echo-canceler and the adaptive threshold estimation. Profiles shows the mean and the standard deviation compared to the true profile (red) for the 60° (top) and 90° (bottom) beam-to-flow angle vessels.

6.5.2 *In vivo*

An *in-vivo* acquisition is performed on a healthy volunteer with no history of cardiovascular disease (27 year old man) after informed consent. The ultrasound scan sequence is acquired on the left common carotid on a longitudinal view. The scans are recorded with the volunteer in supine position and carried out by an experienced radiologist. A 3 second acquisition is recorded, yielding 7,500 velocity estimates at 2,500 frames per second. From which the center scan line is processed using both the MA filter and the proposed adaptive Gaussian model energy based filter. Additionally, on the same scan line the axial velocity of the top vessel wall is estimated using cross-correlations.

The unfiltered velocity estimates are shown in Fig.6.10. The flow data processed using the MA filter, shown in the middle, presents a degradation of flow estimates during the three detected systolic peaks. The degradation of the estimates correlates with regions of high vessel wall movement shown on the top plot. It is also observable that at the depths of 14 to 17 mm the degradation of the estimates is higher. This is due to the clutter level conditions, which are present higher values on the upper wall. The behaviour matches with the results obtained from the straight vessel simulations, where the lower velocities from the vessel wall clutter propagates inside the vessel and overpowers the flow signal.

In contrast, the estimates generated using the proposed adaptive filter do not present such degradation and estimate the complete flow profile regardless of the vessel wall movement. The filter also recovers more energy from the blood scatterers, thus, is able to estimate flow in the vicinities of the vessel wall during the diastole period. However, the filter presents some artefacts outside the vessel, most notably in the lower wall. This artefacts come from the absence of blood flow signal after removing the tissue's, thus, the only signal left is noise. These estimates can be easily filtered in the post-processing stage.

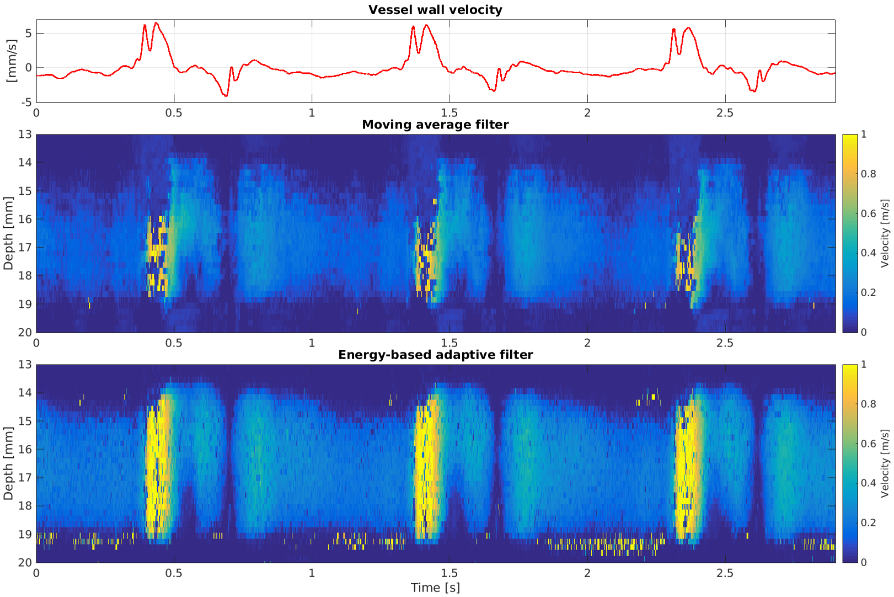

Figure 6.10: Effects of vessel wall movement on the velocity estimation in an *in vivo* example. The estimated vessel wall velocities are shown on top. In the middle, the flow estimates using the MA filter. In the bottom, the flow estimates using the proposed adaptive filtering.

CHAPTER 7

Clinical applications

Summary *This chapter puts forward ideas on clinical applications for the developed ultrasound based velocity estimation method and tissue echo-canceler. The first three sections are devoted to exploring atherosclerosis related applications, as many cardiovascular diseases are related to this process. Firstly, an indirect measurement of local arterial wall stiffness, which relates to the microscopic alterations that occur in the vessel wall, is investigated by the use of the proposed flow velocity estimator. Secondly, the detected complex hemodynamics are used to trace probable regions of plaque formation by the development of a particle resident time estimator. Thirdly, a pressure gradient estimator, which presents a novel way to assess the risk of plaque tear-off is explored. Finally, the chapter is closed with an attempt to provide better quantification of blood flow in small vasculature by the combination of the proposed velocity estimation with the improved tissue echo-canceler.*

7.1 Purpose

The purpose of this chapter is to translate the developed flow estimation techniques to clinical relevant applications, by providing a number of examples where a better insight into the hemodynamics can deliver novel indicators that may have a potential impact on clinical diagnoses. The emphasis is made on atherosclerosis, which is one of the major causes of death in the western world (Naghavi et al. 2003), but many other applications could benefit from novel flow derived indicators.

7.2 Pulse wave velocity estimation

Pulse wave velocity (PWV) has been shown to be strongly correlated to cardiovascular events and all-cause mortality (Laurent et al. 2001). The reason for the correlation is that PWV is an indirect measurement of the arterial wall stiffness, which is associated with hypertension related diseases. For example, a raise in systolic pressure will potentially increase the left ventricular afterload and myocardial work, or a decrease in diastolic pressure could reduce coronary perfusion, resulting in subendocardial ischemia (Watanabe et al. 1993). Arterial wall stiffness, measured by the PWV, is therefore an important indicator for atherosclerosis, since it indirectly measures the microscopic alterations that occur in the vessel wall.

The clinical standard for measuring the PWV is the carotid–femoral pulse delay, which is calculated as the distance between the carotid and the femoral arteries divided by the transit time delay of the pulse wave (Laurent et al. 2001). However, the carotid–femoral distance cannot be accurately measured, due to to the non-uniform geometry of the artery. Additionally, the elastic properties of the arteries are non-uniform along the arterial tree, thus, the method only quantifies an average stiffness of the arteries along the carotid–femoral pathway.

In atherosclerosis, regional differences in mechanical properties exist at different locations of the arterial tree (Mangell et al. 1996). Therefore, local measurements of PWV are also of interest. The local PWV can be measured non-invasively using ultrasound imaging, by estimating the time delay between the diameter waveforms recorded simultaneously at two close positions along the vessel (Benthin et al. 1991). These techniques depend on a reliable identification of the foot of the diameter waveforms and a sufficiently high sampling frequency.

The PWV can also be estimated from area and flow measurements directly, since flow and cross-sectional areas are related by the wave equation. The area-flow (QA) method has previously been applied to ultrasound data (Rabben et al. 2004), however, the performance of the method depends on the accuracy of the basic measurements of vessel area and flow. The main weakness of the QA method is the vulnerability to measurement errors, such as the one introduced by the angle correction in the use of conventional velocity estimation techniques; which would directly influence the slope of the upstroke of the QA loop.

In this section, work on the QA estimator developed during the supervision of the Bsc project of Niclas Møller and Sigbjørn Hokland is presented. Where, the QA estimator is combined with the flow rates estimated from the proposed velocity estimation method, to examine if the increase in precision of the flow estimator would translate to the PWV estimate.

7.2.1 Method

As mentioned, the PWV can be obtained from recordings of the flow rate $Q(t)$ and area $A(t)$, provided that the data is from a reflection-free period during the cardiac cycle (Rabben et al. 2004). A reflection free period is normally found during the early systolic wave, and from this period the PWV is calculated as the slope of the QA-plot,

$$PWV = \frac{dQ}{dA}. \tag{7.1}$$

It is expected that the reflection free period of the heart cycle will be approximately linear on the QA-plot and will be contained within the early systole. In Fig. 7.1, an example of a QA plot is shown, the early systole period is denoted with the red line. The PWV is then estimated from the linear regression of the QA-plot during the linear early systole region.

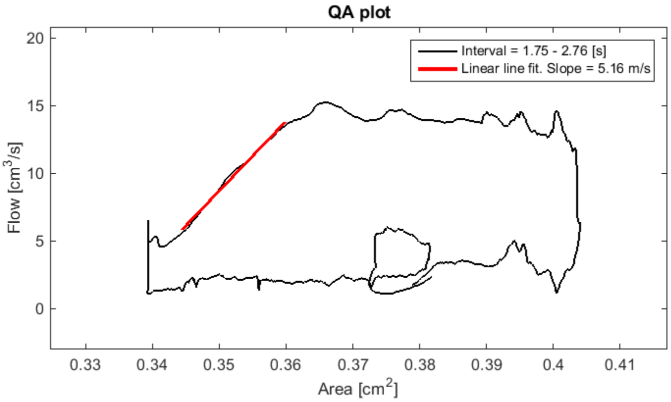

Figure 7.1: QA plot for a complete heart cycle in the common carotid of a healthy individual. The red line denotes linear reflection free period of the heart cycle, from which the PWV is estimated.

In this work, the area signal $A(t)$ is estimated by cross-correlation of the M-mode signals using a longitudinal scan, where the proximal and distal sections of the artery wall are estimated independently to obtain two unique distensions, as shown in Fig. 7.2 (a). The distension is integrated with the assumption of a circular axis-symmetric vessel to obtain the $A(t)$ signal. The flow rate signal $Q(t)$ is estimated directly by integrating the flow from the vector velocity waveforms instead of using the angle compensated Doppler spectrum, and applying the Womersley equation, as described in Rabben's work. Furthermore, the velocity waveforms are cropped and filtered using a small kernel (4.4 ms) median filter to avoid affecting the slope of the upstroke of the waveform. An example of the velocity waveform is shown in Fig. 7.2 (b).

Both the flow rate signal $Q(t)$ and the area signal $A(t)$ are calculated from the same RF-dataset, thus, the $Q(t)$ and $A(t)$ signals are perfectly registered. The estimation was performed at the center line, however, multiple lines could be used for a more robust estimation.

7.2.2 Results

The study was performed in three young healthy males (aged<30) , where 3 s recordings of the left and right CCA were obtained. In the study, the beam and the blood flow angles were kept to approximately 90°, and no angle correction was necessary since the angle is automatically detected.

Table 7.1 lists all the PWV estimations. The result marked **in bold** is the specific test subject and cardiac cycle used for the production of the figures in the above section. With

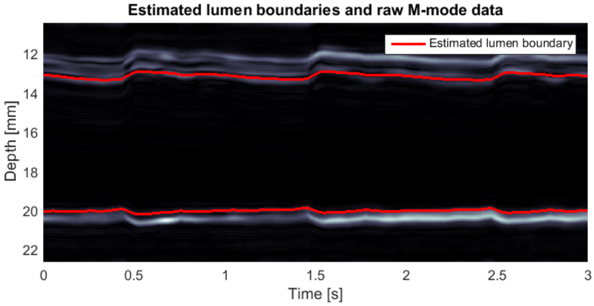

(a)

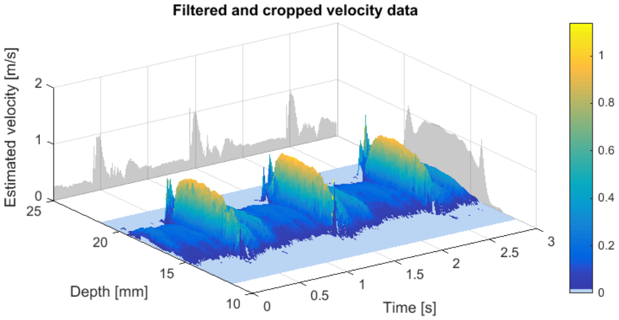

(b)

Figure 7.2: (a) The vessel wall distension waveforms in red, overlaid on the vessel wall M-mode. (b) The estimated flow velocities through time along the same center line of the vessel.

three seconds of data in each set, it was possible to analyse 2-3 well defined heart cycles per test subject from each side. The observed PWV has a good agreement with the known velocities for healthy individuals in that age range (Arterial Stiffness Collaboration 2010). However, the limited amount of cardiac cycles made it difficult to assert any statistical conclusion. Additionally, the method was not fully automated, but it needed manual input from the user for selecting the linear region of the cardiac cycle to apply the regression, possibly influencing the results. The dataset also presents an outlier, which was attributed to the tissue echo-canceling process that had a manually adjusted cut-off frequency value since the proposed energy based tissue echo-canceler was not available at that time.

In conclusion, the technique has the capability of detecting the PWV with the great clinical potential to asses atherosclerosis in an early stage of development, and even before plaques are visible in standard ultrasound screening. However, further improvements in the implementation must be made before conducting a larger study.

Table 7.1: PWV (m/s) of three healthy volunteers

Volunteer	1st cycle	2nd cycle	3rd cycle	μ*
(1) Left	7.19	6.61	NA	6.88 (±0.50)
(1) Right	6.95	6.78	NA	
(2) Left	6.51	5.20	5.72	5.59 (±1.03)
(2) Right	5.67	5.36	5.09	
(3) Left	$14.46^{\#}$	6.82	6.66	6.07 (±1.61)
(3) Right	5.23	6.47	**5.16**	
				$\mu_{QA}^{**} = 6.01 \quad (\pm 1.52)$

* Mean PWV of each TS. The value in parentheses denotes two standard deviations.

** The weighted mean of all test subjects.

$^{\#}$ This value was excluded from the statistical analysis.

7.3 Arterial hemodynamics mapping

Complex blood flow dynamics are thought to play an important role in the development of atherosclerosis; however, the exact nature of this role is incompletely understood owing to the multi-factorial nature of the disease (Lusis 2000).

The observations of atherosclerotic plaques occurring preferentially on sites with low or oscillatory endothelial shear stress are well documented in both animal models (Cheng et al. 2006) and *ex vivo* (Glickman et al. 2003). Therefore, there is an accepted notion that disturbed blood flow dynamics contribute to this disease's initiation and progression; furthermore, as a plaque develops and the arterial wall remodels, local flow patterns evolves.

The dynamics that interplay between flow and the vessel wall during plaque formation are not fully understood. As a result, several attempts to correlate hemodynamic indicators with atherosclerotic plaque distribution have been suggested (Steinman 2004). The studies have been indirect and/or retrospective, relying on post-mortem specimens, animal models, and more recently in computational fluid dynamics (CFD) models. The reason for this is that the measurement of complex hemodynamics *in vivo* has been plagued with limitations; e.g. in ultrasound the limited flow dimensionality, frame rate, and velocity range of conventional approaches has hindered the analysis of complex flow phenomena on the carotid bifurcation (Steinke, Kloetzsch, and Henneric 1990).

Only recently it has become possible to map these hemodynamic factors with enough detail and frame rate (Fadnes et al. 2015; Lenge et al. 2014; Udesen et al. 2008; Villagomez-Hoyos et al. 2016; Yiu, Lai, and Yu 2014). The hemodynamic factors of interest can be derived from the now available vector velocity map; most notably wall shear stress (WSS) and resident times (RT) of the agents (Lee, Antiga, and Steinman 2009).

The WSS and RT might allow the direct knowledge of a probable zone of plaque appearance along the whole cardiac cycle, as the plaque forming agents, namely low density lipoprotein (LDL), should be in contact as long as possible with the artery wall. In this section, the development of an algorithm for estimating particles resident times (RT) is proposed. The algorithm is then evaluated against a constriction flow phantom, and *in vivo* measurements on healthy carotid bifurcations.

7.3.1 Method

The residence time (RT) is by definition the average amount of time that a particle spends in a particular region. Therefore, for this application the residence time computation will be measured as the time that a particle enters a designated area and ends at the time that the same particle leaves the same area. Therefore, the residence time is directly related to the velocity mapping. If the velocity is increased, the residence time of the region will be shorter, and vice-versa.

In this study, the RT is estimated by means of a Monte Carlo simulation, where random particles are added to the entire region. The region is subdivided in subregions of $N \times M$ mm, and the particles are assigned to their sub-region. The particles are propagated in the imaging plane by using the estimated vector velocities. The particles are timed until they leave their assigned sub-region or until a maximum time of T_{max} seconds. The particle residence time is the average along the residence times of the particles of a given region. The process is repeated for each time instance, for obtaining a time dependant RT(t).

7.3.2 Results

The algorithm is first applied to the 70% constricted straight-tube phantom presented in Sec. 4.1.2. It is known that when a constriction is present, residence times before and after the constriction will increase, increasing the probability of plaque formation (Cheng et al. 2006). Consequently for verification purposes, the phantom study is performed during steady flow conditions at a constant flow rate of $15\,\mathrm{ml\,s^{-1}}$. This will keep the relationship between the velocity field and RT times straight forward, where low velocities will directly relate to high residence times and vice-versa. In Fig. 7.3, the estimated velocity map is shown, it presents a developed jet as flow accelerates towards the center of the constriction, and then slowly decelerates as the lumen expands. Below this velocity map, the mean RT map is shown, which, as expected, presents larger residence times at spatial locations with lower velocities. The mean RT is estimated over the full dataset (180 ms) as the experiment is performed during steady flow.

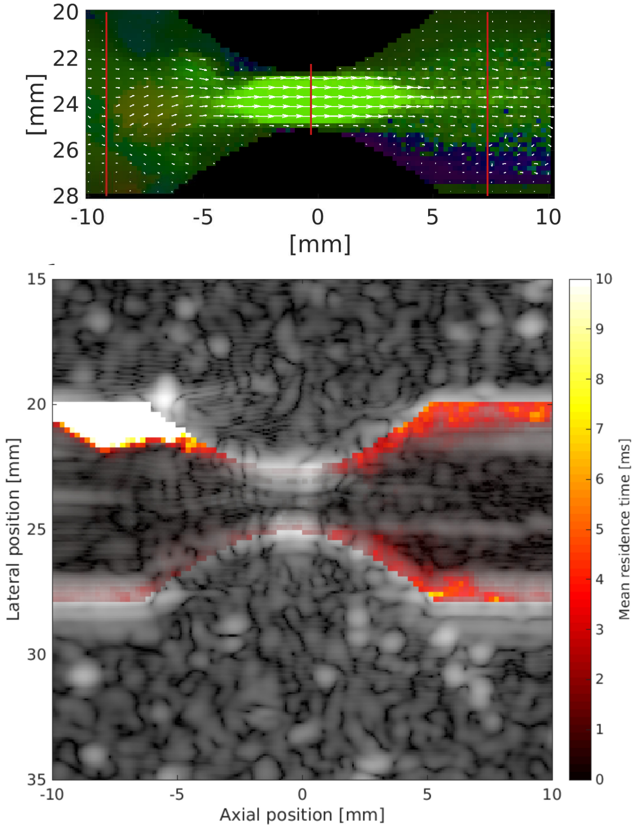

Figure 7.3: Vector flow frame from the 70% constricted straight-tube phantom presented in Sec. 4.1.2 and its corresponding residence time (RT) map. The areas with high residence times, hence lower velocities, are denoted in a brighter red.

The in-vivo investigations are performed in the carotid bifurcation of two healthy individuals, a 52 yo female and a 41 yo male. It is well known that the carotid bifurcation is a predilection site for the formation of plaques, due to the complex vessel geometry that exposes its walls to both oscillatory shear stresses and long resident times. For this study, the mean RTs are calculated for 250 ms around the peak systole pulse. The velocity map and the RT are shown side by side in Fig. 7.4, where the velocity map is selected to show the vortex flow in the carotid bulb.

In both examinations, elevated RTs are found when approximating the vessel wall, however, the values shown in Fig. 7.4 (a) shows an increased RT in the lower left section of the bulb. It is important to note that the RT must not be interpreted by itself but it should be coupled to other factors, such as high and low WSS analysis, oscillatory stresses, etc. Therefore, the current results should be interpreted cautiously since they are preliminary and further investigations must be performed.

7.4 Pressure gradients estimation

For the last 20 years the degree of internal carotid stenosis has been used as a predictor for ischemic stroke in extracranial carotid artery disease (Osarumwense et al. 2005). This is because the size of the stenosis is directly related to plaque build up, which can tear off and generate an ischemic event. However, several angiographic studies made over the coronary and the carotid arteries have demonstrated that even low grade stenoses are capable of creating acute myocardial infarction and cerebrovascular events, suggesting that the size of the stenosis is not the only factor for a plaque rupture and thrombosis (Ambrose et al. 1988).

Several authors have proposed studying not only size of the stenosis, but also assessing distinct plaque vulnerability factors such as the plaque constituents (Lovett et al. 2004; Wasserman et al. 2005). For example, plaques with increased lipid content appear to be more prone to rupture, particularly when the lipid pool is localized eccentrically within the intima. The plaque morphology also has been also used to asses the plaque vulnerability, where marked plaque irregularity is associated with increased risk of ischemic events (Saba et al. 2012).

An additional criteria is to asses the forces that act over the plaque, generated by the flow that passes through the stenosis. The net-force applied to the neck of the stenosis translates to a pressure drop caused by the dissipation of energy that goes into forming localized flow jets, eddies, and overcoming the viscous drag met by the blood cells (Young, Cholvin, and Roth 1975). Pressure drop measurements has been introduced to the clinic for measuring the forces applied to the plaque by using both invasive, by the use of pressure catheters (Donohue et al. 1993), and non-invasive techniques, by measuring velocities and deriving the pressure drop from them (Felix et al. 1976).

A wide spectrum of different approaches has been established in the pursue of deriving non-invasive transstenotic pressures from measured velocity data (Holen, Aaslid, and Landmark 1976; Teirstein, Yock, and Popp 1985). Most of these methods are based on a simplified Bernoulli equation where viscous and temporal effects are neglected. Therefore, only a single velocity estimate found distally to the lesion is required. This is the major disadvantage of the technique, as it becomes very dependent on the method's ability to detect the true peak velocity. The distal peak flow has to be much greater than the peak flow seen up-stream to the constriction for the method to be valid, thus, limiting the method to only severe cases of arterial narrowing stenosis (Yoganathan et al. 1988).

A more appropriate approach is to derive the pressure drops form the pressure gradients

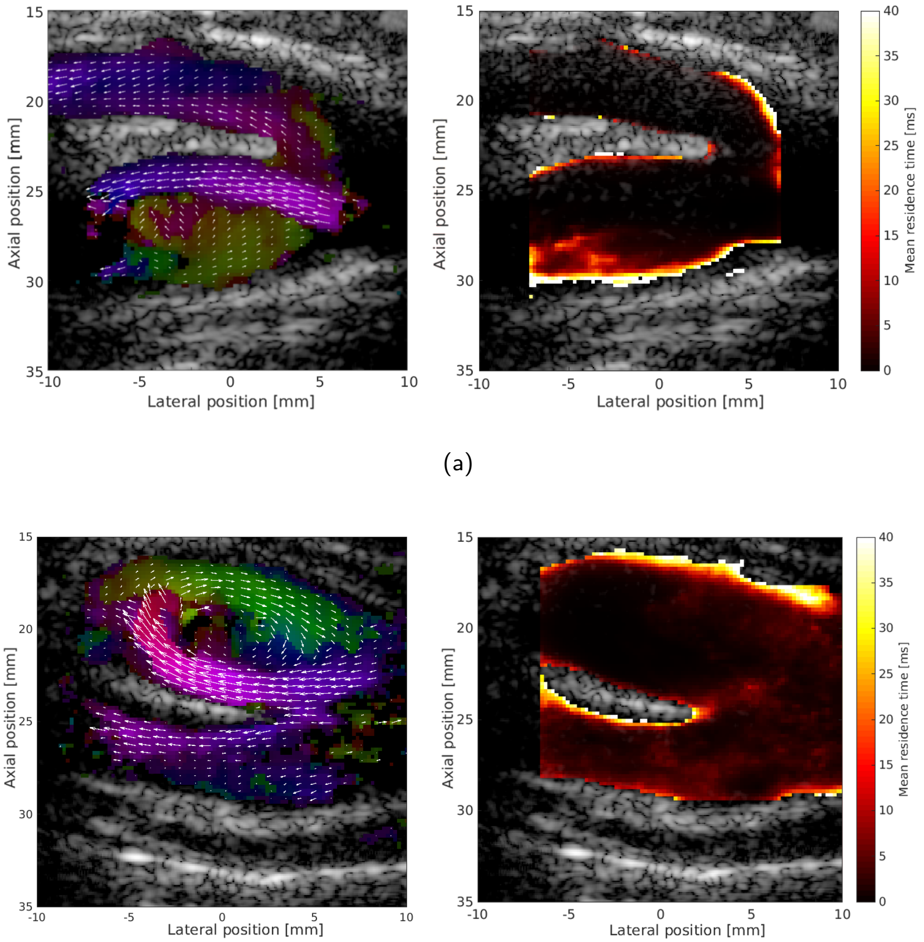

(a)

(b)

Figure 7.4: Longitudinal vector flow frame for the carotid bifurcation during the formation of the vortex (left) and its corresponding residence time for the corresponding period of $250\,\mathrm{ms}$. (a) The carotid bifurcation of a 52 yo healthy female volunteer. (b) The carotid bifurcation of a 41 yo healthy male volunteer.

obtained from the fluid velocity field using the Navier-Stokes equation, which arises from applying Newton's second law to fluid motion. However, this would require the knowledge of the complete 3-D vector flow data-set. As only a 2-D in-plane data set is available, assumptions on the out-of-plane flow velocity field are made, which in this study will be considered zero.

In this work, pressure drops are derived from non-invasive acquired vector velocity data. The work is a collaboration with Jacob B. Olesen PhD and is more thoroughly described in his PhD thesis (Olesen 2015). In the next section, a brief overview of the method and the obtained results is given. Results for a constriction flow phantom, and *in vivo* measurements on a healthy carotid bifurcation are given, for more in-depth discussion and more results the reader is referred to (Olesen 2015).

7.4.1 Method

To estimate the pressure drop across a stenosis, the overall pressure gradients across a desired region must be summed. To simplify the estimation of the pressure drop a stream line representation of the region is proposed. A streamline enables easy calculation of the pressure drop over larger regions, by integrating the individual pressure gradients found along the investigated streamline.

Re-writing the Navier-stoke equation into a scalar equation that follows a streamline, and omitting the influence of gravity and viscosity yields the following,

$$\frac{\partial p}{\partial s} = -\rho \left[\frac{\partial v_s}{\partial t} + v_s \frac{\partial v_s}{\partial s} \right]. \tag{7.2}$$

Here, v_s is the scalar product of $\vec{v}(\vec{r}, t)$ and the vector that lies tangent to the streamline $d\vec{s} = (\hat{s}_x, \hat{s}_y, \hat{s}_z)$, where $d\vec{s}$ is an element of distance along the streamline, which runs in the direction, s. Omitting the effect of viscosity is thought reasonable as the Reynolds number in the presented set-up is found to more than 1,000. Then, integrating the individual pressure gradients from (7.2) along the flow direction of the streamline gives the total drop in pressure that occurs over the course of the flow line,

$$\Delta P(t) = \int_0^L \frac{\partial p}{\partial s} \, ds. \tag{7.3}$$

Again, eqs. (7.2)–(7.3) state the need for having all three spatial vector components of $\vec{v}_s$ available for estimating the pressure gradient $\frac{\partial p}{\partial s}$. This study, however, employs a velocity estimator capable of measuring the two in-plane vector velocity component $\vec{v}_s = (v_x, v_z)$, thus, the proposed method is developed assuming that the out-of-plane velocity v_y is zero. This requirement is in general valid when a longitudinal plane of the constriction is acquired.

7.4.2 Results

The proposed method is first applied to the 70% constricted straight-tube phantom presented in Sec. 4.1.2 during steady flow and a flow rate of $5\,\mathrm{ml\,s^{-1}}$. The vector flow imaging on the constricted phantom is displayed in Fig. 7.5 (a) . The images show flow that accelerates towards the center of the constriction, producing a jet and then slowly decelerates as the lumen expands again. Black streamlines set to start from the center of the vessel are also displayed. The changes in pressure are derived along these dotted streamlines. In Fig. 7.5 (b) , the pressure drop that occurs as the fluid moves through the constricted part of the studied phantoms is displayed. The shaded zone indicates a region of ± one standard deviation normalized to the number of frames recorded.

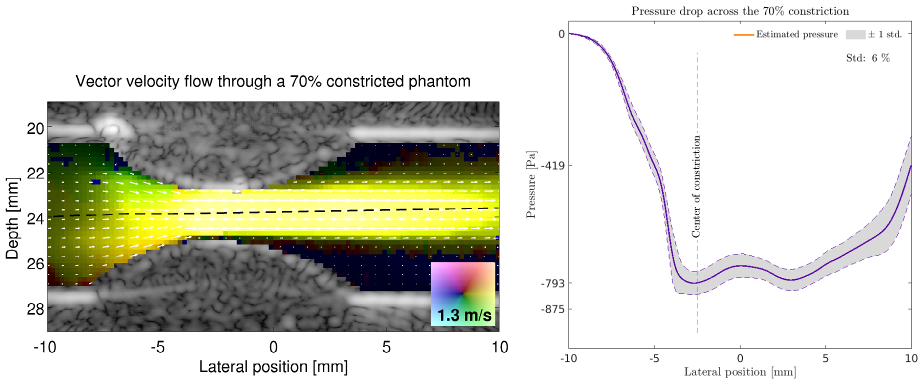

(a) (b)

Figure 7.5: (a) Vector velocity frame from the 70 % constriction during steady flow condition. Black-dotted streamline passes through the center of the constriction. (b) Transstenotic pressure drop along the constriction. The mean estimate is plotted together with ± 1 standard deviation. Obtained from (Olesen 2015)

The *in vivo* example of pressure drop is performed along the vector velocities found in the vortex of the carotid bulb, shown in Fig. 7.6 (a). The resulting pressure drops are shown as 3-D plots in Fig. 7.6 (b). The figure shows pressure changes along the direction of the streamlines as a function of time. The plots' left wall defines the starting point of the streamline data. Changes in pressure are then found relatively to this point, by moving down-right, parallel to the lateral axis. The largest pressure variations are during the systolic phase of the cardiac cycle, with values between 0 Pa and -60 Pa.

The in-vivo results show the feasibility of measuring pressure changes in the carotid artery. An area otherwise avoided by invasive catheters, as contact with the neck's arterial walls could make a vulnerable plaque rupture causing arterial blockage of the vascular beds in the brain (Al-Ameri et al. 2009). The non-invasive nature of the proposed technique, furthermore opens the possibility of running routine examinations for screening purposes, thus, further expanding the application range of pressure sensing techniques.

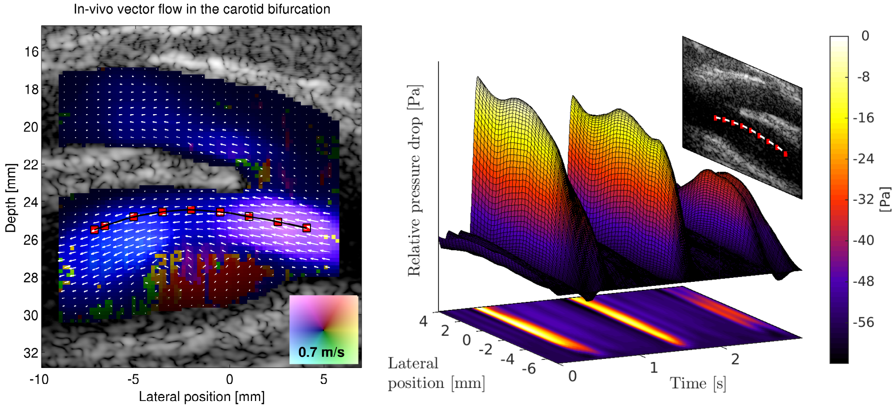

(a) (b)

Figure 7.6: (a) Longitudinal vector flow scan of the carotid bifurcation during peak systole. A vortex is seen formed in the carotid bulb. A streamline following the vector velocity field is also displayed. (b) Changes in intravascular pressure measured as a function of longitudinal position and time along the streamline. The shown pressures are in reference to an arbitrary value, which for this study is set to zero at the beginning of the streamline. Obtained from (Olesen 2015)

7.5 Small vasculature velocity quantification

In the past, power Doppler has been used to increase the sensitivity to slow flow in small vasculature in exchange of the ability for quantifying the blood velocity. The angle independency and the lack of aliasing on power Doppler have made it a valuable tool in the clinic since its introduction in the mid 1990s (Rubin et al. 1994). For some clinical purposes, the rough and ready qualitative assessments that conventional power Doppler provides in small vasculature flow might be adequate. However, many research and clinical applications in small vasculature could benefit from the additional information obtained from quantified flow, e.g. to assess the response to a vaso-active drug.

Quantitative information about blood flow in small vasculature can have potential advantages, especially in some areas, such as the cortex of kidneys and renal allografts, the prepuberal testis, the infant hip, the bowel wall, cancer angiogenesis, etc. Therefore, small vasculature velocity quantification is of clinical interest in the study of healthy tissue, as well as in investigating disease processes.

The power Doppler principle of using the entire energy/power spectrum of the blood signal instead of only the mean frequency component has permitted more confident diagnosis in body regions where the ultrasound signal is weak because blood vessels are small. The same principle is followed by the energy based tissue echo-canceler described in Chapter 6 and the angle estimator in Chapter 3 , which because their abilities to use all the available energy are a suitable candidate for quantifying flow in small vasculature.

In this work, the capability of the method to quantify velocities in small vasculature is examined. An in vivo study is conducted on the testicular parenchyma of a 27 yo healthy male. This area of interest is chosen for this work because is challenging from a flow-detection standpoint, and is normally difficult to quantified and commonly only detected by power Doppler techniques.

7.5.1 Method

The study is performed on the right testicle of a 27 yo healthy male, who is scanned by an experienced radiologist. The same flow sequence described in Sec. 3.2.1, which consists of five diverging wave emissions at an effective PRF of 2.5 kHz is used for a four seconds acquisition. The velocity estimation is performed after the adaptive energy based echo-canceling described in Sec. 6.4, which is used for reconstructing the weak blood signals.

7.5.2 Results

B-mode and Doppler image of the testicular scan are shown in Fig. 7.7 (a). The testicular parenchyma structure is observed at the middle of the testicle, where a main vessel denoted by the yellow arrow, can be seen descending into branches denoted by the purple arrow. The velocity magnitude of the denoted vessels is quantified in Fig. 7.7 (b), where 4-5 heart cycles are visible during the four seconds acquisitions. The variability of the peak velocity along the different vessels can be attributed to the out-of-plane movement of the vasculature as the scan is performed free-handed, and is most notable on the black profile. The velocity values are in accordance to the ones documented in the literature (Cassar et al. 2008). It is important to note that the plotted velocities are the 2-D flow magnitude and not the conventional axial component.

The color maps of the estimated angles and velocities at the first peak systole are shown in Fig. 7.7 (c). On the left, the estimated angle matches with the vessel direction, however, are surrounded by a 90° shifted angle corresponding to the vessel wall movement; to the right, the estimated velocity magnitude, where both the blood flow and vessel wall movement are shown to be around the same range.

In this work, the feasibility of quantifying low velocity flow using the proposed methods has been demonstrated. However, the flow sequence could be improved by using longer sequences as demonstrated in (Demene et al. 2015); which increases the contrast and the amount of blood energy available for the estimation. Additionally, improvements on the echo-canceler and the velocity estimation method could be performed to achieve better results.

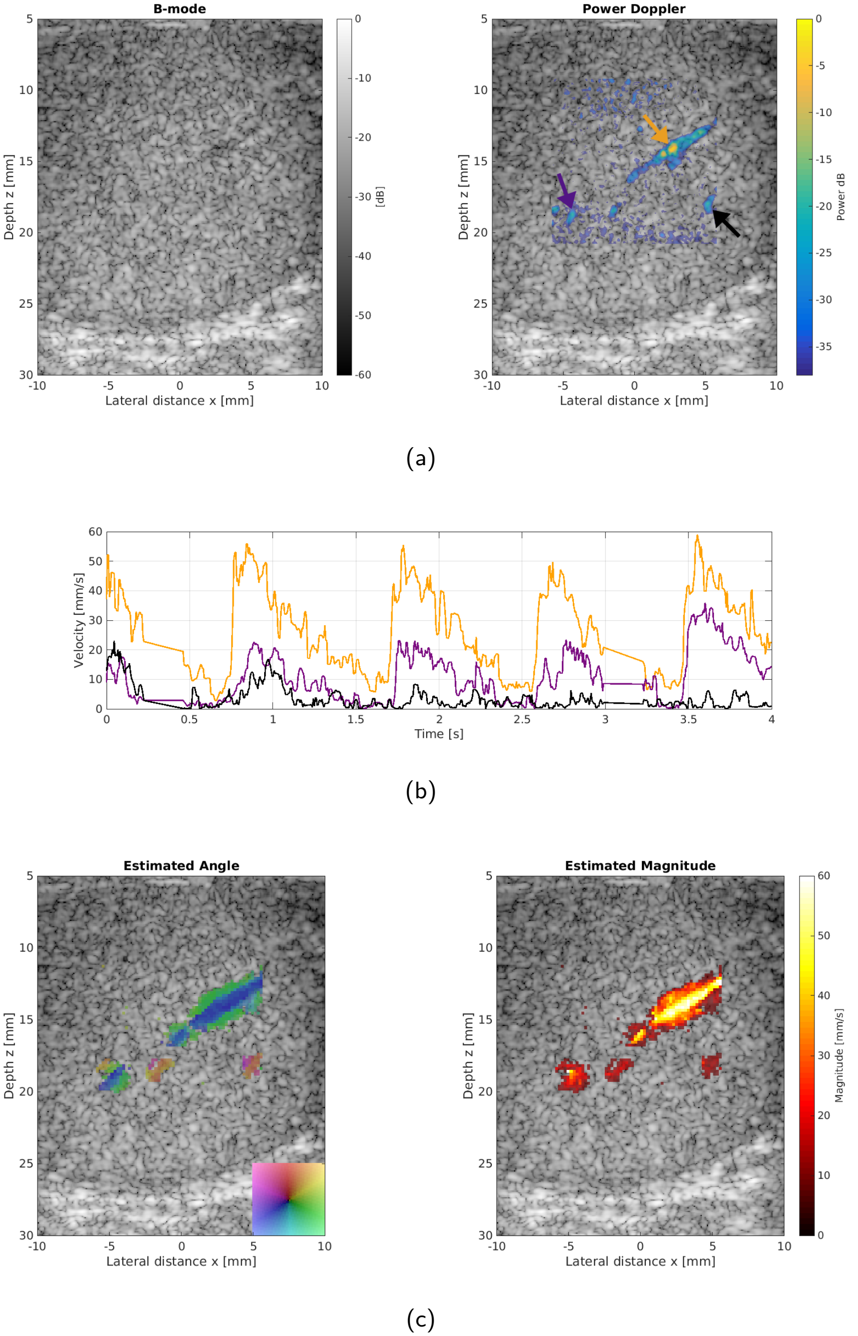

Figure 7.7: (a) B-mode and power Doppler of the right testicle of a healthy volunteer. (b) Flow velocity profiles of the denoted vessels. (c) The estimated angle and velocity map of the testicular parenchyma during the first systolic peak.

CHAPTER 8

Project Conclusion and Perspectives

The main objective of this project was the development technical solutions to overcome the current limitations of ultrasound systems. In particular the inability to detect flow in dimensions other than the one aligned with the beam direction. The author firmly believes that by relieving the operator from the burden of counteracting this limitation, operator-dependant errors in blood flow measurements would be greatly reduced, and a more accurate diagnosis would be obtained.

For this reason, Chapters 3, 4, and 5 were devoted to the investigation of the proposed accurate angle estimator. Firstly, Chapter 3 validated the proposed angle estimator by means of simulation and measurements, assessing its ability to correctly estimate angles and velocities in diverse flow conditions. Here, it was demonstrated that the method is capable of estimating angles with an accuracy in the order of a couple of degrees. In Chapter 4, an attempt was made to maximize the range of detectable velocities, in terms of both the higher and lower bounds. Although the chapter provided insight in the mechanism affecting such limits, the exact limits could not be devised. However, the method proved to be capable of simultaneously estimating velocities in the range of $3\,\mathrm{m\,s^{-1}}$ to $5\,\mathrm{cm\,s^{-1}}$, thus, providing a dynamic velocity range of 35 dB. Finally, Chapter 5 extended the method to a variety of geometries, including a 2-D matrix array for the full 3-D velocity estimation. From these investigations it was found that, although the method is capable of estimating flow velocities for all the investigated geometries without major modifications, several artefacts arose, which will be object of further research.

One current disadvantage of the proposed angle estimation method is the computational cost. The current implementation requires 360° of directional beamformed lines for each estimate. However, pyramidal approaches could be developed to decrease the number of directional beamformed lines used for each estimate. Additionally, the high computational load of high-frame-rate approaches could be loosened by means of cloud computing devices, effectively decreasing the computational time required per estimation and making practical clinical implementations possible.

In Chapter 6, the focus was shifted towards a tissue echo-canceler, which separates blood flow signal from unwanted tissue clutter signal. Here, the developed energy based model has provided a new perspective for removing the tissue signal without affecting an spectrally overlapped flow signal. This is an essential requirement for any tissue echo-canceler to be used in a vector flow systems, since major spectra overlapping will occur at large beam-to-flow angles. The approach demonstrated that is capable of diminish the effects of a moving vessel wall in both simulations and *in vivo* measurements.

Finally, Chapter 7 put forward ideas for clinical applications using the proposed angles estimator and tissue echo-canceling. Here, the additional flow information is used for developing new indicators that can have an impact in the diagnosis capability of diseases, such as atherosclerosis. However, a full understanding of the complex flow dynamics will be only achieved if the full 3-D velocity information is available with enough temporal resolution and high flow sensitivity. Further improvements to the method and additional clinical studies will most likely broaden the list of appropriate applications for this exciting ultrasound modality.

Bibliography

References from Chapter 1

Demene, C., T. Deffieux, M. Perno, B.-F. Osmanski, V. Biran, J.-L. Gennisson, L.-A. Sieu, A. Bergel, S. Franqui, J.-M. Correas, and et al. (2015). “Spatiotemporal clutter filtering of ultrafast ultrasound data highly increases Doppler and fUltrasound sensitivity”. In: *IEEE Trans. Med. Imag.* 34.11, pp. 2271–2285. DOI: `10.1109/TMI.2015.2428634` (cit. on p. 2).

Hansen, P. L., G. Cross, and L. H. Light (1974). “Beam-angle independent Doppler velocity measurement in superficial vessels”. In: *Clinical Blood Flow Measurement*. London: Sector Publishing (cit. on p. 2).

Jensen, J. A., O. Holm, L. J. Jensen, H. Bendsen, H. M. Pedersen, K. Salomonsen, J. Hansen, and S. Nikolov (1999). “Experimental ultrasound system for real-time synthetic imaging”. In: *Proc. IEEE Ultrason. Symp.* Vol. 2, pp. 1595–1599. DOI: `10.1109/ULTSYM.1999.849300` (cit. on p. 2).

Jensen, J. A. and P. Munk (1998). “A New Method for Estimation of Velocity Vectors”. In: *IEEE Trans. Ultrason., Ferroelec., Freq. Contr.* 45, pp. 837–851 (cit. on p. 2).

Novo, S., A. Peritore, R. L. Trovato, F. P. Guarneri, D. D. Lisi, I. Muratori, and G. Novo (2013). “Preclinical Atherosclerosis and Metabolic Syndrome Increase Cardio- and Cerebrovascular Events Rate”. In: *Cardiovasc. Diabetol.* 12.155, pp. 1–8 (cit. on p. 1).

Sandrin, L., S. Catheline, M. Tanter, X. Hennequin, and M. Fink (1999). “Time-resolved pulsed elastography with ultrafast ultrasonic imaging”. In: *Ultrason. Imaging* 21.4, pp. 259–272 (cit. on p. 2).

Yu, A. C. H. and L. Løvstakken (2010). “Eigen-based clutter filter design for ultrasound color flow imaging: a review”. In: *IEEE Trans. Ultrason., Ferroelec., Freq. Contr.* 57.5, pp. 1096–1111. DOI: `10.1109/TUFFC.2010.1521` (cit. on p. 2).

References from Chapter 2

Adrian, R. J. (1991). “Particle-imaging techniques for experimental fluid mechanics”. In: *Annual Review of Fluid Mechanics* 23.1, pp. 261–304. DOI: `10.1146/annurev.fl.23.010191.001401` (cit. on p. 14).

Anderson, M. E. (1998). “Multi-dimensional velocity estimation with ultrasound using spatial quadrature”. In: *IEEE Trans. Ultrason., Ferroelec., Freq. Contr.* 45, pp. 852–861 (cit. on p. 16).

Baker, D. W. and D. W. Watkins (1967). “A phase coherent pulse Doppler system for cardiovascular measurements”. In: *20th Annual conf. Eng. Med. Biol.* Vol. 27, pp. 2–2 (cit. on p. 10).

Bohs, L. N., B. H. Friemal, B. A. McDermott, and G. E. Trahey (1993). “A real-time system for quantifying and displaying two-dimensional velocities using ultrasound”. In: *Ultrasound Med. Biol.* 19, pp. 751–761 (cit. on p. 7).

Bohs, L. N., B. J. Geiman, M. E. Anderson, S. C. Gebhart, and G. E. Trahey (2000). “Speckle tracking for multi-dimensional flow estimation”. In: *Ultrasonics* 38, pp. 369–375 (cit. on p. 7).

Bohs, L., B. Friemel, and G. Trahey (1995). “Experimental velocity profiles and volumetric flow via two-dimensional speckle tracking”. In: *Ultrasound Med. Biol.* 21.7, pp. 885–898 (cit. on p. 7).

Bonnefous, O. (1988). “Measurement of the complete (3D) velocity vector of blood flows”. In: *Proc. IEEE Ultrason. Symp.* Pp. 795–799 (cit. on p. 16).

Bonnefous, O., P. Pesqué, and X. Bernard (1986). “A new Velocity Estimator for Color Flow Mapping”. In: *Proc. IEEE Ultrason. Symp.* Pp. 855–860 (cit. on p. 13).

Delannoy, B., R. Torguet, C. Bruneel, E. Bridoux, J. M. Rouvaen, and H. Lasota (1979). “Acoustical image reconstruction in parallel-processing analog electronic systems”. In: *J. Applied Phys.* 50.5, pp. 3153–3159. DOI: `http://scitation.aip.org/content/aip/journal/jap/50/5/10.1063/1.326397` (cit. on p. 7).

Dunmire, B., K. W. Beach, K.-H. Labs., M. Plett, and D. E. Strandness (2000). “Crossbeam vector Doppler ultrasound for angle independent velocity measurements”. In: *Ultrasound Med. Biol.* 26, pp. 1213–1235 (cit. on p. 15).

Ekroll, I. K., A. Swillens, P. Segers, T. Dahl, H. Torp, and L. Løvstakken (2013). “Simultaneous quantification of flow and tissue velocities based on multi-angle plane wave imaging”. In: *IEEE Trans. Ultrason., Ferroelec., Freq. Contr.* 60.4, pp. 727–738 (cit. on pp. 14, 15).

Fadnes, S., S. A. Nyrnes, H. Torp, and L. Lovstakken (2014). “Shunt Flow Evaluation in Congenital Heart Disease Based on Two-Dimensional Speckle Tracking”. In: *Ultrasound Med. Biol.* 40.10, pp. 2379–2391. DOI: `10.1016/j.ultrasmedbio.2014.03.029` (cit. on p. 15).

Foster, S. G., P. M. Embree, and W. D. O’Brien (1990). “Flow Velocity Profile via Time-Domain Correlation: Error Analysis and Computer Simulation”. In: *IEEE Trans. Ultrason., Ferroelec., Freq. Contr.* 37, pp. 164–175 (cit. on p. 13).

Griffith, J. M., W. R. Brody, and L. Goodman (1976). “Resolution performance of Doppler ultrasound flowmeters”. In: *J. Acoust. Soc. Am.* 60, pp. 607–610 (cit. on p. 15).

Hansen, K. L., J. Udesen, F. Gran, J. A. Jensen, and M. B. Nielsen (2009). “In-vivo examples of flow patterns with the fast vector velocity ultrasound method”. In: *Ultraschall in Med.* 30, pp. 471–476 (cit. on p. 15).

Hansen, K. L., J. Udesen, N. Oddershede, L. Henze, C. Thomsen, J. A. Jensen, and M. B. Nielsen (2009). “In vivo comparison of three ultrasound vector velocity techniques to MR phase contrast angiography”. In: *Ultrasonics* 49, pp. 659–667 (cit. on p. 16).

Hoeks, A. P. G., T. G. J. Arts, P. J. Brands, and R. S. Reneman (1993). “Comparison of the performance of the rf cross correlation and Doppler autocorrelation technique to estimate the mean velocity of simulated ultrasound signals”. In: *Ultrasound Med. Biol.* 19, pp. 727–740 (cit. on p. 13).

Jensen, J. A. (1993). “Implementation of ultrasound time-domain cross-correlation blood velocity estimators”. In: *IEEE Trans. Biomed. Eng.* 40, pp. 468–474 (cit. on p. 13).

— (1996). *Estimation of Blood Velocities Using Ultrasound: A Signal Processing Approach*. New York: Cambridge University Press (cit. on p. 12).

— (2003). “Directional velocity estimation using focusing along the flow direction: I: Theory and simulation”. In: *IEEE Trans. Ultrason., Ferroelec., Freq. Contr.* 50, pp. 857–872 (cit. on pp. 16, 17).

Jensen, J. A., O. Holm, L. J. Jensen, H. Bendsen, H. M. Pedersen, K. Salomonsen, J. Hansen, and S. Nikolov (1999). “Experimental ultrasound system for real-time synthetic imaging”. In: *Proc. IEEE Ultrason. Symp.* Vol. 2, pp. 1595–1599. DOI: `10.1109/ULTSYM.1999.849300` (cit. on pp. 8, 16).

Jensen, J. A. and P. Munk (1998). “A New Method for Estimation of Velocity Vectors”. In: *IEEE Trans. Ultrason., Ferroelec., Freq. Contr.* 45, pp. 837–851 (cit. on p. 16).

Jensen, J., M. B. Stuart, and J. A. Jensen (2015). “High Frame Rate Vector Velocity Estimation using Plane Waves and Transverse Oscillation”. In: *Proc. IEEE Ultrason. Symp.* Pp. 1–4. DOI: `10.1109/ultsym.2015.0423` (cit. on p. 16).

Karaman, M., P. C. Li, and M. O’Donnell (1995). “Synthetic aperture imaging for small scale systems”. In: *IEEE Trans. Ultrason., Ferroelec., Freq. Contr.* 42, pp. 429–442 (cit. on p. 8).

Kim, H. B., J. R. Hertzberg, and R. Shandas (2004). “Echo PIV for flow field measurements in vivo”. In: *Biomedical Sciences Instrumentation* 40. PMID: 15133984, pp. 357–363 (cit. on p. 14).

Lenge, M., A. Ramalli, P. Tortoli, C. Cachard, and H. Liebgott (2015). “Plane-Wave Transverse Oscillation for High-Frame-Rate 2-D Vector Flow Imaging”. In: *IEEE Trans. Ultrason., Ferroelec., Freq. Contr.* 62.12, pp. 2126–2137 (cit. on pp. 14, 16).

Liebgott, H. (2010). “Fourier domain beamforming for transverse-oscillations”. In: *Proc. IEEE Ultrason. Symp.* Pp. 1755–1758 (cit. on p. 16).

Loupas, T., J. T. Powers, and R. W. Gill (1995). “An axial velocity estimator for ultrasound blood flow imaging, based on a full evaluation of the Doppler equation by means of a two-dimensional autocorrelation approach”. In: *IEEE Trans. Ultrason., Ferroelec., Freq. Contr.* 42, pp. 672–688 (cit. on p. 12).

Lu, J., J. Cheng, and J. Wang (2006). “High Frame Rate Imaging System for Limited Diffraction Array Beam Imaging with Square-Wave Aperture Weightings”. In: *IEEE Trans. Ultrason., Ferroelec., Freq. Contr.* 53.10, pp. 1796–1812 (cit. on p. 8).

Mailloux, G. E., F. Langlois, P. Simard, and M. Bertrand (1989). “Restoration of the velocity field of the heart from two-dimensional echocardiograms”. In: *IEEE Trans. Med. Imag.* 8.2, pp. 143–153. DOI: `10.1109/42.24862` (cit. on p. 14).

Montaldo, G., M. Tanter, J. Bercoff, N. Benech, and M. Fink (2009). “Coherent plane-wave compounding for very high frame rate ultrasonography and transient elastography”. In: *IEEE Trans. Ultrason., Ferroelec., Freq. Contr.* 56.3, pp. 489–506. DOI: `10.1109/TUFFC.2009.1067` (cit. on p. 9).

Newhouse, V. L., D. Censor, T. Vontz, J. A. Cisneros, and B. B. Goldberg (1987). “Ultrasound Doppler probing of flows transverse with respect to beam axis”. In: *IEEE Trans. Biomed. Eng.* BME-34, pp. 779–788 (cit. on p. 14).

Nikolov, S. I. (2001). “Synthetic Aperture Tissue and Flow Ultrasound Imaging”. PhD thesis. 2800, Lyngby, Denmark: Ørsted•DTU, Technical University of Denmark (cit. on p. 9).

Oddershede, N., L. Løvstakken, H. Torp, and J. A. Jensen (2008). “Estimating 2-D Vector Velocities Using Multidimensional Spectrum Analysis”. In: *IEEE Trans. Ultrason., Ferroelec., Freq. Contr.* 55.8, pp. 1744–1754 (cit. on p. 14).

O’Donnell, M. and L. J. Thomas (1992). “Efficient synthetic aperture imaging from a circular aperture with possible application to catheter-based imaging”. In: *IEEE Trans. Ultrason., Ferroelec., Freq. Contr.* 39, pp. 366–380 (cit. on p. 8).

Osmanski, B.-F., G. Montaldo, and M. Tanter (2015). “Out-of-plane Doppler imaging based on ultrafast plane wave imaging”. In: *IEEE Trans. Ultrason., Ferroelec., Freq. Contr.* 62.4, pp. 625–636. DOI: `10.1109/TUFFC.2014.006575` (cit. on p. 14).

Ozaki, Y., H. Sumitani, T. Tomoda, and M. Tanaka (1988). “A new system for real-time synthetic aperture ultrasonic imaging”. In: *IEEE Trans. Ultrason., Ferroelec., Freq. Contr.* 35.6, pp. 828–838 (cit. on p. 8).

Raffel, M., C. E. Willert., S. Wereley, and J. Kompenhans (2007). *Particle image velocimetry: a practical guide*. 2nd edition. Springer (cit. on p. 14).

Ramamurthy, B. S. and G. E. Trahey (1991). “Potential and limitations of angle-independent flow detection algorithms using radio frequency and detected echo signals”. In: *Ultrason. Imaging* 13, pp. 252–268 (cit. on p. 15).

Ranganathan, K. and W. F. Walker (2007). “Cystic Resolution: A Performance Metric for Ultrasound Imaging Systems”. In: *IEEE Trans. Ultrason., Ferroelec., Freq. Contr.* 54.4, pp. 782–792. DOI: `10.1109/TUFFC.2007.311` (cit. on p. 10).

Ricci, S., L. Bassi, and P. Tortoli (2014). “Real-time vector velocity assessment through multigate Doppler and plane waves”. In: *IEEE Trans. Ultrason., Ferroelec., Freq. Contr.* 61.2, pp. 314–324 (cit. on p. 15).

Sandrin, L., S. Catheline, M. Tanter, X. Hennequin, and M. Fink (1999). “Time-resolved pulsed elastography with ultrafast ultrasonic imaging”. In: *Ultrason. Imaging* 21.4, pp. 259–272 (cit. on p. 8).

Shattuck, D. P., M. D. Weinshenker, S. W. Smith, and O. T. von Ramm (1984). “Explososcan: A parallel processing technique for high speed ultrasound imaging with linear phased arrays”. In: *J. Acoust. Soc. Am.* 75, pp. 1273–1282 (cit. on p. 7).

Tortoli, P., G. Bambi, and S. Ricci (2006). "Accurate Doppler angle estimation for vector flow measurements". In: *IEEE Trans. Ultrason., Ferroelec., Freq. Contr.* 53.8, pp. 1425–1431 (cit. on p. 14).

Tortoli, P., L. Bassi, E. Boni, A. Dallai, F. Guidi, and S. Ricci (2009). "ULA-OP: An Advanced Open Platform for Ultrasound Research". In: *IEEE Trans. Ultrason., Ferroelec., Freq. Contr.* 56.10, pp. 2207–2216 (cit. on p. 8).

Trahey, G. E., J. W. Allison, and O. T. von Ramm (1987). "Angle independent ultrasonic detection of blood flow". In: *IEEE Trans. Biomed. Eng.* BME-34, pp. 965–967 (cit. on pp. 7, 8, 14).

Udesen, J., F. Gran, K. L. Hansen, J. A. Jensen, C. Thomsen, and M. B. Nielsen (2008). "High Frame-Rate Blood Vector Velocity Imaging Using Plane Waves: simulations and preliminary experiments". In: *IEEE Trans. Ultrason., Ferroelec., Freq. Contr.* 55.8, pp. 1729–1743 (cit. on p. 7).

Villagomez-Hoyos, C. A., M. B. Stuart, K. L. Hansen, M. B. Nielsen, and J. A. Jensen (2016). "Accurate Angle Estimator for High Frame Rate 2-D Vector Flow Imaging". In: *IEEE Trans. Ultrason., Ferroelec., Freq. Contr.* Accepted (cit. on p. 17).

Wilson, L. S. (1991). "Description of broad-band pulsed Doppler ultrasound processing using the two-dimensional Fourier transform". In: *Ultrason. Imaging* 13, pp. 301–315 (cit. on p. 14).

Yeung, F., S. F. Levinson, and K. J. Parker (1998). "Multilevel and motion model-based ultrasonic speckle tracking algorithms". In: *Ultrasound Med. Biol.* 24.3, pp. 427–441. DOI: `10.1016/S0301-5629(97)00281-0` (cit. on p. 14).

References from Chapter 3

Fadnes, S., I. K. Ekroll, S. A. Nyrnes, H. Torp, and L. Løvstakken (2015). "Robust Angle-Independent Blood Velocity Estimation Based on Dual-Angle Plane Wave Imaging". In: *IEEE Trans. Ultrason., Ferroelec., Freq. Contr.* 62.10, pp. 1757–1767. DOI: `10.1109/tuffc.2015.007108` (cit. on pp. 26, 28).

FDA (2008). *Information for Manufacturers Seeking Marketing Clearance of Diagnostic Ultrasound Systems and Transducers*. Tech. rep. Center for Devices, Radiological Health, United States Food, and Drug Administration (cit. on p. 31).

Jensen, J. A. (1993). "Stationary echo canceling in velocity estimation by time-domain cross-correlation". In: *IEEE Trans. Med. Imag.* 12, pp. 471–477 (cit. on p. 28).

— (1996). "Field: A Program for Simulating Ultrasound Systems". In: *Med. Biol. Eng. Comp.* 10th Nordic-Baltic Conference on Biomedical Imaging, Vol. 4, Supplement 1, Part 1, pp. 351–353 (cit. on p. 21).

Jensen, J. A., H. Holten-Lund, R. T. Nilsson, M. Hansen, U. D. Larsen, R. P. Domsten, B. G. Tomov, M. B. Stuart, S. I. Nikolov, M. J. Pihl, Y. Du, J. H. Rasmussen, and M. F. Rasmussen (2013). "SARUS: A Synthetic Aperture Real-time Ultrasound System". In: *IEEE Trans. Ultrason., Ferroelec., Freq. Contr.* 60.9, pp. 1838–1852 (cit. on p. 22).

Jensen, J. A., M. F. Rasmussen, M. J. Pihl, S. Holbek, C. A. Villagomez-Hoyos, D. P. Bradway, M. B. Stuart, and B. G. Tomov (2016). “Safety Assessment of Advanced Imaging Sequences, I: Measurements”. In: *IEEE Trans. Ultrason., Ferroelec., Freq. Contr.* 63.1, pp. 110–119 (cit. on p. 31).

Jensen, J. A. and N. B. Svendsen (1992). “Calculation of Pressure Fields from Arbitrarily Shaped, Apodized, and Excited Ultrasound Transducers”. In: *IEEE Trans. Ultrason., Ferroelec., Freq. Contr.* 39, pp. 262–267 (cit. on p. 21).

Marshall, I., S. Zhao, P. Papathanasopoulou, P. Hoskins, and X. Y. Xu (2004). “MRI and CFD studies of pulsatile flow in healthy and stenosed carotid bifurcation models”. In: *J. Biomech.* 37, pp. 679–687 (cit. on p. 28).

Nikolov, S. I. (2001). “Synthetic Aperture Tissue and Flow Ultrasound Imaging”. PhD thesis. 2800, Lyngby, Denmark: Ørsted•DTU, Technical University of Denmark (cit. on p. 19).

Ramnarine, K. V., D. K. Nassiri, P. R. Hoskins, and J. Lubbers (1998). “Validation of a new blood mimicking fluid for use in Doppler flow test objects”. In: *Ultrasound Med. Biol.* 24, pp. 451–459 (cit. on p. 22).

Swillens, A., L. Løvstakken, J. Kips, H. Torp, and P. Segers (2009). “Ultrasound simulation of complex flow velocity fields based on computational fluid dynamics”. In: *IEEE Trans. Ultrason., Ferroelec., Freq. Contr.* 56.3, pp. 546–556. DOI: `10.1109/TUFFC.2009.1071` (cit. on p. 28).

Taylor, C. A., T. J. R. Hughes, and C. K. Zarins (1998). “Finite element modeling of blood flow in arteries”. In: *Comput. Methods Appl. Mech. Engrg.* 158.1, pp. 155–196 (cit. on p. 28).

Tsai, S. F. and T. W. H. Sheu (2007). “Finite element analysis of three-dimensional vortical flow structure and topology inside a carotid bifurcation model”. In: *IJCFD* 21.1, pp. 29–36 (cit. on p. 28).

Villagomez-Hoyos, C. A., M. B. Stuart, K. L. Hansen, M. B. Nielsen, and J. A. Jensen (2016). “Accurate Angle Estimator for High Frame Rate 2-D Vector Flow Imaging”. In: *IEEE Trans. Ultrason., Ferroelec., Freq. Contr.* Accepted (cit. on pp. 20, 21, 23, 25, 27).

References from Chapter 4

Foster, S. G., P. M. Embree, and W. D. O’Brien (1990). “Flow Velocity Profile via Time-Domain Correlation: Error Analysis and Computer Simulation”. In: *IEEE Trans. Ultrason., Ferroelec., Freq. Contr.* 37, pp. 164–175 (cit. on p. 36).

Jensen, J. A. (2003). “Directional velocity estimation using focusing along the flow direction: I: Theory and simulation”. In: *IEEE Trans. Ultrason., Ferroelec., Freq. Contr.* 50, pp. 857–872 (cit. on p. 36).

Jensen, J. A. and R. Bjerngaard (2003). "Directional velocity estimation using focusing along the flow direction: II: Experimental investigation". In: *IEEE Trans. Ultrason., Ferroelec., Freq. Contr.* 50, pp. 873–880 (cit. on p. 36).

Lai, S. S. M., B. Y. S. Yiu, A. K. K. Poon, and A. C. H. Yu (2013). "Design of Anthropomorphic Flow Phantoms Based on Rapid Prototyping of Compliant Vessel Geometries". In: *Ultrasound Med. Biol.* 39.9, pp. 1654–1664 (cit. on p. 38).

Villagomez-Hoyos, C. A., M. B. Stuart, and J. A. Jensen (2014a). "Adaptive multi-lag for synthetic aperture vector flow imaging". In: *Proc. IEEE Ultrason. Symp.* Pp. 1722–1725 (cit. on pp. 40–42).

— (2014b). "Increasing the dynamic range of synthetic aperture vector flow imaging". In: *Proc. SPIE Med. Imag.* Vol. 9040, pp. 1–12. DOI: `10.1117/12.2043637` (cit. on p. 40).

— (2015). "In-vivo high dynamic range vector flow imaging". In: *Proc. IEEE Ultrason. Symp.* Pp. 1–4. DOI: `10.1109/ULTSYM.2015.0424` (cit. on p. 41).

Walker, W. F. and G. E. Trahey (1995). "A Fundamental Limit on Delay Estimation Using Partially Correlated Speckle Signals". In: *IEEE Trans. Ultrason., Ferroelec., Freq. Contr.* 42.2, pp. 301–308 (cit. on p. 40).

References from Chapter 5

Jensen, J. A., A. H. Brandt, and M. B. Nielsen (2014). "In-vivo Convex Array Vector Flow Imaging". In: *Proc. IEEE Ultrason. Symp.* IEEE, pp. 333–336. DOI: `10.1109/ultsym.2014.0082` (cit. on p. 52).

— (2015). "Convex Array Vector Velocity Imaging Using Transverse Oscillation and Its Optimization". In: *IEEE Trans. Ultrason., Ferroelec., Freq. Contr.* 62.12, pp. 2043–2053. DOI: `10.1109/TUFFC.2015.006970` (cit. on p. 52).

Oddershede, N., F. Gran, and J. A. Jensen (2008). "Multi-frequency encoding for fast color flow or quadroplex imaging". In: *IEEE Trans. Ultrason., Ferroelec., Freq. Contr.* 55.4, pp. 778–786 (cit. on p. 54).

Tanter, M. and M. Fink (2014). "Ultrafast imaging in biomedical ultrasound". In: *IEEE Trans. Ultrason., Ferroelec., Freq. Contr.* 61.1, pp. 102–119. DOI: `10.1109/TUFFC.2014.6689779` (cit. on p. 46).

References from Chapter 6

Bjærum, S., H. Torp, and K. Kristoffersen (2002). "Clutter Filters Adapted to Tissue Motion in Ultrasound Color Flow Imaging". In: *IEEE Trans. Ultrason., Ferroelec., Freq. Contr.* 49.6, pp. 693–704 (cit. on pp. 59, 60).

Demene, C., T. Deffieux, M. Perno, B.-F. Osmanski, V. Biran, J.-L. Gennisson, L.-A. Sieu, A. Bergel, S. Franqui, J.-M. Correas, and et al. (2015). “Spatiotemporal clutter filtering of ultrafast ultrasound data highly increases Doppler and fUltrasound sensitivity”. In: *IEEE Trans. Med. Imag.* 34.11, pp. 2271–2285. DOI: `10.1109/TMI.2015.2428634` (cit. on pp. 60, 63).

Hoeks, A. P. G., J. J. W. van de Vorst, A. Dabekaussen, P. J. Brands, and R. S. Reneman (1991). “An efficient algorithm to remove low frequency Doppler signal in digital Doppler systems”. In: *Ultrason. Imaging* 13, pp. 135–145 (cit. on p. 67).

Kadi, A. P. and T. Loupas (1995). “On the performance of regression ans step-initialized IIR clutter filters for color Doppler systems in diagnostic medical ultrasound”. In: *IEEE Trans. Ultrason., Ferroelec., Freq. Contr.* 42, pp. 927–937 (cit. on p. 62).

Løvstakken, L., S. Bjærum, K. Kristoffersen, R. Haaverstad, and H. Torp (2006). “Real-time adaptive clutter rejection filtering in color flow imaging using power method iterations”. In: *IEEE Trans. Ultrason., Ferroelec., Freq. Contr.* 53, pp. 1597–1608 (cit. on p. 61).

Løvstakken, L., S. Bjærum, and H. Torp (2007). “Optimal velocity estimation in ultrasound color flow imaging in presence of clutter”. In: *IEEE Trans. Ultrason., Ferroelec., Freq. Contr.* 54.3, pp. 539–549 (cit. on p. 60).

Siggia, A. D. and R. E. Passarelli (2004). “Gaussian model adaptive processing (GMAP) for improved ground clutter cancellation and moment calculation”. In: *ERAD*, pp. 67–73 (cit. on p. 64).

Thomas, L. and A. Hall (1994). “Improved wall filter for flow imaging of low velocity flow”. In: *Proc. IEEE Ultrason. Symp.* Pp. 1701–1704 (cit. on p. 60).

Torp, H., K. Kristoffersen, and B. A. J. Angelsen (1994). “Autocorrelation techniques in color flow imaging: Signal model and statistical properties of the autocorrelation estimates”. In: *IEEE Trans. Ultrason., Ferroelec., Freq. Contr.* 41, pp. 604–612 (cit. on pp. 60, 63).

Yu, A. C. H. and R. S. C. Cobbold (2006). “A new eigen-based clutter filter using the Hankel-SVD approach”. In: *Proc. IEEE Ultrason. Symp.* Pp. 1079–1082 (cit. on p. 63).

Yu, A. C. H. and L. Løvstakken (2010). “Eigen-based clutter filter design for ultrasound color flow imaging: a review”. In: *IEEE Trans. Ultrason., Ferroelec., Freq. Contr.* 57.5, pp. 1096–1111. DOI: `10.1109/TUFFC.2010.1521` (cit. on pp. 60, 63).

References from Chapter 7

Ambrose, J. A., M. A. Tannenbaum, D. Alexopoulos, C. E. Hjemdahl-Monsen, J. Leavy, M. Weiss, S. Borrico, R. Gorlin, and V. Fuster (1988). “Angiographic progression of coronary artery disease and the development of myocardial infarction”. In: *J. Am. Coll. Cardiol.* 12.1, pp. 56–62 (cit. on p. 80).

Arterial Stiffness Collaboration, R. V. for (2010). “Determinants of pulse wave velocity in healthy people and in the presence of cardiovascular risk factors: establishing normal and reference values”. In: *Eur. Heart J.* 31.19, pp. 2338–2350 (cit. on p. 76).

Benthin, M., P. Dahl, R. Ruzicka, and K. Lindstrom (1991). “Calculation of pulse-wave velocity using cross correlation-effects of reflexes in the arterial tree”. In: *Ultrasound Med. Biol.* 17.5, pp. 461–469 (cit. on p. 74).

Cassar, S., S. Bhatt, H. J. Paltiel, and V. S. Dogra (2008). “Role of Spectral Doppler Sonography in the Evaluation of Partial Testicular Torsion”. In: *J. Ultrasound Med.* 27, pp. 1629–1638 (cit. on p. 85).

Cheng, C., D. Tempel, R. van Haperen, A. van der Baan, F. Grosveld, M. Daemen, R. Krams, and R. de Crom (2006). “Atherosclerotic Lesion Size and Vulnerability Are Determined by Patterns of Fluid Shear Stress”. In: *Circ. Res.* Pp. 2744–2753 (cit. on pp. 77, 78).

Demene, C., T. Deffieux, M. Perno, B.-F. Osmanski, V. Biran, J.-L. Gennisson, L.-A. Sieu, A. Bergel, S. Franqui, J.-M. Correas, and et al. (2015). “Spatiotemporal clutter filtering of ultrafast ultrasound data highly increases Doppler and fUltrasound sensitivity”. In: *IEEE Trans. Med. Imag.* 34.11, pp. 2271–2285. DOI: `10.1109/TMI.2015.2428634` (cit. on p. 85).

Donohue, T. J., M. J. Kern, F. V. Aguirre, R. G. Bach, T. Wolford, C. A. Bell, and J. Segal (1993). “Assessing the hemodynamic significance of coronary artery stenosis: Analysis of translesional pressure-flow velocity relations in patients”. In: *J. Am. Coll. Cardiol.* 22.2, pp. 449–458 (cit. on p. 80).

Fadnes, S., I. K. Ekroll, S. A. Nyrnes, H. Torp, and L. Løvstakken (2015). “Robust Angle-Independent Blood Velocity Estimation Based on Dual-Angle Plane Wave Imaging”. In: *IEEE Trans. Ultrason., Ferroelec., Freq. Contr.* 62.10, pp. 1757–1767. DOI: `10.1109/tuffc.2015.007108` (cit. on p. 78).

Felix, W. R., B. Sige, R. J. Gibson, J. Williams, G. L. Popky, A. L. Edelstein, and J. R. Justin (1976). “Pulsed Doppler ultrasound detection of flow disturbances in arteriosclerosis”. In: *J. Clin. Ultrasound* 4.4, pp. 275–282 (cit. on p. 80).

Glickman, B., K. Selby, D. Saloner, and O. Savas (2003). “Experimental Flow Studies in Exact-Replica Phantoms of Atherosclerotic Carotid Bifurcations Under Steady Input Conditions”. In: *J. Biomech. Eng.* 125, pp. 38–48 (cit. on p. 77).

Holen, J., R. Aaslid, and K. Landmark (1976). “Determination of pressure gradient in Mitral stenosis with a non-invasive ultrasound Doppler technique”. In: *Acta med. scand.* 32, pp. 455–460 (cit. on p. 80).

Laurent, S., P. Boutouyrie, R. Asmar, I. Gautier, B. Laloux, L. Guize, P. Ducimetiere, and A. Benetos (2001). “Aortic Stiffness Is an Independent Predictor of All-Cause and Cardiovascular Mortality in Hypertensive Patients”. In: *HY* 37, pp. 1236–1241 (cit. on pp. 73, 74).

Lee, S., L. Antiga, and D. A. Steinman (2009). “Correlations Among Indicators of Disturbed Flow at the Normal Carotid Bifurcation”. In: *J. Biomech. Eng.* 131, pp. 1–7 (cit. on p. 78).

Lenge, M., A. Ramalli, E. Boni, H. Liebgott, C. Cachard, and P. Tortoli (2014). “High-frame-rate 2D vector blood flow imaging in the frequency domain”. In: *IEEE Trans. Ultrason., Ferroelec., Freq. Contr.* 61.9, pp. 1504–1514 (cit. on p. 78).

Lovett, J. K., P. J. Gallagher, L. J. Hands, J. Walton, and P. M. Rothwell (2004). “Histological Correlates of Carotid Plaque Surface Morphology on Lumen Contrast Imaging”. In: *Circulation* 110, pp. 2190–2197 (cit. on p. 80).

Lusis, A. J. (2000). “Atherosclerosis”. In: *Nature* 407, pp. 233–241 (cit. on p. 77).

Mangell, P., T. Länne, B. S. B. F. Hansen, and D. Bergqvist (1996). “Regional differences in mechanical properties between major arteries: an experimental study in sheep”. In: *EJV* 12.2, pp. 189–195 (cit. on p. 74).

Naghavi, M., P. Libby, E. Falk, S. W. Casscells, S. Litovsky, J. Rumberger, J. J. Badimon, C. Stefanadis, P. Moreno, G. Pasterkamp, Z. Fayad, P. H. Stone, D. P. Zipes, P. K. Shah, and J. T. Willerson (2003). “From Vulnerable Plaque to Vulnerable Patient A Call for New Definitions and Risk Assessment Strategies: Part 1”. In: *Circulation* 108, pp. 1664–1672 (cit. on p. 73).

Olesen, J. B. (2015). “Imaging of In-Vivo Pressure using Ultrasound”. PhD thesis. Technical University of Denmark (cit. on pp. 82–84).

Osarumwense, D., R. Pararajasingam, P. Wilson, J. Abraham, and S. R. Walker (2005). “Carotid Artery Imaging in the United Kingdom: A Postal Questionnaire of Current Practice”. In: *Vascular* 13.3, pp. 173–177 (cit. on p. 80).

Rabben, S., N. Stergiopulos, L. R. Hellevik, O. A. Smiseth, S. Slordahl, S. Urheim, and B. Angelsen (2004). “An ultrasound-based method for determining pulse wave velocity in superficial arteries”. In: *J. Biomech.* 37, pp. 1615–1622 (cit. on p. 74).

Rubin, J., R. Bude, P. Carson, R. Bree, and R. Adler (1994). “Power Doppler US: a potentially useful alternative to mean frequency-based color Doppler US”. In: *Radiology* 190, pp. 853–856 (cit. on p. 84).

Saba, L., M. Anzidei, R. Sanfilippo, R. Montisci, P. Lucatelli, C. Catalano, R. Passariello, and G. Mallarini (2012). “Imaging of the carotid artery”. In: *Atherosclerosis* 220, pp. 294–309 (cit. on p. 80).

Steinke, W., C. Kloetzsch, and M. Henneric (1990). “Variability of flow patterns in the normal carotid bifurcation”. In: *Atherosclerosis* 84, pp. 121–127 (cit. on p. 77).

Steinman, D. A. (2004). “Image-based Computational Fluid Dynamics: A New Paradigm for Monitoring Hemodynamics and Atherosclerosis”. In: *Cardiovas. & Haemat. Dis.* 4.1, pp. 183–197 (cit. on p. 77).

Teirstein, P. S., P. G. Yock, and R. L. Popp (1985). “The accuracy of Doppler ultrasound measurement of pressure gradients across irregular, dual, and tunnellike obstructions to blood flow”. In: *Circulation* 72, pp. 577–584 (cit. on p. 80).

Udesen, J., F. Gran, K. L. Hansen, J. A. Jensen, C. Thomsen, and M. B. Nielsen (2008). “High Frame-Rate Blood Vector Velocity Imaging Using Plane Waves: simulations and preliminary experiments”. In: *IEEE Trans. Ultrason., Ferroelec., Freq. Contr.* 55.8, pp. 1729–1743 (cit. on p. 78).

Villagomez-Hoyos, C. A., M. B. Stuart, K. L. Hansen, M. B. Nielsen, and J. A. Jensen (2016). “Accurate Angle Estimator for High Frame Rate 2-D Vector Flow Imaging”. In: *IEEE Trans. Ultrason., Ferroelec., Freq. Contr.* Accepted (cit. on p. 78).

Wasserman, B. A., R. J. Wityk, H. H. Trout, and R. Virmani (2005). “Looking beyond the lumen with MRI”. In: *Stroke* 36, pp. 2504–2013 (cit. on p. 80).

Watanabe, H., S. Ohtsuka, M. Kakihana, and Y. Sugishita (1993). “Coronary circulation in dogs with an experimental decrease in aortic compliance”. In: *J. Am. Coll. Cardiol.* 21, pp. 1497–1506 (cit. on p. 73).

Yiu, B. Y., S. S. Lai, and A. C. Yu (2014). “Vector projectile imaging: time-resolved dynamic visualization of complex flow patterns.” In: *Ultrasound Med. Biol.* 40.9, pp. 2295–2309 (cit. on p. 78).

Yoganathan, A. P., E. G. Cape, H.-W. Sung, F. P. Williams, and A. Jimoh (1988). “Review of hydrodynamic principles for the cardiologist: Applications to the study of blood flow and jets by imaging techniques”. In: *J. Am. Coll. Cardiol.* 12.5, pp. 1344–1353 (cit. on p. 80).

Young, D. F., N. R. Cholvin, and A. C. Roth (1975). “Pressure Drop across Artificially Induced Stenoses in the Femoral Arteries of Dogs”. In: *Circ Res.* 36, pp. 735–743 (cit. on p. 80).

Paper I

Accurate Angle Estimator for High-Frame-rate 2-D Vector Flow Imaging

Carlos Armando Villagómez-Hoyos, Matthias Bo Stuart, Kristoffer Lindskov Hansen, Michael Bachmann Nielsen, and Jørgen Arendt Jensen

IEEE Trans. Ultrasons., Ferroelec., Freq. Contr., vol. 63, no. 6, p. 842 – 853, June 2016.

Accurate Angle Estimator for High Frame Rate 2-D Vector Flow Imaging

Carlos Armando Villagómez Hoyos*, Matthias Bo Stuart*, Kristoffer Lindskov Hansen†, Michael Bachmann Nielsen† and Jørgen Arendt Jensen*
*Center for Fast Ultrasound Imaging, Dept. of Elec. Eng., Bldg. 349,
Technical University of Denmark, DK-2800 Kgs. Lyngby, Denmark
†Department of Radiology, Copenhagen University Hospital, Rigshospitalet,DK-2100 Copenhagen, Denmark

***Abstract*—This paper presents a novel approach for estimating 2-D flow angles using a high frame rate ultrasound method. The angle estimator features high accuracy and low standard deviation over the full 360° range. The method is validated on Field II simulations and phantom measurements using the experimental ultrasound scanner SARUS and a flow-rig before being tested *in-vivo*. An 8-MHz linear array transducer is used with defocused beam emissions. In the simulations of a spinning disk phantom a 360° uniform behaviour on the angle estimation is observed with a median angle bias of 1.01° and median angle standard deviation of 1.8°. Similar results are obtained on a straight vessel for both simulations and measurements, where the obtained angle biases are below 1.5° with standard deviations around 1°. Estimated velocity magnitudes are also kept under 10% bias and 5% relative standard deviation in both simulations and measurements. An *in-vivo* measurement is performed on a carotid bifurcation of a healthy individual. A 3 seconds acquisition during three heart cycles are captured. A consistent and repetitive vortex is observed in the carotid bulb during the systoles.**

I. INTRODUCTION

Non-invasive assessment of blood flow is used clinically as a diagnostic marker for various cardiovascular diseases [1]. The flow is usually measured using an ultrasound system capable of determining the velocity component along the propagation of the ultrasonic beam. The magnitude of the flow velocity is calculated from this component under the assumption that blood flow runs parallel to the vessel wall, thus, limiting the technique to areas where the blood flow is laminar and unidirectional. This might be the case in large healthy vessels without any bifurcations or tortuous turns, but not for vessels suffering from a vascular disease such as atherosclerosis.

The last decades' advancement in flow estimation using ultrasound have sought to overcome the challenges of conventional velocity estimation approaches. Among the advancements is 2/3-D flow estimation, which yields two or three vector velocity components within the scan plane of the transducer, thus, providing a more accurate representation of the actual flow pattern.

The first 2-D ultrasonic flow estimation technique was developed in the early 1970s [2]. The method employed two or three transducers set at different angles, where the flow was estimated by combining their individual results. However, the method was restricted to a small region of interest (ROI) which needed to be adjusted depending on the vessel depth. To expand the ROI and avoid the caveats of manual adjustments, several authors proposed distinct 2-D estimation techniques using single array transducers [3]–[5]. The ROI was effectively expanded, however, the frame rate was limited due to the line per line basis of operation in these techniques.

To overcome the issues of having a low frame rate on extended ROIs, techniques that insonify a larger part of the imaging plane per transmission were developed [6], [7]. Less transmits per frame are thus required, enabling the estimation of flow at rates of hundreds to thousands of frames per second [8]–[10].

In 2003, Jensen [11], as an extension of Bonnefous' idea of lateral beamforming [12], introduced the idea of directional lines. This extended ROI technique in which a receive beam could be beamformed in any desirable direction, and not only in the direction of the ultrasound beam, allowed for focusing along the direction of the flow. The advantage of this approach is that the signal correlation is higher along the directionally beamformed lines. The method has been validated in the clinic and showed promising results, especially when used in combination with synthetic aperture techniques [13]. However, the direction of the blood flow needs to be known beforehand. Kortbek proposed an angle estimator for this method [14], based on the fact that the correlation between lines will be higher in the motion direction. Although the angle was precisely detected, the estimation performance was strongly influenced by the choice of correlation time, and varied with flow angle and with flow velocity amplitude.

In this work, a new high frame rate method that accurately estimates flow angles regardless of the beam-to-flow angle is investigated. The proposed angle estimation method is fundamentally based on detecting the blood flow velocity using directional lines, as previously published by Jensen [11]. The suggested technique features a constant low error and low standard deviation over the full 360° range. A brief explanation of the directional velocity estimation is first given in Section II-A, before introducing the theory behind the new approach for estimating the angle in Section II-B. The method implementation details are given in Section III. The experimental setup are described in Section IV. Field II is used for simulation and the SARUS scanner for the measurements. Details on the simulations are found in Section IV-A and on measurements in Section IV-B. The results are found in Section V. Finally, an *in-vivo* acquistion on a carotid bifurcation in a healthy individual is performed, and results are found in Section V-C.

II. THEORY

A. Velocity estimation using directional lines

The basic idea of the velocity estimation process is illustrated in Fig. 1, where each ellipsis is the PSF corresponding to one emission of a moving scatterer from a sequence of $M = 2$ distinct transmit beams. For each emission, the received multichannel data are focused in a directional line $g(r, \theta_{line})$ centered on the estimation point $\vec{p}$ at a beamformed angle θ_{line}, which in this case coincides with the direction of the movement. The signals $g(r, \theta_{line})$ from the same transmitted beam are then correlated, and the displacement is found as illustrated in Fig.1(b). Dividing the displacement by the time between repetitions of distinct transmit beams T_{eff} gives the velocity magnitude directly.

The first step for the velocity estimation is to beamform a focused line $g(r, \theta_{line})$ for every emission along the flow direction θ. This is done by focusing the received signals from the individual elements on the different points along r, as described by Jensen [11].

The focused lines $g(r, \theta_{line})$ are correlated for lines acquired T_{eff} seconds apart. The correlation is calculated along a discrete set of beamformed points, as;

$$R_{12}(l, \theta_{line}) = \sum_{k=-N_{samples}/2}^{N_{samples}/2} g^{t}(k, \theta_{line}) g^{t+T_{eff}}(k+l, \theta_{line}), \quad (1)$$

where l is the correlation lag and $N_{samples}$ is the discrete length of the directional signals.

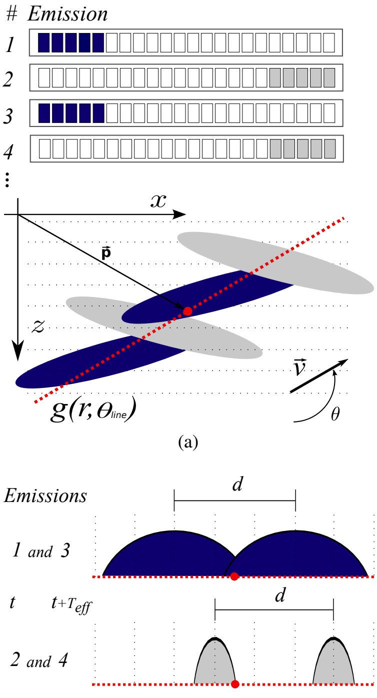

(a)

(b)

Fig. 1. Point spread functions of a moving scatterer from 4 firings of a sequence using $M = 2$ distinct transmit beams. The directional line $g(r, \theta_{line})$ centred at estimation point $\vec{p}$, represented by the red dotted line, is beamformed at each emission in the angle θ_{line} coinciding with the movement direction θ (a). Cross-sectional area of the point spread functions crossed as seen by the directional line. Emissions from the same transmit beam are correlated to obtain the spatial shift d (b).

The velocities are estimated by finding the maximum of the correlation function (1). For increased accuracy, a second-order polynomial is fitted to the cross-correlation around $l_{max}(\theta_{line})$, and the position of the maximum correlation, $\hat{l}_{max}$, is approximated by the interpolation formula given in [15].

The directional velocity estimate along the direction θ_{line} is given by

$$v(\theta_{line}) = \frac{\hat{l}_{max}(\theta_{line}) \cdot d_r}{T_{eff}}, \quad (2)$$

where d_r is the spatial sampling interval.

B. Angle estimation

The angle estimation is based on the discrepancy of estimated velocities from distinct transmit beams M. As illustrated in Fig. 2, a directional velocity estimation in another direction θ_{line} than the flow θ will yield incorrect estimates, with an error dependent on the beam-to-flow angle. The discrepancy allows for a numerical triangulation of the flow angle from the estimation of velocities profiles V_M as a function of beamforming angle θ_{line}.

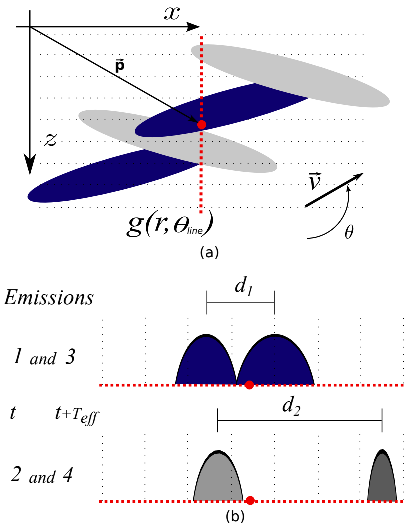

Fig. 2. Point spread functions of a moving scatterer from Fig. 1, when the directional line $g(r,\theta_{line})$ is not beamformed in the movement direction (a); Cross-sections of the point spread functions as seen by the directional line, where a discrepancy of distances exist due to the wrongly selected beamformed angle θ_{line} (b)

The estimation of the angle velocity functions $V_M(\theta_{line})$, for each distinct transmit beam M, is performed by beamforming lines at discrete angles θ_{line} on a polar grid, as illustrated over three simulated PSFs in Fig. 3 (top). Subsequently, for each beamformed line a velocity is estimated as described in Section II-A, producing a velocity magnitude V for every angle θ_{line} forming the angle velocity functions $V_M(\theta_{line})$. An example of obtained angle velocity functions are shown in the bottom of Fig. 3. Here it can be seen that the curves intersect at the correct flow angle denoted by the black dot.

The angle velocity functions shown in Fig. 3 (bottom) resemble an inverse cosine function, thus, the curve segments are, in a second step, approximated by fitting an analytic model either using single or multiple estimation points. However, care should be taken on which points should be included into the fitting, since noisy estimates could heavily influence the approximated profile.

In the first step of angle estimation, the closest coarse angles are selected from the angle velocity functions by the use of a minimum distance criterion (MDC), where the normalized magnitude differences between the curves are estimated. The use of normalization factor, denominator in 3, is to avoid sections of the curve, where low velocity estimates might present smaller absolute differences.

The distance to be minimized in the MDC is defined as the sum of the normalized difference between the angle velocity functions:

$$\theta_{MDC_1} = \underset{\theta_{line}}{\text{Arg min}} \sum_{k=1}^{M-1} \sum_{l=k+1}^{M} \left| \frac{V_k(\theta_{line}) - V_l(\theta_{line})}{\min(V_k(\theta_{line}), V_l(\theta_{line}))} \right| . \tag{3}$$

The robustness of the estimator is enhanced by using more than two distinct transmit beams M. Additionally, a non-equidistant sampling of θ_{line} is used to compensate for the non-linear behaviour of the $V_M(\theta_{line})$ function, when θ_{line} are closer to transverse angles, as shown in Fig. 4.

In the second step, the selected coarse angle θ_{MDC_1} and an adjacent coarse angle θ_{MDC_2}, with the second lowest MDC value of the two neighbouring angles, are used to extract a segment of the curve used to refine the angle estimate. However, before any refinement is performed noisy $V_M(\theta_{MDC})$ estimates from the distinct M transmit beams are removed by discarding outliers. The outliers are classified as the $V_M(\theta_{MDC})$ estimates that deviate more than 50% from the median value of $V_M(\theta_{MDC})$ along the distinct M transmit beams.

The remaining curve segments are then fitted with an inverse cosine function. Only the points θ_{MDC_1} and θ_{MDC_2} are used in the fitting to avoid noisy estimates. The fitted inverse cosine curve is obtained as

$$V'_M(\theta_{line}) = \frac{v_M^{\perp}}{\cos(\theta_{line} - \theta_M^{\perp})}, \tag{4}$$

for each curve segment M. The values $v_M^{\perp}$ and $\theta_M^{\perp}$ are obtained as

$$\theta_M^{\perp} = \arctan\left(\frac{V_M(\theta_{MDC_1})\cos(\theta_{MDC_1}) - V_M(\theta_{MDC_2})\cos(\theta_{MDC_2})}{V_M(\theta_{MDC_2})\sin(\theta_{MDC_2}) - V_M(\theta_{MDC_1})\sin(\theta_{MDC_1})} \right),$$

$$v_M^{\perp} = V_M(\theta_{MDC_1})\cos(\theta_{MDC_1} - \theta_M^{\perp}) . \tag{5}$$

The fitted curves V'_M are evaluated in pairs, where the intersection values for each pair of fitted curves M are calculated trigonometrically as follows:

$$\theta_{(l,k)} = \arctan\left(\frac{v_l^{\perp}\cos(\theta_k^{\perp}) - v_k^{\perp}\cos(\theta_l^{\perp})}{v_k^{\perp}\sin(\theta_l^{\perp}) - v_l^{\perp}\sin(\theta_k^{\perp})} \right), \tag{6}$$

where l and k represent the index for each different pair of fitted V'_M curves.

The estimated flow angle θ is then calculated as

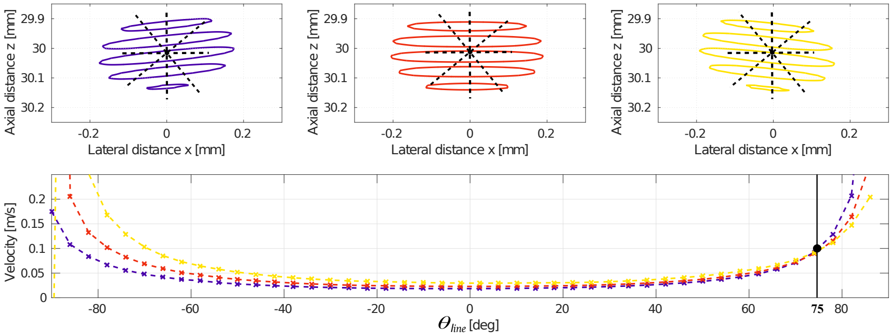

Fig. 3. The top graph shows point spread functions generated from the first, third, and fifth emission in the sequence described in Section III-A, with a set of beamformed lines in a polar grid. The bottom plot shows the angle velocity functions from the center of a Field II simulated straight vessel with flow moving at 0.1 m/s and 75°. The true angle and velocity are marked with a black dot, which coincides with the intersection of the curves.

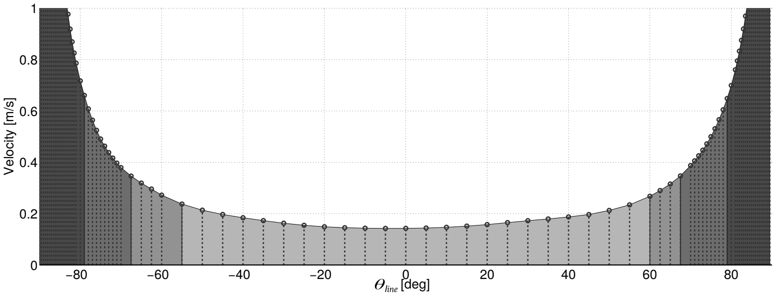

Fig. 4. Non-equidistant sampling rates for four different regions of the angle velocity function on the angular axis. The beamformed polar grid is sampled at step ranges from $0.5°, 1°, 2.5°, 5°$, where the darker tones represent smaller steps.

$$\theta = median(\theta_{(l,k)}). \tag{7}$$

After the angle has been obtained, the velocity magnitude is estimated by beamforming a directional line along the estimated angle and following the procedure describe in Section II-A. However, the final velocity magnitude is obtained from the summation of beamformed lines from distinct transmit beams instead of the individual ones. The summation generates a so called high resolution line as also known from directional synthetic aperture flow imaging [16].

III. EXPERIMENTAL SETUP

This section describes the implementation details of the proposed method. For consistency between simulations and measurements, the imaging, beamformation, velocity and angle estimation setups are kept the same. The only exception is the pulse repetition frequency, which is lowered to 3 kHz when performing a flow-rig measurement to avoid reverberations in the system. The pulse repetition is limited to 15 kHz to avoid exceeding the transducer surface heating limits impose by the U.S. Food and Drug Administration (FDA)[17].

A. Imaging setup

A 128-element linear array probe is used for the investigation. A duplex synthetic aperture sequence is used to acquire both B-mode and flow data sets. The emissions are interleaved, so that for every five flow emissions a B-mode emission is transmitted. An effective flow pulse repetition time is consequently $T_{eff} = T_{prf}/(5+1)$, where T_{prf} is the inverse of the system pulse repetition frequency (PRF). The B-mode image is composed of a synthetic aperture sequence with 128 individual emissions with virtual sources located behind the transducer. The transducer and acquisition/simulation parameters are listed in Table I.

The flow sequence is implemented using a 64-element sub-aperture for each emission to emulate a spherical

Table I
TRANSDUCER AND ACQUISITION/SIMULATION PARAMETERS

Transducer		Transmit Parameters		
Parameter	Value	Parameter	B-mode	Flow
Transducer type	Linear array	Number of emitting elements	16	64
Number of transducer elements	128	Tx Apodization window	Hanning	
Transducer element pitch	0.3 mm	F-number	-1	-3.5
Transducer element kerf	0.035 mm	Number of distinct beams	128	5
Transducer element height	4 mm	Excitation signal	3 sinusoids with 50% Tukey	
Elevation focus	20 mm			
Center frequency	8 MHz	Pulse repetition frequency (PRF)		
		- Simulation / In-vivo	15 kHz	
		- Flow-rig measurement	3 kHz	

Table II
BEAMFORMING PARAMETERS

Receive parameters	Value
Number of receiving elements	128
Apodization window	Hanning
F-number	1
Spatial sampling interval (Δs)	0.07λ

Table III
VELOCITY AND ANGLE ESTIMATION PARAMETERS

Velocity estimation		Value
Sampling interval	dr	0.1λ
Samples in directional signal	$N_{samples}$	75
Correlations averaged	-	31
Effective time	T_{eff}	$T_{prf}/(5+1)$
Angle estimation		
Angle range	θ_{line}	$-90°$ to $89°$
Angle steps	-	$0.5°$, $1°$, $2.5°$ and $5°$

wave emanating from a virtual point source located behind the sub-aperture(negative F-number). The transmitted wavefront is directed towards a region of interest (ROI), so the ROI is completely insonified in every emission (Fig. 5). A 3-cycle sinusoidal pulse weighted by a 50% Tukey window is used as the excitation waveform. The same transmit voltage is used for both B-mode and flow imaging.

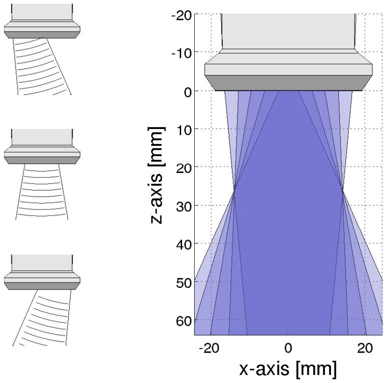

Fig. 5. Example of spherical waves emanated from the first, third, and fifth emission used in the flow sequence (left). Overlay of the insonified area from each emission, and the actual region of interest shown in a darker shade (right).

B. Beamformation setup

The beamforming is performed off-line on a computer cluster using MATLAB (Mathworks, Natick, MA, USA) and the Beamforming Toolbox 3 (BFT3) [18]. For every emission, the RF channel data are matched filtered, Hilbert transformed to form complex IQ data, beamformed in a spatially oversampled 2-D grid with an isotropic spatial sampling interval of Δs, and stored for further processing. The beamforming parameters are listed in Table II. Stationary echo-canceling is applied after beamforming using the approach described by Hoeks [19], which have a -3 dB cut-off frequency at $0.87\frac{1}{T_{eff}\cdot N_{ec}}$, and for $N_{ec} = 32$ consecutive lines the cut-off frequency is 110 Hz which corresponds to an axial velocity of 0.01 m/s.

To reduce the computational burden from beamforming a new set of lines at every estimation point, a set of lines are obtained by resampling the 2-D complex beamformed data into a polar grid centred at the estimation point. This is equivalent to beamforming the lines directly from RF data as described in [11].

C. Velocity and angle estimation setup

The polar grid around the estimation point is sampled uniformly along the radial axis with an interval of dr, with all lines having the same number of samples $N_{samples}$. The angular axis is non-uniformly sampled, and is divided in four regions, as shown in Fig. 4. Here, the outer regions are sampled at a step size of 0.5°, and the step is increased until the inner region is sampled at a step of 5°. This is done to avoid errors due to the non-linear behaviour of the estimates closer to the transverse dimension. The velocity angle estimation parameters are listed in Table III.

IV. EXPERIMENTS

A. *Simulations*

A number of simulations were performed using Field II [20], [21], in which tissue and blood are modeled as a collection of random point scatterers. Approximately 10 point scatterers per resolution cell were sufficient to ensure a Gaussian distributed RF signal. The size of the resolution cell was calculated based on the receive F-number, transmit frequency, and pulse length. In each emission the scatterer position is updated. Two different types of phantoms are simulated; a spinning disk phantom, which provides a range of velocities at all possible angles, and straight vessels with a parabolic flow that can be compared to the available measurements.

1) Spinning Disk Phantom: The phantom consists of a circular collection of scatterers, and a speed-of-sound is set to 1540 m/s. The scatterers are rotated around the disk center at a constant angular velocity. Therefore, the velocity magnitude linearly increases as a function of distance from the disk center. The phantom rotates clock-wise, having a diameter of 1.5 cm, and a maximum velocity v_{max} at the outer edge. The center of the spinning disk is placed at a depth of 2.5 cm below the center line of the array. The elevation extent of the spinning disk is 5 mm. White noise is added by first estimating the average signal power to generate noise powers at the specified signal to noise ratios (SNR) in dB. The estimates are constructed over a grid with a spatial sampling of 0.2 mm in both the lateral and axial dimensions. A binary mask is applied on the velocity estimates to remove the ones outside the phantom's borders.

Two simulation studies are performed with the spinning disk; the first assesses the performance of the method using $v_{max} = 0.5$ m/s, one hundred consecutive estimates, and SNR ratios of 20, 10, and 0 dB. Here no spatial or temporal averaging is performed on the estimates to quantify the method's performance. A second study evaluates the impact of stationary echo-canceling on the method. Estimates with and without echo-canceling are compared. Note that the phantom does not contain tissue. The spinning disk v_{max} is set to 0.2 m/s, the SNR to 30 dB, the estimates were spatially averaged in a region of $1.0\,\text{mm} \times 1.0\,\text{mm}$ with a median filter, and ten consecutive estimates were used to match this study to [22].

2) Simulated Vessel Phantom: Parabolic flow through a rigid vessel is simulated at flow angles of 75° and 90°. The vessel has a radius of 6 mm, centered at 30 mm, and with a non-moving vessel wall. The peak velocity in the vessel is 0.5 m/s. One hundred consecutive pulse emissions are simulated. Velocity direction and magnitude are estimated along the profile through the tube, and the estimated velocities are compared to the expected profile. No spatial or time averaging are performed on the obtained estimates. A binary mask is applied as for the spinning disk.

B. *Flow-rig Measurements*

The experimental ultrasound scanner, SARUS [23], is used for acquiring data. The system acquires RF data from the individual transducer channels, and these data are transferred to a computing cluster, where they are saved and processed off-line. The received RF data contains 128 channels sampled at 35 MHz and have 12 bits resolution for each individual channel.

Measurements are made in a flow-rig system. A Cole-Parmer centrifugal pump (Vernon Hills, IL, USA) circulates a blood-mimicking fluid [24] (Danish Phantom Design, Frederikssund, Denmark) in a closed loop circuit. The vessel radius is 6 mm, and the entrance length is long enough to ensure fully developed laminar flow with a parabolic profile. The volume flow rate is measured by a calibrated MAG1100 flowmeter (Danfoss, Nordborg, Denmark) and used for calculating the true peak velocity based on the expected parabolic profile. The flow rate is adjusted to obtain a peak velocity of approximately 0.1 m/s, which at a PRF of 3 kHz matches the velocity-to-PRF ratio used in the simulations. This setup is used to avoid reverberations in the water tank. The angle of the transducer and the distance to the tube are adjusted to match the geometry of the simulation setup. Two measurements are obtained, one for each simulated vessel. The processing is the same as for the simulations.

C. *In-vivo Measurements*

An *in-vivo* acquisition is performed after approval by The Danish National Committee on Biomedical Research Ethics with approval number H-1-2014-FSP-072. A healthy volunteer with no history of cardiovascular disease (52 year old woman) is scanned after informed consent. An ultrasound scan sequence, as described in Section III, is acquired on the left carotid bifurcation on a longitudinal view. The scans are recorded with the volunteer in supine position and carried out by an experienced radiologist.

Intensity measurements are carried out prior to the scan, the measured intensities must satisfy limits regulated by the U.S. Food and Drug Administration (FDA)[17]. These limits concern the mechanical index, $MI \leq 1.9$, the derated spatial-peak-temporal-average intensity, $I_{spta} \leq 720$ mW/cm^2. The measured values using the scheme described in [25], are $MI = 0.91$ and $I_{spta} = 144.3$ mW/cm^2, which are both below the FDA limits. The transducer surface temperature was also tested, where the transducer surface should not exceed an increase of 30° or 6° Celsius in air and in a simulated usage test, respectively. The maximum pulse repetition frequency (PRF) was adjusted to comply with these regulations and was found to be 15 kHz.

A 3 second acquisition is recorded, yielding 7,500 velocity estimates at 2,500 frames per second. The imaging, beamformation, and velocity estimation are performed with the parameters described in Section III. A binary mask is generated by using the intensity values from the B-mode image. The binary mask is constructed from each B-mode frame after median filtering the log-compressed image using a 0.6 mm x 0.6 mm kernel. All intensities below a certain threshold value in the B-mode image are then considered to be blood, where the velocity estimates are displayed. Additionally, a median filter is applied to the velocity magnitude estimates in the time domain, using a 35 ms sliding window, as well as in the spatial domain where a kernel of 1 mm x 1 mm is applied. Hereby false peak detection errors in the velocity magnitudes are removed. However, no spatial filtering or regularization process is applied to the estimated angles, to actually show the raw performance of the algorithm.

V. RESULTS

A. Spinning disk phantom

The spinning disk with $v_{max} = 0.5$ m/s is used to assess the 360° performance of the method. Mean and standard deviation are calculated based on 100 different measurement realizations. The accuracy of the vector velocity estimates are assessed by calculating an error percentage between the mean estimates and the ground truth. The precision is assessed by using the standard deviation (SD) of the one hundred realizations divided by $v_{max} = 0.5$ to obtain a relative velocity SD. Fig. 6 shows these performance results with 10 dB SNR.

The left column on Fig. 6 contains the angle estimation performance. It can be seen from Fig. 6 (c) and (e) that both the accuracy and precision of the angle estimator is maintained constant along the complete 360° angle range. However, at small curvature radii the angle estimator fails to estimate the correct values. This can be attributed to the line length, since in smaller radii, a line of the same size will transverse larger velocity gradients. A simple solution is to make smaller lines, but this also limits the amount of information available for the correlation.

The right column in Fig. 6 provides the performance of the estimated velocity magnitude. The performance in this case is not homogeneous along the angles. A noticeably larger standard deviation exists, when the flow movement approaches the lateral direction, due to the lower frequency content in that dimension. The issue could be addressed by using longer lines in that dimension, but due to the geometry of the phantom, longer lines will also increase the bias given that they will transverse larger velocity gradients.

The estimator performance is also obtained at different SNR conditions. The observed performance presented a similar pattern as for the presented on Fig. 6 where a SNR of 10 dB is selected. The degradation of the estimates due to the loss of SNR are manifested as a general increase of errors. As the spatial error distribution is not normal, the overall performance measurement for the SNR comparison is taken as the median and interquartile ranges of the errors and standard deviations of the entire disk. However, to avoid the highly wrong estimates at smaller radii, the mean values are calculated using the estimated values inside the radius range of 0.2 cm $\leq r \leq 0.75$ cm, which corresponds to 26% $\leq r \leq$ 100%. The overall performance at different SNRs is summarized in Table IV. The performance decreases significantly when the SNR approaches 0 dB. This effect has previously been investigated for time shift estimators by Jensen [26], establishing a limit around 6 dB as the minimum SNR for a reliable estimation of the velocity. It should be noted that the stationary echo-canceler removes a greater amount of energy from the lower frequency content. Lateral movement estimates in lower SNR scenarios will therefore degrade first, and this will be observed as an expansion of the white areas in Fig. 6 (f).

Table IV
MEDIAN BIAS AND INTERQUARTILE RANGES FROM THE SPINNING DISK PHANTOM AT DIFFERENT SNR.

	Angle		Velocity	
SNR [dB]	bias [deg] med | *iqr*	std. dev. [deg] med | *iqr*	bias [%] med | *iqr*	std. dev. [%] med | *iqr*
20	0.92 | *1.22*	1.35 | *1.04*	2.36 | *4.43*	0.76 | *3.08*
10	1.01 | *1.40*	1.80 | *1.29*	2.57 | *4.99*	1.02 | *3.88*
0	7.96 | *13.2*	17.5 | *20.8*	5.84 | *20.4*	6.78 | *19.4*

The impact of the stationary echo-canceler is also measured on a spinning disk phantom with $v_{max} = 0.2$ m/s as shown in Fig. 7. In this figure the V_x and

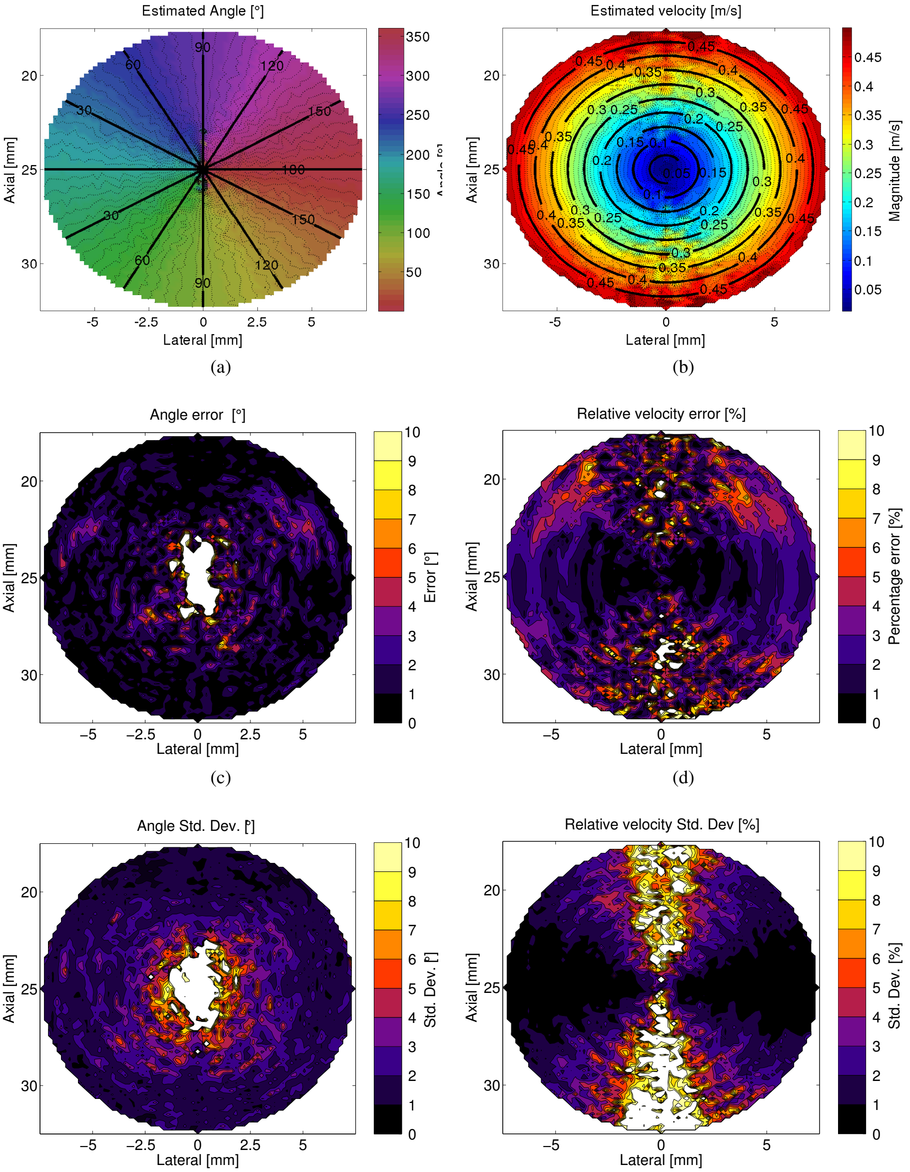

(a) (b)

(c) (d)

(e) (f)

Fig. 6. Vector velocities obtained from a spinning disc phantom with 10 dB SNR. The estimated velocity angle (a). The estimated velocity magnitude (b). The angle error (c). The relative velocity error (d). The angle standard deviation (e). The relative velocity standard deviation (f).

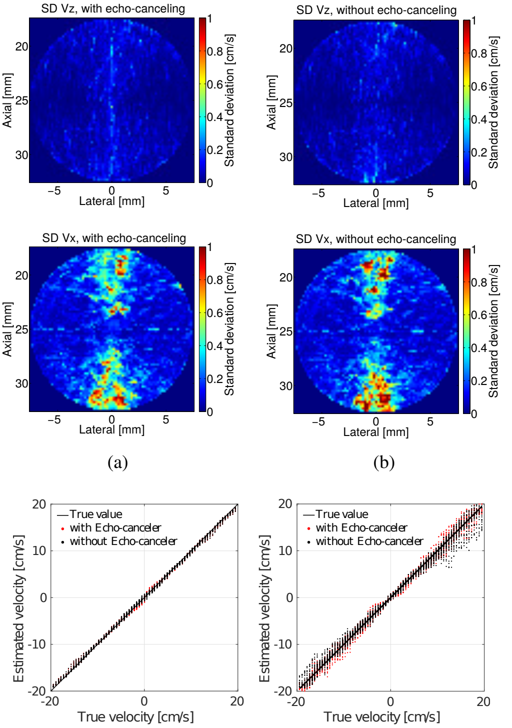

(a)

(b)

(c)

Fig. 7. Standard deviation (SD) of the velocity estimator over 10 realizations of the simulated spinning phantom. The SDs are in centimetres per second and for the V_x and V_z components (top/bottom). SD with and without echo-canceling are shown in (a) and (b), respectively. A scatterer plot from a single realization of the estimated versus the reference velocity is shown in (c). The red dots correspond to the setup with echo-canceler, while the black dots to the setup without echo-canceler.

V_z components are shown instead. These are obtained by simply multiplying the velocity magnitude by the cosine or sine of the corresponding angle. The standard deviations on each of the components for 10 realizations are shown in Fig. 7 (a) and (b), for the echo-canceled and non echo-canceled case, respectively. Fig 7 (c), shows a scatter plot of the estimated versus the reference velocities for the proposed method. Velocity estimates plotted in red are estimates obtained when the echo-canceler is enabled. The results show no significant difference between them. Therefore, the echo-canceling has only an effect on the estimates when the SNR is lower than the 6 dB SNR threshold needed for the estimation. The results are formatted in a similar manner as published in [22] for comparison with speckle tracking and cross-beam Doppler.

B. *Straight vessel phantom*

Corresponding results obtained from the simulated and measured straight vessels are seen in Fig. 8. Here, the estimated mean velocity and angle profiles and their corresponding standard deviations are plotted. The true velocity and angle profiles are plotted in red. A summary of the results are listed in Table V. Statistics are calculated over 100 estimated profiles.

Correspondence is observed between the measurements and the simulations. The peak velocity in the measurement is 5 times lower to match the same velocity-to-PRF ratio as in the simulations. All the estimated profiles approximate the true values denoted in red. However, different angle biases are present between measurements and simulations. In the 75° vessel simulation, the angle was overestimated generating an overestimation of the velocity magnitude. In the measurement, the angle was slightly underestimated, but a larger underestimation is present in the velocity magnitude. The same underestimation is present in both simulations and measurements of the 90° vessel regardless of the negative or positive angle bias. The underestimation appears to be quantitatively reproducible and may be correctable in post-processing. The large deviations on the angle plots on the edges of the vessel are simply due to the echo-canceler, which removes all blood/tissue energy, leaving only noise for the velocity estimator.

Table V
MEAN BIAS AND STANDARD DEVIATION OF THE VESSEL ESTIMATES.

Type	rel. vel.[%] bias	rel. vel.[%] std. dev.	angle [deg] bias	angle [deg] std. dev.
Angle	75°			
Simulated	2.42	1.87	1.20	0.45
Measured	-3.88	2.81	-0.31	0.67
Angle	90°			
Simulated	-6.44	4.06	0.13	1.05
Measured	-9.73	4.65	-1.38	1.09

C. *In-vivo imaging of the carotid bifurcation*

One image frame from the *in-vivo* acquisition in the left carotid bifurcation during systole is shown in Fig. 9.A B-mode image is overlayed with the 2-D velocity estimates. The velocity color map depends on both the flow magnitude and direction according to the color wheel map provided in the lower right corner of Fig. 9. The provided longitudinal view shows both the internal and external carotid, which are seen as the deep and shallower vessel, respectively.

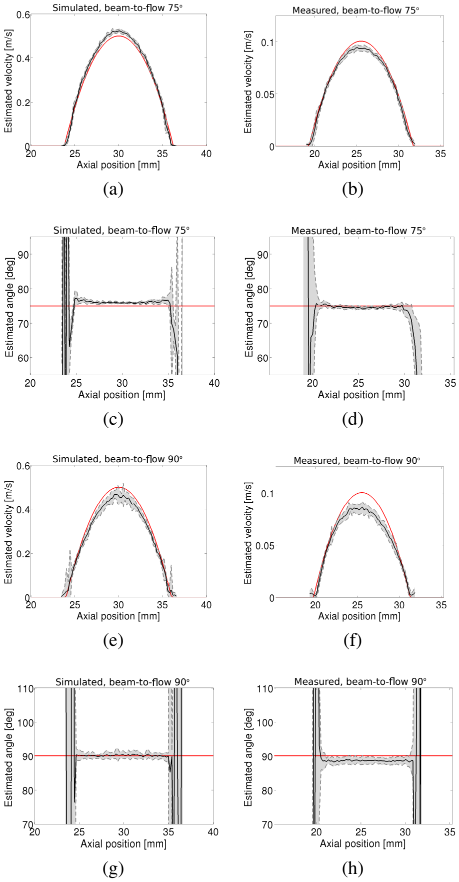

Fig. 8. Comparison between the estimated velocities profiles from the simulated (left) and measured (right) straight vessels. The peak velocity in the measurement is 5 times lower to match the same velocity-to-PRF ratio as in the simulations. The plots show the profiles for the true (red), the mean magnitude with standard deviation (a, b, e and f), and the mean angle with standard deviation (c, d, g and h) for beam-to-flow angles of 75° and 90°.

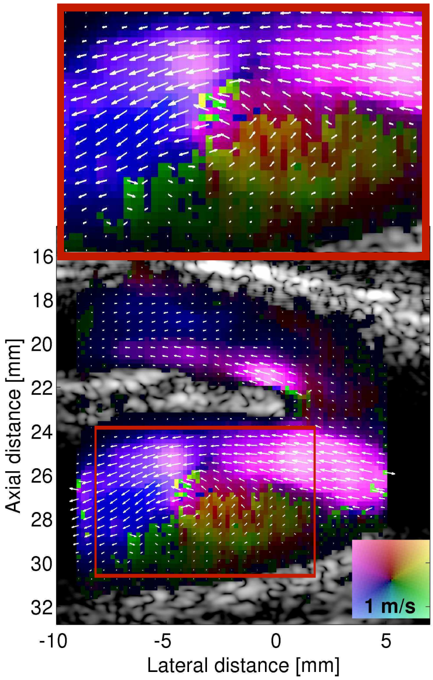

Fig. 9. A vortex was present in the carotid bulb of the internal carotid artery during the entire cardiac cycle. The internal carotid artery is seen as the deep vessel.

A vortex with low velocities in the carotid bulb of the internal carotid artery is shown as the zoom in area in Fig. 9. Apart from this vortical recirculation in the bulb, no retrograde flow was present during the entire heart cycle. A non axis-symmetric flow can also be observed in the upper part of the vortex as the presence of two distinct peaks in the flow trajectory. This is probably due to the presence of out of plane motion in the internal carotid artery.

Fig. 10 (a,b,c) shows the 2-D velocity estimates at different stages of the cardiac cycle, where a low velocity vortex is present in the carotid sinus at the three stages.

Three distinct heart cycles are captured during the 3 seconds acquisition. Fig. 10 (d) shows the quantitative velocity estimates after aligning the peak systole in the cardiac cycles for the same anatomical position at the entrance of the internal carotid denoted by the white circle in Fig. 10 (c). The peak velocity at the denoted location is 0.55 m/s and is consistent for the three heart cycles. The alignment was performed during the peak period, however, during the rest of the cardiac cycle the same spatial position is used. Therefore, vasculature movement can generate misalignment, which could be the reason why the velocity values differ after the peak.

Two video sequences are available as a multimedia attachment. The first contains a preview movie of the full acquisition at a frame rate of 90 frames per second. The second contains a high frame rate segment during the peak systole at the full frame rate of 2,500 frames per second.

VI. DISCUSSION

In this paper, a new method for determining the flow angle in 2-D vector velocity estimation was presented.

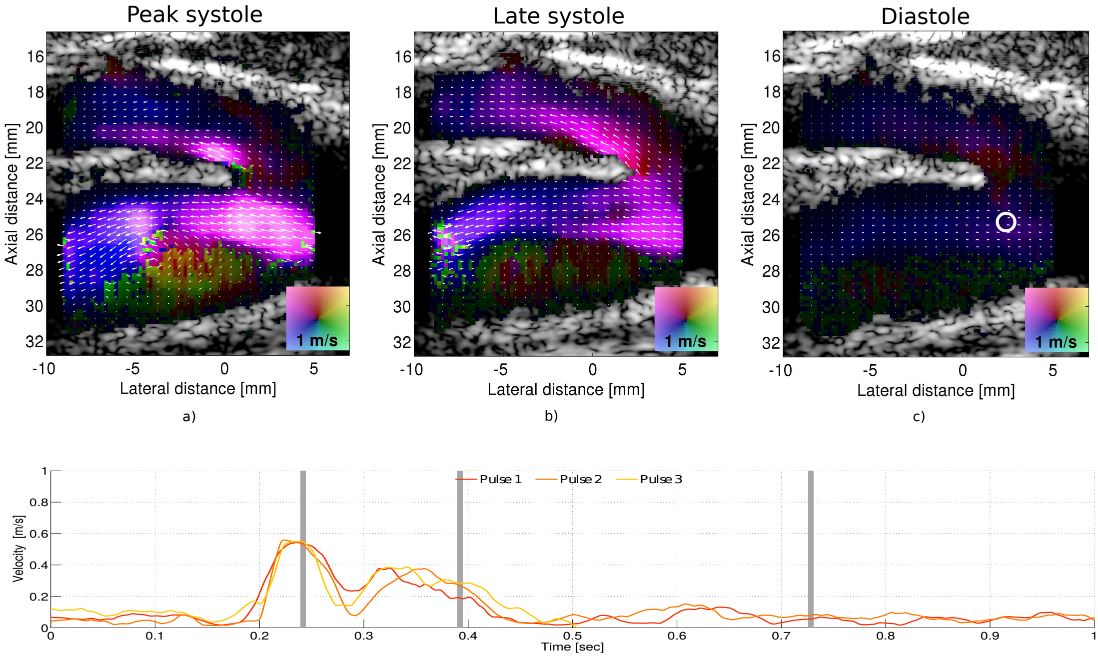

a)

b)

c)

d)

Fig. 10. Carotid bifurcation of a 52 year old healthy individual. Time aligned velocity magnitude profiles at the entrance of the internal carotid at the position denoted by the white circle in (c) is shown in the bottom graph. Vector flow frames during three different stages of the cardiac cycle are shown above. The first frame (b) corresponds to time point ≈0.25 s, the second frame (b) to time point at ≈0.39 s, and the third frame (c) to time point at ≈0.73 s.

The velocity magnitude is based on the previously introduced directional beamforming method[11], which is extended in this work to obtain a robust angle estimation.

The method is fully described and validated; Field II simulations and experiments confirmed the capability for estimating the true flow angle regardless of the beam-to-flow angle. The results of a simulation analysis on a spinning disk phantom (Fig. 6) confirm that in all cases the angle errors are in the order of 1°, and the standard deviations are kept under 3°. The method performs better than the previously published angle estimator using the maximum of the normalized correlation function, in which the correlation time had to be "tuned" to a range of angles and velocities, thus, it did not present an uniform behaviour along all angles[14]. The method also shows an improved performance compared to state-of-the-art methods such as the robust angle estimation proposed in [22]. Results on a similar spinning disk setup showed improved biases and standard deviations on the lateral estimates (Fig. 7). The axial estimates were kept with low biases and standard deviations equivalent to the cross-beam Doppler approach as reported in [22]. However, as the center frequency and imaging depth are not exactly the same, a direct comparison cannot be done between the methods. The method also presented robust performance to the echo-canceler process (Fig. 7), most likely due to the broadband nature of the velocity estimator. Simulations and experiments on straight vessels also confirm the spinning disk findings (Fig. 8). On the *in-vivo* scan, the proposed method showed consistent vector velocity estimates and the velocities matches with data from the literature for healthy individuals[27], and it also presented a complex vortex observed in previous studies[28], [29]. However, has not in previous studies the vortex in the carotid bulb been captured with such a high frame rate and in such a detail. The recorded video shows the vortex to be initiated upstream in the bulb during the early systole, after which the vortical formation moves downstream to fill the entire carotid sinus during peak systole. In the late systolic phase and in the diastole, the bulb produced a steady discrete retrograde flow.

The independency to the beam-to-flow angle is an important feature for complex flow analysis. Other 2-D vector methods doesn't have an uniform behaviour and fail when low beam-to-flow angles are examined [8], [30]–[33]. The reason for this, as explained in [31], is the anisotropy of the spatial frequencies between the lateral and axial dimensions, which results in different rates of decorrelation of the speckle pattern dependant on the beam-to-flow angle. Therefore, techniques that relies on correlation coefficients, where strong anisotropies are present (RF speckle tracking), are prone to a non-uniform behaviour. Reducing the anisotropy, e.g. envelope detecting, increases the uniformity of the estimator but at the cost of resolution. Other 2-D techniques where correlation coefficients don't play a direct role on the angle determination, such as cross-beam Doppler, are less susceptible to this anisotropy. However, these techniques rely on an axial velocity estimator where small errors in the velocity measurement have a greater impact on the angle estimate, when beam-to-flow angles larger than 60° are present, thus, having an error amplification effect on the lateral estimates, observed as larger standard deviations. The proposed estimator overcomes the beam-to-flow dependency by estimating velocities from beamformed lines along the flow direction and not along the beam, therefore, presenting a constant angle performance along the full 360° range. Another advantage of the estimator is since lines are focused along the flow, the correlation of the signal is maintained for longer periods of time enabling detection of higher velocities than what is usually observed in phase shift estimators, which are prone to aliasing[11]. Detection of high velocities at lower PRFs may become useful when deeper structures are examined, e.g. transthoracic cardiac scans.

A limitation of the technique is the lower available energies at deeper depths, due to the use of broader beams and tissue absorption. This is aggravated by the fact that short pulses are used to generate the broadband signals that the directional flow method usually uses. However, this could be resolved by extending the time-bandwidth product using coded excitations [34].

Finally, the technique could be expanded to 3-D imaging with 2-D arrays by adding a new set of angles and expanding the current polar grid to a spherical one. However, the computationally intensive nature of the method implies a higher computational load than traditional methods.

VII. CONCLUSION

This paper presented a novel technique for estimating angles robustly in high frame rate imaging sequences. The method possesses three key features. First, it performs uniformly along the full 360° range regardless of the beam-to-flow angle with errors on the order of 1°, and standard deviations kept under 3°. Second, the method presents accurate estimates with a 10% bias in its worst case. Third, the method presents 2-D velocity vectors at frame rates in the order of thousands; giving the unique ability to see transient flow events not visible before. Finally, the availability of quantified estimates across the whole insonified region at high frame rates opens possibilities for new clinically relevant measures.

REFERENCES

[1] E. G. Grant, C. B. Benson, and G. L. M. et al, "Carotid artery stenosis: Gray-scale and Doppler US diagnosis - society of radiologists in ultrasound consensus conference," *Radiology*, vol. 229, no. 2, pp. 340–346, 2003.

[2] B. Dunmire and K. W. Beach, "A Brief History of Vector Doppler," in *Proc. SPIE Med. Imag.*, vol. 4325, Feb. 2001, pp. 200–214.

[3] P. J. Phillips, A. P. Kadi, and O. T. von Ramm, "Feasibility study for a two-dimensional diagnostic ultrasound velocity mapping system," *Ultrasound Med. Biol.*, vol. 21, no. 2, pp. 217–229, 1995.

[4] J. A. Jensen and P. Munk, "A new method for estimation of velocity vectors," *IEEE Trans. Ultrason., Ferroelec., Freq. Contr.*, vol. 45, pp. 837–851, 1998.

[5] M. E. Anderson, "Multi-dimensional velocity estimation with ultrasound using spatial quadrature," *IEEE Trans. Ultrason., Ferroelec., Freq. Contr.*, vol. 45, pp. 852–861, 1998.

[6] J. Y. Lu, "2D and 3D high frame rate imaging with limited diffraction beams," *IEEE Trans. Ultrason., Ferroelec., Freq. Contr.*, vol. 44, pp. 839–855, 1997.

[7] S. I. Nikolov and J. A. Jensen, "In-vivo Synthetic Aperture Flow Imaging in Medical Ultrasound," *IEEE Trans. Ultrason., Ferroelec., Freq. Contr.*, vol. 50, no. 7, pp. 848–856, 2003.

[8] J. Udesen, F. Gran, K. L. Hansen, J. A. Jensen, C. Thomsen, and M. B. Nielsen, "High frame-rate blood vector velocity imaging using plane waves: simulations and preliminary experiments," *IEEE Trans. Ultrason., Ferroelec., Freq. Contr.*, vol. 55, no. 8, pp. 1729–1743, 2008.

[9] J. Bercoff, G. Montaldo, T. Loupas, D. Savery, F. Meziere, M. Fink, and M. Tanter, "Ultrafast compound Doppler imaging: providing full blood flow characterization," *IEEE Trans. Ultrason., Ferroelec., Freq. Contr.*, vol. 58, no. 1, pp. 134–147, January 2011.

[10] B. Denarie, T. A. Tangen, I. K. Ekroll, N. Rolim, H. H. Torp, T. Bjastad, and L. Løvstakken, "Coherent plane wave compounding for very high frame rate ultrasonography of rapidly moving targets," *IEEE Trans. Ultrason., Ferroelec., Freq. Contr.*, vol. 32, no. 7, pp. 1265–1276, 2013.

[11] J. A. Jensen, "Directional velocity estimation using focusing along the flow direction: I: Theory and simulation," *IEEE Trans. Ultrason., Ferroelec., Freq. Contr.*, vol. 50, pp. 857–872, 2003.

[12] O. Bonnefous, "Measurement of the complete (3D) velocity vector of blood flows," in *Proc. IEEE Ultrason. Symp.*, 1988, pp. 795–799.

[13] K. L. Hansen, J. Udesen, N. Oddershede, L. Henze, C. Thomsen, J. A. Jensen, and M. B. Nielsen, "In vivo comparison of three ultrasound vector velocity techniques to MR phase contrast angiography," *Ultrasonics*, vol. 49, pp. 659–667, 2009.

[14] J. Kortbek and J. A. Jensen, "Estimation of velocity vector angles using the directional cross-correlation method," *IEEE Trans. Ultrason., Ferroelec., Freq. Contr.*, vol. 53, pp. 2036–2049, 2006.

[15] S. G. Foster, P. M. Embree, and W. D. O'Brien, "Flow velocity profile via time-domain correlation: Error analysis and computer simulation," *IEEE Trans. Ultrason., Ferroelec., Freq. Contr.*, vol. 37, pp. 164–175, 1990.

[16] J. A. Jensen and S. I. Nikolov, "Directional synthetic aperture flow imaging," *IEEE Trans. Ultrason., Ferroelec., Freq. Contr.*, vol. 51, pp. 1107–1118, 2004.

[17] FDA, "Information for manufacturers seeking marketing clearance of diagnostic ultrasound systems and transducers," Center for Devices and Radiological Health, United States Food and Drug Administration, Tech. Rep., 2008.

[18] J. M. Hansen, M. C. Hemmsen, and J. A. Jensen, "An object-oriented multi-threaded software beamformation toolbox," in *Proc. SPIE Med. Imag.*, vol. 7968, March 2011, pp. 79 680Y–1–79 680Y–9.

[19] A. P. G. Hoeks, J. J. W. van de Vorst, A. Dabekaussen, P. J. Brands, and R. S. Reneman, "An efficient algorithm to remove low frequency Doppler signal in digital Doppler systems," *Ultrason. Imaging*, vol. 13, pp. 135–145, 1991.

[20] J. A. Jensen, "Field: A program for simulating ultrasound systems," *Med. Biol. Eng. Comp.*, vol. 10th Nordic-Baltic Conference on Biomedical Imaging, Vol. 4, Supplement 1, Part 1, pp. 351–353, 1996.

[21] J. A. Jensen and N. B. Svendsen, "Calculation of pressure fields from arbitrarily shaped, apodized, and excited ultrasound transducers," *IEEE Trans. Ultrason., Ferroelec., Freq. Contr.*, vol. 39, pp. 262–267, 1992.

[22] S. Fadnes, I. K. Ekroll, S. A. Nyrnes, H. Torp, and L. Lovstakken, "Robust angle-independent blood velocity estimation based on dual-angle plane wave imaging," *IEEE Trans. Ultrason., Ferroelec., Freq. Contr.*, vol. 62, no. 10, pp. 1757–1767, October 2015.

[23] J. A. Jensen, H. Holten-Lund, R. T. Nilsson, M. Hansen, U. D. Larsen, R. P. Domsten, B. G. Tomov, M. B. Stuart, S. I. Nikolov, M. J. Pihl, Y. Du, J. H. Rasmussen, and M. F. Rasmussen, "SARUS: A synthetic aperture real-time ultrasound system," *IEEE Trans. Ultrason., Ferroelec., Freq. Contr.*, vol. 60, no. 9, pp. 1838–1852, 2013.

[24] K. V. Ramnarine, D. K. Nassiri, P. R. Hoskins, and J. Lubbers, "Validation of a new blood mimicking fluid for use in Doppler flow test objects," *Ultrasound Med. Biol.*, vol. 24, pp. 451–459, 1998.

[25] J. A. Jensen, M. F. Rasmussen, M. J. Pihl, S. Holbek, C. A. Villagomez-Hoyos, D. P. Bradway, M. B. Stuart, and B. G. Tomov, "Safety assessment of advanced imaging sequences, I: Measurements," *IEEE Trans. Ultrason., Ferroelec., Freq. Contr.*, vol. 63, no. 1, pp. 110–119, 2016.

[26] J. A. Jensen, "Stationary echo canceling in velocity estimation by time-domain cross-correlation," *IEEE Trans. Med. Imag.*, vol. 12, pp. 471–477, 1993.

[27] A. Harloff, T. Zech, F. Wegent, C. Strecker, C. Weiller, and M. Markl, "Comparison of blood flow velocity quantification by 4D flow MR imaging with ultrasound at the carotid bifurcation," *Am. J. Neuroradiol.*, vol. 34, pp. 1407–1413, 2013.

[28] D. N. Ku and D. P. Giddens, "Pulsatile flow in a model carotid bifurcation." *Arterioscler. Thromb. Vasc. Biol.*, vol. 3, pp. 31–39, 1983.

[29] K. L. Hansen, J. Udesen, F. Gran, J. A. Jensen, and M. B. Nielsen, "In-vivo examples of flow patterns with the fast vector velocity ultrasound method," *Ultraschall in Med.*, vol. 30, pp. 471–476, 2009.

[30] J. Udesen and J. A. Jensen, "Investigation of Transverse Oscillation Method," *IEEE Trans. Ultrason., Ferroelec., Freq. Contr.*, vol. 53, pp. 959–971, 2006.

[31] L. N. Bohs, B. J. Geiman, M. E. Anderson, S. C. Gebhart, and G. E. Trahey, "Speckle tracking for multi-dimensional flow estimation," *Ultrasonics*, vol. 38, pp. 369–375, 2000.

[32] M. Lenge, A. Ramalli, E. Boni, H. Liebgott, C. Cachard, and P. Tortoli, "High-frame-rate 2D vector blood flow imaging in the frequency domain," *IEEE Trans. Ultrason., Ferroelec., Freq. Contr.*, vol. 61, no. 9, pp. 1504–1514, 2014.

[33] M. Lenge, A. Ramalli, P. Tortoli, C. Cachard, and H. Liebgott, "Plane-wave transverse oscillation for high-frame-rate 2-D vector flow imaging," *IEEE Trans. Ultrason., Ferroelec., Freq. Contr.*, vol. 62, no. 12, pp. 2126–2137, December 2015.

[34] T. Misaridis and J. A. Jensen, "Use of modulated excitation signals in ultrasound, Part III: High frame rate imaging," *IEEE Trans. Ultrason., Ferroelec., Freq. Contr.*, vol. 52, pp. 220–230, 2005.

Paper II

Increasing the Dynamic Range of Synthetic Aperture Vector Flow Imaging..

Carlos Armando Villagómez-Hoyos, Matthias Bo Stuart, and Jørgen Arendt Jensen

Proceeding of SPIE Ultrasound Imaging. Symp., Vol. 9040, p. 1,

Accepted for oral presentation in San Diego, California, United States, 2014.

Increasing the Dynamic Range of Synthetic Aperture Vector Flow Imaging

Carlos Villagomez Hoyos, Matthias Bo Stuart,
Jørgen Arendt Jensen

Center for Fast Ultrasound Imaging, Technical University of Denmark, 2800 Lyngby, Denmark

ABSTRACT

In current ultrasound systems the dynamic range of detectable velocities is susceptible to the selected pulse repetition frequency, thus limiting the dynamic range of flow mapping. To establish the feasibility of extending the range of detectable velocities towards low velocity vessels, results are presented using synthetic aperture which increases the frame-to-frame signal correlation of the scatterer displacement while providing continuous data. In this paper, recursive synthetic aperture acquisition, directional beamforming, and cross-correlation are used to produce B-mode and vector velocity images. The emissions for the two imaging modes are interleaved 1-to-1 ratio, providing a high frame rate equal to the effective pulse repetition frequency of each imaging mode. The direction of the flow is estimated, and the velocity is then determined in that direction. This method works for all angles, including fully axial and transverse flows. The method is investigated using Field II simulations and data from the experimental ultrasound scanner SARUS, acquired from a circulating flow rig with a parabolic flow. A 7 MHz linear array transducer is used, and several pulse repetition frequencies are synthesized in a simulated flow phantom with linearly increasing velocity and in a dual-vessel phantom with laminar flow with peak velocities of 0.05 m/s and 0.5 m/s. The experimental measurements are made with laminar flow as in the simulations. For the simulated and experimental vessel with peak velocity of 0.05 m/s and flow angle of 75°, the relative bias is -0.29% and -3.19%, and the relative standard deviations are 2.39% and 5.75% respectively. For the simulated and experimental vessel with peak velocity of 0.5 m/s and flow angle of -90°, the relative biases are -4.30% and -7.37%, and the relative standard deviations are 1.59% and 6.12%, respectively. The presented method can improve the estimates by synthesizing a lower pulse repetition frequency, thereby increasing the dynamic range of the vector velocity imaging.

Keywords: vector flow imaging, high dynamic range, synthetic aperture

1. INTRODUCTION

Ultrasound can be used for blood flow imaging using a number of different approaches. Modern scanners utilize the autocorrelation estimator,[1] which measures the phase shift as a function of time. Another approach is to use a time-shift based estimator,[2] which determines the velocity by estimating the time-shift using the cross-correlation function. Both estimators are traditionally used along the ultrasound beam direction, therefore they only find the velocity projected along this direction. Consequently blood flow imaging is highly susceptible to the beam-to-flow angle. Additionally, blood flow velocities varies in several orders of magnitude, e.g., pulsatile flow which in the carotid can vary from 0 to over 1 m/s over the cardiac cycle.

In traditional ultrasound systems a trade-off is made between the range of detectable velocities and the number of estimation points. This can be overcome by using synthetic aperture for vector velocity estimation.[3–6] Having continuous data available in all points enables estimation of velocities without compromising the pulse repetition frequency. In previous studies, Stuart et al[7] estimated the vector velocity using synthetic aperture, but the high pulse repetition frequency hinders the angle estimation for slowly moving flow, hence providing incorrect estimates.

In this work, the approach suggested by Jensen,[8] which merges the cross-correlation estimator with directional beamforming, is used in combination with a synthesized pulse repetition frequency. The basic principle is that as the data is continuously available at all estimation points, a lower pulse repetition frequency can be synthesized

---

Further information send correspondence to Carlos Villagomez Hoyos. E-mail: cavh@elektro.dtu.dk

by simply skipping emissions. Then the direction of the flow can be estimated by cross-correlating time-shifted signals acquired in all directions. The direction of the flow is found where the correlation has its maximum, while the magnitude can be determined from the lag of the maximum correlation value.

The hypothesis investigated in this paper is that the method is not susceptible to the beam-to-flow angle and provides velocity estimates with a low standard deviation and an increased range.

This paper is organized as follows: Section 2 explains directional beamforming, recursive synthetic aperture, and presents the velocity estimation method, Section 3 describes the experimental setup for both simulations and measurements, Section 4 presents the results, and Section 5 gives discussion and conclusions.

2. METHODS

The following section describes the method for beamforming the directional signals and the approach taken for estimating vector velocities.

2.1 Synthetic aperture

The beamformation of the directional signals is performed as described by Jensen et al.[9,10] The directional beamforming in synthetic aperture is obtained by focusing signals received by the transducer elements in a set of arbitrary points. These points can be located on a straight line in any direction.

The focusing of any of these points, is based on the total transmit and receive time-of-flight and a sample of the directional signal corresponding to the point $\mathbf{r_x}$ is calculated as

$$L_i(\mathbf{r_x}) = \sum_{j=1}^{N_E} A_{ij}(\mathbf{r_x}) s_j \left(\frac{|\mathbf{r_t} - \mathbf{r_x}| + |\mathbf{r_x} - \mathbf{r_j}|}{c} \right) , \tag{1}$$

where N_E is the number of transducer elements, $A_{ij}(\mathbf{r_x})$ is the dynamic apodization coefficient, $s_j(t)$ is the received signal from transducer element j, $\mathbf{r_t}$ is the position of the transmit source and $\mathbf{r_j}$ is the position of the j'th transducer element.

To make a fully focused image, the beamformed signal $L_i(\mathbf{r_x})$ from each of the individual emissions are summed to give a high resolution image.

$$g(\mathbf{r_x}) = \sum_{i=1}^{N_e} L_i(\mathbf{r_x}) , \tag{2}$$

where N_e is the number of emissions. The image is constructed over a number of emissions, and if the emission sequence is repeating with no delay between the last emission of one iteration of the sequence and the first the first emission of the next iteration, data will be continuously available. In this case, recursive synthetic aperture (RSA) imaging is possible.[11] In RSA imaging, the low-resolution image contribution from a given emission is replaced when that emission is repeated. In this way, new high-resolution images can be created at the rate of the pulse repetition frequency (PRF). This makes it possible to average over more measurements when estimating velocities, and thus improves the standard deviation of the estimates.

RSA imaging can be applied to blood flow imaging when using cross-correlation estimators.[12] For velocity estimation it is necessary to compare two measurements obtained in exactly the same way, so the difference is only the blood's movement between measurements. This implies that the time between the signals to be correlated is T_{HR} seconds apart.

$$T_{HR} = t_{prf} \cdot N_e , \tag{3}$$

where t_{prf} is the time between emissions.

This paper combines RSA, directional beamforming, and synthetic aperture duplex imaging, which is a combination of two emission sequences in a 1-to-1 ratio to produce high-quality anatomical images and vector velocity estimates with high dynamic range and high frame rate.

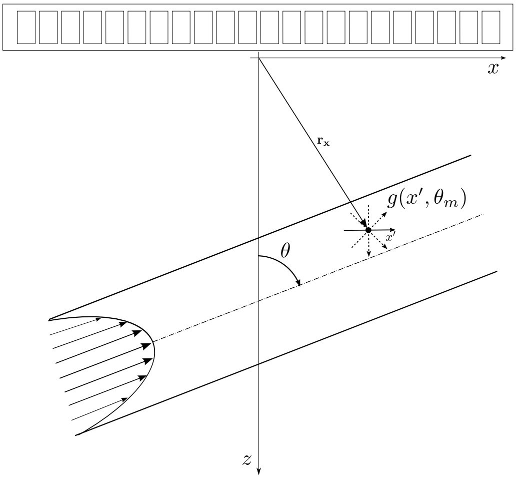

Figure 1: Directional signals $g(x', \theta_m)$ around estimation point $\mathbf{r_x}$.

2.2 Velocity vector estimation

The angle and magnitude for the velocity vector estimation used in this paper are based on beamformed data generated by the RSA technique and directional beamforming, as explained in Section 2.1. The advantage of using SA compared to traditional beamforming in flow estimation is that SA produces continuous data for all estimation points. Therefore the number of samples for velocity estimation is only restricted by the time which the flow can be assumed quasi-stationary. In SA, lines can be focused in any direction, thus beamforming lines along the direction of the flow is possible, therefore estimating the true velocity magnitude using the cross-correlation approach. Directional signals $g_1(x', \theta_m)$ and $g_2(x', \theta_m)$ are obtained at angle θ_m as illustrated in Fig. 1. Here the x'-axis is parallel to the θ_m angle direction and centred at a given estimation point $\mathbf{r_x}$, and the signals are T_{cc} seconds apart:

$$T_{cc} = k_{tprf} \cdot T_{HR} \,, \tag{4}$$

where T_{HR} is the time between high resolution lines made with the same emission sequence, as defined in (3), and k_{tprf} indicates the number of frames to skip in the correlation. Cross-correlating the discrete version of the signals gives

$$R_{12}(l, \theta_m) = \sum_{n=-N_{xcorr}/2}^{N_{xcorr}/2} g_1(n, \theta_m) g_2(n + l, \theta_m) \,, \tag{5}$$

where l is the correlation lag and N_{xcorr} is the discrete length of the directional signals.

To have a correct estimate of the velocity magnitude, the directionally beamformed line should match the direction of the flow. In general, this direction is not known and can be time dependent for non-constant flow.

The direction of the flow is found by cross-correlating along lines with different angles centered on the estimation point $\mathbf{r_x}$. The true direction is the one that has the highest peak in the cross-correlation given that the signals decorrelate slower in the direction of the flow. This can be stated as:

$$\begin{aligned} R_{12}(\theta_m) &= \frac{\max(R_{12}(l, \theta_m))}{\sqrt{R_{11}(0, \theta_m) R_{22}(0, \theta_m)}} && (6) \\ \theta &= \underset{\theta_m}{\operatorname{Arg\,max}}\ R_{12}(\theta_m), && (7) \end{aligned}$$

where $\max(R_{12}(l,\theta_m))$ is the maximum value of the cross-correlation function across angles θ_m,and $R_{11}(0,\theta_m)$ and $R_{22}(0,\theta_m)$ are the corresponding power of the cross-correlated signals. The correct angle θ is found where the normalized correlation function as a function of angle, $R_{12}(\theta_m)$, has its peak value.

Once the direction of the flow is known, $g_2(n,\theta)$ can be considered as $g_1(n,\theta)$ time-shifted, and therefore the lag where the cross-correlation function has a maximum

$$l_{max} = \underset{l}{\arg}\max\left\{R_{12}(l,\theta)\right\}, \tag{8}$$

is, thus, the discrete shift in spatial position of the scatterers over the time interval T_{cc}. For increased accuracy, a second order polynomial is fitted to the cross-correlation around l_{max}, and the position of the maximum correlation, $\hat{l}_{max}$, is found by the interpolation formula[13]

$$\hat{l}_{max} = l_{max} - \frac{R_{12}(l_{max}+1,\theta) - R_{12}(l_{max}-1,\theta)}{2R_{12}(l_{max}+1,\theta) - 2R_{12}(l_{max},\theta) + R_{12}(l_{max}-1,\theta)}. \tag{9}$$

The velocity along the flow direction is then given by

$$\hat{v}_{x'} = \frac{\hat{l}_{max}\cdot d_r}{T_{cc}}, \tag{10}$$

where d_r is the spatial sampling interval.

The probability of false peak detection is reduced by averaging over several estimates of R_{12} using the assumption that the velocity of the scatterers can be considered constant for several pulses. A number of cross-correlations, N_{xc} can, thus, be averaged in the estimation.

The maximum detectable velocity is limited by the search range l_{range} and the minimum time interval T_{cc}, which corresponds to a k_{tprf} of 1,

$$v_{max} = (l_{range}\cdot d_r)/T_{HR}, \tag{11}$$

The size of the search range which must be chosen carefully as the use of a large search range may increase the probability of false peak detection.[14]

At the other end, the minimum detectable velocity is dependent on the echo canceling filter, performed by subtracting the average of a moving window of N_{ec} high resolution lines. The minimum detectable velocity can be roughly estimated using the cut-off frequency of the stationary echo canceling filter and the distance between samples.

$$v_{min} \approx \frac{d_r}{T_{cc}\cdot N_{ec}} \tag{12}$$

where N_{ec} is the number of emissions used in the filter.

The parameters used in estimating the flow are listed in Table 1.

Table 1: Flow estimation parameters

Parameter	Symbol	Value
Spatial sampling interval	dr	0.1 λ
Spatial extent of directional signals	X_{corr}	-12.5 λ:12.5 λ
Number of correlations for each estimate	N_{xc}	15
Angular distance between directional lines	$d\theta_m$	5
HR lines frequency	$1/T_{HR}$	625 Hz
Correlation time factor	k_{tprf}	1,2,4,6
Number of HR lines used for echo canceling	N_{ec}	16

Table 2: Default parameters used in all simulations.

Parameter	Value
Number of transmit elements	64
Number of receive elements	128
Transducer center frequency	7 MHz
Pitch of transducer element	0.208 mm
Height of transducer element	4.5 mm
Kerf	0.035 mm
Speed of sound	1480 m/s
Transmit apodization	Hanning
Receive apodization	Rectangular (Boxcar)
Excitation Pulse	2 period sinusoid
Pulse repetition frequency	10 kHz (Duplex)
RF sampling frequency	100 MHz
Virtual emission focus (flow)	Linear sweep at depth of -80 mm
Emissions per high resolution line (flow)	8
Number of frames	150

3. EXPERIMENTAL SETUP

This section describes the simulations and measurements used for validating the method. First, the performance of the method is assessed for different conditions using simulations showing the capability of the method to extend the range of detectable velocities with the same data-set. Second a dual vessel simulation is done for evaluating the method during clinical conditions. Finally measurements are setup to match the dual-vessel simulation.

3.1 Field II Simulations

Field II[15, 16] is used to evaluate the performance of the estimator under different conditions. The velocity and angle estimates are obtained from simulated data without any added noise. A 7 MHz, 192 element, λ-pitch, linear array transducer is used with a sequence of eight defocused emissions for flow, interleaved with a standard synthetic aperture B-mode sequence. A 2-cycle sinusoidal pulse with a center frequency of 7 MHz is used for both B-mode and flow. The parameter values for the simulations are listed in Table 2.

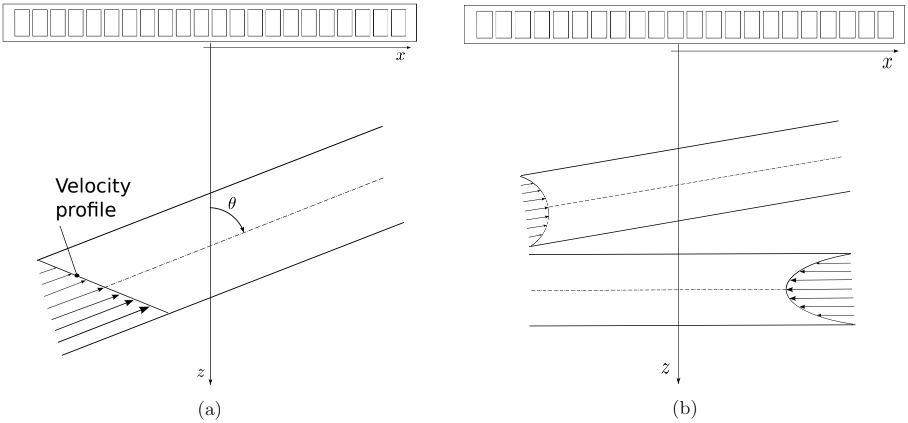

(a) (b)

Figure 2: Phantoms used in simulations. (a) Gradient phantom. (b) Dual-vessel phantom.

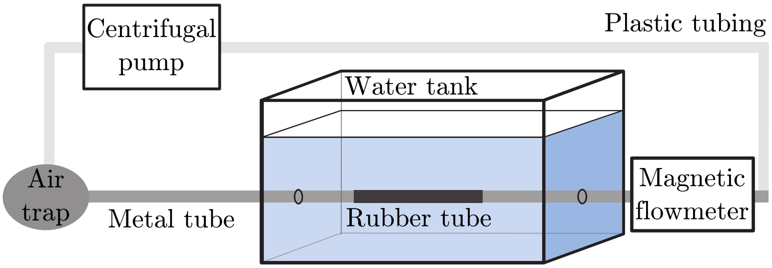

Figure 3: Illustration of the flow-rig system. It consists of a centrifugal pump, an air trap, a long rigid metal tube extending into a water tank followed by a magnetic flow meter. A transducer fixation device can be lowered into the water tank at adjustable beam-to-flow angles.

3.1.1 Gradient phantom

In order to evaluate the performance of the estimator at different velocities and angles, a gradient phantom is designed. Specifically, the phantom consists of blood mimicking scatterers moving with a Couette flow profile, see Fig. 2 (a). The velocity varies from 0 cm/s at one vessel wall to 50 cm/s at the other vessel wall. This flow is simulated at different angles $\theta = \{0, 30, 60, 90\}$. The size of the simulated phantom is 2x2 cm, which includes stationary scatterers using 10 scatterers per resolution cell for fully-developed speckle. The vessel radius is 1 cm.

The velocity and direction are estimated at 0.2 mm intervals along a line orthogonal to the vessel to cover the same velocity profile. Estimates are done for different $k_{tprf} = \{1, 2, 4, 6\}$, and the performance of the estimator is evaluated.

To evaluate the performance, the ratio between correct estimates and the total number of estimates is used. An estimate is considered acceptable when the estimated angle is within ±5° of the true angle and a maximum 20% error from the true velocity is estimated. The number of estimates is {1072, 944, 688, 432} for each k_{tprf}, respectively.

3.1.2 Dual-vessel phantom

Parabolic flow profiles are simulated using Field II. The simulated vessels have a diameter of 10 mm, are centred at 25 and 43 mm and have an angle of 75° and 90°, respectively as seen in Fig. 2 (b). The peak velocities simulated for each parabolic flow profile are 0.05 m/s for the top vessel and 0.50 m/s for the lower vessel. The direction of the flow is in the positive x-axis direction for the top vessel and negative x-axis direction for the lower vessel.

3.2 Measurement setup

The experimental ultrasound scanner, SARUS,[17] and a 7 MHz linear array transducer, type 8804 (BK Medical, Herlev, Denmark), are used for all measurements. The system acquires RF data from the individual transducer channels, and these data are transferred to a PC, where they are saved and processed off-line. The received RF data contains 192 channels sampled at 35 MHz and has 12 bits resolution for each individual channel.

All measurements are made in a flow-rig system as illustrated in Figure 3. A Cole-Parmer centrifugal pump (Vernon Hills, IL, USA) circulates a blood-mimicking fluid[18] (Danish Phantom Design, Frederikssund, Denmark) in the closed loop circuit. The vessel radius is 6 mm, and length long enough to ensure fully-developed laminar flow with a parabolic profile. The volume flow rate is measured by a calibrated MAG1100 flowmeter (Danfoss, Nordborg, Denmark) and used for calculating the peak velocity based on the expected parabolic profile. In its concentrated form, the fluid contains 5 μm-sized orgasol particles dissolved in glycerol, detergent, and demineralized water. For use, it is diluted in a ratio 1:20 with demineralized water, and dextran is added to obtain a viscosity μ of 3.9 mPa·s. The density ρ is 1.0×10^3 kg/m^3. The peak velocity can be set based on the flow rate. The flow rate was adjusted to obtain a peak velocity of approximately 0.05 and 0.5 m/s.

Inside the water tank a fixture for the transducer is inserted. The angle of the transducer and the distance to the tube are adjusted to match the geometry of the simulation setup. Two measurements are obtained, one for each simulated vessel.

4. RESULTS

The angle and velocity are estimated for simulations and measurements as described in Section 2.2. For all the results, the bias and standard deviation are calculated from the true angle, and the relative bias and relative standard deviation are calculated from the true velocity profiles. For both simulated and measured vessels, the velocity profile used as reference is a parabolic laminar flow described by;

$$v(r) = v_0 \left(1 - \left(\frac{r}{R}\right)^2\right), \tag{13}$$

where R is the tube radius, v_0 is the maximum velocity at the center of the tube, and r is the radial distance from the center of the tube.

All data are then processed off-line using a beamformation toolbox developed in-house (BFT3).[19]

4.1 Simulations results

4.1.1 Gradient phantom

The influence of the variation of k_{tprf} on the method is evaluated. As the method estimates the direction first and then the velocity, a wrongly detected direction most likely leads to an erroneous velocity estimate. For this reason, the estimates are split in two groups. A group of correct estimates, which are these that fall within a ±5° and ±20% of the true direction and velocity, and a second group that are those outside this region. The performance of the estimator is then defined as the ratio of the number of correct estimates to the total number of estimates.

The angle bias and standard deviation are calculated for all the estimates, but the relative velocity bias and relative velocity standard deviation are solely based on the estimates that fall within ±5° of the true direction. This consideration is based on the influence of the outliers on the relative bias and relative standard deviation which therefore do not represent the performance properly.

As seen in Fig. 4, for a k_{tprf} of 2, a range of velocities can be estimated accurately with a low standard deviation and bias, in both angle an magnitude, for any given angle. When the k_{tprf} is changed, as seen in Fig. 4 (b), the range of detected velocities is shifted towards the lower speeds. This is explained by the increased T_{cc} causing fast moving scatterers to move further and thereby decorrelate between observations. Similarly, slow moving scatterers are better detected since the echo canceling filter is also shifted.

4.1.2 Dual-vessel phantom

Fig. 5 shows the mean and standard deviation of the velocity profiles using different k_{tprf}. The velocity vector is accurately determined without previous knowledge of the flow direction. However, for the vessel with $v_{peak} = 0.05$ m/s, a higher $k_{tprf} = 6$ is needed to keep the standard deviation low. This can be achieved by taking advantage of the continuous existence of data in synthetic aperture, therefore removing any theoretical limit on the lower limit of the detectable velocities.

In Table 3 the relative bias and relative standard deviation of the simulated vessels is shown for different k_{tprf}. It can be seen that when increasing k_{tprf} the relative standard deviation for the vessel with $v_{peak} = 0.05$ m/s is improved, but for the vessel with $v_{peak} = 0.5$ m/s the standard deviation is worsened. This happens because as more time passes the blood scatterers move out the beamformed line, and the signal decorrelates.

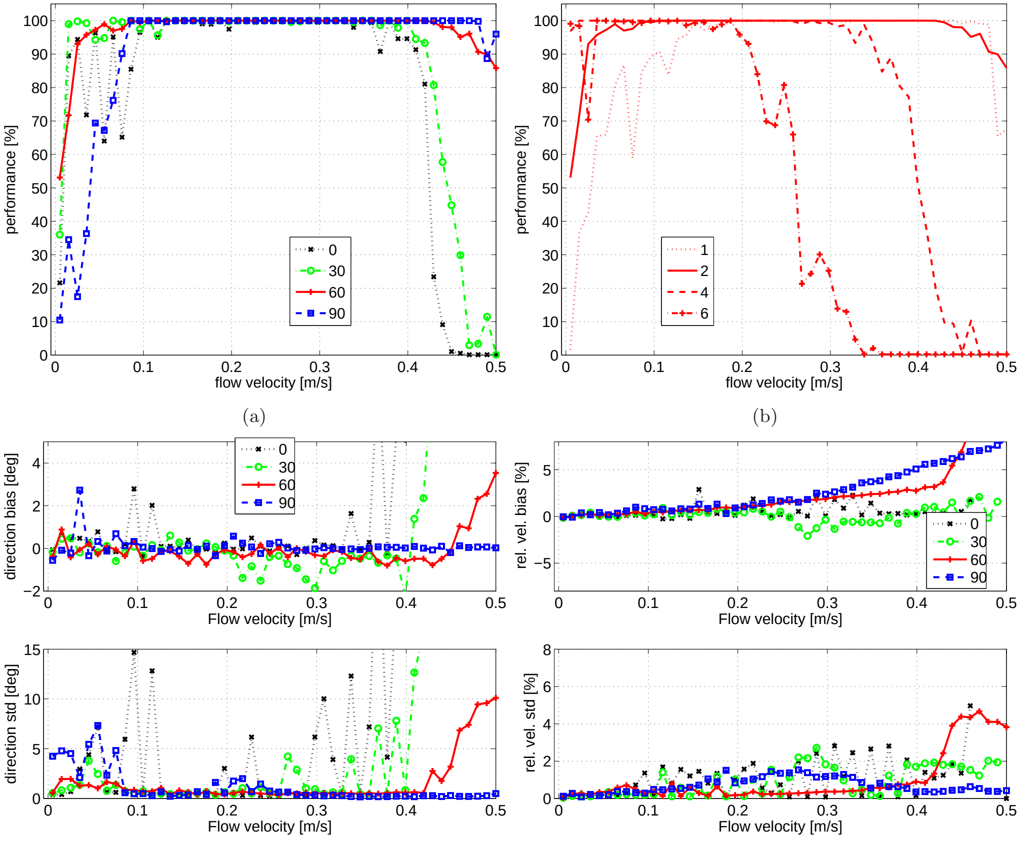

(a) (b)

(c) (d)

Figure 4: Performance of the estimation as a function of true velocity. (a)Percentage of correct estimates, i.e, estimates within ±5° and 20% of the true velocity vector for $\theta = 0°, 30°, 60°, 90°$ at k_{tprf} of 2. (b)Percentage of correct estimate for $\theta = 60°$ and $k_{tprf} = 1, 2, 4, 6$. (c)Bias and standard deviation for the angle at k_{tprf} of 2. (d)Relative bias and relative standard deviation for the velocity magnitude for the subset of estimates that are within ±5° of the true direction at k_{tprf} of 2.

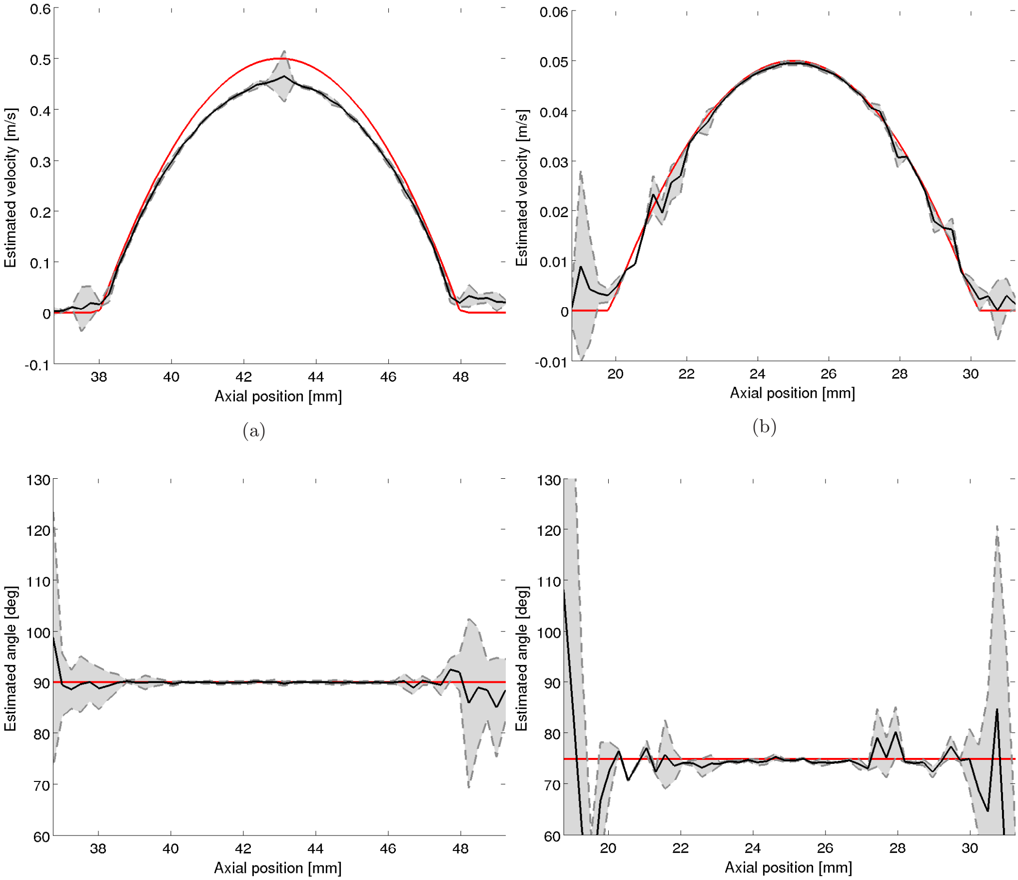

(a) (b)

(c) (d)

Figure 5: Simulated results for crossectional flow profile of the vessel with $v_{peak} = 0.5$ m/s and $\theta = 90°$ for k_{tprf} of 2 (left), and the vessel with $v_{peak} = 0.05$ m/s and $\theta = 75°$ for k_{tprf} of 6 (right). The top graphs show the estimated mean velocity profile and the standard deviation. The lower graphs show the bias and the standard deviation of the angle when radial lines are beamformed at 5° steps.

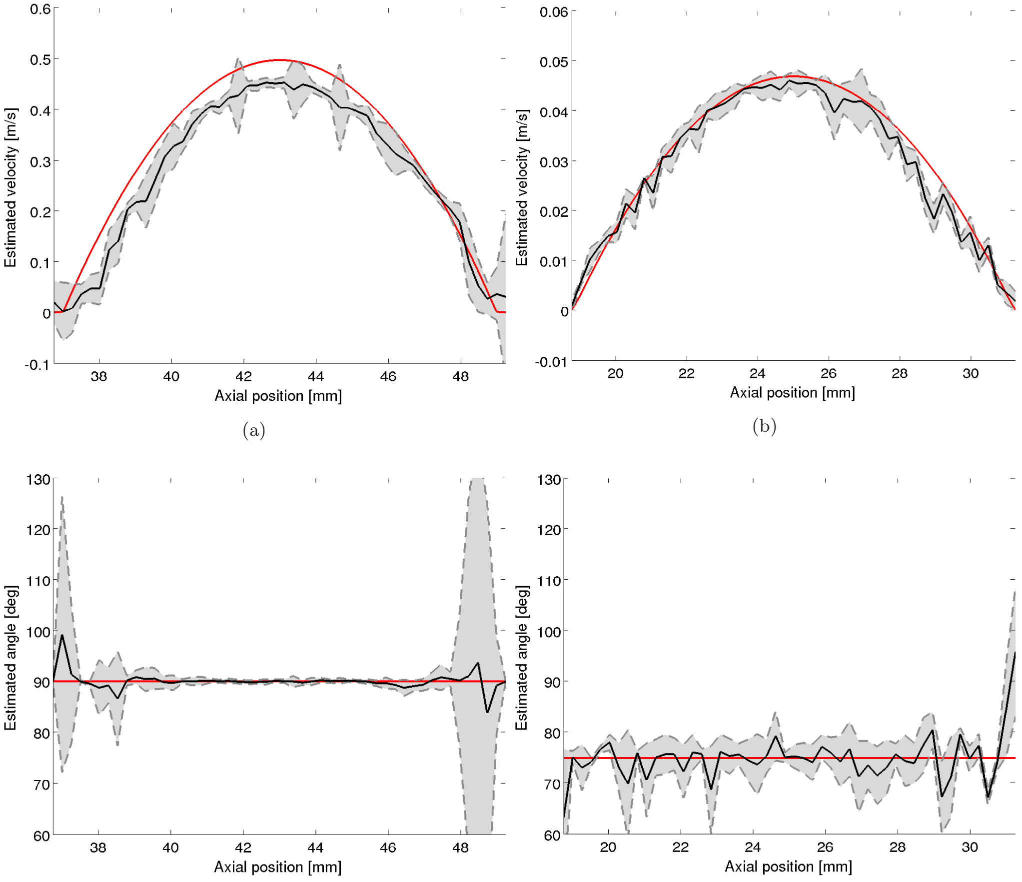

(a) (b)

(c) (d)

Figure 6: Measured results for crossectional flow profile of the vessel with $v_{peak} = 0.5$ m/s and $\theta = 90°$ for k_{tprf} of 2 (left), and the vessel with $v_{peak} = 0.05$ m/s and $\theta = 75°$ for k_{tprf} of 6 (right). The top graphs show the estimated mean velocity profile and the standard deviation. The lower graphs show the bias and the standard deviation of the angle when radial lines are beamformed at 5° steps.

Table 3: Bias and standard deviation of the estimates for the simulated vessels

v_{peak}	0.05 m/s				0.5 m/s			
	rel. vel.		angle		rel. vel.		angle	
k_{tprf}	bias	std. dev.	bias	std. dev.	bias	std. dev.	bias	std. dev.
1	-8.97	35.91	-0.45	17.80	-4.87	1.77	-0.05	2.00
2	-4.50	18.03	-2.48	8.83	-4.30	1.59	-0.03	0.58
4	-2.10	5.95	-0.80	3.24	-8.24	19.51	-0.07	2.53
6	0.29	2.39	-0.27	1.71	-37.68	14.02	0.54	12.43

4.2 Experimental results

The measurements are setup to match the geometry of the simulated vessels. However, due to the limitation that the flow rig only contains one mimicking vessel, the acquisitions for the two vessels are made independently. Fig. 6 show the estimated velocity profiles from the measurements. This is comparable with the simulation results. The estimated vector velocities for the two vessels, $v_{peak} = 0.5$ and 0.05 m/s, have a relative bias for the magnitude of -7.37% and -3.19% with a relative standard deviation of 6.12% and 5.75%, and the angle has a bias of -0.09° and -0.38°, with a standard deviation of 5.65° and 4.24°, respectively.

5. DISCUSSION

The fact that SA provides continuous data of the scatterer displacement, enables the synthesis of lower pulse repetition frequencies which allows the detection of lower velocities with the same dataset. Figure 4 (b), shows the result of applying different synthesized pulse repetition frequencies, represented as the change of k_{tprf}. From this figure, it can be seen that the range of detectable velocity is shifted towards lower velocities. Since the same data set is used, the k_{tprf} can be selected independently for any estimation point, removing the lower limit on the velocity estimation. The selection of the appropriate k_{tprf} is a topic of further research. When measuring lower velocities vessels, the movement of the tissue can be on the same order of magnitude as the movement of the blood, lowering the performance of the echo-canceling filter and yielding erroneous blood velocity estimates. This challenge also requires further study.

Another advantage is that vector velocities can be estimated for every point independently without previous knowledge of the direction of the flow, allowing the detection of complex flows. Fig. 4 (a), shows the detection of the correct angle is practically independent from the magnitude of the velocity, and shows that the bias and standard deviations for both angle and magnitude are kept low for a range of velocities, Fig. 4 (c,d).

However, there is an issue for higher ($k_{tprf} > 4$) where the angle estimates start failing more frequently for true flow directions lower than 30°. This can be attributed to the gradient phantom used in the study, as the phantom contains a large range of velocities in a small area. The faster moving scatterers in the vicinity can influence a higher decorrelation in the lower velocity scatterers, hence giving a lower maximum in the cross-correlation and an erroneous angle detection. This primary seen in angles lower than 30°, since the point spread function is asymmetric. It is important to mention that Couette flow is not seen in a clinical environment, and it therefore remains to be seen if this effect has any influence in a real environment.

Finally, it should be noted that the method can accurately estimate the vector velocities for simulations and measurements, as shown in Fig. 5 and Fig. 6. Both show agreement with the true velocity profile with low standard deviations and bias. The simulations give better estimates since it is a noise free environment.In a measurement setup there are several noise sources lowering the signal-to-noise ratio which leads to higher standard deviation.

Additionally, the method can reduce the operator dependence of flow imaging since it can select the appropriate k_{tprf} for every estimation point. It also enables the possibility of new applications, such as pressure gradients, perfusion imaging.

6. CONCLUSION

The performance of synthetic aperture, directional beamforming vector velocity estimator has been presented. It has been shown that the estimates can be done without previous knowledge of the direction of the flow, and with an extended range of detectable velocities it will be possible to accurately estimate velocities across the entire cardiac circle.

REFERENCES

1. C. Kasai, K. Namekawa, A. Koyano, and R. Omoto, "Real-Time Two-Dimensional Blood Flow Imaging using an Autocorrelation Technique," *IEEE Trans. Son. Ultrason.* **32**, pp. 458–463, 1985.
2. D. Dotti, E. Gatti, V. Svelto, A. Uggè, and P. Vidali, "Blood flow measurements by ultrasound correlation techniques," *Energia Nucleare* **23**, pp. 571–575, 1976.
3. S. I. Nikolov and J. A. Jensen, "Velocity estimation using synthetic aperture imaging," in *Proc. IEEE Ultrason. Symp.*, pp. 1409–1412, 2001.
4. J. A. Jensen and S. I. Nikolov, "Transverse flow imaging using synthetic aperture directional beamforming," in *Proc. IEEE Ultrason. Symp.*, pp. 1488–1492, 2002.
5. S. I. Nikolov and J. A. Jensen, "In-vivo Synthetic Aperture Flow Imaging in Medical Ultrasound," *IEEE Trans. Ultrason., Ferroelec., Freq. Contr.* **50**(7), pp. 848–856, 2003.
6. J. A. Jensen and S. I. Nikolov, "A method for real-time three-dimensional vector velocity imaging," in *Proc. IEEE Ultrason. Symp.*, pp. 1582–1585, 2003.
7. M. B. Stuart, B. G. Tomov, M. J. Pihl, and J. A. Jensen, "High frame rate synthetic aperture duplex imaging," in *Proc. IEEE Ultrason. Symp.*, July 2013.
8. J. A. Jensen, "Velocity vector estimation in synthetic aperture flow and B-mode imaging," in *IEEE International Symposium on Biomedical imaging from nano to macro*, pp. 32–35, 2004.
9. J. A. Jensen, "Directional velocity estimation using focusing along the flow direction: I: Theory and simulation," *IEEE Trans. Ultrason., Ferroelec., Freq. Contr.* **50**, pp. 857–872, 2003.
10. J. A. Jensen and R. Bjerngaard, "Directional velocity estimation using focusing along the flow direction: II: Experimental investigation," *IEEE Trans. Ultrason., Ferroelec., Freq. Contr.* **50**, pp. 873–880, 2003.
11. S. I. Nikolov, K. Gammelmark, and J. A. Jensen, "Recursive ultrasound imaging," in *Proc. IEEE Ultrason. Symp.*, **2**, pp. 1621–1625, 1999.
12. J. A. Jensen and S. I. Nikolov, "Directional synthetic aperture flow imaging," *IEEE Trans. Ultrason., Ferroelec., Freq. Contr.* **51**, pp. 1107–1118, 2004.
13. S. G. Foster, *A pulsed ultrasonic flowmeter employing time domain methods.* PhD thesis, Dept. Elec. Eng., University of Illinois, Urbana, Ill., 1985.
14. J. A. Jensen, *Estimation of Blood Velocities Using Ultrasound: A Signal Processing Approach*, Cambridge University Press, New York, 1996.
15. J. A. Jensen, "Field: A program for simulating ultrasound systems," *Med. Biol. Eng. Comp.* **10th Nordic-Baltic Conference on Biomedical Imaging, Vol. 4, Supplement 1, Part 1**, pp. 351–353, 1996.
16. J. A. Jensen and N. B. Svendsen, "Calculation of Pressure Fields from Arbitrarily Shaped, Apodized, and Excited Ultrasound Transducers," *IEEE Trans. Ultrason., Ferroelec., Freq. Contr.* **39**, pp. 262–267, 1992.
17. J. A. Jensen, O. Holm, L. J. Jensen, H. Bendsen, S. I. Nikolov, B. G. Tomov, P. Munk, M. Hansen, K. Salomonsen, J. Hansen, K. Gormsen, H. M. Pedersen, and K. L. Gammelmark, "Ultrasound Research Scanner for Real-time Synthetic Aperture Image Acquisition," *IEEE Trans. Ultrason., Ferroelec., Freq. Contr.* **52 (5)**, pp. 881–891, May 2005.
18. K. V. Ramnarine, D. K. Nassiri, P. R. Hoskins, and J. Lubbers, "Validation of a new blood mimicking fluid for use in Doppler flow test objects," *Ultrasound Med. Biol.* **24**, pp. 451–459, 1998.
19. J. M. Hansen, M. C. Hemmsen, and J. A. Jensen, "An object-oriented multi-threaded software beamformation toolbox," in *Proc. SPIE Med. Imag.*, **7968**, pp. 79680Y 1–9, March 2011.

Paper III

Adaptive Multi-Lag for Synthetic Aperture Vector Flow Imaging

Carlos Armando Villagómez-Hoyos, Matthias Bo Stuart, and Jørgen Arendt Jensen

Proceeding of IEEE International Ultrasonics Symposium, p. 1722-1725, Accepted for poster presentation in Chicago,Illinois, United States, 2014.

Adaptive Multi-Lag for Synthetic Aperture Vector Flow Imaging

Carlos A. Villagomez Hoyos, Matthias Bo Stuart and Jørgen Arendt Jensen

Center for Fast Ultrasound Imaging, Department of Electrical Engineering,
Technical University of Denmark, DK-2800 Lyngby, Denmark

***Abstract*—The range of detectable velocities in ultrasound flow imaging is linked to the user selection of pulse repetition frequency. Whenever a region with large differences in velocity magnitude is visualized, a trade-off has to be made. This work suggests an adaptive spatio-temporaly independent, multi-lag method, which is performed in synthetic aperture vector flow data. Measurements are made on laminar and pulsatile, transverse flow profiles. A 7 MHz linear array is connected to the SARUS research, and acquisitions are made on a vessel phantom with recirculating blood mimicking fluid driven by a software controlled pump. A multi-lag velocity estimation is performed, and a lag is adaptively selected for every estimation point. Results from the constant flow compared to a true parabolic profile show an improvement in relative bias from 76.99% to 0.91% and standard deviation from 13.60% to 1.83% for the low velocity flow of 0.04 m/s; and relative bias from -2.23% to -1.87% and standard deviation from 3.71% to 2.29% for the high velocity flow of 0.4 m/s.**

I. INTRODUCTION

Measuring blood flow using ultrasound is a well established tool and has proven to be a valuable resource in the clinic. However, the scanner must be carefully adjusted to the range of velocities to be mapped. Whenever a region with large differences in velocity magnitudes is visualized, a trade-off has to be made to visualize either low or high velocity flow. This occurs frequently due to the pulsatile nature of blood flow, during the different stages of the cardiac cycle, or when imaging vessels of different nature such as an artery and a vein. Some scanner systems provide an automatic pulse repetition frequency (PRF) feature, which adjusts the system PRF to obtain better estimates, but they fail to provide good accuracy for both low and high velocity flow at the same time.

Advances in ultrasound imaging techniques, such as synthetic aperture technique, firstly adopted from radar 35 years ago [1], are now being used to measure blood flow such as in the work by Jensen and co-workers [2], [3], [4], [5].

More recently, Stuart et al [6] presented a high dynamic vector velocity range using synthetic aperture, but the high pulse repetition frequency required for this technique hindered the vector velocity estimation for slowly moving flow.

This is, as stated by Foster [7], due to the fact that the point of maximum correlation and the corresponding velocity estimate will vary randomly as a consequence of the random noise in the backscattered signal, if the time between echoes decreases to a small value. On the other hand, if the time between emissions is too large, more scatterers will enter and leave the investigated region during the time between echoes, and the maximum correlation of the consecutive emissions will decrease. Thus, the precision of the estimate will decrease after an increased time between echoes.

To improve the precision of the estimate, an adaptive multi-lag algorithm is introduced. The basic principle was presented in [8], and is based on the fact that in syntethic aperture (SA) continuous data is available, making it feasible to correlate signals for any lag at every estimation point independent of its position.

An approach suggested by Jensen [9], that merges the cross-correlation estimator with directional beamforming, is used in combination with the multi-lag approach. An adaptive algorithm is then used to select the optimal lag. The criteria used for optimization is the standard deviation of the estimates contained in an overlapping window through time.

A quick overview of the theory behind the vector velocity estimation is given in Section II-A . The multi-lag approach is introduced in Section II-B, and the details of the adaptive algorithm are given in Section II-C. The performance of the approach is assessed through measurements on parabolic laminar flows in Section III. Results obtained on a vessel-mimicking phantom with an emulated pulsatile flow profile are presented.

II. METHODS

The beamformation of the directional signals is performed as described in [10], [11]. A time domain cross-correlation is applied to obtain the true velocity magnitude for several lags; finally the adaptive algorithm selects the estimate with the lowest standard deviation.

A. Vector Flow Imaging

In SA vector flow imaging (VFI), lines are beamformed along the direction of the flow. The directional beamforming is based on the total transmit and receive time-of-flight, also known as a delay and sum (DAS) beamformer.

To make a fully focused line, the DAS beamformed signals $L_i(\mathbf{r_x})$ from each of the individual emission i are summed to give a high resolution line

$$g(\mathbf{r_x}) = \sum_{i=1}^{N_e} L_i(\mathbf{r_x}), \tag{1}$$

where N_e is the number of emissions. If the emission sequence is repeating with no delay between the last emission of one iteration of the sequence and the first emission of the next iteration, then recursive synthetic aperture (RSA) imaging is possible [12].

The directional lines $g^t(x', \theta_m)$ and $g^{t+\Delta t}(x', \theta_m)$ are obtained at the flow angle θ_m as illustrated in Fig. 1. Here the signals are Δt seconds apart and centred at a given estimation point $\mathbf{r_x}$. The cross-correlation approach is used to estimate the true velocity magnitude, and can be estimated by obtaining the correlation lag at the maximum of the correlation function,

$$R_{12}(l, \theta_m) = \sum_{n=-N_{xcorr}/2}^{N_{xcorr}/2} g^t(n, \theta_m) g^{t+\Delta t}(n+l, \theta_m), \tag{2}$$

where l is the correlation lag and N_{xcorr} is the discrete length of the directional signals.

The probability of false peak detection is reduced by averaging over several estimates of R_{12} using the assumption that the scatterers can be considered quasi-static during several pulses. A number of cross-correlations, N_{xc} can thus, be averaged in the estimation.

For increased accuracy, a second-order polynomial is fit to the cross-correlation around l_{max}, and the position of the maximum correlation, $\hat{l}_{max}$, is found by the interpolation formula given in [13].

The velocity along the flow direction is then given by

$$\hat{v}_{x'} = \frac{\hat{l}_{max} \cdot d_r}{\Delta t}, \tag{3}$$

where d_r is the spatial sampling interval. The parameters used in estimating the flow are listed in Table I.

TABLE I
FLOW ESTIMATION PARAMETERS

Parameter	Symbol	Value
Spatial sampling interval	dr	0.1 λ
Number of samples in directional signals	N_{corr}	250
Number of correlations for each estimate	N_{xc}	15
Number of emissions	N_e	8
Pulse repetition frequency	f_{prf}	12500 Hz

B. Synthetic Aperture Multi-Lag

In SA, the whole region of interest is beamformed per emission. The image beamformed from a single emission will contain higher sidelobes, therefore it is necessary to synthesize a larger aperture to regain the sidelobe level and resolution obtained with traditional techniques. This means that a sequence of emissions have to be made before a high resolution image can be obtained, as expressed in (2). Given the high system f_{prf} used in SA, several emissions N_e can be used to synthesize a larger aperture without decreasing significantly the SNR due to the scatter motion, as investigated by Oddershede [14]; this number is normally between 3-16 emissions.

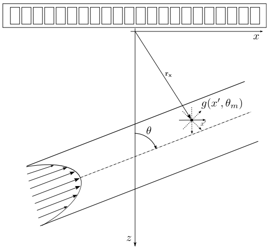

Fig. 1. Directional signals $g(x', \theta_m)$ around estimation point $\mathbf{r_x}$.

Velocity estimation using SA require two measurements obtained in exactly the same way, so the difference is only the blood's movement between the measurements. This implies that the time between the signals that can be correlated is

$$\Delta t = Lag \cdot \left(\frac{N_e}{f_{prf}}\right), \tag{4}$$

where $Lag = \{1, 2, 3, \ldots, N\}$.

Therefore, a multi-lag velocity estimate is available for each Lag value at every estimation point $\mathbf{r_x}$ in any sampled time t_n

$$\hat{v}_{x'}(\mathbf{r_x}, t_n, Lag), \tag{5}$$

where $t_n = \{t_0, t_0 + \frac{1}{f_{prf}}, t_0 + \frac{2}{f_{prf}}, \ldots\}$, when the recursive approach is used.

C. Adaptive Algorithm

An optimal Lag needs to be selected to attain more accurate estimates. Since the magnitude of the velocity is not known a priori, the exactitude of the estimates cannot be used as a criteria. However, the precision of the estimates can be improved by selecting the measurement with the lowest standard deviation, and this is the criteria used for selecting the optimal Lag.

As the nature of the blood flow is pulsatile, the standard deviation cannot be estimated over the whole measurement period. Therefore, it is necessary to generate a piecewise linear approximation of the flow waveform by fitting a line to the velocity estimates. The size of the segments is selected, so that the approximation resembles the flow waveform as close as possible . The value used in this work is 2 ms or 25 velocity estimates.

The optimal Lag is selected by minimizing the standard deviation of subtracting a piecewise linear approximation from the velocity estimate at each point as denoted by

$$Lag(\mathbf{r_x}, tn) = \arg\min_{Lag} \left[std\{\hat{v}'(\mathbf{r_x}, t_n, Lag) - \hat{v}_{pl}(\mathbf{r_x}, t_n, Lag)\}\right], \tag{6}$$

where $\hat{v}'(\mathbf{r_x}, t_n, Lag)$ is the segment from the estimated velocity and $\hat{v}_{pl}(\mathbf{r_x}, t_n, Lag)$ is the piecewise linear approximation at that segment.

Finally the $Lag(\mathbf{r_x}, tn)$ is smoothed using a Gaussian filter to reduce Lag jumps due to noise. For this work the size of the window used was 49x49 (4.9[mm] x 3.9[ms]).

III. MEASUREMENT RESULTS

Data for the velocity estimation approach is recorded using the SARUS experimental scanner [15]. A 7 MHz linear array transducer, type 8670 (BK Medical, Herlev, Denmark), is employed, and velocity estimates are obtained by beamforming directionally at an estimation point and cross-correlating the two measurements. Eight emissions are used in the sequence and the virtual sources are equally distributed around the center of the aperture. The virtual sources are located 40 mm behind the transducer ($F\# = -2$). The system f_{prf} is set at 12.5 kHz. A 1-cycle sinusoidal pulse with 64 elements are used in transmit, while all 128 elements are used in receive. All 128 channels are sampled at a frequency of 35 MHz.

A flow vessel phantom with a beam-to-flow angle of 90 degrees is used. The vessel has an internal diameter of 7 mm at a depth of 18 mm. For the measurements, a Shelley Medical software controlled pump (Toronto, Canada) is used to circulate blood-mimicking fluid[16] (Danish Phantom Design, Frederikssund, Denmark) in a closed loop circuit. The pump was used to imitate two different flow profiles: constant flow and a carotid flow.

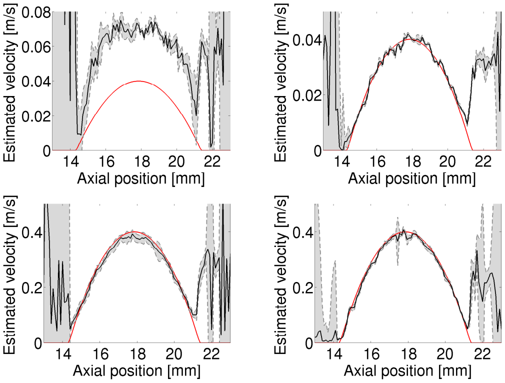

Fig. 2. Velocity profiles obtained at a beam-to-flow angle of 90 degrees with true parabolic profile in red. (Top) Peak velocity of 0.04 m/s; (Left) without adaptive multi-lag; and (Right) with adaptive multi-lag . (Bottom) Peak velocity of 0.4 m/s; (Left) without adaptive multi-lag; and (Right) with adaptive multi-lag.

A. Parabolic Constant Flow

The velocities are estimated with the adaptive multi-lag method and compared to the fixed lag approach. Data are acquired for 80 ms, yielding 1000 profiles from which the mean, standard deviation, and bias are calculated relative to a parabolic true profile. Two distinct flow rates are used for assessing the performance in both high and low velocity flow; the flow rate is set to 10 ml/sec corresponding to an estimated peak velocity of 0.4 m/s for the high velocity flow, and a flow rate of 1 ml/sec corresponding to an estimated peak velocity of 0.04 m/s for the low velocity flow.

A side-by-side comparison between the flow profiles is shown in Fig. 2. On top, the low velocity flows are shown for the traditional approach (left) and the proposed algorithm (right). The relative standard deviation and bias are 13.60% and 76.99%, for the traditional approach and 1.83% and 0.91%, for the proposed algorithm respectively.

On the bottom, the high velocity flows are shown. The relative standard deviation and bias are 3.71% and -2.23%, for the traditional approach and 2.29% and -1.87%, for the proposed algorithm respectively.

B. Pulsatile flow

A pulsatile carotid flow is programmed in the pump. The peak flow rate is set to 25 ml/sec and the period between pulses is set to 0.820 seconds. Three seconds of data are acquire yielding around 37000 estimates. A multi-lag velocity estimation is performed and a lag is adaptively selected at every estimation point, and are shown as the XY plane in Fig. 3. The velocity estimates are shown as a surface, where the X axis is the spatial dimension and the center line, and the Y axis is the temporal dimension showing the progression of the pulse through time. In the lower part of Fig. 3 a fixed lag is used, represented by a solid color on the XY plane, and the velocity estimates are also shown as a surface. The estimates in this figure are more noisy compared to the multi-lag approach. The lower velocities are specially affected when using a lower lag, since the backscattered noise degrades the signal. In contrast the XY plane in upper part of Fig. 3, which represent the used lag, follows correctly the shape of the pulse; selecting a lower lag around the peak flow in the center of the vessel and increasing it towards the outer part of the vessel. Since the velocity range of adjacent lags overlap each other a more uniform lag selection map is not needed.

IV. CONCLUSION

This paper demonstrates that with SA flow imaging it is possible to measure both low and high velocities with good accuracy and a high frame rate. The results show that there is a substantial improvement in the low velocity flow, and by using a different lag not only the standard deviation is lowered but also the bias in the estimates. This paper demonstrates that availability of continuous data that SA provides is a great asset for obtaining better velocity estimates in a wider range of velocities without loss of spatial resolution.

ACKNOWLEDGEMENT

This work was supported by grant 82-2012-4 from the Danish Advanced Technology Foundation and by BK Medical Aps.

REFERENCES

[1] C. B. Burckhardt, P.-A. Grandchamp, and H. Hoffmann, “An experimental 2 MHz synthetic aperture sonar system intended for medical use,” *IEEE Trans. Son. Ultrason.*, vol. 21, no. 1, pp. 1–6, January 1974.

[2] S. I. Nikolov and J. A. Jensen, “Velocity estimation using synthetic aperture imaging,” in *Proc. IEEE Ultrason. Symp.*, 2001, pp. 1409–1412.

[3] J. A. Jensen and S. I. Nikolov, “Transverse flow imaging using synthetic aperture directional beamforming,” in *Proc. IEEE Ultrason. Symp.*, 2002, pp. 1488–1492.

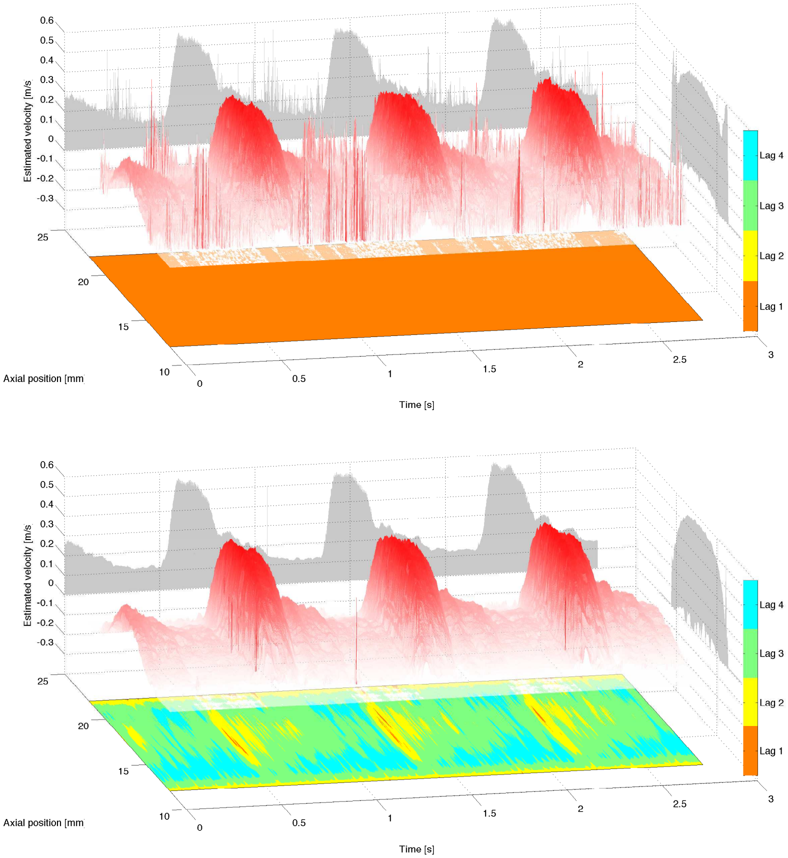

Fig. 3. Velocity profiles of the center line of the vessel through time. Projections of the two axis are shown as shadows. (Top) The velocity estimates using a fixed lag. (Bottom) The velocity estimates using the adaptive algorithm.

[4] S. I. Nikolov and J. A. Jensen, "In-vivo Synthetic Aperture Flow Imaging in Medical Ultrasound," *IEEE Trans. Ultrason., Ferroelec., Freq. Contr.*, vol. 50, no. 7, pp. 848–856, 2003.

[5] J. A. Jensen and S. I. Nikolov, "A method for real-time three-dimensional vector velocity imaging," in *Proc. IEEE Ultrason. Symp.*, 2003, pp. 1582–1585.

[6] M. B. Stuart, B. G. Tomov, M. J. Pihl, and J. A. Jensen, "High frame rate synthetic aperture duplex imaging," in *Proc. IEEE Ultrason. Symp.*, July 2013, pp. 623–626.

[7] S. G. Foster, P. M. Embree, and W. D. O'Brien, "Flow velocity profile via time-domain correlation: Error analysis and computer simulation," *IEEE Trans. Ultrason., Ferroelec., Freq. Contr.*, vol. 37, pp. 164–175, 1990.

[8] C. Villagomez-Hoyos, M. B. Stuart, and J. A. Jensen, "Increasing the dynamic range of synthetic aperture vector flow imaging," in *Proc. SPIE Med. Imag.*, vol. 9040, 2014, p. In press.

[9] J. A. Jensen, "Velocity vector estimation in synthetic aperture flow and B-mode imaging," in *IEEE International Symposium on Biomedical imaging from nano to macro*, 2004, pp. 32–35.

[10] ——, "Directional velocity estimation using focusing along the flow direction: I: Theory and simulation," *IEEE Trans. Ultrason., Ferroelec., Freq. Contr.*, vol. 50, pp. 857–872, 2003.

[11] J. A. Jensen and R. Bjerngaard, "Directional velocity estimation using focusing along the flow direction: II: Experimental investigation," *IEEE Trans. Ultrason., Ferroelec., Freq. Contr.*, vol. 50, pp. 873–880, 2003.

[12] S. I. Nikolov, K. Gammelmark, and J. A. Jensen, "Recursive ultrasound imaging," in *Proc. IEEE Ultrason. Symp.*, vol. 2, 1999, pp. 1621–1625.

[13] S. G. Foster, "A pulsed ultrasonic flowmeter employing time domain methods," Ph.D. dissertation, Dept. Elec. Eng., University of Illinois, Urbana, Ill., 1985.

[14] N. Oddershede and J. A. Jensen, "Effects influencing focusing in synthetic aperture vector flow imaging," *IEEE Trans. Ultrason., Ferroelec., Freq. Contr.*, vol. 54, no. 9, pp. 1811–1825, 2007.

[15] J. A. Jensen, H. Holten-Lund, R. T. Nilsson, M. Hansen, U. D. Larsen, R. P. Domsten, B. G. Tomov, M. B. Stuart, S. I. Nikolov, M. J. Pihl, Y. Du, J. H. Rasmussen, and M. F. Rasmussen, "SARUS: A synthetic aperture real-time ultrasound system," *IEEE Trans. Ultrason., Ferroelec., Freq. Contr.*, vol. 60, no. 9, pp. 1838–1852, 2013.

[16] K. V. Ramnarine, D. K. Nassiri, P. R. Hoskins, and J. Lubbers, "Validation of a new blood mimicking fluid for use in Doppler flow test objects," *Ultrasound Med. Biol.*, vol. 24, pp. 451–459, 1998.

Paper IV

In Vivo
High Dynamic Range Vector Flow Imaging.

Carlos Armando Villagómez-Hoyos, Matthias Bo Stuart, and Jørgen Arendt Jensen

Proceeding of IEEE International Ultrasonics Symposium, p. 1-4,
Accepted for poster presentation in Taipei, Taiwan, 2015.

In-Vivo High Dynamic Range Vector Flow Imaging

Carlos A. Villagomez-Hoyos, Matthias Bo Stuart and Jørgen Arendt Jensen
Center for Fast Ultrasound Imaging, Department of Electrical Engineering,
Technical University of Denmark, DK-2800 Lyngby, Denmark

Abstract—**Current vector flow systems are limited in their detectable range of blood flow velocities. Previous work on phantoms has shown that the velocity range can be extended using synthetic aperture directional beamforming combined with an adaptive multi-lag approach. This paper presents a first *in-vivo* example with a high dynamic velocity range. Velocities with an order of magnitude apart are detected on the femoral artery of a 41 years old healthy individual. Three distinct heart cycles are captured during a 3 secs acquisition. The estimated vector velocities are compared against each other within the heart cycle. The relative standard deviation of the measured velocity magnitude between the three peak systoles was found to be 5.11% with a standard deviation on the detected angle of 1.06°. In the diastole, it was 1.46% and 6.18°, respectively. Results proves that the method is able to estimate flow *in-vivo* and provide quantitative results in a high dynamic velocity range. Providing velocity measurements during the whole cardiac cycle for both arteries and veins.**

I. INTRODUCTION

Vector flow systems using ultrasound have become more appealing as they can accurately capture complex flow features presented in the vasculature compared to their 1-D counterpart. These newly available features have the potential of providing more insight into the progression of vascular diseases, and prove more useful for an accurate quantification of blood flow derived parameters (e.g. vorticity, pressure gradients).

Vector flow systems have been traditionally based on phase shift estimators [1]. These systems are limited in their detectable range of blood flow velocities due to the limited amount of data for velocity estimation. A choice between visualizing diastolic or systolic flow needs to be made by the physician. An adjustment of the pulse repetition frequency f_{prf} is frequently performed to avoid aliasing. Aliasing occurs when the frequency being sampled is greater than half the sampling rate, and this is a well known artefact in 1-D flow systems. However, in vector flow systems aliasing errors are more complex to detect than for 1-D estimators. For 2-D imaging, aliasing could be present in either or both of the velocity components. For example, in the particular case of cross-beam techniques, if only one receive signal is aliased a large and dominant lateral component is detected, as investigated in [2]. To mitigate these effects, several authors have proposed the use of higher number of emissions in combination with least-squares methods [3] and aliasing resistant algorithms [4].

Time shift estimators were introduced for ultrasound flow estimation in the mid 80s by Bonnefous[5], and it was shown to overcome the aliasing limit. Time shift estimators use the displacement between successive echo signals of the scatterers. The technique showed promising results, as it presented a better performance than phase shift techniques [6]. Additionally, time shift estimators perform better with short pulses, thus, no spatial resolution is sacrificed. However, the performance of the method severely deteriorates for larger beam-to-flow [7]. This was due to the rapid decorrelation of the blood signal, since the blood scatterers stayed inside the ultrasound beam for a shorter amount of time. To compensate for this the use of broader beams and parallel beamformers was suggested by Bonnefous [8], which generated a signal transverse to the ultrasound field. However, the approach solely worked for flow that was transverse to the ultrasound beam. Later, Jensen and Lacasa suggested using signals focused along the flow direction to solve the problem [9]. The approach, called directional beamforming, proved to be highly accurate in estimating flow velocities, and therefore was further investigated in [10], [11]. Jensen and Nikolov, furtherly improved the method by combining it with synthetic aperture techniques[12], which made the method more robust at detecting the correct angle with the proposed angle estimator [13]. Finally, the velocity range of the method was extended by Villagomez [14] using a multi-lag approach using the fact that synthetic aperture techniques provides continuous data. The method was validated on simulations and phantoms.

In this paper an *in-vivo* example of the proposed method is shown. The method is first described in Section II. The imaging sequence is described in Section II-C. A brief description of the algorithm is given in Section II-A. Finally, the results of an *in-vivo* acquisition on the femoral artery and vein of a 41 years old individual are presented in Section II-D.

II. METHODS

The directional velocity estimation is performed using the synthetic aperture approach developed by Jensen and Nikolov [15], and briefly described in Section II-A. Here diverging ultrasound waves are emitted using virtual sources, as described in Section II-C. The received multi-channel data are focused at any set of points within the interrogated region. The consecutive beamformed lines are correlated at mutiple lags and an adaptive algorithm selects the correct lag, as proposed in [14] and briefly described in Section II-B.

A. Vector Flow Imaging

The blood flow is tracked by focusing along directional lines $g(r', \theta_m)$ in the polar grid (r', θ_m), centred at the estimation point $\vec{x}$, as shown in Fig 1. Vessel wall echo-canceling is performed before the velocity estimation in a similar fashion

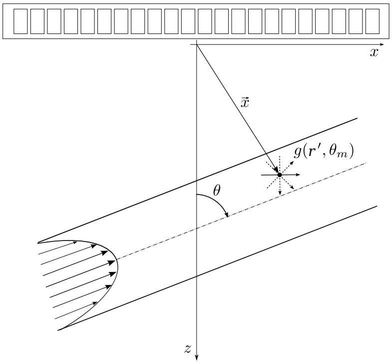

Fig. 1. Directional beamforming setup for a polar grid $g(r', \theta_m)$ centred at a single estimation point $\vec{x}$.

as described in [16]. The directional velocity estimation is performed as described by Jensen [10], by beamforming focused lines.

The focused lines $g(r', \theta_m)$ are correlated for lines acquired T_{eff} seconds apart. The correlation is calculated along a discrete set of angles θ_m, as follows,

$$R_{12}(l, \theta_m) = \sum_{k=-N_{xcorr}/2}^{N_{xcorr}/2} g^t(k, \theta_m) g^{t+T_{eff}}(k+l, \theta_m), \quad (1)$$

where l is the correlation lag and N_{xcorr} is the discrete length of the directional signals.

A number of cross-correlations, N_{xc} are averaged under the assumption that the scatterer's motion can be considered quasi-static during successive acquisitions. The velocities are estimated by finding the maximum of the correlation function (1). For increased accuracy, a second-order polynomial is fitted to the cross-correlation around $l_{max}(\theta_m)$, and the position of the maximum correlation, $\hat{l}_{max}$, is found by the interpolation formula given in [7].

The directional velocity estimate along the direction θ_m is given by

$$V(\theta_m) = \frac{\hat{l}_{max}(\theta_m) \cdot d_r}{T_{eff}}, \quad (2)$$

where d_r is the spatial sampling interval.

B. Adaptive multi-lag

The correlation time T_{eff} is selected adaptively from a set of discrete times multiple of the pulse repetition frequency $T_{eff} = Lag \cdot T_{PRF}$, where Lag is a positive integer value.

An optimal Lag is selected to attain more accurate estimates. The criteria for selecting the optimal Lag is to lower the relative standard deviations. As the nature of the blood flow is pulsatile, the relative standard deviation cannot be estimated over the whole measurement period. Therefore, it is necessary to generate a piecewise linear approximation of the flow waveform by fitting a line to the velocity estimates into a small time window. The size of the time window segments is selected, so that the approximation resembles the flow waveform as close as possible. The value used in this work is 6 ms or 15 velocity estimates.

The optimal Lag is selected by minimizing the standard deviation of subtracting a piecewise linear approximation from the velocity estimate at each point as denoted by

$$Lag(\mathbf{r_x}, tn) = \arg\min_{Lag} \left[std\{\hat{v'}(\mathbf{r_x}, t_n, Lag) - \hat{v}_{pl}(\mathbf{r_x}, t_n, Lag)\}\right], \quad (3)$$

where $\hat{v'}(\mathbf{r_x}, t_n, Lag)$ is the segment from the estimated velocity and $\hat{v}_{pl}(\mathbf{r_x}, t_n, Lag)$ is the piecewise linear approximation at that segment.

Finally, the $Lag(\mathbf{r_x}, tn)$ is smoothed using a median filter (3 [mm] x 20 [ms]) to reduce Lag jumps.

C. Measurement setup

A 128-element linear array probe connected to the experimental ultrasound scanner, SARUS [17], is used in the scanning. A duplex synthetic aperture (SA) sequence with virtual sources is emitted to acquire both B-mode and flow data sets. The emissions are interleaved, so that a B-mode emission is transmitted for every five flow emissions . An effective pulse repetition frequency is consequently $PRF_{eff} = PRF/(5+1)$.

The SA B-mode image consist of 128 individual emissions with virtual sources located behind the transducer using a 16 element sub-aperture. A 3-cycle sinusoidal pulse weighted by a 50% Tukey window is used as excitation waveform.

The flow sequence is implemented using a 64-element sub-aperture to increase the amount of emitted energy. The virtual sources are located behind the transducer as well. The transmitted wavefront is directed towards a region of interest (ROI), so the ROI is completely insonified in every emission (Fig. 2). A linear frequency modulated (FM) chirp tapered with a Tukey window is used as excitation wave. The excitation has a duration of 1.5 microseconds including the tapered region, with a frequency span from 3.5 MHz to 9.5 MHz. A 40% tapering is applied to reduce the effects of sidelobes. [18]. The transducer and acquisition parameters are listed in Table I.

The acoustic output of the sequence is measured for the two imaging modes using the scheme described in [19]. The measured intensities must satisfy limits regulated by the U.S. Food and Drug Administration (FDA). These limits concern the mechanical index, $MI \leq 1.9$, the derated spatial-peak-temporal-average intensity, $I_{spta} \leq 720\ mW/cm^2$ [20]. The measured values are $MI = 0.83$ and a $I_{spta} = 534\ mW/cm^2$, which are both below the FDA limits. The transducer surface temperature was also tested, where the transducer surface should not exceed an increase of 30°C and 6°C Celsius in air and in a simulated usage test, respectively. The maximum pulse repetition frequency (PRF) was adjusted to comply with these regulations, and was found to be 15 kHz for the current emission setup.

Table I
TRANSDUCER AND ACQUISITION PARAMETERS

Transducer		Transmit Parameters		
Parameter	Value	Parameter	B-mode	Flow
Trandsucer type	Linear array	F-number	-1	-3.5
Number of transducer elements	128	Number of emitting elements	16	64
Transducer element pitch	0.3 mm	Apodization window	Hanning	
Transducer element kerf	0.035 mm	Number of emissions	128	5
Transducer element height	4 mm	Pulse repetition frequency (PRF)	15 kHz	
Elevation focus	20 mm			
Center frequency	8 MHz			

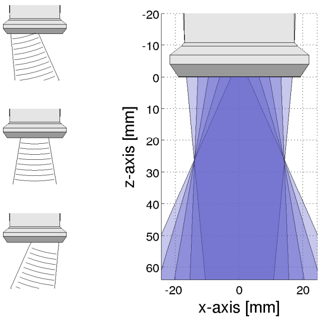

Fig. 2. Example of spherical waves used in the flow sequence (left). Overlay of the insonified area from each emission, and the actual region of interest shown in a darker shade (right).

D. *In vivo acquisition*

In-vivo acquisition are performed upon approval by The Danish National Committee on Biomedical Research Ethics. A healthy volunteer with no history of vascular or cardiac disease (41 years old male) entered the study after informed consent. The scan sequence was acquired during 3 seconds on a longitudinal view of the femoral artery and vein. The scan was recorded with the volunteer in standing position while performing dorsal and plantar flexion to simulate walking. The scan was carried out by an experienced radiologist.

III. MEASUREMENT RESULTS

A 3 sec acquisition is recorded on a femoral artery and vein simultaneously. The effective pulse repetition is 2500 Hz yielding 7500 velocity estimates in total. Fig. 3 (a) shows a single frame from the estimated vector flow image (VFI) at the time of a systole peak. The femoral artery presented no disturbed flow during the heart cycles, but marked reversed flow was seen during the beginning of diastole at the edges of the vessel. The magnitude of the reverse flow did not surpassed 0.05 m/s. A valve is also observed to disrupt the flow in the vein. However, this valve is not always visible in the B-mode image.

The velocity estimates were aligned at the three distinct peaks on the systole at the denoted line. Fig. 3 (b) and (c) shows the spatial and temporal repeatability of the measurement. The relative standard deviation (rel. std. dev.) respect the detectable velocity of 1 m/s is the performance metric for the velocity magnitude. A standard deviation (std. dev.) is also calculated for the estimated angles. The spatial rel. std. dev. at the systole was 5.11% with an angle std. dev. of 1.06°. In the diastole, it was 1.46% and 6.18°, respectively. The temporal rel. std. dev. during the whole cardiac cycle was 5.06% with an angle std.dev. of 8.06°.

IV. CONCLUSION

It has been shown that with the SA directional beamforming method flow during the whole cardiac cycle is available. Complex flow patterns are observed and the achieved high frame rate achieved make it possible to distinguish transient events that in other cases would be impossible to detect. The method have shown here to be robust and reliable as low standard deviations are obtained for distinct heart cycles at a high range of velocities.

ACKNOWLEDGEMENT

This work was supported by grant 82-2012-4 from the Danish Advanced Technology Foundation and by BK Medical Aps.

REFERENCES

[1] B. Dunmire, K. W. Beach, K.-H. Labs., M. Plett, and D. E. Strandness, “Cross-beam vector Doppler ultrasound for angle independent velocity measurements,” *Ultrasound Med. Biol.*, vol. 26, pp. 1213–1235, 2000.

[2] A. Swillens, L. Løvstakken, J. Kips, H. Torp, and P. Segers, “Ultrasound simulation of complex flow velocity fields based on computational fluid dynamics,” *IEEE Trans. Ultrason., Ferroelec., Freq. Contr.*, vol. 56, no. 3, pp. 546–556, 2009.

[3] B. Y. Yiu, S. S. Lai, and A. C. Yu, “Vector projectile imaging: time-resolved dynamic visualization of complex flow patterns.” *Ultrasound Med. Biol.*, vol. 40, no. 9, pp. 2295–2309, sept 2014.

[4] J. Flynn, R. Daigle, L. Pflugrath, P. Kaczkowski, and K. Linkhart, “Estimation and display for vector doppler imaging using planewave transmissions,” *Proc. IEEE Ultrason. Symp.*, pp. 413–418, 2011.

[5] O. Bonnefous and P. Pesqué, “Time domain formulation of pulse-Doppler ultrasound and blood velocity estimation by cross correlation,” *Ultrason. Imaging*, vol. 8, pp. 73–85, 1986.

[6] A. P. G. Hoeks, T. G. J. Arts, P. J. Brands, and R. S. Reneman, “Comparison of the performance of the rf cross correlation and Doppler autocorrelation technique to estimate the mean velocity of simulated ultrasound signals,” *Ultrasound Med. Biol.*, vol. 19, pp. 727–740, 1993.

[7] S. G. Foster, P. M. Embree, and W. D. O’Brien, “Flow velocity profile via time-domain correlation: Error analysis and computer simulation,” *IEEE Trans. Ultrason., Ferroelec., Freq. Contr.*, vol. 37, pp. 164–175, 1990.

[8] O. Bonnefous, “Measurement of the complete (3D) velocity vector of blood flows,” in *Proc. IEEE Ultrason. Symp.*, 1988, pp. 795–799.

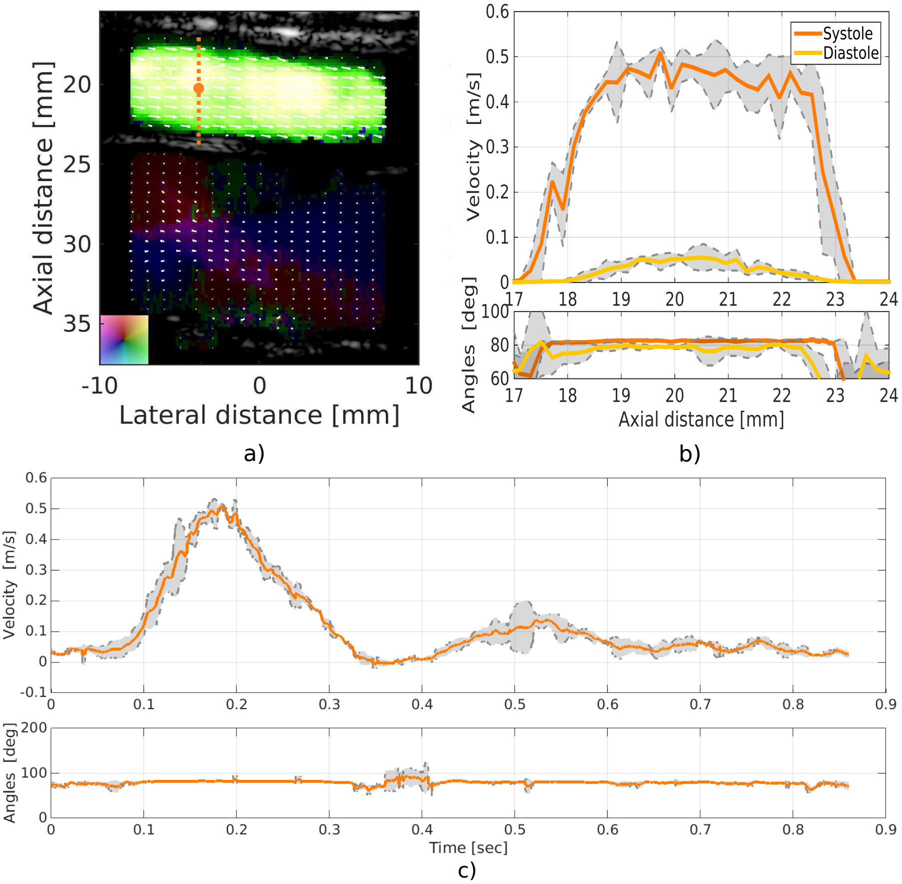

Fig. 3. In-vivo vector flow estimates of the femoral artery and vein of a healthy 41 years old male. Vector flow image of the flow during the systole is shown in (a). The three distinct systole peaks were aligned on the denoted line. The spatial repeatability of the measurement is plotted in (b) for both the systole and diastole. The temporal repeatability during the whole cardiac cycle in the denoted point is plotted in (c).

[9] J. A. Jensen and I. R. Lacasa, “Estimation of blood velocity vectors using transverse ultrasound beam focusing and cross-correlation,” in *Proc. IEEE Ultrason. Symp.*, 1999, pp. 1493–1497.

[10] J. A. Jensen, “Directional velocity estimation using focusing along the flow direction: I: Theory and simulation,” *IEEE Trans. Ultrason., Ferroelec., Freq. Contr.*, vol. 50, pp. 857–872, 2003.

[11] J. A. Jensen and R. Bjerngaard, “Directional velocity estimation using focusing along the flow direction: II: Experimental investigation,” *IEEE Trans. Ultrason., Ferroelec., Freq. Contr.*, vol. 50, pp. 873–880, 2003.

[12] J. A. Jensen and S. I. Nikolov, “Directional synthetic aperture flow imaging,” *IEEE Trans. Ultrason., Ferroelec., Freq. Contr.*, vol. 51, pp. 1107–1118, 2004.

[13] J. A. Jensen and N. Oddershede, “Estimation of velocity vectors in synthetic aperture ultrasound imaging.” *IEEE Trans. Ultrason., Ferroelec., Freq. Contr.*, vol. 25, pp. 1637–1644, 2006.

[14] C. A. Villagomez-Hoyos, M. B. Stuart, and J. A. Jensen, “Adaptive multi-lag for synthetic aperture vector flow imaging,” in *Proc. IEEE Ultrason. Symp.*, 2014, pp. 1722–1725.

[15] J. A. Jensen and S. I. Nikolov, “Transverse flow imaging using synthetic aperture directional beamforming,” in *Proc. IEEE Ultrason. Symp.*, 2002, pp. 1488–1492.

[16] A. D. Siggia and R. E. Passarelli, “Gaussian model adaptive processing (GMAP) for improved ground clutter cancellation and moment calculation,” *ERAD*, pp. 67–73, 2004.

[17] J. A. Jensen, O. Holm, L. J. Jensen, H. Bendsen, S. I. Nikolov, B. G. Tomov, P. Munk, M. Hansen, K. Salomonsen, J. Hansen, K. Gormsen, H. M. Pedersen, and K. L. Gammelmark, “Ultrasound research scanner for real-time synthetic aperture image acquisition,” *IEEE Trans. Ultrason., Ferroelec., Freq. Contr.*, vol. 52 (5), pp. 881–891, May 2005.

[18] T. Misaridis and J. A. Jensen, “Use of modulated excitation signals in ultrasound, Part II: Design and performance for medical imaging applications,” *IEEE Trans. Ultrason., Ferroelec., Freq. Contr.*, vol. 52, pp. 208–219, 2005.

[19] J. A. Jensen, M. F. Rasmussen, M. B. Stuart, and B. G. Tomov, “Rapid measurements of intensities for safety assessment of advanced imaging sequences,” in *Proc. SPIE Med. Imag.*, vol. 9040 90400Z-1, 2014.

[20] FDA, “510(k) guide for measuring and reporting acoustic output of diagnostic medical devices,” Center for Devices and Radiological Health, FDA, Tech. Rep., 1985.

Paper V

High Frame Rate Synthetic Aperture Vector Flow Imaging for Transthoracic Echocardiography.

Carlos Armando Villagómez-Hoyos, Matthias Bo Stuart, Thor Bechsgaard, Michael Bachmann Nielsen, and Jørgen Arendt Jensen

Proceeding of SPIE Ultrasound Imaging. Symp., Vol. 9790, p. 1,

Accepted for oral presentation in San Diego, California, United States, 2016.

High frame rate synthetic aperture vector flow imaging for transthoracic echocardiography

Carlos A. Villagómez-Hoyos[a], Matthias B. Stuart[a], Thor Bechsgaard[b]
Michael Bachmann Nielsen[b] and Jørgen Arendt Jensen[a]

[a]Center for Fast Ultrasound Imaging, Department of Electrical Engineering, Technical University of Denmark, DK-2800 Lyngby, Denmark;
[b]Department of Radiology, Rigshospitalet, Copenhagen University Hospital, DK-2100 Copenhagen, Denmark;

ABSTRACT

This work presents the first *in vivo* results of 2-D high frame rate vector velocity imaging for transthoracic cardiac imaging. Measurements are made on a healthy volunteer using the SARUS experimental ultrasound scanner connected to an intercostal phased-array probe. Two parasternal long-axis view (PLAX) are obtained, one centred at the aortic valve and another centred at the left ventricle. The acquisition sequence was composed of 3 diverging waves for high frame rate synthetic aperture flow imaging. For verification a phantom measurement is performed on a transverse straight 5 mm diameter vessel at a depth of 100 mm in a tissue-mimicking phantom. A flow pump produced a 2 ml/s constant flow with a peak velocity of 0.2 m/s. The average estimated flow angle in the ROI was $86.22^\circ \pm 6.66^\circ$ with a true flow angle of 90°. A relative velocity bias of -39% with a standard deviation of 13% was found. In-vivo acquisitions show complex flow patterns in the heart. In the aortic valve view, blood is seen exiting the left ventricle cavity through the aortic valve into the aorta during the systolic phase of the cardiac cycle. In the left ventricle view, blood flow is seen entering the left ventricle cavity through the mitral valve and splitting in two ways when approximating the left ventricle wall. The work presents 2-D velocity estimates on the heart from a non-invasive transthoracic scan. The ability of the method detecting flow regardless of the beam angle could potentially reveal a more complete view of the flow patterns presented on the heart.

Keywords: Medical Ultrasound, Vector Flow Imaging, Cardiac Imaging, Blood Flow, Synthetic Aperture

1. INTRODUCTION

Doppler echocardiography is an important tool for noninvasive assessment of cardiac function and management of cardiac patients.[1] It provides valuable insights to the pathophysiology of cardiac diseases and contributes to clinical decision making. Blood flow, pressures, and pressure gradients can be derived to assess systolic and diastolic performance as well as valve function. Therefore, accurate assessment of cardiac function during all phases of the heart cycle is a central issue in cardiac imaging.

Conventional cardiac ultrasound technologies allow for the measurement of blood or tissue velocity along the ultrasound beam at frame rates ranging from 20 to 100 Hz. However, a tradeoff between the field of view and the achievable frame rate is present due to the line per line nature of these conventional systems.[2]

High frame rate techniques, such as synthetic aperture and plane wave imaging, present an alternative to conventional techniques.[3–5] These techniques, which make use of wider transmit beams, allow for breaking the usual tradeoff between field of view and temporal resolution.[6] In transthoracic cardiac imaging, the use of high temporal resolutions for B-mode and 1-D Doppler modalities have been recently introduced.[7,8]

High frame rate 2-D vector velocity algorithms provides a more complete representation of the blood flow, but have only been implemented on linear arrays.[9–12] Studies of the heart, therefore, have been limited to intraoperative[13] or newborn[14] scans with the heart on a shallower depth. In transthoracic cardiac imaging, the

---

Further author information: Send correspondence to Villagomez-Hoyos, E-mail: cavh@elektro.dtu.dk.

heart is located at deeper depths and available only through limited acoustic windows through the rib cage. Therefore, the use of a smaller phased array is preferred. Diverging waves based algorithms, such as synthetic aperture, presents an attractive solution to high frame rate transthoracic scanning. Diverging waves present wider field of view than their focused counterpart and are, therefore, more suitable to smaller apertures such as the one present on the phased array.

Recently, the introduction of a novel 2-D high frame rate vector velocity algorithm, based on synthetic aperture,[9] has been investigated for linear arrays.[15] The algorithm has shown accurate estimates with hundreds to thousands of frames per second over large field of views. This accurate estimation of 2-D velocity vectors provides the removal of the need for manual angle correction, which would be difficult or impossible in conventional systems due to the complex nature of the hemodynamics in the heart.

In this paper, the first known demonstration of *in vivo* high frame rate cardiac vector flow imaging (VFI) using a noninvasive, transthoracic approach is presented. A brief theoretical description of the vector velocity estimation and a energy based echo-canceler is presented in Section 2. Section 3 describes the methods and imaging setup used in the pre-clinical testing. In Section 4, the flow phantom and *in vivo* results are presented and discussed, and Section 5 discusses the conclusions of this work.

2. THEORY

2.1 Velocity estimation

The velocity estimation idea, illustrated in Fig. 1, is based on the directional beamforming approach proposed by Jensen et al.[16] The velocity of a moving scatterer, represented by an elliptical point spread function (middle), is estimated by measuring the scatterer displacement during a sequence of consecutive emissions. The emission sequence is composed of at least two distinct transmit/receive aperture pairs, illustrated as the distinctly rotated point spread functions (PSF). For each emission, the received multichannel data are focused in a directional line $g(r, \theta_m)$, represented in Fig. 1 (bottom) as the semi-elliptic sections on which the directional line cuts the elliptic PSFs. The directional velocity estimation is then performed by correlating the directional lines $g(r, \theta_m)$ from the same type of rotated PSFs and obtaining a displacement distance d. Dividing this displacement by the time between emissions T_{eff} gives a velocity magnitude.

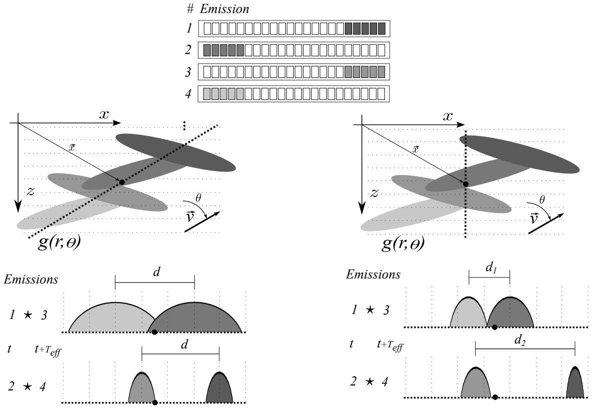

Figure 1: Point spread functions of a moving scatterer represented by ellipses. A directional line $g(r, \theta_m)$ is beamformed in the direction of the movement (left) and in an incorrect direction (right). Semi-elliptic sections on which the directional line cuts the rotated elliptic PSFs is shown at the bottom.

The measured velocity magnitude is only correct, if the directional line coincides with the direction of the movement as seen in Fig 1(left). In any other case, the obtained velocity magnitude will be erroneous, with an error dependent on the beam-to-flow-angle as seen in Fig. 1 (right). Therefore, for estimating the true velocity direction and magnitude, a set of angular velocity functions are calculated from a polar grid $g(r, \theta_m)$, as shown in the top of Fig. 2. The angular velocity function is the estimated velocities in each beamformed direction, where consecutive beamformed lines are cross-correlated and the displacement is detected. By dividing with the time between emitted signals, the magnitude of the angle velocity function at that beamformed angle is obtained. To obtain the true flow direction from the calculated angle velocity functions $\tilde{V}(\vec{x}, t, \theta_m)$, a set of M distinct steered PSF is needed. The true flow direction is estimated as the angle at the intersection of the angular velocity functions, see Fig. 2. Only two distinct steered PSFs are needed for a 2-D velocity estimation. However, in practice the use of a higher number of transmit/receive aperture combinations increases the robustness of the estimator.

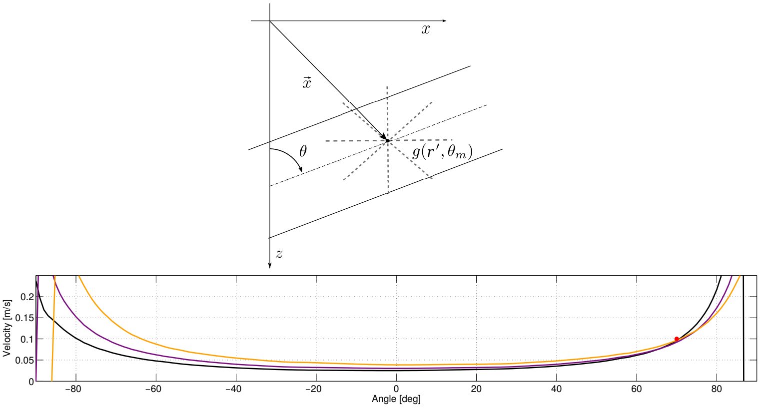

Figure 2: Directional beamformed lines in a polar grid (top). The angle velocity functions intersecting at the true flow direction shown as a red dot (bottom).

To calculate the intersection a two step approach is employed; first the closest coarse angles, where the intersection takes place, are selected. Then, the angle is refined by curve fitting between these two points and analytically finding the intersection angle.

In the first step, the closest coarse angles are selected by the use of a minimum distance criterion (MDC). The distance to be minimized in the MDC is defined as the sum of the normalized difference between the angle velocity functions:

$$\theta_{MDC_1} \quad = \quad \underset{\theta_m}{\text{Arg min}} \sum_{k=1}^{M-1} \sum_{l=k+1}^{M} \left| \frac{V_k(\theta_m) - V_l(\theta_m)}{\min(V_k(\theta_m), V_l(\theta_m))} \right| . \tag{1}$$

In the second step, the selected coarse angle θ_{MDC_1} and the adjacent coarse angle with the second lowest MDC value θ_{MDC_2} are used to extract the segments of the curves used to refine the angle estimate. The points θ_{MDC_1} and θ_{MDC_2} are used for the an inverse cosine curve fitting. The intersection of each pair of angle velocity functions is then estimated, and the angle estimate is the median of these values

$$\theta = median(\theta_{(l,k)}). \tag{2}$$

where l and k are the different pairs of fitted V_M curves.

After the angle has been obtained, the velocity magnitude is obtained by beamforming a directional line at the estimated angle. The final velocity magnitude is obtained using the summation of beamformed lines from distinct emissions instead of individual emissions. The summation generates a high resolution line as also known from synthetic aperture flow techniques.[9]

2.2 Energy-based tissue echo-canceler

A major challenge in blood velocity estimation is the cancellation of the tissue signal, thereby enhancing the low signal from blood cells. This is especially important in the heart, where the tissue velocities are significantly higher than in other organs. This problem is aggravated for vector velocity estimation as the frequency content of the signal from blood is strongly dependent on the flow angle,[17] thus, it is in general difficult to choose a single cut-off frequency that discriminates between moving tissue and the flowing structure. Therefore, to avoid the selection of a cut-off frequency a energy-based filter is proposed.

The energy filter is used to attenuate tissue motion that otherwise overpowers the signal from flowing structures. The filter operates on the velocity spectrum components. However, instead of selecting a conventional frequency cut-off threshold it selects an energy cut off threshold as shown in Fig. 3. The energy cut-off threshold can be adaptively selected as suggested by Siggia et al,[18] or it can be a pre-set value heuristically calculated given the characteristics of the imaging system.

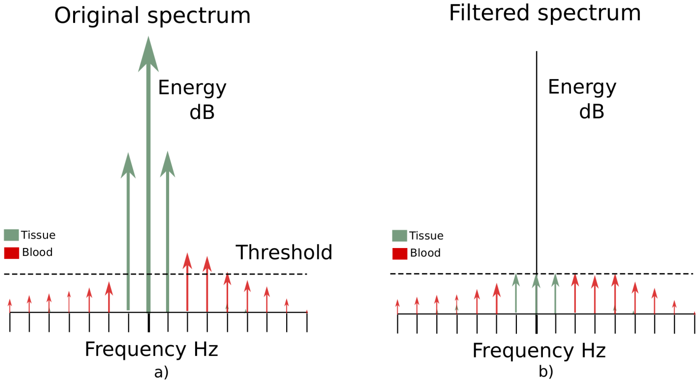

Figure 3: Illustration of the energy based filter on the velocity spectrum (a). The tissue energy is represented by the green arrows, and the blood energy by the red arrows. An energy level threshold is used to limit the amount of energy from the tissue scatterers (b).

The energy filter operates on the basis that blood signal have lower energy and broader velocity spectrum compared to tissue signals. Therefore, by limiting the amplitude of the velocity spectrum the energy of the tissue signal is overpowered by the energy of a more broad-band blood signal. Thus, the selected limiting threshold is the mean amplitude level of the blood signal spectrum.

The implementation of the pre-set energy filter is described as follows:

1. Fourier transform the RF data to obtain velocity spectrum.
2. Energy limit the spectrum amplitude to the pre-determined threshold conserving the phase information of the signals.
3. Inverse Fourier transform to obtain the filtered RF data.

3. METHOD

A 128-element phased array probe is used for the investigation. A synthetic aperture sequence is used to acquire the flow data set. The flow sequence is implemented using the full 128-element aperture for each emission to emulate a spherical wave emanating from a virtual point source located behind the aperture. The transmitted wavefront is directed towards a region of interest (ROI), so the ROI is completely insonified in every emission

Table 1: Transducer and Acquisition parameters

Transducer		Transmit Parameters	
Parameter	Value	Parameter	Value
Transducer type	Phased array	Excitation signal	3 period sine
Number of transducer elements	128	Number of emitting elements	128
Transducer element pitch	0.22 mm	Apodization window	Hanning
Transducer element kerf	0.022 mm	Number of distinct emissions	3
Transducer element height	15 mm	Pulse repetition frequency (PRF)	6.2 KHz
Elevation focus	85 mm	F-number	-1.6
Center frequency	3.5 MHz		

(Fig. 4). A 3-cycle sinusoidal pulse weighted by a 50% Tukey window is used as the excitation waveform. An effective pulse repetition time is $T_{eff} = \frac{T_{prf}}{3}$, where T_{prf} is the inverse of the system pulse repetition frequency (PRF). The transducer and acquisition parameters are listed in Table 1.

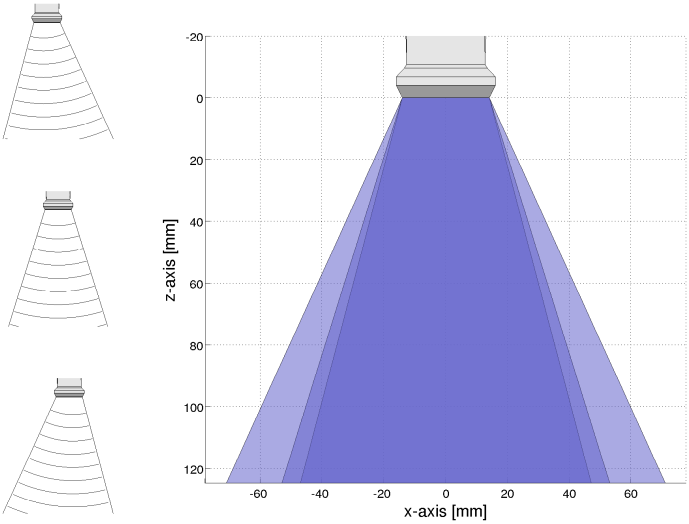

Figure 4: Example of spherical waves emanated from the first, second, and third emission used in the flow sequence (left). Overlay of the insonified area from each emission, and the actual region of interest shown in a darker shade (right).

The experimental ultrasound scanner SARUS[19] is used for acquiring data. The system acquires RF data from the individual transducer channels, and data are transferred to a computing cluster, where they are stored and processed off-line. The received RF data contains 128 channels sampled at 35 MHz with 12 bits resolution.

3.1 Flow phantom

Measurements are made in a straight vessel phantom. A Shelley Medical software controlled pump (Toronto, Canada) is used to circulate blood-mimicking fluid[20] (Danish Phantom Design, Frederikssund, Denmark) in a closed loop circuit. The system is set for a constant flow rate of 2 ml/s in a 5 mm diameter wide vessel. The straight vessel is embedded in tissue-mimicking material and is located 100 mm in depth and is completely transverse to the ultrasound beam.

3.2 In-vivo

An in-vivo acquisition is performed after approval by The Danish National Committee on Biomedical Research Ethics. A healthy volunteer with no history of cardiovascular disease (29 year old man) is scanned after informed consent. An ultrasound scan sequence, as described in Section 3, is acquired on a parasternal long-axis view (PLAX). The scans are obtained with the patient in left lateral decubitus position and the transducer placed near the sternum in the left third or fourth intercostal space.

Intensity measurements are carried out prior to the scan, since measured intensities must satisfy limits regulated by the U.S. Food and Drug Administration (FDA).[21] These limits concern the mechanical index, $MI \leq 1.9$, the derated spatial-peak-temporal-average intensity, $I_{spta} \leq 720$ mW/cm^2. The measured values using the scheme described by Jensen,[22] are $MI = 0.62$ and a $I_{spta} = 106.8$ mW/cm^2, which are both below the FDA limits. The transducer surface temperature was also tested, where the transducer surface did not exceeded an increase of 30° in air or 10° Celsius in simulated usage test.

4. RESULTS

The generated 2-D velocity vectors are overlayed on the high frame rate B-mode image frames. The overlaying colors are change depending on the flow magnitude and direction of the estimated flow, and are in accordance to the color wheel map provided in the lower right corner of each frame. The estimates are generated at a frame rate of 2,000 Hz.

4.1 Phantom study

Results from the flow phantom acquisition are shown in Fig. 5. The flow within the vessel is masked with a marked ROI. The angle of flow in the ROI had a mean angle of 86.22 ± 6.66 degrees at one standard deviation. The relatively small bias may be caused by misalignment in the physical setup. The measured velocities presented distinct biases depending on their spatial position. The worst case is at the middle of the vessel, where the bias reaches -34% with standard deviations of 32%. For the left and right profiles the relative bias are -33% and 23% with a standard deviation of -39% and 13%, respectively. The source of this underestimation respect to the true reference is unknown and must be further investigated.

4.2 In-vivo

A parasternal long-axis (PLAX) view centred on the aortic valve (AoV) during systole is shown in Fig. 6 (top). A high quality B-mode PLAX view obtained using a commercial scanner seconds prior to the experimental scan is presented in the upper right corner as an anatomical reference. The left ventricle (LV) is observed on the left of image sector, while the AoV and aorta are observed on the right. The blood flow in Fig. 6 (top) is detected flowing from the LV cavity through the AoV into the aorta artery. The flow direction is consistent with the anatomy as the flow is detected parallel to the artery wall and heading towards the aorta during the systole at velocity magnitudes of around 1 m/s.

A second view, in Fig. 6 (bottom), shows a centred LV during the filling state with the mitral valve located in the right left corner, more clearly seen in the reference image. Blood flow is seen emanating from the mitral valve and splitting in two ways when approximating the left ventricle wall. A complex flow pattern is formed when the blood flow fills the left ventricle showing a consistent behaviour with the mitral valve position.

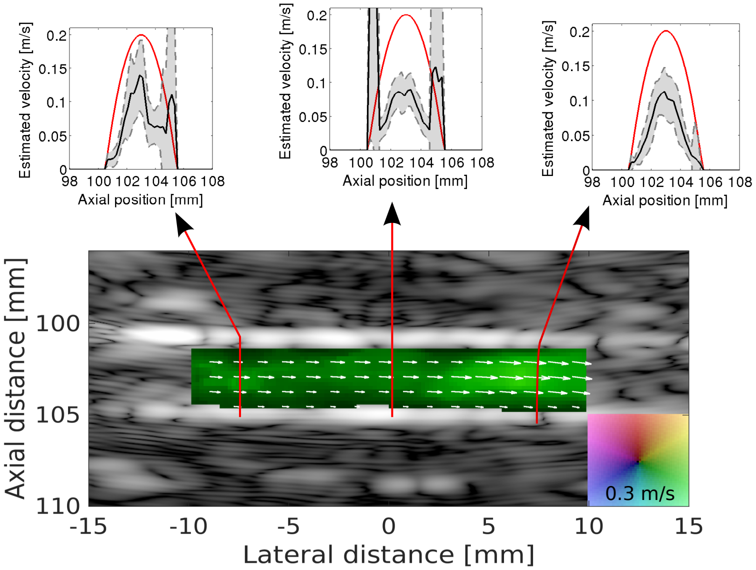

Figure 5: Mean velocity profiles and standard deviations for three different positions (top). 2-D velocity vectors in a vessel phantom at 100 mm depth, with arrows indicating velocity direction and relative magnitude with corresponding 2-D color wheel map (bottom).

5. CONCLUSION AND PERSPECTIVES

In this work, we investigated the ability of synthetic aperture flow techniques to map 2-D velocity vectors of ventricular blood flow with a frame rate of 2,000 images per second over a full two-dimensional sector view. A major advantage of the technique is the ability to estimate flow regardless of the beam-to-flow angle. The technique also provides velocity information at every location in the image simultaneously and at high frame rate.

Finally, vector velocity techniques have the capability to improve guidance and feedback to researchers and cardiologists through improved visualization of turbulence and the removal of the angle-correction of conventional spectral Doppler estimation.

REFERENCES

1. R. A. Nishimura and A. J. Tajik, “Evaluation of diastolic filling of left ventricle in health and disease: Doppler echocardiography is the clinician rosetta stone,” *J. Am. Coll. Cardiol.* **30**(1), pp. 8–18, 1997.
2. N. S. Anavekar and J. K. Oh, “Doppler echocardiography: A contemporary review,” *J. Cardiology* **54**, pp. 347–358, 2009.
3. J. T. Ylitalo, “A fast ultrasonic synthetic aperture imaging method: application to NDT,” *Ultrasonics* , pp. 331–333, 1996.
4. J. Y. Lu, “2D and 3D high frame rate imaging with limited diffraction beams,” *IEEE Trans. Ultrason., Ferroelec., Freq. Contr.* **44**, pp. 839–855, 1997.
5. L. Sandrin, S. Catheline, M. Tanter, X. Hennequin, and M. Fink, “Time-resolved pulsed elastography with ultrafast ultrasonic imaging,” *Ultrason. Imaging* **21**(4), pp. 259–272, 1999.
6. S. I. Nikolov and J. A. Jensen, “In-vivo Synthetic Aperture Flow Imaging in Medical Ultrasound,” *IEEE Trans. Ultrason., Ferroelec., Freq. Contr.* **50**(7), pp. 848–856, 2003.
7. M. B. Stuart, J. Jensen, A. H. Brandt, S. I. Nikolov, M. B. Nielsen, and J. A. Jensen, “In-vivo synthetic aperture and plane wave high frame rate cardiac imaging,” in *Proc. IEEE Ultrason. Symp.*, pp. 1209–1212, 2014.

8. B.-F. Osmanski, D. Maresca, E. Messas, M. Tanter, and M. Pernot, “Transthoracic ultrafast Doppler imaging of human left ventricular hemodynamic function,” *IEEE Trans. Ultrason., Ferroelec., Freq. Contr.* **61**, pp. 1268–1275, August 2014.
9. J. A. Jensen and S. I. Nikolov, “Directional synthetic aperture flow imaging,” *IEEE Trans. Ultrason., Ferroelec., Freq. Contr.* **51**, pp. 1107–1118, 2004.
10. J. Udesen, F. Gran, K. L. Hansen, J. A. Jensen, C. Thomsen, and M. B. Nielsen, “High frame-rate blood vector velocity imaging using plane waves: simulations and preliminary experiments,” *IEEE Trans. Ultrason., Ferroelec., Freq. Contr.* **55**(8), pp. 1729–1743, 2008.
11. J. Bercoff, G. Montaldo, T. Loupas, D. Savery, F. Meziere, M. Fink, and M. Tanter, “Ultrafast compound Doppler imaging: providing full blood flow characterization,” *IEEE Trans. Ultrason., Ferroelec., Freq. Contr.* **58**, pp. 134–147, January 2011.
12. B. Denarie, T. A. Tangen, I. K. Ekroll, N. Rolim, H. H. Torp, T. Bjastad, and L. Løvstakken, “Coherent plane wave compounding for very high frame rate ultrasonography of rapidly moving targets,” *IEEE Trans. Ultrason., Ferroelec., Freq. Contr.* **32**(7), pp. 1265–1276, 2013.
13. K. L. Hansen, H. Møller-Sørensen, M. M. Pedersen, P. M. Hansen, J. Kjaergaard, J. T. Lund, J. C. Nilsson, J. A. Jensen, and M. B. Nielsen, “First report on intraoperative vector flow imaging of the heart among patients with healthy and diseased aortic valves,” *Ultrasonics* **56**, pp. 243–250, 2014.
14. S. Fadnes, S. A. Nyrnes, H. Torp, and L. Lovstakken, “Shunt flow evaluation in congenital heart disease based on two-dimensional speckle tracking,” *Ultrasound Med. Biol.* **40**(10), pp. 2379–2391, 2014.
15. C. A. Villagomez-Hoyos, M. B. Stuart, K. L. Hansen, M. B. Nielsen, and J. A. Jensen, “Accurate angle estimator for high frame rate 2-D vector flow imaging,” *IEEE Trans. Ultrason., Ferroelec., Freq. Contr.* , p. Submitted, 2016.
16. J. A. Jensen, “Directional velocity estimation using focusing along the flow direction: I: Theory and simulation,” *IEEE Trans. Ultrason., Ferroelec., Freq. Contr.* **50**, pp. 857–872, 2003.
17. M. E. Anderson, “Vector flow estimator isomorphism and wall filter requirements,” in *Proc. SPIE Med. Imag.*, **4325**, pp. 215–226, 2001.
18. A. D. Siggia and R. E. Passarelli, “Gaussian model adaptive processing (GMAP) for improved ground clutter cancellation and moment calculation,” *ERAD* , pp. 67–73, 2004.
19. J. A. Jensen, O. Holm, L. J. Jensen, H. Bendsen, S. I. Nikolov, B. G. Tomov, P. Munk, M. Hansen, K. Salomonsen, J. Hansen, K. Gormsen, H. M. Pedersen, and K. L. Gammelmark, “Ultrasound research scanner for real-time synthetic aperture image acquisition,” *IEEE Trans. Ultrason., Ferroelec., Freq. Contr.* **52 (5)**, pp. 881–891, May 2005.
20. K. V. Ramnarine, D. K. Nassiri, P. R. Hoskins, and J. Lubbers, “Validation of a new blood mimicking fluid for use in Doppler flow test objects,” *Ultrasound Med. Biol.* **24**, pp. 451–459, 1998.
21. FDA, “Information for manufacturers seeking marketing clearance of diagnostic ultrasound systems and transducers,” tech. rep., Center for Devices and Radiological Health, United States Food and Drug Administration, 2008.
22. J. A. Jensen, M. F. Rasmussen, M. J. Pihl, S. Holbek, C. A. Villagomez-Hoyos, D. P. Bradway, M. B. Stuart, and B. G. Tomov, “Safety assessment of advanced imaging sequences, I: Measurements,” *IEEE Trans. Ultrason., Ferroelec., Freq. Contr.* **63**(1), pp. 110–119, 2016.

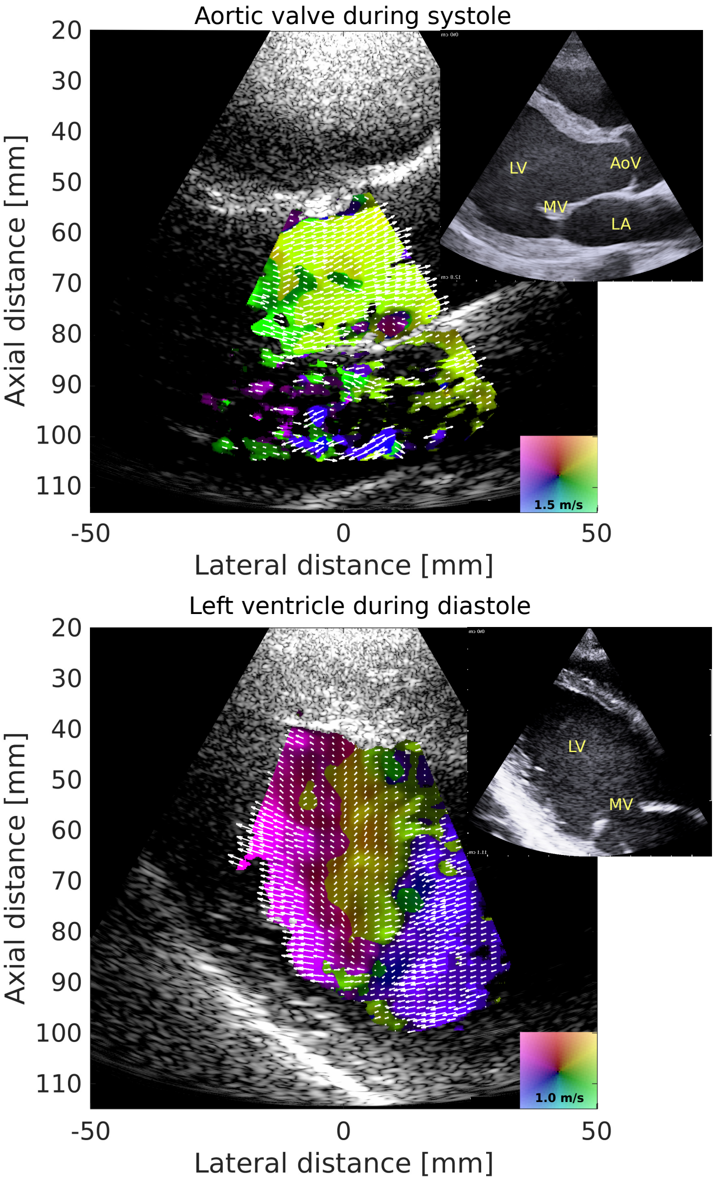

Figure 6: Vector Flow imaging frames of transthoracic scans on the heart. Two parasternal long-axis views of the heart; one centred on the aortic valve during systole (top) and the other on the left ventricle during the filling stage (bottom). A high quality B-mode on the right corner is provided as anatomical reference.

Abstract I

High frame rate synthetic aperture 3D vector flow imaging.

Carlos Armando Villagómez-Hoyos, Simon Holbek, Matthias Bo Stuart, and Jørgen Arendt Jensen

Proceeding of SPIE Ultrasound Imaging. Symp., TBC,

Accepted for oral presentation in Tours, France, 2016.

Submission ID: 826
Subject Classification: MBF Blood Flow Measurement
Presentation Preference: Oral
Student Paper: No
Invited Speaker: No

Keywords: synthetic aperture, 3-D, Vector flow imaging

High Frame Rate Synthetic Aperture 3D Vector Flow Imaging

Carlos Armando Villagómez Hoyos[1], Simon Holbek[1], Matthias Bo Stuart[1], Jørgen Arendt Jensen[1]
[1]*Technical University of Denmark, Copenhagen, Denmark*

Background, Motivation and Objective

Blood flow in the cardiovascular system is complex as it generally moves in all three spatial dimensions and varies as a function of time. Transient events, such as vortices, can arise and vanish within hundreds of milliseconds. Current methods for high frame rate flow velocity estimations are restricted to 1-D or 2-D rendering or 3-D estimation in a single plane. To solve these problems, a method for obtaining 3-D velocities using a matrix array and diverging waves is described. The aim of the work is to show synthetic aperture ability to measure the temporal evolution of complex flow patterns within a 3-D-volume at high frame rates (>1000 Hz).

Statement of Contribution/Methods

A 2-D 32x32 Vermon matrix array was used in combination with the experimental ultrasound scanner SARUS to transmit and acquire data from 1024 channels. Unfocused synthetic aperture emissions (using 3.0 MHz; 1-cycle pulse; 10 kHz PRF; 5 emissions) are transmitted to insonify a volume of interest. The received signals are then directionally beamformed in a spherical grid along all directions, where directional velocity estimates are obtain for each of them. The angle is resolved by using a minimum distance criterion (MDC) on the calculated velocity estimates. The velocity magnitude is then obtained along the estimated angle.

Results/Discussion

Results for an experiment performed on a straight vessel flow phantom (Ø = 8 mm), with constant flow rate of 4 ml/s are shown in the figure. The surface plot of the mean velocity magnitude, in the XZ plane when Y = 0, shows a parabolic flow profile obtained from 160 estimates corresponding to 100 ms (Fig. a). The estimated flow rate was found to be 3.23 ml/s. The expected parabolic profiles are shown in red for the distinct velocity components (Fig. b) along the Z (top) and X (bottom) axis. The relative standard deviation is found to be 20%, 12%, 1.1%; for Vx, Vy, and Vz components, respectively. The method was able to estimate 3-D velocities in a 1x1x1cm 3-D-volume with a high temporal resolution (1.6 kHz). The work shows that it is feasible, with synthetic aperture techniques, to estimate 3-D velocities on 3-D-volumes at high temporal resolution without any ECG gating, providing more insight into the hemodynamics of the cardiovascular system.

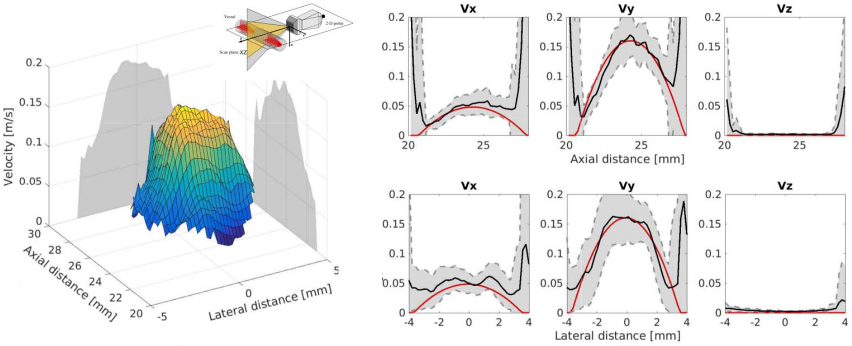

a) b)